TESIS DE LA UNIVERSIDAD DE ZARAGOZA

2021 135

Anna Vráblova

# 3d, 4f and 3d-4f complexes based on selected N,O- and O-donor ligands

Director/es
Falvello, Larry
Cernak, Juraj



ISSN 2254-7606

Prensas de la Universidad
Universidad Zaragoza

ISSN 2254-7606

Universidad Zaragoza
1542

Tesis Doctoral

# 3D, 4F AND 3D-4F COMPLEXES BASED ON SELECTED N,O- AND O-DONOR LIGANDS


Autor

Anna Vráblova

Director/es

Falvello, Larry
Cernak, Juraj



**UNIVERSIDAD DE ZARAGOZA**
**Escuela de Doctorado**

Programa de Doctorado en Química Inorgánica

2021

**PAVOL JOZEF ŠAFÁRIK UNIVERSITY IN KOŠICE**

**FACULTY OF SCIENCE**

**&**

**UNIVERSITY OF ZARAGOZA**

**FACULTY OF SCIENCE**

# 3*d*, 4*f* AND 3*d*-4*f* COMPLEXES BASED ON SELECTED N,O- AND O-DONOR LIGANDS

**2020** **Mgr. Anna VRÁBLOVÁ**

PAVOL JOZEF ŠAFÁRIK UNIVERSITY IN KOŠICE
FACULTY OF SCIENCE
&
UNIVERSITY OF ZARAGOZA
FACULTY OF SCIENCE

# 3*d*, 4*f* AND 3*d*-4*f* COMPLEXES BASED ON SELECTED N,O- AND O-DONOR LIGANDS

**DISSERTATION THESIS**

| | |
|---|---|
| Study program: | Inorganic Chemistry |
| Institute: | Institute of Chemistry / Department of Inorganic Chemistry |
| Supervisors: | prof. Juraj Černák, DrSc.<br>prof. Lawrence R. Falvello |

Košice 2020

**Mgr. Anna VRÁBLOVÁ**

## Acknowledgements

At this point, I would like to thank my supervisors Juraj Černák and Lawrence R. Falvello for their professional leadership and scientific support. I am much obligated also to Milagros Tomás for her suggestive ideas and experimental advice. Special thanks belong to Isabel Mayoral who has never refused to help in the laboratory or wherever her help was needed.

I would like to acknowledge Roman Boča and his team for the magnetic measurements and interpretations of their results.

I thank both universities, P. J. Šafárik University in Košice (Slovakia) and University of Zaragoza (Spain) for the unparalleled opportunity to undergo the double degree doctorate programme. Joint doctorate opens not only borders but also our minds.

My research and travelling was financialy supported by National Scholarship Programme (Slovakia), Erasmus programme (P. J. Šafárik University in Košice, Slovakia), Slovak grant agencies (APVV-14-0078, APVV-14-0073, APVV-18-0016, VEGA 1/0534/16, VEGA 1/0063/17 and VEGA 1/0075/13), P. J. Šafárik University (VVGS-PF-2016-72623 and VVGS-PF-2018-777), Ministerio de Ciencia, Innovación y Universidades (Spain, Grants MAT2011-27233-C02-01, MAT2011-27233-C02-02, MAT2015-68200-C2-1-P, PGC2018-093451-B-I00), European FEDER funds (Spain), the Diputación General de Aragón (Spain, Project M4, E11_17R) and the project NFP313010V954 of call OPVaI-VA/DP/2018/1.1.3-07 (Spain).

**Abstract**

The present work is focused on the study of single-molecule magnets based on selected transition metals and lanthanides using a selected Schiff base ligand. The first part deals with the theoretical interpretation of the magnetic phenomenon of SMM as well as the coordination and magnetic properties of complexes containing central atoms Ni(II), Co(II)/(III), Ce(III), Gd(III) and Dy(III). In the experimental part, the method of preparation of the required complexes was determined in the first place - the so-called "self-assembly" method. According to the synthetic procedures thus determined, 21 compounds were prepared, which were physically and chemically characterized and their crystal structure was determined by X-ray structure analysis. One chapter is focused on the crystallographic study of polymorphism, where FIM methods and analysis of Hirshfeld surfaces were used for a more detailed examination of two polymorphs $[Co^{III}_2(o\text{-}van\text{-}en)_3]\cdot 4CH_3CN$. The work also includes a crystallographic study of a topotactic reaction of the SC-SC (Single Crystal-to-Single Crystal) type in which the complex $[Ni(o\text{-}van\text{-}en)DyCl_3(H_2O)]$ dehydrates at a higher temperature and subsequently dimerizes to form a new complex $[Ni_2(o\text{-}van\text{-}en)_2Dy_2Cl_6]$. From the prepared substances, 4 complexes were selected and subjected to magnetic examination with respect to SMM properties. For all four substances, the slow relaxation of magnetization, typical for single-molecule magnets, was confirmed. The most significant result was the observation of slow magnetic relaxation in a Ni-Gd sample, where the Ni(II) central atom is diamagnetic and Gd(III) is generally magnetically isotropic. The geometry and the electron density of the coordination sites has been proved to exert a very important influence on the SMM behaviour of lanthanide ions which has contributed to the theoretical knowledge of SMMs.

**Abstrakt**

Predkladaná práca je zameraná na štúdium jednomolekulových magnetov na báze vybraných prechodných kovov a lantanoidov s použitím vybraného ligandu Schiffovej zásady. Prvá časť práce sa venuje teoretickému opisu jednomolekulového magnetizmu ako aj koordinačnej chémii a magnetickým vlastnostiam komplexov obsahujúcich centrálne atómy Ni(II), Co(II)/(III), Ce(III), Gd(III) a Dy(III). V rámci experimentálnej časti bola najprv vypracovaná metóda prípravy požadovaných komplexov – tzv. „self-assembly“ metóda. Podľa takto určených syntetických postupov

bolo pripravených 21 látok, ktoré boli fyzikálne a chemicky charakterizované a pomocou rtg. štruktúrnej analýzy bola stanovená ich kryštálová štruktúra. Jedna kapitola práce je zameraná na kryštalografickú štúdiu polymorfie, kde sa použili metódy FIM a analýza Hirshfeldových povrchov na detailnejšie preskúmanie dvoch polymorfov $[Co^{III}_2(o\text{-}van\text{-}en)_3]\cdot 4CH_3CN$. Práca zahŕňa aj kryštalografické štúdium topotaktickej reakcie typu SC-SC (Single Crystal-to-Single Crystal), pri ktorej sa komplex [Ni(*o-van-en*)$DyCl_3(H_2O)$] pri vyššej teplote dehydratuje a v jej dôsledku dimerizuje za vzniku nového komplexu $[Ni_2(o\text{-}van\text{-}en)_2Dy_2Cl_6]$. Spomedzi pripravených látok boli vybrané 4 komplexy, u ktorých sa študovali ich magnetické vlastnosti s ohľadom na ich SMM charakter. U všetkých štyroch látkach bola potvrdená pomalá relaxácia magnetizácie, ktorá je typická pre jednomolekulové magnety. Najvýznamnejším výsledkom bolo pozorovanie pomalej magnetickej relaxácie v Ni-Gd vzorke, kde centrálny atóm Ni(II) je diamagnetický a Gd(III) je vo všeobecnosti magneticky izotropný. Ukázalo sa, že geometria a elektrónová hustota koordinačných miest majú veľmi dôležitý vplyv na SMM správanie lantanoidových iónov, čo porispelo k doplneniu teoretických poznatkov o SMMs.

**Resumen**

El presente trabajo se centra en el estudio de imanes monomoleculares (SMM) basados en metales de transición y lantánidos seleccionados utilizando un ligando base de Schiff seleccionado. La primera parte aborda la interpretación teórica del fenómeno magnético de SMMs, así como las propiedades de coordinación y magnetismo de los complejos que tienen como átomos centrales Ni(II), Co(II)/(III), Ce(III), Gd(III) y Dy(III). En la parte experimental, el método de preparación de los complejos se estableció en primer lugar, el llamado método de "autoensamblaje". De acuerdo con los procedimientos sintéticos así determinados, se prepararon 21 compuestos, que fueron caracterizados físicamente y químicamente mediante las técnicas habituales, mientras se analizaron sus estructuras cristalinas mediante la difracción de rayos X en monocristal. Un capítulo se centra en el estudio cristalográfico del polimorfismo, donde se utilizaron los métodos FIM (full interaction mapping) y el análisis de las superficies de Hirshfeld para una exploración detallada de dos polimorfos de $[Co^{III}_2(o\text{-}van\text{-}en)_3]\cdot 4CH_3CN$. El trabajo también incluye el estudio cristalográfico de una reacción topotáctica del tipo SC-SC (Single Crystal-to-Single Crystal) en el que el complejo [Ni(*o-van-*

*en*)$DyCl_3(H_2O)$] se deshidrata a una temperatura elevada con dimerización concomitante para formar un nuevo complejo $[Ni_2(o\text{-}van\text{-}en)_2Dy_2Cl_6]$. Cuatro de los compuestos preparados sometidos a estudios magnéticos dirigidos a sus posibles propiedades de SMMs. Para todos los cuatro complejos, se confirmó la relajación lenta de la magnetización, típica de los SMMs. El resultado más significativo fue la observación de la relajación magnética lenta en una muestra de Ni-Gd, donde el átomo central de Ni(II) es diamagnético y Gd(III) es generalmente magnéticamente isotrópico. Se ha demostrado que la geometría y la densidad electrónica del entorno de coordinación ejercen una influencia muy importante en el comportamiento SMM de los iones lantánidos, lo que ha contribuido al conocimiento teórico de los SMM.

# Contents

# List of Abbreviations

| | |
|---|---|
| *ac* | acetato |
| *acac* | acetylacetonato |
| $CH_3CN$ / MeCN | acetonitrile |
| CSD | Cambridge Structural Database |
| DMF | dimethylformamide |
| DMSO | dimethylsulfoxide |
| H*dpt* | *N´*-[bis(dimethylamino)phosphoryl]-2,2,2-trichloroacetamide |
| *en* | ethylenediamine |
| EtOH | ethanol |
| FIM | Full Interaction Map |
| H*hfac* | hexafluoroacetylacetone |
| iPrOH | isopropanol |
| Ln | lanthanide |
| MeOH | methanol |
| *obPc* | dianion of 2,3,9,10,16,17,23,24-octabutoxyphthalocyanine |
| *Pc* | dianion of phthalocyanine |
| *phen* | 1,10-phenanthroline |
| QTM | Quantum Tunnelling Magnetization |
| SCSC | Single-Crystal-to-Single-Crystal |
| SMM | Single-Molecule Magnet |
| *thf* | tetrahydrofuran |
| Tr | transition metal |

# 1 Introduction

Since the discovery of the first single-molecule magnet (SMM) {$Mn_{12}$} in 1993 [Sessoli *et al.*, 1993], research on this phenomenon has been amplified in the lanthanide based materials [Ishikawa *et al.*, 2003]. Dating from 2004, advanced investigation culminated in heteronuclear 3*d*-4*f* complexes showing slow magnetic relaxation [Osa *et al.*, 2004]. The advantage of complexes containing both, transition metal and lanthanide atoms lies in a fusion of the properties of both kinds.

Concerning 4*f* elements, heavy lanthanide ions were widely used for the construction of the SMM materials due to their large angular momentum *J* and large magnetic anisotropy [Jin *et al.*, 2017; Kostin *et al.*, 2018; Petrosyants *et al.*, 2018]. However, recent study of light lanthanide ions showed surprising magnetic behaviour of cerium(III) [Pointillart *et al.*, 2017]. Despite the small magnetic moment, which arises from its small angular momentum *J* and small Landé's *g* factor, the spin-orbit coupling is strong enough to create significant magnetic anisotropy and so an energy barrier between the two orientations of the magnetization. The first cerium(III) based SMM was published recently in 2013 [Hino *et al.*, 2013] and later other cerium(III) complexes were reported to be SMMs [Hino *et al.*, 2013; Le Roy *et al.*, 2014; Khélifa *et al.*, 2015; Singh *et al.*, 2015].

Among the lanthanide ions, the case of gadolinium(III) complexes shows another breakthrough in the theory of slow relaxation of magnetization. Despite its essentially isotropic ground state with $L = 0$, there were several compounds published where magnetic anisotropy around gadolinium(III) ion was induced by local coordination, magnetic exchange coupling or electron density donation [Izougu *et al.*, 2018; Kanetomo *et al.*, 2017; Calahorro *et al.*, 2016]. All these stimuli strongly depend on design of the molecular structure. With this goal achieved, we can establish a new class of SMMs containing gadolinium(III) with the highest known spin state ($4f^7$) for a single ion.

Significant effort has been extended to produce a strictly dinuclear 3*d*-4*f* complex molecules [Pasatoiu *et al.*, 2011; Pasatoiu *et al.*, 2011; Costes *et al.*, 2015] as building block for design and study of polynuclear clusters [Dinca *et al.*, 2015; Feng *et al.*, 2012; Huang *et al.*, 2013, Jiang *et al.*, 2017] and polymers [Im & Lee, 2015; Visinescu *et al.*, 2009; Visinescu *et al.*, 2012]. *Salen*-type Schiff bases originating from

*o*-vanillin and related aldehydes have been widely used in coordination chemistry due to their ability to form complexes with a rich variety of geometries and structural dimensionalities [Andruh, 2015].

# 2 Theoretical Background

## 2.1 Molecular Magnetism

In the last three decades, first-row transition metals such as Mn(III), Fe(III), Fe(II), Co(II) and Ni(II) were studied from the point of view of molecular magnetism. Undoubtedly, the most intensive attention is paid to so-called single-molecule magnets (SMMs) which are molecular species that display several characteristic magnetic properties such as tunnelling of the magnetization and slow magnetization relaxation.

The fundamental aspect of SMMs is that they can be magnetized by an external magnetic field and after the field is removed they are able to preserve this magnetization for a certain time (at a certain temperature). This magnetic hysteresis is called slow relaxation of magnetization (Fig. 2.1.1. right). As this relaxation has a purely molecular origin, the material is a so-called single-molecule magnet. When a complex exhibits such behaviour, but there is a metal ion, they are often referred to as single-ion magnets (SIMs) and alternatively for chain-like structures – single-chain magnets (SCMs). These materials can be used in spin-based electronic devices for information storage of high density.

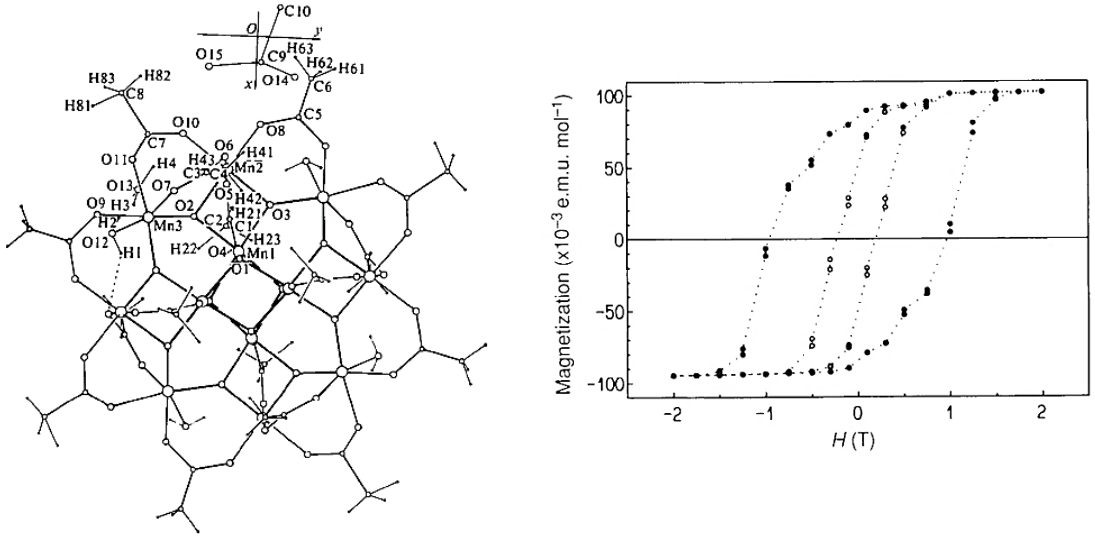


Figure 2.1.1 Left: The crystal structure of $[Mn_{12}(CH_3COO)_{16}(H_2O)_4O_{12}]\cdot 2CH_3COOH\cdot 4H_2O$: projection on the (001) plane [Lis, 1980]. Right: Hysteresis loops of $[Mn_{12}(CH_3COO)_{16}(H_2O)_4O_{12}]\cdot 2CH_3COOH\cdot 4H_2O$ recorded parallel to the *c* axis with a SQUID magnetometer at 2.2 K (full circles) and 2.8 K (empty circles). The dotted lines are only a guide for the eye [Sessoli *et al*., 1993].

Slow relaxation of magnetization can be described by the simple 'double-well' diagram (Scheme 2.1.2.). All the energy levels $M_S$ are localised in two equal wells, $-M_S$ in the left, $+M_S$ in the right one. When no external field is applied all the energy levels of $\pm M_S$ are degenerate pairs (except $M_S = 0$) and the wells are equally populated. In an external magnetic field parallel to the magnetization axis the $-M_S$ levels are stabilised to the prejudice of those of $+M_S$ (note: applied field is parallel to the z axis, $+M_S$ levels correspond to a projection of the magnetization antiparallel to the field and $-M_S$ levels correspond to magnetization parallel to the applied external field). When the external field is removed the system returns to thermal equilibrium.

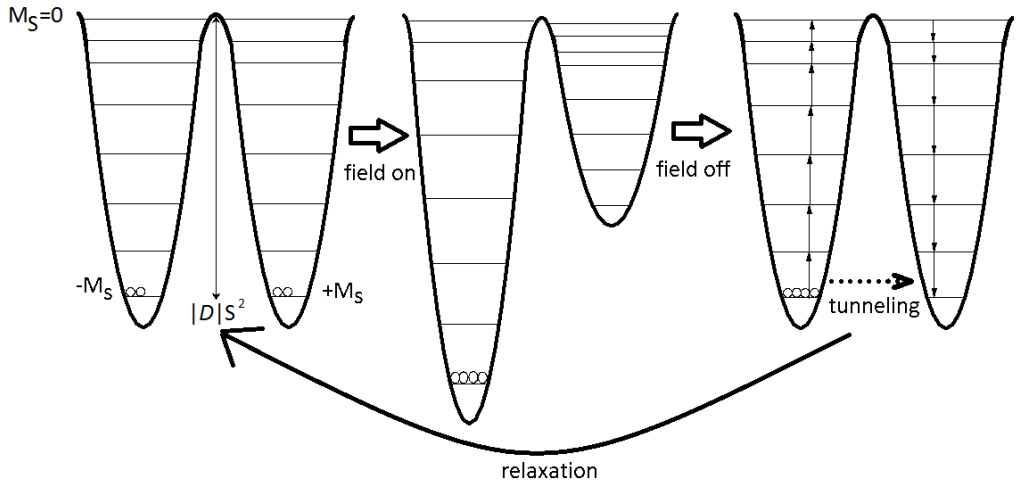


Scheme 2.1.2 'Double well' diagram showing magnetization and relaxation process in SMM.

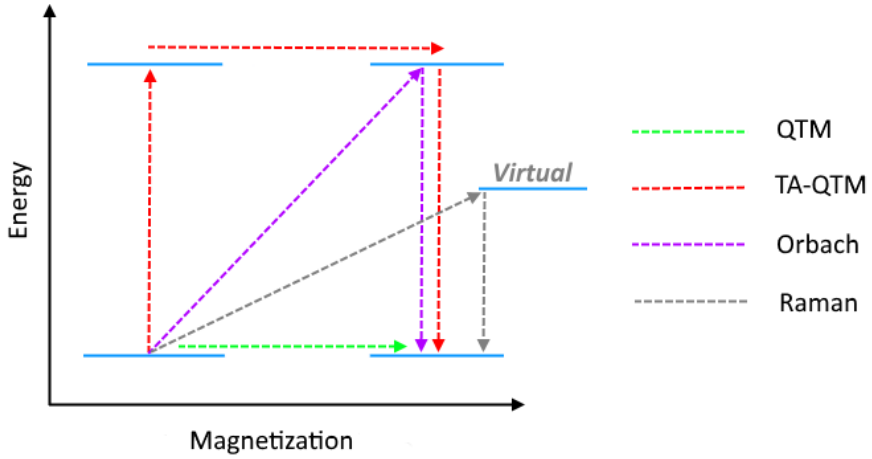


Scheme 2.1.3 Schematic mechanisms of relaxation processes: QTM, TA-QTM, Orbach and Raman process.

The relaxation pathway can differ from one system to another. There are several processes known – direct, Orbach, Raman, quantum tunnelling and thermally assisted quantum tunnelling of magnetization (Scheme 2.1.3). The magnetization can tunnel through the anisotropy barrier between ground states or between excited states *via* thermally assisted mechanisms. An Orbach process involves absorption of a lattice phonon followed by phonon emission and relaxation from an excited state, while in a Raman process the relaxation occurs from a virtual state.

The size of the effective energy barrier ($U_{eff}$) is affected by two parameters, namely the ground spin state ($S$) and the magnetic anisotropy parameter ($D$):

$$U_{eff} = |D|S^2 \quad \text{(integer spins)}$$

$$U_{eff} = |D|\left(S^2 - \frac{1}{4}\right) \quad \text{(non-integer spins)}$$

By the simple approach, the larger the energy barrier $U_{eff}$ between reversal spin levels the longer will be the observed relaxation time. In general, a high spin ground state combined with a strong magnetic anisotropy is the required feature for SMMs [Neese & Pantazis, 2011]. Magnetic anisotropy is governed by the axial $D$ and rhombic $E$ zero-field splitting parameters according to the Hamiltonian

$$\hat{H} = DS_z^2 + E\left(S_x^2 - S_y^2\right)$$

where $S$ is the total spin quantum number. These two parameters reflect the distortion of symmetry around the magnetic centre and correlate with analogous structural parameters $D_{str}$ and $E_{str}$ describing the structural distortion of the central ion [Ivaníková *et al.*, 2006].

## 2.2 Introduction of Lanthanides to Molecular Magnetism

In contrast to transition metals, *f* elements play an important role in single-molecule magnetism due to their highly anisotropic magnetic moments. A view of the asphericity of the 4*f* electron density facilitates understanding of the magnetic anisotropy of lanthanide ions [Jiang & Qin, 2015] (Fig. 2.2.1).

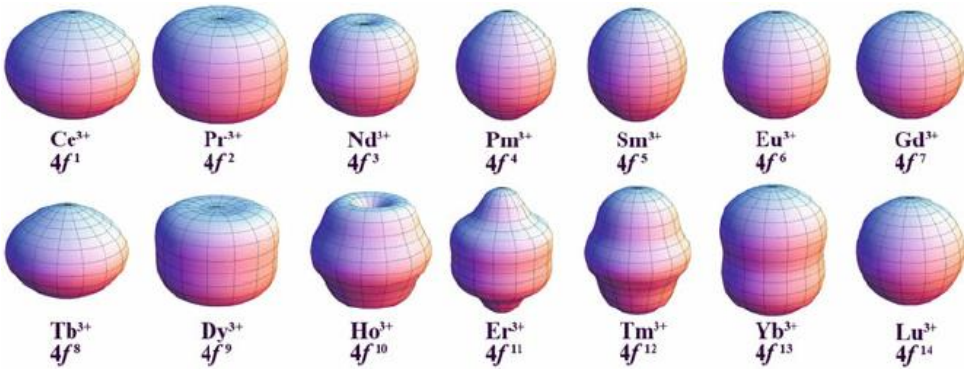


Fig. 2.2.1 The 4*f*-shell electron cloud shapes of Ln(III) ions in their Ising limit state. Ce(III), Pr(III), Nd(III), Tb(III), Dy(III) and Ho(III) are so-called oblate ions (axially compressed), Pm(III), Sm(III), Er(III), Tm(III) and Yb(III) are prolate ions (axially elongated) and Eu(III), Gd(III) and Lu(III) are isotropic ions (spherical) [Jiang & Qin, 2015].

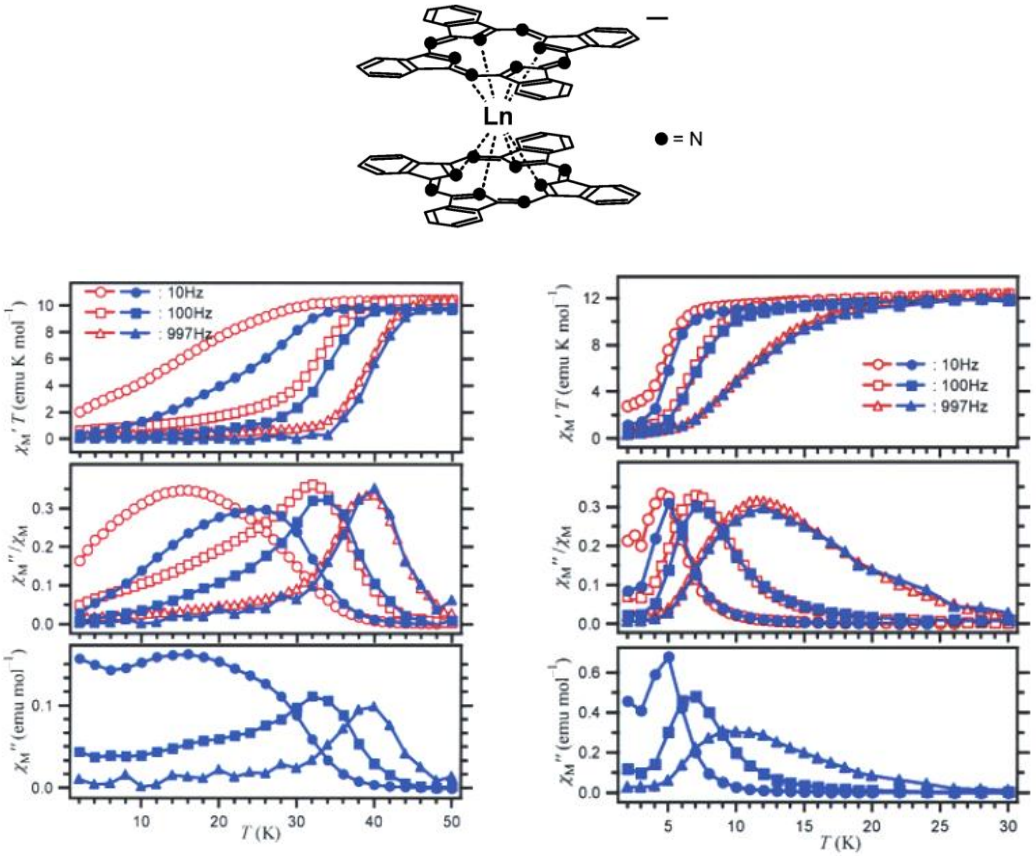


Figure 2.2.2 Upper: Scheme of the molecular structure of $[Pc_2Ln]^-$ (Ln = Tb or Dy). Lower: Plots of (top) $\chi_M'T$ and (bottom) $\chi_M''/\chi_M$ against temperature $T$, where $\chi_M'$, $\chi_M''$, and $\chi_M$ are in-phase-AC, out-of-phase-AC, and DC molar magnetic susceptibilities, respectively, for a powder sample of $[Pc_2Ln]^-\cdot TBA^+$ (left: Ln = Tb; right: Ln = Dy; open marks) and corresponding complex diluted in $[Pc_2Y]^-\cdot TBA^+$ (filled marks) measured in a 3.5 G AC magnetic field oscillating at indicated frequencies [Ishikawa *et al*., 2003].

Concerning the right choice of lanthanides, 4*f* ions with the highest magnetic anisotropy and highest spin value are the most appropriate for enhancing the relaxation time in SMM. The first lanthanide single-molecule magnet was described in 2003 by Ishikawa *et al*.; phthalocyanine double-decker complexes of Tb(III) and Dy(III) showed slow magnetization relaxation in the temperature ranges significantly higher than those of the transition metal cluster SMMs and thus a new class of magnets at the molecular level was established [Ishikawa *et al*., 2003] (Fig. 2.2.2). From then on, the number of studies of lanthanide based SMMs increased rapidly; there are more than 1 500 published articles up-to-now and they are still a current topic among materials scientists.

Moreover, the magnetic properties of lanthanide ions are different from those of transition metal ions, whose magnetism mainly comes from spin magnetic moment, the orbital contribution being influenced by the ligand field. In contrast to that behaviour, the magnetic moment of the Ln(III) ions is essentially independent of environment, therefore one cannot distinguish between coordination geometries as is common for transition metals, for example, in the case of octahedral, tetrahedral and square planar $Ni^{II}$ complexes.

Two parameters that affect the size of the effective energy (anisotropic) barrier ($U_{eff}$) for SMMs based on transition metals, namely the ground spin state ($S$) and the magnetic anisotropy parameter ($D$), are inversely proportional to each other which prevents a significant improvement in SMM properties [Ahmed *et al.*, 2014]. With regard to that a combination of lanthanides and transition metal ions has been used in an effort to increase maximal magnetic anisotropy. The other benefit of such structures is the already observed ferromagnetic coupling between Cu(II)–Ln(III) and Ni(II)–Ln(III) ions offering great potential for SMM study [Ahmed *et al.*, 2014]. The first investigation of the magnetic properties of a 3*d*–4*f* heterometallic complex is due to Bencini *et al.*, who observed and characterized the ferromagnetic interaction between Cu(II) and Gd(III) [Bencini *et al.*, 1985]. Researchers began to see the 3*d*-4*f* complexes from the molecular magnetism point of view only in the last decade or two. Osa *et al.* established a new class of SMMs by publishing two cyclic 3*d*-4*f* tetranuclear compounds, namely $[CuLTb(hfac)_2]_2$ and $[CuLDy(hfac)_2]_2$ ($H_2L$ = 1-(2-hydroxybenzamido)-2-(2-hydroxy-3-methoxy-benzylideneamino)ethane [Osa *et al.*, 2004].

However, research in recent years has revealed a few examples of a significant reduction in quantum tunnelling magnetization (QTM) due to non-negligible magnetic exchange interaction between lanthanide and transition metal ions [Langley *et al.*, 2013]. On the other hand, recent study on the 3*d*-4*f* complexes with diamagnetic 3*d* metal ions such as zinc(II) or cobalt(III) showed the enhancement of the $U_{\text{eff}}$ barrier compared to their mononuclear lanthanide analogues [Fondo *et al.*, 2017]; it was suggested that the presence of a diamagnetic 3*d* cation near the lanthanide central atom, both sharing oxygen bridging atoms, induces a large charge polarization on the bridging oxygen atom that favours an increase in the $U_{\text{eff}}$ barrier. This observation invokes a new strategy in designing the 3*d*-4*f* complexes with diamagnetic 3*d* ions [Langley *et al.*, 2012; Langley *et al.*, 2013; Upadhyay *et al.*, 2014; Sun *et al.*, 2016; Upadhyay *et al.*, 2017].

Further possibilities for crystallographic and magnetic studies emerge with the synthesis of complexes with non-equimolar ratios of 3*d* and 4*f* ions. In 1985, Bencini *et al.* first reported the crystal structures along with their magnetic properties of two heterotrinuclear 3*d*-4*f*-3*d* complexes, observing ferromagnetic interaction between adjacent Cu(II) and Gd(III) ions [Bencini *et al.*, 1985]. Further research of such trinuclear complexes with diamagnetic Ln(III) ions demonstrated also the presence of the interaction between two terminal transition metals [Shiga *et al.*, 2007].

In the past two decades or so, heterobinuclear complexes were used as building blocks in designing extended structures *via* additional anionic ligands bridging monomeric units. This term also encompasses oligonuclear complexes, multimetallic complexes, coordination polymers, multidimensional arrays and related structures [Gheorghe *et al.*, 2002; Gheorghe *et al.*, 2007; Jin Im & Lee, 2015; Yao *et al.*, 2015].

Additionally, they have an advantage of ease of synthesis, low cost, flexible steric effects and supporting electronic effects. Properties of these molecules are widely useful in a broad spectrum of fields in physics or in chemistry as well as in biological sciences. From these we can mention magnetism, luminescence, optical properties, selectivity towards specific molecules, catalysis and antimicrobial activity [Cristóvão *et al.*, 2014; Jin Im & Lee, 2015; Yao *et al.*, 2015].

## 2.3 Coordination Chemistry of Co(II) and Co(III)

Up to now, there are almost 40 000 crystal structures containing Co(II) or Co(III) ions in the Cambridge Structural Database (CSD; version 5.40, update February 2019) [Allen *et al.*, 1994]. More than 25 000 of them are hexacoordinated, exhibiting octahedral geometry, slightly distorted in the case of unequal ligands. The population of four- and five-coordinated Co(II) ions is comparable (ca. 5 000 structures each, up to now) and these complexes exhibit tetrahedral or square planar geometries in the case of coordination number 4; trigonal-bipyramidal and the square pyramidal geometries in five-coordinated complexes.

When working with paramagnetic Co(II) and diamagnetic Co(III) compounds, we should remember the following facts about the stability of such compounds and the oxidation, which is an essential storyline in the solution chemistry. There are two particular aspects influencing the favourable route of the reactions. Co(III) exhibits a strong affinity for nitrogen donor atoms and complexes of Co(III) are kinetically inert [Cotton *et al.*, 1999; Greenwood & Earnshaw, 1997]. Even only a change of the ligand can have an effect on oxidation-reduction behaviour [Chambers & Holliday, 1975]. Table 2.3.1 illustrates the remarkable sensitivity of the reduction potential of the Co(III)/Co(II) couple to different ligands. Thus, the presence of some ligands such as *salen* type Schiff bases makes Co(II) unstable in an air atmosphere [Greenwood & Earnshaw, 1997].

Table 2.3.1 $E°$ for some Co(III)/Co(II) couples in acidic solution [Greenwood & Earnshaw, 1997].

| **Couple** | $E°$**/V** |
|---|---|
| $[Co(H_2O)_6]^{3+} + e^- \leftrightarrows [Co(H_2O)_6]^{2+}$ | 1.83 |
| $[Co(C_2O_4)_3]^{3-} + e^- \leftrightarrows [Co(C_2O_4)_3]^{4-}$ | 0.57 |
| $[Co(edta)]^- + e^- \leftrightarrows [Co(edta)]^{2-}$ | 0.37 |
| $[Co(bpy)_3]^{3+} + e^- \leftrightarrows [Co(bpy)_3]^{2+}$ | 0.31 |
| $[Co(en)_3]^{3+} + e^- \leftrightarrows [Co(en)_3]^{2+}$ | 0.18 |
| $[Co(NH_3)_6]^{3+} + e^- \leftrightarrows [Co(NH_3)_6]^{2+}$ | 0.11 |
| $[Co(CN)_6]^{3-} + H_2O + e^- \leftrightarrows [Co(CN)_5(H_2O)]^{3-} + CN^-$ | -0.8 |
| $½\ O_2 + 2\ H^+ + 2\ e^- \leftrightarrows H_2O$ | 1.23 |

With respect to the aforementioned facts, the synthesis of the complexes with Co(II) ion coordinated by a number of nitrogen donor atoms can be achieved by the reaction conducted under non-oxidative conditions, such as an argon atmosphere. The other possibility of achieving the Co(II) complex is to use strictly O-donor ligand.

The coordination chemistry of Co(III) is very simple since the majority of its complexes contain the central atom with the coordination number 6 and octahedral symmetry, subtly distorted if needed. As has already been pointed out, cobalt(III) shows a particular affinity for nitrogen and its complexes are kinetically inert and low-spin. However, Co(III) complexes are diamagnetic in general and themselves are not suitable as magnetic functional materials, the dichotomy between the inertness of the two oxidation states has enabled the development of Co(III) hexacoordinated complexes as anticancer or antiviral prodrugs. Co(III) complexes with neutral N-donor ligands undergo reduction in biological systems to form labile Co(II) complexes, which subsequently release their ligands as a cytotoxic payload. For example, complexes of the general structural formula $[Co(SB)(L)_2]^+$ (where SB = Schiff base of the *salen* type and $L$ = a neutral N-donor ligand) exhibited activity to A549 lung cancer cells [King *et al.*, 2019].

Tetra- and penta-coordinated Co(III) complexes are generally less common than those with hexacoordination. Applications of such complexes were investigated in various fields, such as biological implications or catalysis. As an example, a Co(III)/Co(II) based redox cycle in square-planar Co(III) complexes with pyrrolecarboxamide ligands is used in catalysis in nitro reduction reactions [Yaday *et al.*, 2017], or series of square-pyramidal *salen* type Co(III) complexes were tested as catalysts for the copolymerization of cyclohexene oxide and $CO_2$ [Cohen *et al.*, 2006].

On the other hand, Co(II) complexes display a large variety of coordination environments; namely high-spin and low-spin octahedral, tetrahedral, square and high-spin and low-spin five-coordinate complexes (trigonal-bipyramidal and square pyramidal) as well as intermediate configurations [Cotton *et al.*, 1999]. The interesting class of Co(II) complexes is $\{CoA_2X_2\}$ – tetrahedral dihalido Co(II) complexes with heteroaromatic N,N-donor chelating ligands possessing easy-plane magnetic anisotropy showing field-induced slow magnetic relaxation [Smolko *et al.*, 2015; Smolko *et al.*, 2016]. There are also Co(II) complexes with coordination number higher than 6 which

are reached by using polyhapto or polydentate ligands like cyclopentadiene, benzene or crown-ethers.

## 2.4 Coordination Chemistry of Ni(II)

There are more than 37 000 Ni(II) complexes in the CSD from the recent version of February 2019. The most frequent coordination numbers of Ni(II) complexes are 6 (approx. 18 000 hits) and 4 with more than 15 000 structurally characterized complexes. The origin of the stable polyhedra of transition metals lies in the localization of outer valence *d* orbitals which have directional character. Hexacoordinated Ni(II) complexes have the principal stereochemistry of an octahedron, slightly distorted when needed. The coordination number 4 in Ni(II) complexes produces two different geometries, namely square-planar, tetrahedral and complexes with intermediate geometries between these two. According to crystal field theory, square-planar coordination complexes are, other than a few particular examples, essentially diamagnetic while those of tetrahedral geometry are paramagnetic.

Octahedral Ni(II) complexes are studied in many fields, for instance they are good candidates for studying the sign and magnitude of the zero-field splitting parameter *D* [Ivaniková *et al.*, 2006] or their catalytic activity is used to stimulate organic reactions such as arylation and methylation of allenamides [Liu *et al.*, 2018] or synthesis of indeno-pyrimidine derivatives [Gangu *et al.*, 2019].

Tetrahedral Ni(II) complexes are rare and usually achieved by the selection of ligand set. For example, the use of an *N,N'*-ligand with the combination of halide ligands produces a tetrahedral Ni(II) complex acting as a catalyst in which the coordination sites occupied by halide ligands represent the catalytic centres [Zhang *et al.*, 2019]. On the other hand, square-planar Ni(II) complexes are more common and used as functional materials in various areas such as catalysis [Fogeron *et al.*, 2019; Shen *et al.*, 2018] or biological activity [Sreekumar *et al.*, 2017; Biswas *et al.*, 2018].

## 2.5 Coordination Chemistry of Ln(III)

For understanding the coordination chemistry of the *f*-block, it is necessary to clarify the properties of lanthanides as elements. The large, highly charged, Ln(III) ions are hard Lewis acids, and therefore prefer to coordinate hard donor atoms such as oxygen and nitrogen. In contrast, sulphur and phosphorous will be less favoured as donor atoms. Highly preferred coordination of water molecules is an important factor

caused by the high hydration energy of the Ln(III) ion which means that the syntheses of complexes with mono- and bidentate ligands often need to be carried out in nonpolar solvents, weakly coordinating to minimize competition, such as $CH_3CN$ [Kaltsoyannis & Scott, 1999].

As a consequence of the large size of the lanthanide ions, high coordination numbers (up to 12) are found. An important fact is that the *f*-orbitals are 'inner' orbitals, shielded from the effects of the surrounding anions and therefore not able to participate in directional bonding. There are none of the ligand-field effects as in transition metal chemistry with the preference for octahedral or other polyhedral coordination. The coordination number is, therefore, dominantly determined by steric requirements, i.e. how many ligands can be packed round the central lanthanide ion [Cotton, 2006].

As already noted, for lanthanides, there is no characteristic coordination number as there is in the case of transition metals, coordination number cannot be deduced even from the colour of the compound, not even from the absorption spectrum. The majority of Ln(III) ions are colourless to the eye and have very weak absorption spectra, not very much influenced by their environment. Single crystal X-ray diffraction studies are often the only way of determining the coordination polyhedron.

Coordination numbers 3, 4, 5 and 6 in lanthanide complexes are not very common; this arrangement is obtained by ligands with high second-order steric effects. The most frequent coordination numbers are 7, 8 and 9. The most common geometries encountered with the seven-coordination of Ln(III) ion are capped octahedral and capped trigonal prismatic; several complexes adopt pentagonal bipyramidal geometry. In the structures of eight-coordinate Ln(III) ions, two geometries predominate – dodecahedral and square antiprismatic, while the energy difference between them is likely to be small. Less common, but still occurring is the cubic coordination. However, the ideal polyhedra are rarely observed; most of the real geometries are deformed forms of ideal polyhedra.

Tricapped trigonal prismatic is the most familiar example of nine-coordinate geometry. This polyhedral geometry is adopted for the $[Ln(H_2O)_9]^{3+}$ ions (Ln = Nd, Eu, Tb) which were investigated for a new phenomenon, namely charge transfer from the noncoordinated anions to the coordinated water molecules *via* hydrogen bonds [Nelyubina *et al.*, 2014].

Because of donor atom repulsion, it is hard to obtain coordination number higher than 9. To relieve this first-order effect it is possible to use bidentate chelate ligands having small bite angles, such as nitrate. Polyhedra of such complexes are necessarily irregular [Atwood, 2012].

## 2.6 Coordination Chemistry of *Salen* Type Schiff Bases and the Ligand $H_2$(*o-van-en*)

The increasing interest in heterometallic complexes in various fields has inspired the design of ligands able to coordinate a targeted number and kind of metal centre. Self-assembly syntheses handling precursors as building blocks are a useful facility for obtaining desirable products, especially when we want to achieve a complex with special physical or/and chemical properties. Control over the charge, nuclearity or dimensionality of the final products can be the critical factor in the success of a targeted synthesis.

Schiff bases are often used as ligands for the coordination of transition metals and lanthanides due to their multidonor properties and consequent versatility [Andruh, 2015]. They can be easily synthesized by the organic Schiff base reaction of an aldehyde and an amine. More specifically, *salen* type Schiff bases, prepared from salicylaldehyde and any diamine in the molar ratio 2:1, are widely used as ligands offering an $\{N_2O_2\}$ cavity of an ideal geometry to chelate a 3*d* ion [Khandar *et al.*, 2006]. An extension of these ligands made by the addition of a methoxy (or ethoxy) substituent on the *ortho* position of salicylaldehyde transforms them into compartmental ligands with two different cavities (Scheme 2.6.1).

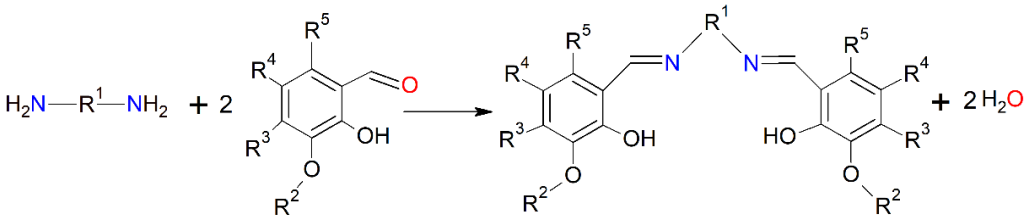

Scheme 2.6.1 Schematic view of Schiff reaction of a diamine and 2,3-disubstitued benzaldehyde forming *salen* type Schiff base.

An inner $\{N_2O_2\}$ cavity is capable of coordination of a 3*d* ion while the outer and larger $\{O_4\}$ coordination site can link a 4*f* ion [Andruh *et al.*, 2009] (Scheme 2.6.2). In addition, the specific chemical nature of 3*d* and 4*f* ions facilitates the selectivity of coordination sites of the ligand [Liu *et al.*, 2015]. According to the hard and soft acids

and bases (HSAB) concept [Pearson, 1963], 3*d* and 4*f* metal ions have priority to coordinate with different donor atoms such as nitrogen and oxygen, respectively. The most commonly used such aldehydes and diamines are *o*-vanillin, 5-bromo-2-hydroxy-3-methoxybenzaldehyde, 3-ethoxy-salicylaldehyde, ethylenediamine, 1,3-diaminopropane or 2-hydroxy-1,3-diaminopropane.

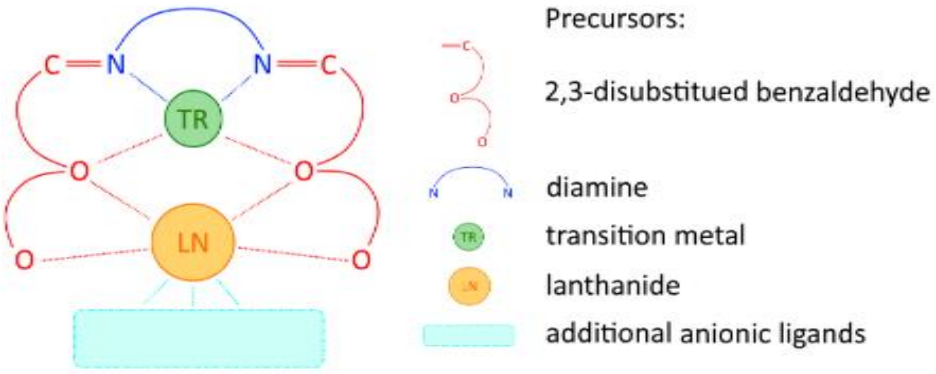


Scheme 2.6.2 Self-assembly concept of using precursors as building blocks to create a general heterodinuclear 3*d*-4*f* complex with *salen* type Schiff base ligand.

The synthesis of the Schiff base $H_2$(*o-van-en*) ($H_2$(*o-van-en*) = *bis*(2-hydroxy-3-methoxybenzylidene)ethylenediamine), widely used as compartmental N,O-donor ligand, was first described by B. N. Ghose in 1983 [Ghose, 1983; Ghose 1984]. Ghose describes the synthesis of ethylenediamine and *o*-vanillin in molar ratio 1:2 as a one-hour reflux in dry benzene at room temperature with 80 % yield. The product of this reaction is a dark yellow solid with melting point 165.5 – 166.5 °C. Up to now, there are two different polymorphic structures of $H_2$(*o-van-en*) published. In 2004, Cunningham *et al.* published the crystal structure of $H_2$(*o-van-en*) crystallizing in monoclinic $P2_1/n$ space group [Cunningham *et al.*, 2004] and one year later, the other stereoisomer with lower symmetry (Pc space group) and higher melting point (170 – 172 °C) was published [Correia *et al.*, 2005] (Fig. 2.6.1).

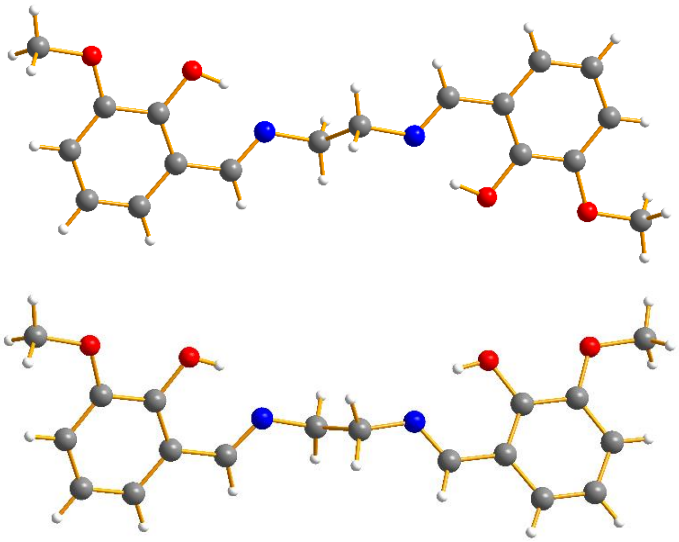

Figure 2.6.1 Molecular structure of the two polymorphs of $H_2$(*o-van-en*); red: oxygen, blue: nitrogen, grey: carbon, white hydrogen atoms. Top: $P2_1/n$ space group [Cunningham *et al.*, 2004]. Bottom: P*c* space group [Correia *et al.*, 2005].

A search in the Cambridge Structural Database (CSD; version 5.40, update February 2019) with 283 hits serves to confirm the versatility of the $H_2$(*o-van-en*) ligand which was firstly used in 1970; and in last two decades, the use of the ligand has increased exponentially (Fig. 2.6.2). However, the rise of the use of $H_2$(*o-van-en*) as a ligand in the CSD also reflects the development of coordination chemistry as a vehicle for producing functional materials and of crystallography as a front-line tool for characterizing them.

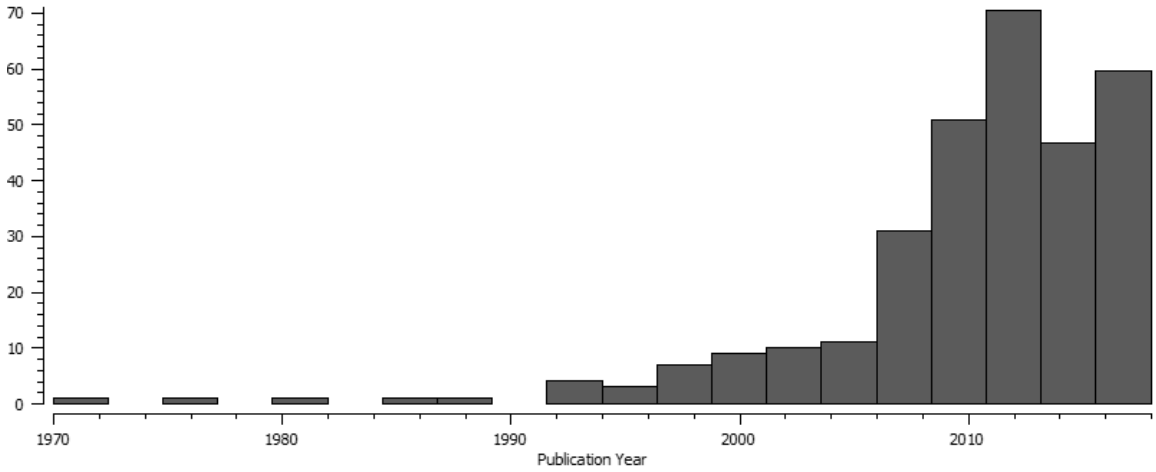


Figure 2.6.2 Histogram showing the use of $H_2$(*o-van-en*) ligand over the years.

Molecular structures found in the CSD also confirm what was discussed earlier in Section 1.3, $H_2$(*o-van-en*) as a *salen* type Schiff base ligand always fully deprotonates

and thereby generates two coordination sites. The inner one best fits for the accommodation of a first-row transition metal. The outer coordination site fits for a bigger central ion such as alkali metals [Finelli *et al.*, 2018], lanthanides [Jin *et al.*, 2011]; alternatively, the space between methoxy groups can be occupied by an inclusion (e.g. solvent) held by hydrogen bonding interactions [Cucos *et al.*, 2011; Hazra *et al.*, 2016]. As the interest in lanthanide complexes arose later, $H_2$(*o-van-en*) was first used as a compartmental ligand in Tr-Ln compounds in 2002 and up to now, there are 94 crystal structures of such complexes in the database. The majority of them are discrete (i.e., 0D) molecular structures; only few examples record 1D (3 hits) or 2D (3 hits) polymers where additional linking ligands were used. The first mentioned class (0D) contains 88 compounds and these can be categorized as dinuclear (21 hits), trinuclear (35 hits), tetranuclear molecular structures (7 hits) and complexes with higher nuclearity (25 hits).

Up to now, there are only 9 crystal structures of complexes with $H_2$(*o-van-en*) ligand with Co atoms in their inner coordination sites reported in the CSD; among them, only one belongs to the family of heterodinuclear 3*d*-4*f* complexes (Tab. 2.6.1).

Table 2.6.1 List of the known complexes with the {Co(*o-van-en*)} structural unit found in the CSD (update February 2019).

| **Formula** | **Refcode** | **Structure type** | **Ref.** |
|---|---|---|---|
| $[Co_2(o\text{-}van\text{-}en)_3]\cdot DMSO\cdot 2H_2O$ | COMSAL | homodinuclear | [Calligaris *et al.*, 1970] |
| $[Co(o\text{-}van\text{-}en)(ac)_2Dy(NO_3)_2]$ | IKENIX | heterodinuclear | [Hazra *et al.*, 2016] |
| [Co(*o-van-en*)(*acac*)]·DMSO | KUHRIQ | mononuclear | [Schieber *et al.*, 2011] |
| [Co(*o-van-en*)]·DMF | LAPFEQ | mononuclear | [Reath *et al.*, 2017] |
| [Co(*o-van-en*)Na(*thf*)$_2$] [Co$_2$(*o-van-en*)$_2$Na$_2$(*thf*)$_2$] | NALJUF | mononuclear | [De Angelis *et al.*, 1996] |
| $[Co(o\text{-}van\text{-}en)(H_2O)Cl]\cdot H_2O$ | NOQQOA | mononuclear | [Xing, 2009] |
| $[Co(o\text{-}van\text{-}en)(H_2O)]$ | VIKFAX | mononuclear | [Jiang *et al.*, 2007] |
| $[Co(o\text{-}van\text{-}en)(H_2O)(ac)]\cdot MeOH$ | XECXAG | mononuclear | [Assey *et al.*, 2012] |
| $[Co(o\text{-}van\text{-}en)(H_2O)Cl]\cdot DMF$ | YATZOK | mononuclear | [Wei *et al.*, 2012] |

Despite the very stable coordination mode of chelating a Tr ion in the $\{N_2O_2\}$ cavity, $(o\text{-}van\text{-}en)^{2-}$ ligand rarely acts also as a bridging ligand. Such a situation is typical in the case of Tr(III) metal centre when the dinuclear molecular structure is fo rmed to balance the charge of the compound, e.g. $[Co^{III}_2(o\text{-}van\text{-}en)_3]\cdot DMSO\cdot 2H_2O$ [Calligaris *et al.*, 1970] or $[Fe^{III}_2(o\text{-}van\text{-}en)_3]\cdot CH_2Cl_2\cdot H_2O$ [Costes *et al.*, 2010].

The ligand $(o\text{-}van\text{-}en)^{2-}$ is more frequently used for accommodating Ni(II) in its inner coordination site. Some 39 such structures can be found in the CSD while 12 complexes contain lanthanide ions and only 4 of them are heterodinuclear (Tab. 2.6.2).

Table 2.6.2 List of the known complexes with the {Ni(*o-van-en*)} structural unit found in the CSD (update February 2019), divided into 4 main categories.

| **Formula** | **Refcode** | **Structure** | **Ref.** |
|---|---|---|---|
| **{Ni(*o-van-en*)} complexes** | | | |
| [Ni(*o-van-en*)][$SnCl_6$]$H_2$(*en*) | AXUTOE | mononuclear | [Hazra *et al.*, 2016] |
| $K_2$[Ni(*o-van-en*)]$_2$[$CuCl_4$]·0.5$H_2O$ | DERYAD | mononuclear | [Costes *et al.*, 2018] |
| ($NH_4$)[Ni(*o-van-en*)]$_2$($ClO_4$) | IQEFAM | mononuclear | [Cucos *et al.*, 2011] |
| ($NH_4$)[Ni(*o-van-en*)]$_2$($PF_6$) | IQEFEQ | mononuclear | [Cucos *et al.*, 2011] |
| ($NH_4$)$_2$[Ni(*o-van-en*)]$_3$($ClO_4$)$_2$ | IQEFOA | mononuclear | [Cucos *et al.*, 2011] |
| ($NH_4$)[Ni(*o-van-en*)]$_2$ [$Cr(NCS)_4(NH_3)_2$]·MeOH | IQEGAN | mononuclear | [Cucos *et al.*, 2011] |
| $K_4$[Ni(*o-van-en*)]$_4$[$NiCl_4$]$_2$·2$H_2O$ | MOJPIM | mononuclear | [Liu *et al.*, 2014] |
| [Ni(*o-van-en*)] [Cu(*phen*)(*acac*)($H_2O$)]$ClO_4$ | TEGCEO | mononuclear | [Madalan *et al.*, 2006] |
| [Ni(*o-van-en*)]·$CHCl_3$ | TEJGIZ | mononuclear | [Yu, 2006] |
| [Ni(*o-van-en*)]·DMF | ULAMIE | mononuclear | [Ayikoé *et al.*, 2011] |
| [Ni(*o-van-en*)][Sn($H_2O$)$Cl_2$ ($CH_3$)$_2$]·$CHCl_3$ | WAVYOH | mononuclear | [Cunningham *et al.*, 1993] |
| [Ni(*o-van-en*)][Sn($H_2O$)$Cl_2$($Ph$)$_2$] | WAVYUN | mononuclear | [Cunningham *et al.*, 1993] |
| [Ni(*o-van-en*)]·$H_2O$ | WAVZAU | mononuclear | [Cunningham *et al.*, 1993] |
| {$K_3$[$Ni_4$(*o-van-en*)$_4$($ClO_4$)$_2$] $ClO_4$}$_n$ | XEMJOQ | 1D | [Zhang & Zhao, 2012] |
| [Ni(*o-van-en*)($H_2O$)] | YUDFIN | mononuclear | [Guo *et al.*, 2009] |
| **{Ni(*o-van-en*) - *s*/*p*/*d*} complexes** | | | |
| [$Ni_2$(*o-van-en*)$_2$Pb(*ac*)]Ac·1.5$H_2O$ | AYAKUG | trinuclear | [Thurston *et al.*, 2004] |
| [Ni(*o-van-en*)Na($NO_3$)(MeOH)] | BOQXIQ01 | dinuclear | [Finelli *et al.*, 2018] |
| [Ni(*o-van-en*)K($NO_3$)]$_n$ | QEWCUT | 1D | [Finelli *et al.*, 2018] |
| [Ni(*o-van-en*)Rb($NO_3$)]$_n$ | VEKQUA | 1D | [Finelli *et al.*, 2018] |
| [$Ni_2$(*o-van-en*)$_2$$Li_2$($NO_3$)$_2$($H_2O$)] | QEWDEE | tetranuclear | [Finelli *et al.*, 2018] |
| [$Ni_2$(*o-van-en*)$_2$Cs($NO_3$)]·$CHCl_3$ | VEKRIP | trinuclear | [Finelli *et al.*, 2018] |

| | | | |
|---|---|---|---|
| $[Ni_2(o\text{-}van\text{-}en)_2Mn(N_3)_2]$ | CIBPAF | tetranuclear | [Jia *et al.*, 2007] |
| $[Ni(o\text{-}van\text{-}en)Na(H_2O)(C_2N_3)]$ | LORYOH | dinuclear | [Wang & Shen, 2009] |
| $[Ni(o\text{-}van\text{-}en)Na(ClO_4)(MeOH)]$ | NOQMEM | dinuclear | [Xiao, 2009] |
| $[Ni(o\text{-}van\text{-}en)Na(ClO_4)]_n$ | VILXUL | 1D | [Bhowmik *et al.*, 2013] |
| $[Ni_2(o\text{-}van\text{-}en)_2Na]BF_4$ | VILYAS | trinuclear | [Bhowmik *et al.*, 2013] |
| $[Ni(o\text{-}van\text{-}en)Na(NO_3)]$ | VILYEW | dinuclear | [Bhowmik *et al.*, 2013] |
| **{Ni(*o-van-en*) - 4*f* } complexes** | | | |
| $[Ni(o\text{-}van\text{-}en)Sm(NO_3)_3]\cdot CH_3COCH_3$ | ARIDEL01 | dinuclear | [Jin *et al.*, 2011] |
| $[Ni(o\text{-}van\text{-}en)Eu(NO_3)_3]\cdot CH_3COCH_3$ | QAPXIQ | dinuclear | [Jin *et al.*, 2011] |
| $[Ni(o\text{-}van\text{-}en)Tb(NO_3)_3]\cdot CH_3COCH_3$ | QAPXOW | dinuclear | [Jin *et al.*, 2011] |
| $[Ni(o\text{-}van\text{-}en)Ce(NO_3)_2]NO_3$ | MEFYAA | trinuclear | [Güngör & Kose, 2017] |
| $[Ni(o\text{-}van\text{-}en)La(NO_3)_2(dpt)]$ | NOFLAX | dinuclear | [Amirkhanov *et al.*, 2014] |
| **{Ni(*o-van-en*) - 4*f* - 3*d*/4*d*} complexes** | | | |
| $[Ni(o\text{-}van\text{-}en)Ho(H_2O)_4Co(CN)_6]\cdot 3H_2O$ | BIKBAB | trinuclear | [Dong *et al.*, 2018] |
| $[Ni(o\text{-}van\text{-}en)Ho(H_2O)_4Fe(CN)_6]\cdot 3H_2O$ | BIKBEF | trinuclear | [Dong *et al.;*, 2018] |
| $[Ni_4(o\text{-}van\text{-}en)_4Tb_4(H_2O)_{14}Mo_2(CN)_{16}][Mo(CN)_8]\cdot 21H_2O$ | KUNBUR | cluster | [Long *et al.*, 2010] |
| $[Ni(o\text{-}van\text{-}en)Gd(H_2O)_4Cr(CN)_6]\cdot MeOH\cdot 2H_2O$ | QUXWAJ | trinuclear | [Chen *et al.*, 2015] |
| $[Ni(o\text{-}van\text{-}en)Tb(H_2O)_4Cr(CN)_6]\cdot MeOH\cdot 2H_2O$ | QUXWEN | trinuclear | [Chen *et al.*, 2015] |
| $[Ni(o\text{-}van\text{-}en)Tb(H_2O)_4Fe(CN)_6]\cdot MeOH\cdot 2H_2O$ | QUXWIR | trinuclear | [Chen *et al.*, 2015] |
| $[Ni(o\text{-}van\text{-}en)Gd(H_2O)_4Fe(CN)_6]\cdot MeOH\cdot 2H_2O$ | QUXWOX | trinuclear | [Chen *et al.*, 2015] |

## 2.7 Coordination Chemistry of the Benzoato Ligand

Benzoic acid, H*Bz*, $C_6H_5COOH$ is a colourless compound, solid at room temperature. It possesses good solubility in alcohols, ether and benzene, lower in water. Its solubility in water at room temperature is only 0.29 g / 100 ml [Hrnčiar, 1982]. Benzoic acid has a melting point of 122.3 °C. This exceptionally high value is a consequence of its compact crystal structure. It crystallizes as anhydrous and its crystal structure contains two molecules forming dimeric units in which the individual molecules are linked by a pair of O-H···O hydrogen bonds (HBs) between two carboxylic groups (Fig. 2.7.1) [Bruno & Randaccio, 1980].

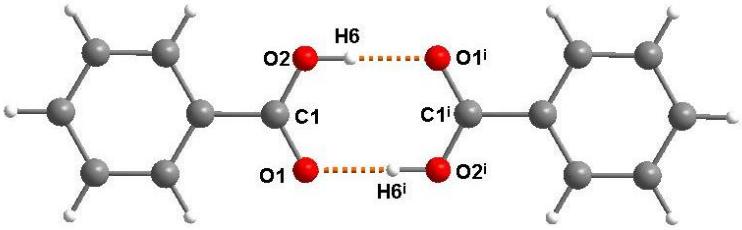


Figure 2.7.1 Dimeric supramolecular structure of H*Bz*; red: oxygen, grey: carbon, white hydrogen atoms [Bruno & Randaccio, 1980].

After its deprotonation, benzoic acid forms the benzoate ligand $C_6H_5COO^-$, *Bz* which is widely used in coordination chemistry as an O-donor ligand. A search in the CSD shows more than 2 700 published crystal structures containing benzoate in any form. Benzoate ligand can donate up to eight electrons to the central atom/s which leads to a rich variety of coordination modes (Scheme 2.7.1).

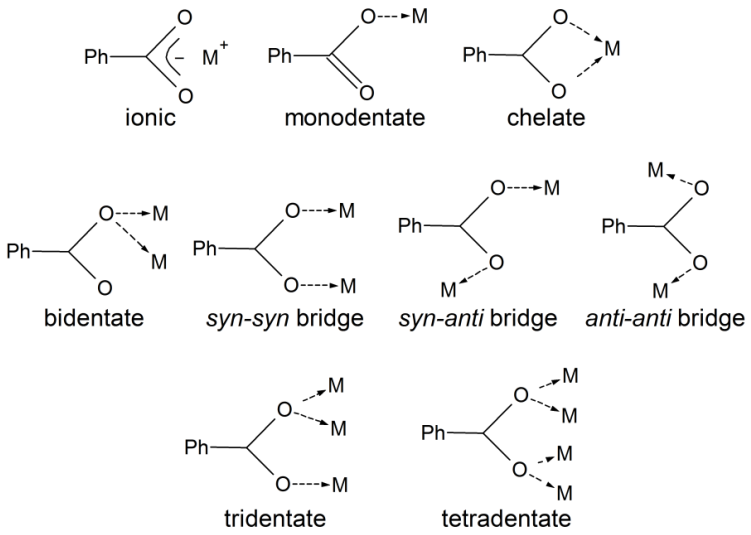


Scheme 2.7.1 Possible modes of coordination of *Bz* ligand.

In regard to the previously mentioned facts about the stability of Co(II)/Co(III) complexes depending on the donor atom selection, the synthesis of the complexes with Co(II) ion can be achieved by using strictly O-donor ligands. The last update of CSD gives 124 complexes with *Bz* ligand coordinated to Co atoms, 105 of them contain the metal ion in oxidation state II. Additionally, our previous work with the {$Ni^{II}$*Bz*} system suggests the possibility of similar behaviour of Co and this in turn opens the possibility of examination of Co(II) in molecular magnetism [Vráblová *et al.*, 2016].

# 3 Aims of thesis

The aim of the ensuing dissertation is to prepare and study a series of novel Ni(II), Co(II) and lanthanide compounds as well as bimetallic 3*d*-4*f* complexes using N,O- and/or O-donor ligands. The goal is to design and subsequently improve synthetic procedures leading to the preparation of desirable products which will be chemically, spectroscopically and crystallographically studied. Magnetic study of selected complexes will be carried out in the final phase. To achieve this purpose, the following partial goals were established:

1. Recent review of theoretical background and literature will be carried out using modern crystallographic and bibliographic databases. The review will be focused on the preparation, crystal structure and properties of known Ni(II), Co(II), Gd(III), Ce(III) and Dy(III) complexes as well as their bimetallic 3*d*-4*f* combinations. Special emphasis will be placed on the selection of ligands, mainly Schiff base and carboxylato ligands.
2. According to previous theoretical research, the proper synthetic procedures will be designed and carried out in an effort to prepare and isolate novel 3*d*, 4*f* and 3*d*-4*f* compounds. The aim is to prepare a rich variety of geometries of molecular species which leads to different properties, especially magnetic, of the resulting compounds. The preparation of single crystals is highly preferred. A convenient Schiff base ligand will be synthesized, isolated and used as a starting material for syntheses with metal ions.
3. The preparation and isolation of a large number of new compounds is assumed. The final products as well as side ones will be chemically (elemental analysis) and spectroscopically (IR, UV-VIS) characterized and their crystal and molecular structures will be determined using X-ray structure analysis. The combination of all available techniques will be used to determine the exact geometry of molecular species and ascertain the purity of final samples.
4. In the case of selected compounds their magnetic properties will be studied. The observed magnetic properties will be correlated with known crystal structures of the studied complexes.
5. The experimental results obtained will be published in the scientific journals, posters or lectures at scientific events such as conferences, meetings etc.

# 4 Experimental section

## 4.1 Materials

Benzoic acid, ethylenediamine, *o*-vanillin, $CoCO_3$, $Co(OH)_2$, $NiCl_2$, $NiCO_3$, $Gd(NO_3)_3 \cdot 6H_2O$, $GdCl_3 \cdot 6H_2O$, $CeCl_3 \cdot 7H_2O$, $DyCl_3 \cdot 6H_2O$ and solvents ethanol, methanol, isopropanol, acetonitrile and diethylether, all of analytical grade were purchased from commercial sources and used as received.

## 4.2 Syntheses

### 4.2.1 Synthesis of Schiff base as N,O-donor ligand

$H_2$(*o-van-en*) (**1**)

For the synthesis of $H_2$(*o-van-en*) a modified method to that already reported [Ghose, 1984] was used. Ethylenediamine (0.1 ml, 1.5 mmol) was added to 50 ml of ethanolic solution of *o*-vanillin (0.4542 g, 3 mmol). The mixture was placed in a boiling flask and refluxed for 5 hours. The final solution was filtered and left for crystallization. After few hours, dark yellow crystals of our product appeared. The crude product was filtered, washed with 2 ml of diethylether.

Yield: 90 %.

Anal. (%), calculated for $C_{18}H_{20}O_4N_2$ (M = 328.36 $g.mol^{-1}$):C, 65.83; H, 6.15; N, 8.53; found: C, 66.30; H, 6.33; N, 8.57.

FT-IR ($cm^{-1}$): 3746w, 2997w, 2931w, 2848w, 1631s, 1463s, 1438m, 1408m, 1325w, 1295w, 1246vs, 1189m, 1170m, 1133m, 1080s, 1054m, 1010m, 987m, 962s, 836s, 791s, 782s, 740s, 729s, 620m, 521m, 441m.

UV-Vis (nm) in EtOH: 219, 264; in $CHCl_3$: 265, 334.

$^1$H-NMR (ppm): 3.92m, 6.84m, 7.267s, 8.323s, 13.5s,b.

$^{13}$C-NMR (ppm): 56.056, 59.467, 114.084, 118.032, 118.419, 123.149, 148.269, 151.402, 166.643.

### 4.2.2 {Tr – (*o-van-en*)} complexes as precursors for 3*d*-4*f* complexes

[Ni(*o-van-en*)]·n$H_2O$ (**4**)

Solid $H_2$(*o-van-en*) (2 g, 6 mmol) and nickel(II) carbonate (0.7 g, 6 mmol) were placed in 100 ml of water and heated in an open beaker. After one hour of reaction the resulting brown microcrystalline product was separated by filtration, washed with 2 ml of ethanol and dried in air. Single crystals suitable for X-ray data collection were obtained by dissolving of the microcrystalline product in acetone; from the resulting clear brown-yellow solution the garnet red crystalline product **4** precipitated overnight.

Anal. (%), calculated for $C_{18}H_{20}O_5N_2Ni$ ([Ni(*o-van-en*)]·n$H_2O$, n = 1; M = 403.05 g.mol$^{-1}$): C, 53.64; H, 5.00; N, 6.95; found: C, 52.14; H, 4.79; N, 6.54.

FT-IR (cm$^{-1}$): 3454b, 3055w, 2934w, 2835w, 1621s, 1602s, 1547m, 1472s, 1447s, 1392w, 1314s, 1232s, 1167m, 1109m, 1092m, 1080m, 1001m, 973m, 860m, 777w, 722s, 662w, 619m, 571w, 543w, 480m, 426m, 401m.

[Ni(*o-van-en*)]·$H_2O$·EtOH (**5**)

Single crystals of complex **5** were obtained by the same procedure as was used for complex **4**, with the difference that the crude product was recrystallized from ethanol. After dissolving the crude product a clear brown-yellow solution was obtained which yielded overnight red prisms of **5** exhibiting low stability upon standing in air.

FT-IR (cm$^{-1}$): 3446b, 3055w, 2934w, 2834w, 1621s, 1602s, 1547m, 1471s, 1447s, 1392w, 1313s, 1232s, 1167m, 1109m, 1079s, 1000m, 973m, 859m, 777w, 722s, 667w, 619m, 571w, 542w, 480m, 425m, 401s.

[Ni(*o-van-en*)]·$H_2O$·iPrOH (**6**)

Single crystals of complex **6** were obtained by the same procedure as was used for complex **4**, with the difference that the crude product was recrystallized from isopropanol. Single crystals of **6**, in the form of brown tiny needles, separated overnight, were filtered, quickly washed with a small portion of cold isopropanol and dried in air.

Anal. (%), calculated for $C_{21}H_{28}O_6N_2Ni$ (M = 463.15 g.mol$^{-1}$): C, 54.46; H, 6.09; N, 6.05; found: C, 52.04; H, 5.13; N, 6.59.

FT-IR (cm$^{-1}$): 3508w, 3478w, 3330w, 3056w, 2961w, 2937w, 2840w, 1621s, 1603s, 1548m, 1473s, 1449s, 1408m, 1335w, 1314s, 1243s, 1232s, 1168m, 1136w, 1108m,

1080s, 1000m, 972m, 958m, 893w, 858m, 820w, 782w, 727s, 660w, 620m, 572w, 542w, 480m, 463w, 425m, 400s.

$[Co^{II}(o\text{-}van\text{-}en)(H_2O)]$ (**7**)

Solid $Co(OH)_2$ (0.07 g, 0.76 mmol) was added to a deoxygenated water suspension of $H_2$(*o-van-en*) (0.25 g, 0.76 mmol, 35 ml) at room temperature under an inert argon atmosphere. An orange solid appeared after a few minutes of stirring. The mixture was stirred overnight and the final dark orange microcrystalline product **7** was filtered, washed with water and dried in air.

Yield based on Co: 80 %.

Anal. (%), calculated for $CoC_{18}H_{20}N_2O_5$ (M = 403.29 $g.mol^{-1}$): C, 53.61; H, 5.00; N, 6.95; found: C, 53.80; H, 4.88; N, 6.87.

FT-IR ($cm^{-1}$): 3315b, 3055w, 2899w, 2827w, 1651m, 1625m, 1600m, 1545m, 1468m, 1438s, 1391m, 1310m, 1239s, 1213s, 1169m, 1078m, 980m, 967m, 853m, 743m, 723s, 640m, 421m.

$[Co^{III}_2(o\text{-}van\text{-}en)_3]\cdot 4MeCN$, Form I (**8**)

The microcrystalline product **7** was dissolved in acetonitrile in air with stirring at room temperature and after dissolution was left aside for crystallization. Within a few hours the resulting solution had changed colour from dark red to brown-black. Black block crystals of **8** were obtained after a few days. As the crystals were unstable when separated from the mother liquor, presumably due to loss of solvent molecules, they were mounted for diffraction data collection immediately after removing from the mother liquor.

$[Co^{III}_2(o\text{-}van\text{-}en)_3]\cdot 4MeCN$, Form II (**9**)

Solid $Co(OH)_2$ (0.07 g, 0.76 mmol) was added to a water suspension of $H_2$(*o-van-en*) (0.25 g, 0.76 mmol, 20 ml) at room temperature in air and stirred overnight until the microcrystalline solid had changed colour from yellow-brown to black. The product thus formed was filtered, dried in air and recrystallized from hot acetonitrile solution (~60 - 70 °C). Black block crystals of **9** appeared after a few days. The crystals of **9** were not stable in air, so they were mounted for diffraction data collection immediately after removing from acetonitrile solution.

$[Co^{III}(o\text{-}van\text{-}en)(H_2O)Cl]$ (**10**)

The previously prepared solid of $[Co^{II}L(H_2O)]$ (**7**, 0.0217 g, 0.054 mmol) was added to an ethanol solution of $GdCl_3$ (0.02 g of $GdCl_3 \cdot 6H_2O$, 0.054 mmol). The orange solution turned to dark brown (almost black) in a few seconds. The solution was filtered and left for crystallization at ambient conditions. After a few days, a few dark red-brown crystals suitable for X-ray diffraction analysis appeared.

$[Co^{III}(o\text{-}van\text{-}en)(H_2O)Cl] \cdot 2MeCN$ (**11**)

Solid $GdCl_3 \cdot 6H_2O$ and the previously prepared $[Co^{II}(o\text{-}van\text{-}en)(H_2O)]$ (**7**) in molar ratio 1 : 1 were both dissolved in acetonitrile at mild conditions. Single crystals of **11** were collected from mother liquor after several days. Unfortunately, details of the synthesis were lost in the lab notebook destroyed in a fire in the chemistry building of P. J. Šafárik University in Košice.

### 4.2.3 Syntheses of {Tr – (*o-van-en*) – Ln} complexes

$[Ni(o\text{-}van\text{-}en)Gd(NO_3)_3] \cdot 2MeCN$ (**12**)

Solid $H_2(o\text{-}van\text{-}en)$ (**1**), $Ni(NO_3)_2 \cdot 6H_2O$ and $Gd(NO_3)_3 \cdot 6H_2O$ in molar ratio 1 : 1 : 1 were dissolved in acetonitrile under mild conditions. Single crystals of **12** were collected from mother liquor after several days. Unfortunately, details of the synthesis were lost in the lab notebook destroyed in a fire in the chemistry building of P. J. Šafárik University in Košice. Crystals were not stable due to loss of $CH_3CN$ and therefore, the diffraction data were collected using the single crystal mounted on a MiTeGen support (MicroMount™) immediately after removing from mother liquor.

$[Ni(o\text{-}van\text{-}en)CeCl_3(H_2O)]$ (**13**)

Solid $H_2(o\text{-}van\text{-}en)$ (2 g, 6 mmml) and nickel(II) carbonate (0.7 g, 6 mmol) were placed in 100 ml of water and heated in an open beaker. After one hour of reaction the resulting brown microcrystalline product (crude nickel complex of **4**) was separated by filtration, washed with 2 ml of ethanol and dried in air. The dry product was used in the next step of the synthesis without further purification. Solid $CeCl_3 \cdot 7H_2O$ (0.3 g, 0.8 mmol) was dissolved in 10 ml of ethanol and the resulting clear solution was added to the brown ethanolic solution of **4** (50 ml of ethanol). After 15 minutes of stirring, the resulting orange microcrystalline complex of **13** was separated by filtration and washed three times with 2 ml of ethanol. Single crystals of **13** were obtained by recrystallization

of the microcrystalline complex using room temperature diffusion of the MeOH solution into iPrOH.

Yield: 81 %.

Anal. (%), calculated for $CeNiC_{18}H_{20}Cl_3O_5N_2$ (M = 649.53 g.mol$^{-1}$): C, 33.28; H, 3.10; N, 4.31; found: C, 32.50; H, 3.39; N, 4.30.

FT-IR (cm$^{-1}$): 3334wm, 3248m, 2952w, 2926w, 1638m, 1622s, 1608s, 1560m, 1459s, 1431m, 1410w, 1390w, 1342w, 1324w, 1291s, 1243s, 1230s, 1198m, 1165m, 1139w, 1101w, 1077s, 1053m, 989m, 980m, 956s, 900m, 864m, 847m, 783s, 739vs, 686m, 667w, 626m, 579m, 549m, 536m, 494m, 440s, 408s.

[Ni(*o-van-en*)$GdCl_3(H_2O)$] (**14**)

For the synthesis of **14,** the same procedure was used as for the Gd(III) complex with the modification that $GdCl_3 \cdot 6H_2O$ (0.3 g, 0.8 mmol) was used instead of $CeCl_3 \cdot 7H_2O$. Single crystals suitable for X-ray analysis were obtained by recrystallization using diffusion of a MeOH solution of $GdCl_3$ into an iPrOH solution of [Ni(*o-van-en*)] at room temperature.

Yield: 65 %.

Anal. (%), calculated for $GdNiC_{18}H_{20}Cl_3O_5N_2$ (M = 666.66 g.mol$^{-1}$): C, 32.43; H, 3.02; N, 4.20; found: C, 31.82; H, 2.73; N, 4.23.

FT-IR (cm$^{-1}$): 3347wm, 3242m, 2949w, 2927w, 1622s, 1609s, 1560m, 1471s, 1462s, 1435m, 1409m, 1390w, 1340w, 1323w, 1295s, 1247s, 1230s, 1198m, 1166m, 1142w, 1100w, 1077s, 1053m, 988m, 980m, 957s, 902m, 866m, 845m, 783s, 739vs, 692m, 669w, 629m, 580m, 550m, 539m, 497m, 442m, 409s.

[Ni(*o-van-en*)$DyCl_3(H_2O)$] Form I (**15**)

For the synthesis of **15**, the same procedure was used as for the Ce(III) complex with the modification that $DyCl_3.6H_2O$ (0.3 g, 0.8 mmol) was used instead of $CeCl_3 \cdot 7H_2O$. Crystals of **15** were obtained by recrystallization using diffusion of a methanolic solution of the microcrystalline product into iPrOH with a temperature gradient from 70 °C at the bottom of the beaker to room temperature at the top of solution.

Yield: 70 %.

Anal. (%), calculated for $DyNiC_{18}H_{20}Cl_3O_5N_2$ (M = 671.91 g.mol$^{-1}$): C, 32.18; H, 3.00; N, 4.17; found: C, 31.36; H, 3.23; N, 4.00.

FT-IR ($cm^{-1}$): 3342wm, 3242m, 2949w, 2928w, 1623s, 1610s, 1560m, 1462s, 1436m, 1400m, 1389w, 1340w, 1323w, 1294s, 1248s, 1229s, 1197m, 1166m, 1077s, 1053m, 988m, 978m, 958s, 903w, 866m, 788s, 739vs, 693m, 669w, 630m, 580m, 550m, 497m, 443m, 409s.

$[Ni_2Ce_2(o\text{-}van\text{-}en)_2Cl_6]$ (**16**)

A previously prepared solid of $[Ni(o\text{-}van\text{-}en)CeCl_3(H_2O)]$ (**13**) was dissolved in ethanol. A closed flask with a very dilute solution was kept in the oven at 80 °C for 3 days. The oven was allowed to cool to room temperature over a period of 13 hours and the flask was opened. Red-orange rhombic crystals were filtered and washed with cold ethanol.

FT-IR ($cm^{-1}$): 2936w, 2840w, 1628s, 1606s, 1560m, 1470s, 1453s, 1431s, 1410m, 1389m, 1335w, 1319m, 1289s, 1231s, 1176m, 1104m, 1076s, 990m, 960s, 859m, 801s, 771m, 751m, 730s, 681s, 666m, 625m, 604w, 588w, 575m, 542m, 492m, 473m, 439s.

$[Ni(o\text{-}van\text{-}en)DyCl_3]$ (**17**)

A previously prepared solid of $[NiLDyCl_3(H_2O)]$ (**15**) was dissolved in ethanol. A closed flask with a very dilute solution was kept in the oven at 80 °C for 3 days. The oven was allowed to cool to room temperature over a period of 13 hours and the flask was opened. A few fragile small orange crystals were collected manually and studied by single crystal X-ray diffraction.

$[Ni(o\text{-}van\text{-}en)DyCl_3]\cdot EtOH$ (**18**)

A previously prepared solid of $[NiLDyCl_3(H_2O)]$ (**15**) was dissolved in ethanol and layered with isopropanol at room temperature. After several hours orange-red crystals of **18** in the form of needles, suitable for X-ray diffraction analysis, were collected.

$[Ni(o\text{-}van\text{-}en)DyCl_3(H_2O)]$ Form II (**19**)

A previously prepared solid of $[Ni(o\text{-}van\text{-}en)DyCl_3(H_2O)]$ (**15**) was dissolved in ethanol and a layer of isopropanol was carefully added and the flask was closed. After diffusion finished, the beaker was opened and put on a metallic surface held at 70°C. After several hours, red-orange rhombic crystals were filtered and washed with cold isopropanol.

$[Ni_2(o\text{-}van\text{-}en)_2Dy_2Cl_6]$ (**20**)

A single crystal of $[Ni(o\text{-}van\text{-}en)Dy(H_2O)Cl_3]$ (Form II, **19**) was mounted on a MiTeGen support (MicroMount™), fixed to the goniometer head and put on the diffractometer. The temperature controlled by nitrogen current was set to 84°C. After several hours, single-crystal diffraction data revealed that a full transformation to $[Ni_2(o\text{-}van\text{-}en)_2Dy_2Cl_6]$ (**20**) had occurred.

### 4.2.4 Synthesis of Co(II) complex with O-donor ligand

$[Co\mathit{Bz}(H_2O)_2]\mathit{Bz}\cdot H_2O$ (**21**)

0.0975 g of solid $CoCO_3$ (0.82 mmol) and 0.1 g of solid benzoic acid (0.82 mmol) were placed in a beaker with 75 $cm^3$ of water. The reaction system was stirred and heated to boiling. After 3.5 hours of boiling the solution turned pink. The hot solution was filtered and left for crystallization at room temperature. Brown-green crystals of **21** suitable for a single crystal X-ray study appeared after three weeks.

Yield: 64 %.

Anal. (%), calculated for $C_{14}H_{16}CoO_7$ (M = 355.20 $g.mol^{-1}$): C, 47.34; H, 4.54; found: C, 47.05; H, 4.07.

FT-IR ($cm^{-1}$): 3054vw, 2977sb, 1591m, 1539s, 1495s, 1420s, 1383s, 1301m, 1070m, 1020m, 905m, 710s, 683s, 669s, 606s, 501s, 429m.

## 4.3 Physical measurements

**Elemental analysis.** Elemental analyses (C, H, N) were performed on a Perkin Elmer 2400 Series II CHNS/O analyser.

**IR spectroscopy.** Infrared spectra were recorded on a Perkin Elmer Spectrum 100 CsI DTGS FT-IR Spectrometer with UATR 1 bounce-KRS-5 in the range of 4000–300 $cm^{-1}$.

**UV-Vis spectroscopy.** The absorption spectra were measured on a SPECORD 250 spectrophotometer (Analytik Jena) in the 200–500 nm range.

**NMR spectroscopy.** NMR spectra for **1** were recorded at room temperature on a Varian VNMRS spectrometer operating at 599.87 MHz for $^1H$ and 150.84 MHz for $^{13}C$. Spectra were recorded in $CDCl_3$ and the chemical shifts were referenced to the residual solvent signal.

**Single-crystal X-ray diffraction analysis.** X–ray experiments were carried out on a four–circle κ–axis Xcalibur2 diffractometer equipped with a CCD detector Sapphire3 (Oxford Diffraction). The CrysAlis software package [Oxford Diffraction 2006 and later: CrysAlisPro CCD and CrysAlisPro RED] was used for data collection and reduction. The structures were solved using *SHELXT*. Refinement based on intensities was performed using *SHELXL-2014/7* and later versions of *ShelxL*. All non–hydrogen atoms were refined anisotropically. Hydrogen atoms were located in difference Fourier maps. For the final refinement, H atoms bound to C were placed at calculated positions and refined as riders with $U_{iso}$(H) = 1.2$U_{eq}$(C) for non-methyl H and with $U_{iso}$(H) = 1.5$U_{eq}$(C) for methyl H. Using the program CALC–OH the positions of the water hydrogen atoms for the water molecules and aqua ligands were found; their isotropic thermal parameters were tied with the parent atom [$U_{iso}$(H) = 1.2$U_{eq}$(O)]. The structure figures were drawn using Diamond. Crystal data and final parameters for the structure refinements are summarized in Table 4.3.1. We note that the geometric parameters of the water molecule (in the form of an aqua ligand or solvate) in **4**, **10** and **11** were restrained.

**Powder X-ray diffraction analysis.** Powder X-Ray data were collected using a RIGAKU D/max 2500 diffractometer equipped with a copper rotating anode, operating at 40 kV and 80 mA, with a graphite monochromator. Measurements were made for $2\theta$ from 2.5° to 40° in steps of 0.02° with a rate of 1 s/step. The Le Bail method [Le Bail *et al.*, 1988; Le Bail, 2005] incorporated in the program Jana2006 [Petříček *et al.*, 2014] was used for fitting the powder diffraction patterns. In the Le Bail refinements presented in this work, the best appropriate least-squares-fitted peak profile option was using the Pseudo-Voigt function [Thompson *et al*., 1987], convoluting the Gaussian and Lorentzian functions. Asymmetry corrections were performed using Bérar-Baldinozzi method [Bérar & Baldinozzi, 1993] or by divergence [Finger *et al*., 1994]. Background corrections were achieved using Legendre polynomials and shift parameters incorporated in Jana2006. Refined parameters of the functions mentioned above are listed within every refinement separately in section 5 Results and discussion along with the resulting unit cell parameters, respective *R* factors and goodness of fit.

**Magnetic measurements.** The magnetic susceptibility (determined as $\chi = M/H$) was taken at $B$ = 0.1 T using a SQUID magnetometer (Quantum Design, MPMS-XL7) in the temperature range from 1.9 to 300 K. Raw susceptibility data was corrected for

the diamagnetic contribution. The magnetization data was acquired at low temperature $T$ = 2.0 and 4.6 K until $B_{DC}$ = 7.0 T. The AC susceptibility data was taken at the applied external fields using the amplitude of the oscillating field $B_{AC}$ = 0.38 mT for a set of temperatures and for 22 frequencies between $f$ = 0.1 to 1500 Hz.

Table 4.3.1 Crystal data and the results of refinements for **1** – **21**.

| | **1** | **2** | **3** |
|---|---|---|---|
| Empirical formula | $C_{18}H_{20}N_2O_4$ | $C_2H_{10}Cl_2N_2$ | $C_9H_8O_6$ |
| Formula weight [g.mol$^{-1}$] | 326.36 | 133.02 | 212.15 |
| Crystal system, space group | monoclinic, *Pc* | monoclinic, $P2_1/c$ | orthorhombic, *Pbca* |
| Unit cell dimensions [Å, °, Å$^3$] | *a* = 9.2917 (4)<br>*b* = 6.2208 (2)<br>*c* = 14.3902 (6)<br>*α* = 90<br>*β* = 93.178 (3)<br>*γ* = 90<br>*V* = 830.50 (6) | *a* = 4.4203 (7)<br>*b* = 6.8752 (10)<br>*c* = 9.9336 (17)<br>*α* = 90<br>*β* = 91.300 (16)<br>*γ* = 90<br>*V* = 301.81 (8) | *a* = 10.2800 (7)<br>*b* = 7. 1643 (7)<br>*c* = 23.1902 (14)<br>*α* = 90<br>*β* = 90<br>*γ* = 90<br>*V* = 1707.9 (2) |
| *Z* | 2 | 2 | 8 |
| Calculated density [Mg.m$^{-3}$] | 1.313 | 1.464 | 1.650 |
| Abs. coeff. [mm$^{-1}$] | 0.094 | 0.944 | 0.142 |
| Crystal form, colour, size [mm] | yellow prism<br>0.260 x 0.149 x 0.083 | pale yellow-orange needle<br>0.70 x 0.03 x 0.02 | yellow block<br>0.481 x 0.164 x 0.092 |
| Temperature [K] | 173 (2) | 293 (2) | 293 (2) |
| Radiation [Å] | Mo$K_\alpha$ ($\lambda$ = 0.71073) | Mo$K_\alpha$ ($\lambda$ = 0.71073) | Mo$K_\alpha$ ($\lambda$ = 0.71073) |
| Diffractometer | XCalibur, CCD detector | XCalibur, CCD detector | XCalibur, CCD detector |
| $\theta$ range for data collection [°] | 4.788 - 25.480 | 3.604 - 25.000 | 3. 514 - 25.498 |
| Index ranges | $-11 \le h \le 11$, $-7 \le k \le 7$, $-17 \le l \le 17$ | $-5 \le h \le 5$, $-8 \le k \le 8$, $-11 \le l \le 11$ | $-12 \le h \le 8$, $-8 \le k \le 8$, $-28 \le l \le 28$ |
| Refl. coll. / indp. | 7573 / 2703 | 3099 / 532 | 6525 / 1586 |
| GooF (S) | 1.012 | 1.022 | 0.985 |
| Final *R* indices [$I > 2\sigma(I)$] | *R*1 = 0.0339, w*R*2 = 0.0668 | *R*1 = 0.0620, w*R*2 = 0.1503 | *R*1 = 0.0704, w*R*2 = 0.1929 |
| *R* indices (all data) | *R*1 = 0.0480, w*R*2 = 0.0733 | *R*1 = 0.1030, w*R*2 = 0.1792 | *R*1 = 0.1164, w*R*2 = 0.2395 |
| Largest diff. peak and hole [e.Å$^{-3}$] | $-0.132 \le \Delta\rho \le 0.120$ | $-0.420 \le \Delta\rho \le 0.471$ | $-0.281 \le \Delta\rho \le 0.570$ |

Table 4.3.1. Continued.

| | **4 (RT)** | **4 (LT)** | **5** |
|---|---|---|---|
| Empirical formula | $C_{18}H_{20}N_2NiO_5$ | $C_{18}H_{20}N_2NiO_5$ | $C_{20}H_{26}N_2NiO_6$ |
| Formula weight [g.mol$^{-1}$] | 403.07 | 403.07 | 449.14 |
| Crystal system, space group | orthorhombic, *Pbcn* | orthorhombic, *Pbcn* | triclinic, *P*-1 |
| Unit cell dimensions [Å, °, Å$^3$] | *a* = 19.6427 (8)<br>*b* = 11.8972 (5)<br>*c* = 15.2443 (8)<br>*α* = 90<br>*β* = 90<br>*γ* = 90<br>*V* = 3562.5 (3) | *a* = 19.6607 (6)<br>*b* = 11.8032 (4)<br>*c* = 15.0266 (4)<br>*α* = 90<br>*β* = 90<br>*γ* = 90<br>*V* = 3487.05 (18) | *a* = 7.8460 (2)<br>*b* = 11. 4533 (3)<br>*c* = 12.2907 (3)<br>*α* = 76.702 (2)<br>*β* = 79.967 (2)<br>*γ* = 70.233 (2)<br>*V* = 1005.90 (5) |
| *Z* | 8 | 8 | 2 |
| Calculated density [Mg.m$^{-3}$] | 1.503 | 1.536 | 1.483 |
| Abs. coeff. [mm$^{-1}$] | 1.121 | 1.145 | 1.004 |
| Crystal form, colour, size [mm] | red block<br>0.38 x 0.14 x 0.11 | red block<br>0.503 x 0.240 x 0.217 | red block<br>0.355 x 0.232 x 0.121 |
| Temperature [K] | 293 (2) | 100 (2) | 100 (2) |
| Radiation [Å] | Mo$K_\alpha$ ($\lambda$ = 0.71073) | Mo$K_\alpha$ ($\lambda$ = 0.71073) | Mo$K_\alpha$ ($\lambda$ = 0.71073) |
| Diffractometer | XCalibur, CCD detector | XCalibur, CCD detector | XCalibur, CCD detector |
| $\theta$ range for data collection [°] | 3.339 - 25.996 | 2.902 - 26.497 | 3.411 - 26.242 |
| Index ranges | $-24 \le h \le 24$, $-14 \le k \le 14$, $-18 \le l \le 18$ | $-23 \le h \le 24$, $-14 \le k \le 14$, $-18 \le l \le 18$ | $-9 \le h \le 9$, $-14 \le k \le 14$, $-15 \le l \le 15$ |
| Refl. coll. / indp. | 57900 / 3497 | 28538 / 3615 | 35818 / 4154 |
| GooF (S) | 1.015 | 1.032 | 1.050 |
| Final *R* indices [$I > 2\sigma(I)$] | *R*1 = 0.0480, w*R*2 = 0.1135 | *R*1 = 0.0339, w*R*2 = 0.0855 | *R*1 = 0.0255, w*R*2 = 0.0676 |
| *R* indices (all data) | *R*1 = 0.0789, w*R*2 = 0.1343 | *R*1 = 0.0407, w*R*2 = 0.0907 | *R*1 = 0.0280, w*R*2 = 0.0693 |
| Largest diff. peak and hole [e.Å$^{-3}$] | $-0.265 \le \Delta\rho \le 0.523$ | $-0.293 \le \Delta\rho \le 0.383$ | $-0.321 \le \Delta\rho \le 0.384$ |

Table 4.3.1. Continued.

| | **6** | **8** | **9** |
|---|---|---|---|
| Empirical formula | $C_{21}H_{28}N_2NiO_6$ | $C_{62}H_{66}Co_2N_{10}O_{12}$ | $C_{62}H_{66}Co_2N_{10}O_{12}$ |
| Formula weight [g.mol$^{-1}$] | 463.16 | 1261.10 | 1261.10 |
| Crystal system, space group | monoclinic, $P2_1/n$ | monoclinic, $P2_1/c$ | triclinic, $P$-1 |
| Unit cell dimensions [Å, °, Å$^3$] | $a$ = 14.1325 (7)<br>$b$ = 7.4085 (4)<br>$c$ = 20.1164 (8)<br>$\alpha$ = 90<br>$\beta$ = 93.527 (4)<br>$\gamma$ = 90<br>$V$ = 2102.21 (18) | $a$ = 12.4355 (3)<br>$b$ = 21.6501 (4)<br>$c$ = 11.9462 (43)<br>$\alpha$ = 90<br>$\beta$ = 115.364 (4)<br>$\gamma$ = 90<br>$V$ = 2906.25 (15) | $a$ = 10.4971 (5)<br>$b$ = 11. 6195 (5)<br>$c$ = 13.7158 (6)<br>$\alpha$ = 70.471 (4)<br>$\beta$ = 71.667 (4)<br>$\gamma$ = 72.466 (4)<br>$V$ = 1460.26 (13) |
| $Z$ | 4 | 2 | 1 |
| Calculated density [Mg.m$^{-3}$] | 1.463 | 1.441 | 1.434 |
| Abs. coeff. [mm$^{-1}$] | 0.963 | 0.644 | 0.641 |
| Crystal form, colour, size [mm] | brown needle<br>0.379 x 0.033 x 0.017 | black block<br>0.188 x 0.173 x 0.044 | black block<br>0.212 x 0.144 x 0.049 |
| Temperature [K] | 293 (2) | 100 (2) | 100 (2) |
| Radiation [Å] | Mo$K_\alpha$ ($\lambda$ = 0.71073) | Mo$K_\alpha$ ($\lambda$ = 0.71073) | Mo$K_\alpha$ ($\lambda$ = 0.71073) |
| Diffractometer | XCalibur, CCD detector | XCalibur, CCD detector | XCalibur, CCD detector |
| $\theta$ range for data collection [°] | 3.240 - 26.500 | 2.613 - 27.500 | 3. 245 - 26.497 |
| Index ranges | $-17 \le h \le 17$, $-8 \le k \le 9$, $-25 \le l \le 25$ | $-10 \le h \le 16$, $-28 \le k \le 28$, $-14 \le l \le 15$ | $-13 \le h \le 13$, $-14 \le k \le 14$, $-17 \le l \le 17$ |
| Refl. coll. / indp. | 15533 / 4351 | 24772 / 6530 | 20710 / 6041 |
| GooF (S) | 1.032 | 1.021 | 1.038 |
| Final $R$ indices [$I > 2\sigma(I)$] | $R1$ = 0.0460, w$R2$ = 0.1006 | $R1$ = 0.0450, w$R2$ = 0.0954 | $R1$ = 0.0373, w$R2$ = 0.0890 |
| $R$ indices (all data) | $R1$ = 0.0786, w$R2$ = 0.1122 | $R1$ = 0.0707, w$R2$ = 0.1063 | $R1$ = 0.0466, w$R2$ = 0.0940 |
| Largest diff. peak and hole [e.Å$^{-3}$] | $-0.384 \le \Delta\rho \le 0.898$ | $-0.393 \le \Delta\rho \le 0.544$ | $-0.348 \le \Delta\rho \le 0.889$ |

Table 4.3.1. Continued.

| | **10** | **11** | **12** |
|---|---|---|---|
| Empirical formula | $C_{18}H_{20}ClCoN_2NiO_5$ | $C_{22}H_{26}ClCoN_4O_5$ | $C_{22}H_{24}GdN_7NiO_{13}$ |
| Formula weight [g.mol$^{-1}$] | 438.74 | 520.85 | 810.44 |
| Crystal system, space group | orthorhombic, *Pbca* | monoclinic, $P2_1/n$ | orthorhombic, $Pna2_1$ |
| Unit cell dimensions [Å, °, Å$^3$] | $a$ = 13.8127 (5)<br>$b$ = 15.0784 (7)<br>$c$ = 17.1178 (5)<br>$\alpha$ = 90<br>$\beta$ = 90<br>$\gamma$ = 90<br>$V$ = 3565.2 (2) | $a$ = 13.3890 (9)<br>$b$ = 11.0995 (5)<br>$c$ = 16.0031 (10)<br>$\alpha$ = 90<br>$\beta$ = 101.805 (7)<br>$\gamma$ = 90<br>$V$ = 2327.9 (2) | $a$ = 28.3598 (17)<br>$b$ = 11. 1664 (4)<br>$c$ = 9.40200 (4)<br>$\alpha$ = 90<br>$\beta$ = 90<br>$\gamma$ = 90<br>$V$ = 2856.4 (2) |
| $Z$ | 8 | 4 | 4 |
| Calculated density [Mg.m$^{-3}$] | 1.635 | 1.486 | 1.885 |
| Abs. coeff. [mm$^{-1}$] | 1.146 | 0.893 | 3.038 |
| Crystal form, colour, size [mm] | dark red-brown block<br>0.106 x 0.080 x 0.052 | dichroic dark orange/black block<br>0.205 x 0.110 x 0.018 | yellow-orange plate<br>0.285 x 0.131 x 0.028 |
| Temperature [K] | 300 (2) | 100 (2) | 100 (2) |
| Radiation [Å] | Mo$K_\alpha$ ($\lambda$ = 0.71073) | Mo$K_\alpha$ ($\lambda$ = 0.71073) | Mo$K_\alpha$ ($\lambda$ = 0.71073) |
| Diffractometer | XCalibur, CCD detector | XCalibur, CCD detector | XCalibur, CCD detector |
| $\theta$ range for data collection [°] | 2.800 - 25.496 | 3.301 - 25.992 | 3. 239 - 25.497 |
| Index ranges | $-16 \le h \le 16$, $-18 \le k \le 12$, $-19 \le l \le 20$ | $-16 \le h \le 15$, $-13 \le k \le 13$, $-19 \le l \le 19$ | $-34 \le h \le 34$, $-13 \le k \le 14$, $-10 \le l \le 10$ |
| Refl. coll. / indp. | 10813 / 3323 | 17719 / 4565 | 16034 / 4960 |
| GooF (S) | 1.026 | 0.999 | 1.066 |
| Final $R$ indices [$I > 2\sigma(I)$] | $R1$ = 0.0452, w$R2$ = 0.0778 | $R1$ = 0.0629, w$R2$ = 0.1351 | $R1$ = 0.0411, w$R2$ = 0.1043 |
| $R$ indices (all data) | $R1$ = 0.0898, w$R2$ = 0.1021 | $R1$ = 0.0953, w$R2$ = 0.1558 | $R1$ = 0.0508, w$R2$ = 0.1152 |
| Largest diff. peak and hole [e.Å$^{-3}$] | $-0.331 \le \Delta\rho \le 0.358$ | $-0.792 \le \Delta\rho \le 1.129$ | $-1.068 \le \Delta\rho \le 1.255$ |

Table 4.3.1. Continued.

| | **13** | **14** | **15** |
|---|---|---|---|
| Empirical formula | $C_{18}H_{20}Cl_3CeN_2NiO_5$ | $C_{18}H_{20}Cl_3GdN_2NiO_5$ | $C_{18}H_{20}Cl_3DyN_2NiO_5$ |
| Formula weight [g.mol$^{-1}$] | 649.54 | 666.67 | 671.92 |
| Crystal system, space group | monoclinic, $P2_1/n$ | monoclinic, $P2_1/n$ | monoclinic, $P2_1/n$ |
| Unit cell dimensions [Å, °, Å$^3$] | $a$ = 7.1269 (3)<br>$b$ = 14.4698 (6)<br>$c$ = 21.0732 (12)<br>$\alpha$ = 90<br>$\beta$ = 93.014 (4)<br>$\gamma$ = 90<br>$V$ = 2170.18 (18) | $a$ = 7.0236 (3)<br>$b$ = 14.3753 (9)<br>$c$ = 20.9662 (13)<br>$\alpha$ = 90<br>$\beta$ = 92.216 (5)<br>$\gamma$ = 90<br>$V$ = 2115.3 (2) | $a$ = 7.00940 (10)<br>$b$ = 14.3916 (3)<br>$c$ = 20.9556 (5)<br>$\alpha$ = 90<br>$\beta$ = 91.833 (2)<br>$\gamma$ = 90<br>$V$ = 2112.85 (7) |
| $Z$ | 4 | 4 | 4 |
| Calculated density [Mg.m$^{-3}$] | 1.988 | 2.093 | 2.112 |
| Abs. coeff. [mm$^{-1}$] | 3.341 | 4.411 | 4.813 |
| Crystal form, colour, size [mm] | dichroic red-orange/colourless block<br>0.091 x 0.057 x 0.018 | pale pink block<br>0.175 x 0.079 x 0.034 | dichroic red/colourless prism<br>0.08 x 0.04 x 0.02 |
| Temperature [K] | 299 (2) | 295 (2) | 293 (2) |
| Radiation [Å] | Mo$K_\alpha$ ($\lambda$ = 0.71073) | Mo$K_\alpha$ ($\lambda$ = 0.71073) | Mo$K_\alpha$ ($\lambda$ = 0.71073) |
| Diffractometer | XCalibur, CCD detector | XCalibur, CCD detector | XCalibur, CCD detector |
| $\theta$ range for data collection [°] | 3.653 - 28.384 | 3.230 - 24.997 | 2. 831 - 30.302 |
| Index ranges | $-9 \le h \le 9$, $-19 \le k \le 19$, $-28 \le l \le 26$ | $-8 \le h \le 8$, $-10 \le k \le 17$, $-24 \le l \le 23$ | $-9 \le h \le 8$, $-20 \le k \le 19$, $-29 \le l \le 28$ |
| Refl. coll. / indp. | 6159 / 6159 | 9912 / 3716 | 26349 / 5820 |
| GooF (S) | 0.972 | 0.943 | 1.038 |
| Final $R$ indices [$I > 2\sigma(I)$] | $R1$ = 0.0370, w$R2$ = 0.0990 | $R1$ = 0.0589, w$R2$ = 0.0692 | $R1$ = 0.0338, w$R2$ = 0.0587 |
| $R$ indices (all data) | $R1$ = 0.0642, w$R2$ = 0.1051 | $R1$ = 0.1320, w$R2$ = 0.0864 | $R1$ = 0.0577, w$R2$ = 0.0671 |
| Largest diff. peak and hole [e.Å$^{-3}$] | $-0.640 \le \Delta\rho \le 0.708$ | $-1.148 \le \Delta\rho \le 1.613$ | $-0.821 \le \Delta\rho \le 0.677$ |

Table 4.3.1. Continued.

| | **16** | **17** | **18** |
|---|---|---|---|
| Empirical formula | $C_{18}H_{18}CeCl_3N_2NiO_4$ | $C_{18}H_{18}Cl_3DyN_2NiO_4$ | $C_{20}H_{24}Cl_3DyN_2NiO_5$ |
| Formula weight [g.mol$^{-1}$] | 631.52 | 653.90 | 699.97 |
| Crystal system, space group | triclinic, *P*-1 | triclinic, *P*-1 | monoclinic, $P2_1/c$ |
| Unit cell dimensions [Å, °, Å$^3$] | *a* = 9.5527 (3)<br>*b* = 11.0298 (3)<br>*c* = 11.4447 (3)<br>$\alpha$ = 69.564 (3)<br>$\beta$ = 82.214 (3)<br>$\gamma$ = 66.225 (3)<br>*V* = 1034.06 (6) | *a* = 8.1516 (9)<br>*b* = 10.1225 (5)<br>*c* = 12.7149 (11)<br>$\alpha$ = 81.526 (6)<br>$\beta$ = 84.239 (8)<br>$\gamma$ = 76.196 (7)<br>*V* = 1005.41 (15) | *a* = 11.4426 (3)<br>*b* = 8. 8478 (2)<br>*c* = 23.5430 (4)<br>$\alpha$ = 90<br>$\beta$ = 96.376 (2)<br>$\gamma$ = 90<br>*V* = 2368.79 (9) |
| *Z* | 2 | 2 | 4 |
| Calculated density [Mg.m$^{-3}$] | 2.028 | 2.160 | 1.963 |
| Abs. coeff. [mm$^{-1}$] | 3.499 | 5.051 | 4.298 |
| Crystal form, colour, size [mm] | red-orange-brown block<br>0.165 x 0.094 x 0.031 | pale brown-orange slat<br>0.071 x 0.040 x 0.009 | red-orange needle<br>0.586 x 0.095 x 0.084 |
| Temperature [K] | 299 (2) | 100 (2) | 173 (2) |
| Radiation [Å] | Mo$K_\alpha$ ($\lambda$ = 0.71073) | Mo$K_\alpha$ ($\lambda$ = 0.71073) | Mo$K_\alpha$ ($\lambda$ = 0.71073) |
| Diffractometer | XCalibur, CCD detector | XCalibur, CCD detector | XCalibur, CCD detector |
| $\theta$ range for data collection [°] | 2.484 - 30.139 | 2.579 - 27.800 | 2. 887 - 30.053 |
| Index ranges | -1 3≤ $h$ ≤ 13, -15 ≤ $k$ ≤ 14, -16 ≤ $l$ ≤ 15 | -10 ≤ $h$ ≤ 10, -12 ≤ $k$ ≤ 13, -16 ≤ $l$ ≤ 14 | -16 ≤ $h$ ≤ 16, -11 ≤ $k$ ≤ 12, -32 ≤ $l$ ≤ 32 |
| Refl. coll. / indp. | 20870 / 5626 | 10592 / 4082 | 38460 / 6535 |
| GooF (S) | 1.143 | 1.036 | 1.072 |
| Final *R* indices [$I > 2\sigma(I)$] | *R*1 = 0.0303, w*R*2 = 0.0722 | *R*1 = 0.0500, w*R*2 = 0.0899 | *R*1 = 0.0231, w*R*2 = 0.0522 |
| *R* indices (all data) | *R*1 = 0.0406, w*R*2 = 0.0863 | *R*1 = 0.0965, w*R*2 = 0.1077 | *R*1 = 0.0289, w*R*2 = 0.0546 |
| Largest diff. peak and hole [e.Å$^{-3}$] | -0.826 ≤ $\Delta\rho$ ≤ 0.929 | -1.653 ≤ $\Delta\rho$ ≤ 0.850 | -0.699 ≤ $\Delta\rho$ ≤ 1.225 |

Table 4.3.1. Continued.

| | **19** | **20** | **21** |
|---|---|---|---|
| Empirical formula | $C_{18}H_{20}Cl_3DyN_2NiO_5$ | $C_{18}H_{18}Cl_3DyN_2NiO_4$ | $C_{14}H_{16}CoO_7$ |
| Formula weight [g.mol$^{-1}$] | 671.92 | 653.90 | 355.20 |
| Crystal system, space group | monoclinic, $P2_1/n$ | monoclinic, $P2_1/n$ | monoclinic, $I2/a$ |
| Unit cell dimensions [Å, °, Å$^3$] | $a$ = 13.5202 (3)<br>$b$ = 9.4039 (2)<br>$c$ = 17.2556 (3)<br>$\alpha$ = 90<br>$\beta$ = 91.0114 (19)<br>$\gamma$ = 90<br>$V$ = 2193.57 (8) | $a$ = 12.118 (3)<br>$b$ = 9.3732 (9)<br>$c$ = 18.545 (3)<br>$\alpha$ = 90<br>$\beta$ = 88.535(16)<br>$\gamma$ = 90<br>$V$ = 2105.7 (6) | $a$ = 6.2299 (4)<br>$b$ = 34.115 (3)<br>$c$ = 6.9101 (4)<br>$\alpha$ = 90<br>$\beta$ = 95.689 (7)<br>$\gamma$ = 90<br>$V$ = 1461.38 (17) |
| $Z$ | 4 | 4 | 4 |
| Calculated density [Mg.m$^{-3}$] | 2.035 | 2.063 | 1.614 |
| Abs. coeff. [mm$^{-1}$] | 4.636 | 4.823 | 1.207 |
| Crystal form, colour, size [mm] | orange needle<br>0.249 x 0.068 x 0.057 | pale orange slat<br>0.336 x 0.088 x 0.010 | pale plate<br>0.134 x 0.084 x 0.043 |
| Temperature [K] | 301 (2) | 173 (2) | 293 (2) |
| Radiation [Å] | Mo$K_\alpha$ ($\lambda$ = 0.71073) | Mo$K_\alpha$ ($\lambda$ = 0.71073) | Mo$K_\alpha$ ($\lambda$ = 0.71073) |
| Diffractometer | XCalibur, CCD detector | XCalibur, CCD detector | XCalibur, CCD detector |
| $\theta$ range for data collection [°] | 2.880 - 30.362 | 2.748 - 28.046 | 4.204 - 26.487 |
| Index ranges | $-18 \le h \le 18$, $-13 \le k \le 12$, $-24 \le l \le 23$ | $-14 \le h \le 15$, $-11 \le k \le 11$, $-14 \le l \le 24$ | $-7 \le h \le 7$, $-42 \le k \le 42$, $-8 \le l \le 8$ |
| Refl. coll. / indp. | 18511 / 5946 | 8808 / 4228 | 4564 / 1513 |
| GooF (S) | 1.018 | 1.048 | 1.175 |
| Final $R$ indices [$I > 2\sigma(I)$] | $R1$ = 0.0299, w$R2$ = 0.0546 | $R1$ = 0.0953, w$R2$ = 0.1426 | $R1$ = 0.0397, w$R2$ = 0.0962 |
| $R$ indices (all data) | $R1$ = 0.0446, w$R2$ = 0.0600 | $R1$ = 0.1893, w$R2$ = 0.1760 | $R1$ = 0.0566, w$R2$ = 0.1323 |
| Largest diff. peak and hole [e.Å$^{-3}$] | $-0.704 \le \Delta\rho \le 0.519$ | $-0.998 \le \Delta\rho \le 2.450$ | $-0.813 \le \Delta\rho \le 1.049$ |

# 5 Results and discussion

## 5.1 Schiff base ligand (*o-van-en*)$^{2-}$ as N,O-donor ligand

Schiff base $H_2$(*o-van-en*) was prepared by the reaction of ethylenediamine and *o*-vanillin in a 1:2 molar ratio. The preparation and the basic characterization were already described by Ghose [1983; 1984] and its crystal structure was published by Cunningham *et al.* [2004] (*cis* isomer) and Correia *et al.* [2005] (*trans* isomer); see Section 2.6 in the theoretical background of this work. By modifying the reaction conditions, the Schiff reaction was carried out in ethanol under reflux conditions while producing water as a side product (Scheme 5.1.1).

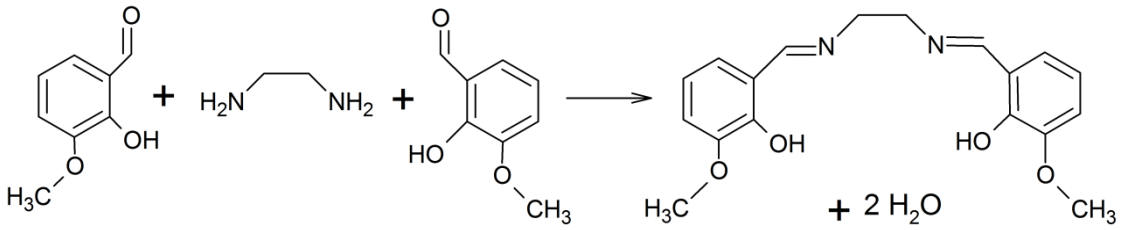


Scheme 5.1.1 The Schiff reaction of ethylenediamine and *o*-vanillin in a 1:2 molar ratio.

The product **1** was prepared in microcrystalline form by filtration from a hot solution. The identification and the purity of the product were confirmed by various techniques, including $^{1}$H-NMR, $^{13}$C-NMR, IR, UV-Vis spectroscopies and elemental analysis. The crystalline form was produced by slow evaporation of the mother liquor after several hours. The needle like yellow single crystals were characterized by single-crystal X-ray analysis.

The Schiff base $H_2$(*o-van-en*) (**1**) prepared by us crystallizes in the non-centrosymmetric monoclinic space group P*c*. The molecular structure of the *cis* stereoisomer is supported by intramolecular hydrogen bonds between N atoms of the imine groups, acting as acceptors, with hydroxo groups as donors (Fig. 5.1.1a); Tab. 5.1.1). Additionally, its crystal structure displays two weaker intermolecular hydrogen bonds coming from aromatic C5 and imine C11 donor atoms forming the 3D packing in **1** (Fig. 5.1.1b); Tab. 5.1.1).

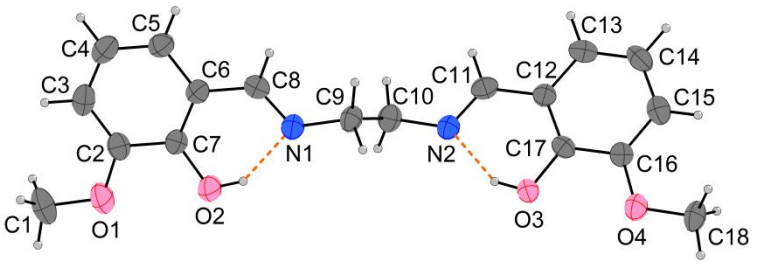


a)

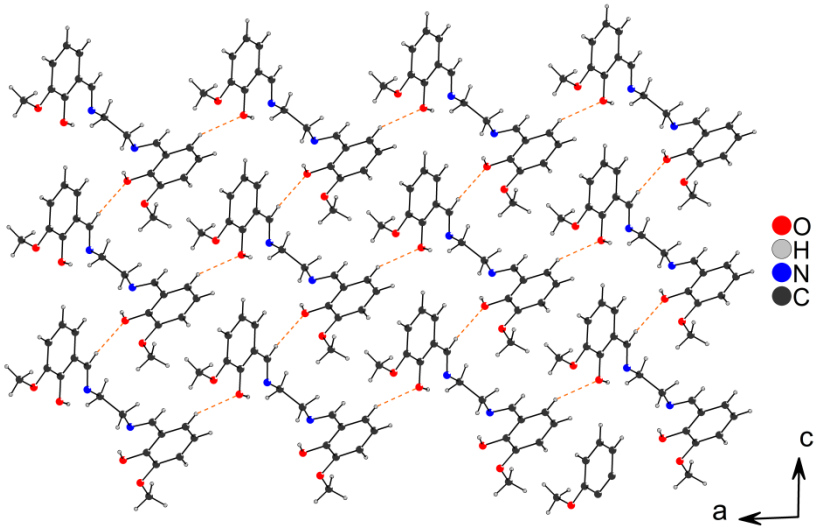


b)

Figure 5.1.1 a) The molecular structure of **1**. The thermal ellipsoids are drawn at the 50 % probability level. Intramolecular hydrogen bonds are drawn as orange dashed lines.

b) Crystal structure of **1**. Intermolecular hydrogen bonds are drawn as orange dashed lines. The *ac* plane is shown.

Table 5.1.1 Potential hydrogen bonds in **1**.

| **D–H···A** | **D–H [Å]** | **H···A [Å]** | **D···A [Å]** | **D–H···A [°]** |
|---|---|---|---|---|
| O2–H2O···N1 | 0.84 | 1.86 | 2.605 (3) | 146 |
| O3–H3O···N2 | 0.84 | 1.82 | 2.561 (3) | 147 |
| C5–H5···O3$^{i}$ | 0.95 | 2.47 | 3.255 (3) | 140 |
| C11–H11···O2$^{ii}$ | 0.95 | 2.47 | 3.404 (3) | 168 |

Symmetry codes: i: –1 + *x*, 1 + *y*, *z*; ii: *x*, 2 – *y*, 1/2 + *z*.

## 5.2 {Tr – (*o-van-en*)} complexes as precursors for 3*d*-4*f* complexes

In an attempt to synthesize bimetallic complexes, our first synthetic experiments in the laboratory included the *in situ* approach. We conducted several experiments using nickel(II), cobalt(II) and lanthanide(III) salts combined with our compartmental ligand $H_2$(*o-van-en*) under mild conditions. Of them, two can be mentioned in more detail.

Firstly, nickel(II) chloride, cerium(III) chloride and the Schiff base ligand $H_2$(*o-van-en*) were put together in ethanol and the solution was refluxed for an hour. The final solid product was filtered out immediately and the filtrate was left for crystallization at room temperature. The major product was characterized as [Ni(*o-van-en*)$CeCl_3(H_2O)$]. This product was prepared with higher purity and yield using a modified synthetic procedure and it will be analysed (compound **14**) later in Section 5.4 of this work. After a few hours, pale yellow prismatic crystals of **2** were collected from the filtrate, suitable for single-crystal X-ray analysis.

Crystalline product **2** mentioned above was characterized as ethylenediammonium chloride and its formation can be explained as the result of the decomposition of the Schiff base $H_2$(*o-van-en*) in acidic medium. Further analysis of the processes in the reaction system lead to the hypothesis that the acidic medium is formed after the deprotonation of the ligand (releasing the two protons) and the coordination of the nickel central atom (releasing two chloride anions from the nickel(II) chloride).

Ethylenediammonium chloride (**2**) crystallizes in space group $P2_1/c$ where only half of the ethylenediammonium cation and one chloride ion form the asymmetric unit. The rest of the formula is generated through the centre of symmetry [$1 - x$, $1 - y$, $1 - z$] (Fig. 5.2.1a). Cations and anions are held together by three hydrogen bonds of the N–H···Cl type generating the hydrogen bonding system forming a 2D layered crystal structure parallel to the *bc* plane (Fig. 5.2.1b); Tab. 5.2.1).

We note that the crystal structure of ethylenediammonium chloride was already reported by several research groups [Ashida & Hirokawa, 1963; Reuter & Kastner, 1997; Bujak *et al*., 2000; Kooijman *et al.*, 2006; Dickman, 2007; Seidel, 2009; Gabro *et al*., 2009; Liu *et al*., 2010; Kubicki, 2009]. Consequently, the results of our structure analysis were deposited as a CSD communication [Vráblová *et al.*, 2017].

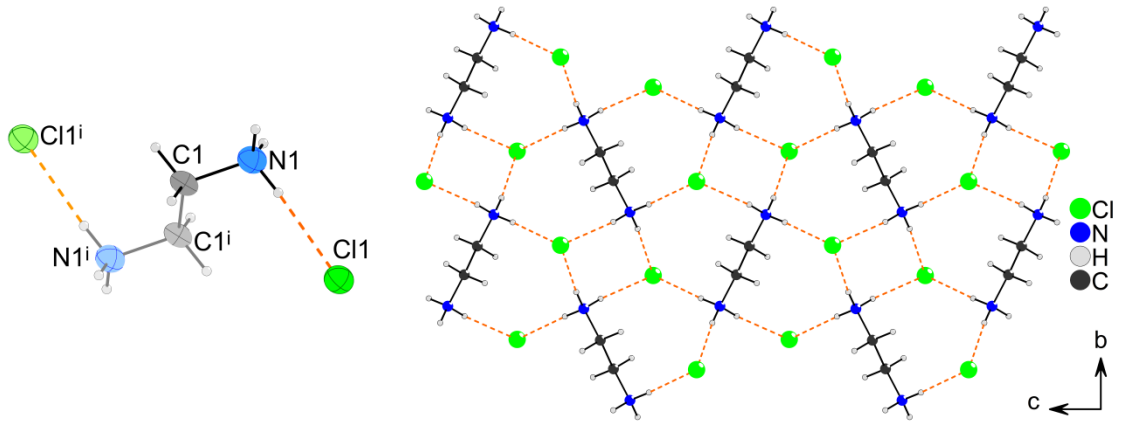


a) b)

Figure 5.2.1

a) Molecular structure of **2**. The hydrogen bonds are drawn as orange dashed lines. The asymmetric unit consists of only half of the molecule. The other half generated through the centre of symmetry is drawn in light colours. Symmetry code: i: 1 – *x*, 1 – *y*, 1 – *z*. The thermal ellipsoids are drawn at the 50 % probability level.

b) The crystal structure of **2** held by hydrogen bonding system (orange dashed lines); the *bc* plane is depicted.

Table 5.2.1 Potential hydrogen bonds in **2**.

| **D-H···A** | **D-H [Å]** | **H···A [Å]** | **D···A [Å]** | **D-H···A [°]** |
|---|---|---|---|---|
| N1-H1A···Cl1$^{i}$ | 0.89 | 2.28 | 3.169 (4) | 174 |
| N1-H1B···Cl1$^{ii}$ | 0.89 | 2.25 | 3.142 (4) | 177 |
| N1-H1C···Cl1$^{iii}$ | 0.89 | 2.32 | 3.197 (4) | 167 |

Symmetry codes: i: 1 – *x*, – 1/2 + *y*, 1/2 – *z*; ii: *x*, 1/2 – *y*, 1/2 + *z*; iii: – 1 + *x*, *y*, *z*.

The second synthetic experiment with *in situ* approach we will mention in this work is the reaction of cobalt(II) carbonate, dysprosium(III) chloride and $H_2$(*o-van-en*) ligand where as in the previous case, ethanol was used as solvent. The reaction system was stirred and heated to 80 °C and after 15 minutes, the solid product precipitated. The re-crystallization experiments were not successful, only the experiment of the diffusion of the ethanol solution into isopropanol yielded the crystalline form of the side product 1,5-dicarboxy-2-hydroxy-3-methoxybenzene (**3**). This compound may be the result of several potential processes, including the decomposition of the Schiff base ligand $H_2$(*o-van-en*) yielding back *o*-vanillin, oxidation of the aldehyde group of *o*-vanillin and finally, carboxylation of the previous intermediate. This hypothesis is based on the

assumption that the excess of $CO_3^{2-}$ coming from cobalt(II) carbonate is the origin of the acidic medium and also caused the final carboxylation.

The 1,5-dicarboxy-2-hydroxy-3-methoxybenzene (**3**) crystallizes in the orthorhombic space group P*bca*. Its molecular structure consists of one molecule of 1,5-dicarboxy-2-hydroxy-3-methoxybenzene with one H atom of the carboxylic group in the fifth position of the aromatic ring positionally disordered between the two O atoms of the same carboxy group (Fig. 5.2.2a). The delocalization can be clearly seen in the difference map in Fig. 5.2.3. The real position of the H34 atom indicated by the diagram is located between O3 and O4 of the neighbouring molecule. It should be noted that this compound in the form of the dihydrate was already reported in the literature [Vladimirova *et al.*, 2016].

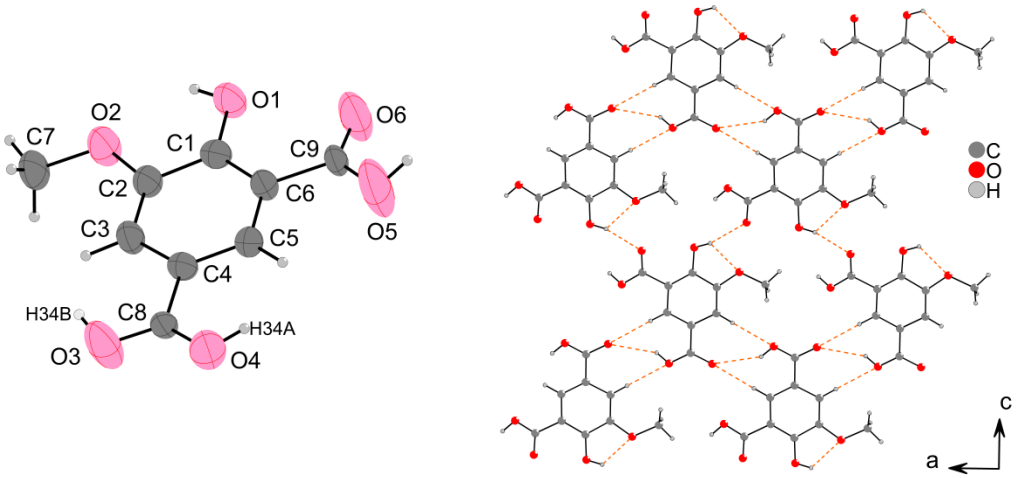


a) b)

Figure 5.2.2

a) The molecular structure of **3**. Both H-atoms, H34A and H34B are present (with occupancy factor being 0.5). The thermal ellipsoids are drawn at the 50 % probability level.

b) The crystal structure of **3** held by hydrogen bonding system (orange dashed lines); the *ac* plane is depicted.

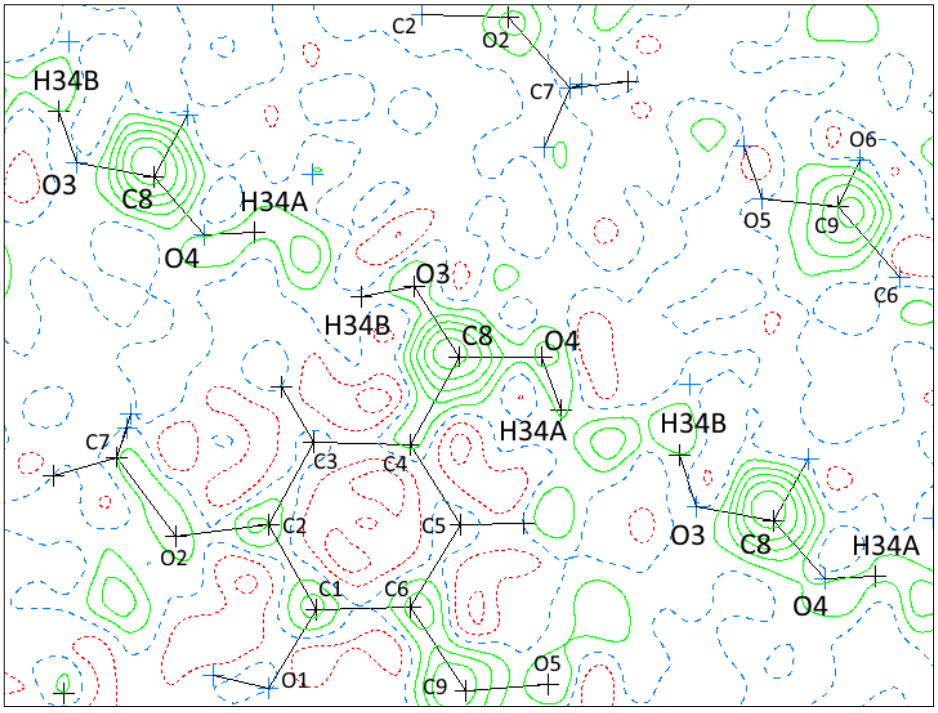


Figure 5.2.3 The difference map diagram showing the electron density around the atoms H34B-O3-C8-O4-H34A of the disordered carboxylic group.

Table 5.2.2 Potential hydrogen bonds in **3**.

| **D-H···A** | **D-H [Å]** | **H···A [Å]** | **D···A [Å]** | **D-H···A [°]** |
|---|---|---|---|---|
| O1-H1···O2 | 0.82 | 2.09 | 2.571 (3) | 117 |
| O1-H1···O6i | 0.82 | 2.19 | 2.973 (4) | 160 |
| O3-H34B···O4ii | 0.82 | 2.46 | 3.150 (4) | 143 |
| O4-H34A···O3iii | 0.82 | 2.44 | 3.150 (4) | 145 |
| C3-H3···O4ii | 0.93 | 2.49 | 3.409 (4) | 170 |
| C5-H5···O3iii | 0.93 | 2.53 | 3.453 (4) | 170 |

Symmetry codes: i: – 1/2 + *x*, 1/2 – *y*, 1 – *z*; ii: – 1/2 + *x*, *y*, 3/2 – *z*; 1/2 + *x*, *y*, 3/2 – *z*.

In conclusion, one cannot say that this type of reaction was not productive but besides our desired product we isolated also several side products resulting from the decomposition of the ligand. The presence of the side product contaminates the final product and lowers its yield. After this initial investigation, the syntheses of heterodinuclear {Tr-Ln} complexes were conducted using the stepwise approach schematically depicted in the Scheme 5.2.1. The self-assembly preparation method was designed considering general reaction pathways summarized in [Costes *et al.*, 1997]; Schiff reaction conditions described in [Ghose, 1984] were taken in account and

modified, too. Firstly, the synthesis and isolation of the Schiff base ligand was described in Chapter 4.2. The second step is the preparation of the intermediate {Tr-*L*} complex as precursor. The isolation of this precursor may prevent the formation of undesired side products arising from the decomposition of the ligand in acidic medium.

1. Step: Synthesis of the Schiff base ligand $H_2$(*o-van-en*)

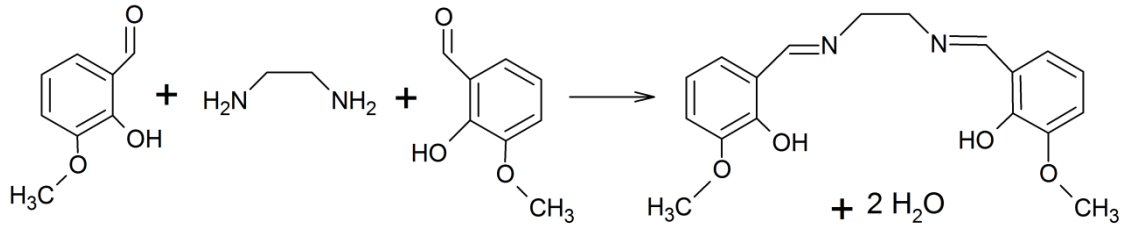


2. Step: Isolation of the intermediate – [Tr(*o-van-en*)] complex

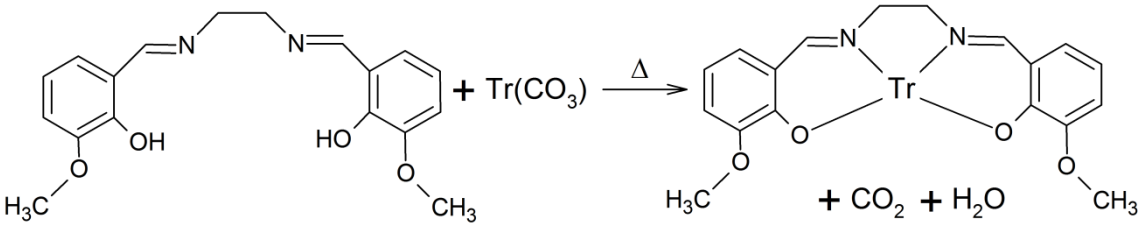


3. Step: Synthesis of the dinuclear [Tr(*o-van-en*)$LnX_3$] complex

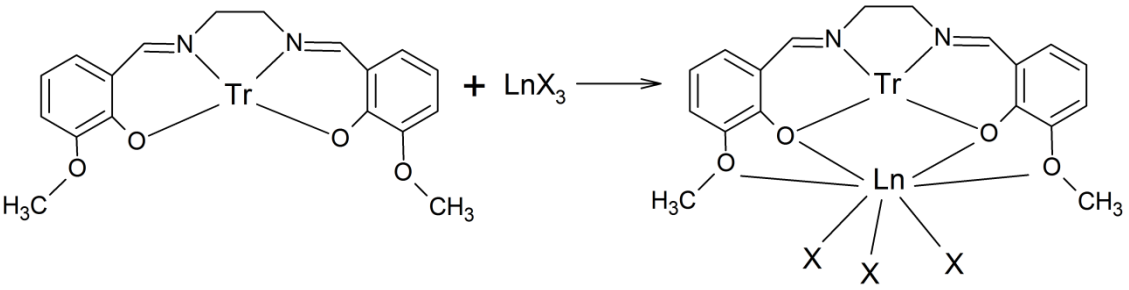


Scheme 5.2.1 Synthetic route of the general stepwise preparation of dinuclear [Tr(*o-van-en*)$LnX_3$] complexes.

### 5.2.1 {Ni – (*o-van-en*)} complexes

In order to prepare a [Ni(*o-van-en*)] precursor, we tried to use nickel(II) carbonate as the source of Ni(II). The nickel(II) salt was added to a boiling water suspension of $H_2$(*o-van-en*). The aim was to decompose the carbonate anion to carbon dioxide and water, remove it from the reaction system as a gas and so avoid the acidic environment which may decompose the Schiff base ligand $H_2$(*o-van-en*). The resulting microcrystalline product was filtered off when no more green nickel(II) carbonate was present in the reaction mixture. Before we used the prepared sample as a precursor for the next reactions with lanthanides, we recrystallized the powder sample from different solvents to assure ourselves about the crystal structure of our intermediate product. Three different crystalline samples, namely [Ni(*o-van-en*)]·*n*$H_2O$ (**4**), [Ni(*o-van-en*)]·$H_2O$·EtOH (**5**) and [Ni(*o-van-en*)]·$H_2O$·iPrOH (**6**) suitable for single-crystal X-ray analysis were isolated from acetone, ethanol and isopropanol, respectively.

[Ni(*o-van-en*)]·*n*$H_2O$ (**4**)

X-ray diffraction data sets of single crystals isolated from acetone were collected at two different temperatures (two different single crystals). Firstly, the single crystal was measured at room temperature. We note that the RT crystal structure of **4** was already reported [Cunningham *et al.*, 1993; Liu *et al.*, 1993]. The compound **4** crystallizes in orthorhombic space group *Pbcn*. Its molecular structure consists of the [Ni(*o-van-en*)] complex molecule with the Ni(II) central atom square-coordinated by the (*o-van-en*)$^{2-}$ Schiff base ligand with the donor set of {$N_2O_2$} (Fig. 5.2.1.1a). Ni–O and Ni–N bond distances are in line with the corresponding values found in the subsequently characterized [Ni(*o-van-en*)]·$H_2O$·EtOH (**5**), [Ni(*o-van-en*)]·$H_2O$·iPrOH (**6**) and previously reported complex [Ni(*o-van-en*)]·$H_2O$ [Cunningham *et al.*, 1993] and [Ni(*o-van-en*)]·$CHCl_3$ [Yu, 2006] (Tab. 5.2.1.1). In addition, the asymmetric unit of **4** contains one solvate molecule of water located in the outer coordination site of the Schiff base ligand held by a quadruple O–H···O type hydrogen bonding system (Tab. 5.2.1.2). The crystal structure is additionally stabilized by weaker C–H···O type hydrogen bonds of the C11–H11 imine group of the Schiff base ligand and O1 of the neighbouring complex molecule forming supramolecular chains along the *b* axis (Fig.

5.2.1.1b); Tab. 5.2.1.2). The rest of the packing forces in **4** are only weaker intermolecular contacts.

Table 5.2.1.1 Selected bond lengths [Å] for **4** (room temperature (RT) and low temperature data set (LT)), **5** and **6**, compared with [Ni(*o-van-en*)]·$H_2O$ (***a***) [Cunningham *et al.*, 1993] and [Ni(*o-van-en*)]·$CHCl_3$ (***b***) [Yu, 2006].

| | **4 (RT / LT)** | **5** | **6** | ***a*** | ***b*** |
|---|---|---|---|---|---|
| Ni1-O2 | 1.856 (2) / 1.8604 (14) | 1.8597 (10) | 1.865 (2) | 1.854 (10) | 1.8392 (17) |
| Ni1-O3 | 1.844 (2) / 1.8469 (13) | 1.8577 (10) | 1.865 (2) | 1.847 (10) | 1.8458 (17) |
| Ni1-N1 | 1.834 (3) / 1.8510 (16) | 1.8547 (13) | 1.854 (3) | 1.837 (14) | 1.846 (2) |
| Ni1-N2 | 1.855 (3) / 1.8549 (18) | 1.8457 (13) | 1.850 (3) | 1.869 (12) | 1.843 (2) |

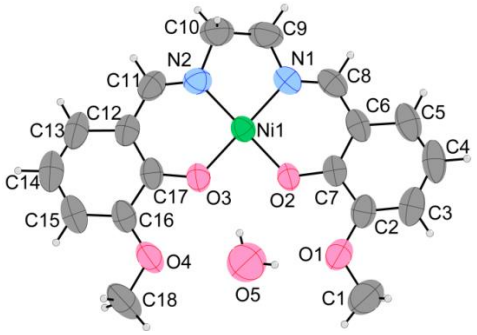


a)

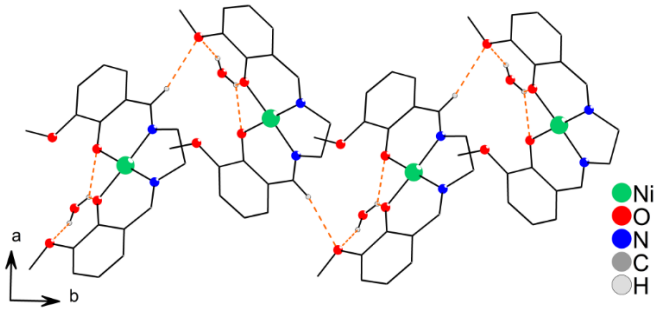


b)

Figure 5.2.1.1 a) The asymmetric unit of **4** along with the atom numbering scheme. The thermal ellipsoids are drawn at the 50 % probability level.

b) The supramolecular chains made by hydrogen bonds in **4**. Hydrogen bonds are denoted as orange dashed lines. For clarity, hydrogen atoms not involved in hydrogen bonds are omitted and carbon atoms are drawn in „sticks“ model.

Table 5.2.1.2 Potential hydrogen bonds in **4** (room temperature data set).

| **D–H···A** | **D–H [Å]** | **H···A [Å]** | **D···A [Å]** | **D–H···A [°]** |
|---|---|---|---|---|
| O5–H5A···O1 | 0.838 (10) | 2.52 (4) | 3.291 (6) | 153 (6) |
| O5–H5B···O2 | 0.839 (11) | 2.55 (5) | 3.041 (5) | 119 (5) |
| O5–H5B···O3 | 0.839 (11) | 2.34 (4) | 3.026 (5) | 139 (6) |
| C11–H11···O1$^{i}$ | 0.93 | 2.61 | 3.511 (5) | 162.6 |

Symmetry code: i: 3/2 – *x*, 1/2 + *y*, *z*.

The low temperature data set shows minor differences in the molecular structure of **4**. The noteworthy feature was a suspiciously high residual electron density, located in vacancies of the crystal packing, sitting on the special position – on the twofold rotation axis parallel to *b*. This electron density was refined as a water molecule with partial occupancy of 1/6. The crystal structure thus contains three hydrogen bonded water molecules located in the vacancies of the crystal packing, related through the twofold rotation axis (Fig. 5.2.1.3a). The newly found evidence changes the molecular formula of **4** to [Ni(*o*-*van*-*en*)]·*n*$H_2O$, n = 1.17. The crystal structure is now extended by additional O6-H6···O5 hydrogen bonds between solvate water molecules. In addition, the intermolecular contact C8–H8···O5$^{i}$ (i = *x*, 1 – *y*, 1/2 + *z*) now appears within the limits for hydrogen bonding which strengthens the packing forces in comparison with the crystal structure at room temperature (Fig. 5.2.1.3b) The whole hydrogen bonding network thus forms a 3D packing pattern in the extended structure.

New evidence from the crystal structure of **4** measured at low temperature make us look back to the structure of **4** measured at room temperature. The detailed study of the vacancies around the water solvate molecules shows the electron density left at the same place as in the low-temperature data set. However, the electron density is too low for further analysis. The water molecule located at this site would have only ca. 5 % of occupancy.

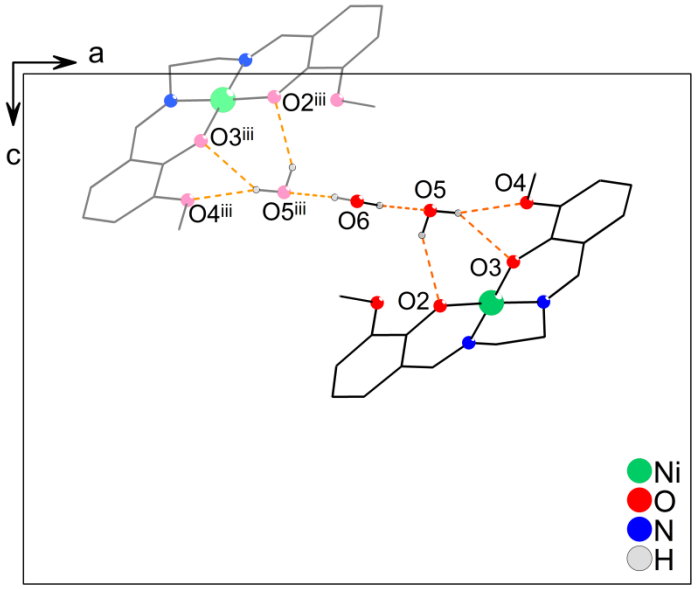


a)

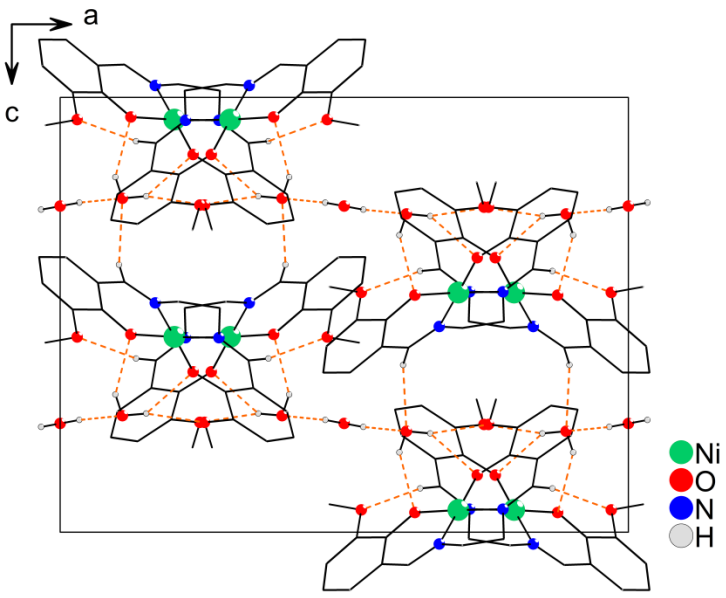


b)

Figure 5.2.1.3 a) The molecular structure of **4** (low temperature data set) along with the hydrogen bonded water solvate molecules shown. The [1 – *x*, *y*, 1/2 - *z*] congener is depicted in bright colours for clarity. Symmetry code: i: 1 – *x*, *y*, 1/2 – *z*.

b) The packing diagram of **4** (low temperature data set); the *ac* plane view direction depicted. Hydrogen bonds are denoted as orange dashed lines. For clarity, hydrogen atoms not involved in hydrogen bonds are omitted and carbon atoms are drawn in „sticks“ model.

Table 5.2.1.3 Potential hydrogen bonds in **4** (low temperature data set).

| **D–H···A** | **D–H [Å]** | **H···A [Å]** | **D···A [Å]** | **D–H···A [°]** |
|---|---|---|---|---|
| O5–H5A···O3 | 0.835 (10) | 2.40 (3) | 3.018 (2) | 131 (2) |
| O5–H5A···O4 | 0.835 (10) | 2.223 (13) | 3.021 (2) | 160 (3) |
| O5–H5B···O2 | 0.831 (10) | 2.271 (18) | 3.014 (2) | 149 (3) |
| O6–H6···O5 | 0.841 (10) | 1.746 (11) | 2.583 (4) | 173 (5) |
| C8–H8···O5$^{i}$ | 0.95 | 2.60 | 3.476 (3) | 154.0 |
| C11–H11···O1$^{ii}$ | 0.95 | 2.57 | 3.492 (3) | 164.2 |

Symmetry codes: i: *x*, 1 – *y*, 1/2 + *z*; ii: 3/2 – *x*, –1/2 + *y*, *z*.

In general, the crystal structure of **4** possesses a vacancy big enough for one extra water molecule, with ideal possibilities for hydrogen bonding. However, its intermolecular contacts are not strong enough to keep the molecule in the crystal packing at higher temperatures. The loss of the crystal water was observed also using IR spectroscopy. The freshly prepared sample of **4** was mixed with potassium(I) bromide forming the KBr pellet. The resulting pellet was placed in the cell with controlled temperature and the IR spectrum was collected at 14 different temperatures rising from 30 to 145°C. The spectra are depicted in Fig. 5.2.1.4. The loss of the intensity of ν(OH) is continual up to 145°C which was the upper instrumental limit.

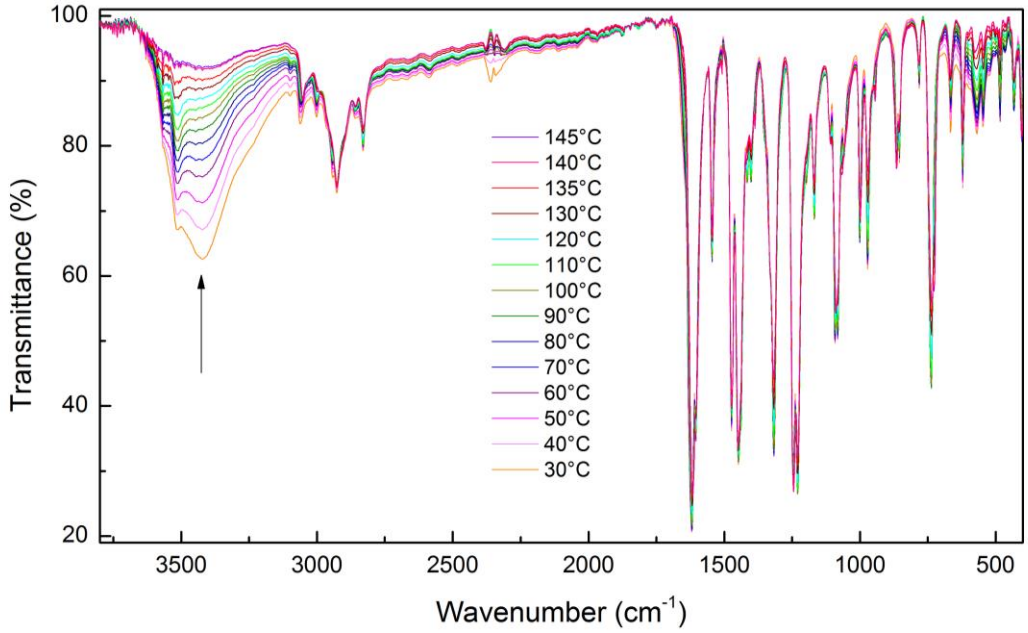


Figure 5.2.1.4 Temperature dependence of the IR spectrum of **4**. The loss of intensity of the ν(OH) signal is assigned with the arrow.

The identity of the prepared microcrystalline product was determined by the Le Bail refinement of the pattern calculated using both sets of structural data of **4** compared with its measured powder diffraction pattern using the program Jana2006 [Le Bail *et al.*, 1988; Le Bail, 2005; Petříček *et al.*, 2014]. We note that the experimental powder diffraction data was collected at room temperature.

Using the room-temperature CIF file, the following results were obtained (Fig. 5.2.1.5). In the Pseudo-Voigt function, Gaussian parameters *U* (basic broadening by slits), *V* (wave length dispersion) and *W* (influence of monochromator) and Lorentzian parameter *X* (particle broadening) were refined. Peak asymmetry was corrected using the Bérar-Baldinozzi model with 4 parameters; the first three were refined and the fourth was fixed. Background was corrected using Legendre polynomials (10 terms) and by refining the shift parameter. The refined cell parameters for orthorhombic space group *Pbcn* are (the values from the CIF are given in brackets) *a* = 19.624 (3) [19.6427 (8)] Å, *b* = 11.873 (2) [11.8972 (5)] Å, *c* = 15.224 (3) [15.2443 (8)] Å. The resulting *R*-values are *R*(*p*) = 0.0172, *R*(*wp*) = 0.0258 and goodness of fit = 8.34.

Using the low-temperature CIF file, the refined cell parameters for orthorhombic space group *Pbcn* are (the values from the CIF are given in brackets) *a* = 19.6059 (15) [19.6607 (6)] Å, *b* = 11.8568 (9) [11.8032 (4)] Å, *c* = 15.2096 (12) [15.0266 (4)] Å. The resulting *R*-values are *R*(*p*) = 0.0230, *R*(*wp*) = 0.0359 and goodness of fit = 11.58. The refinement was done using the Pseudo-Voigt function, Gaussian parameters *V*, *W* and *P* (Scherrer coefficient) and Lorentzian parameters *X* and *Y* (strain broadening) were refined. The peak asymmetry due to axial divergence was corrected by Jana2006, too. As in the previous refinement, background was corrected using Legendre polynomials (10 terms) and by refining the shift parameter.

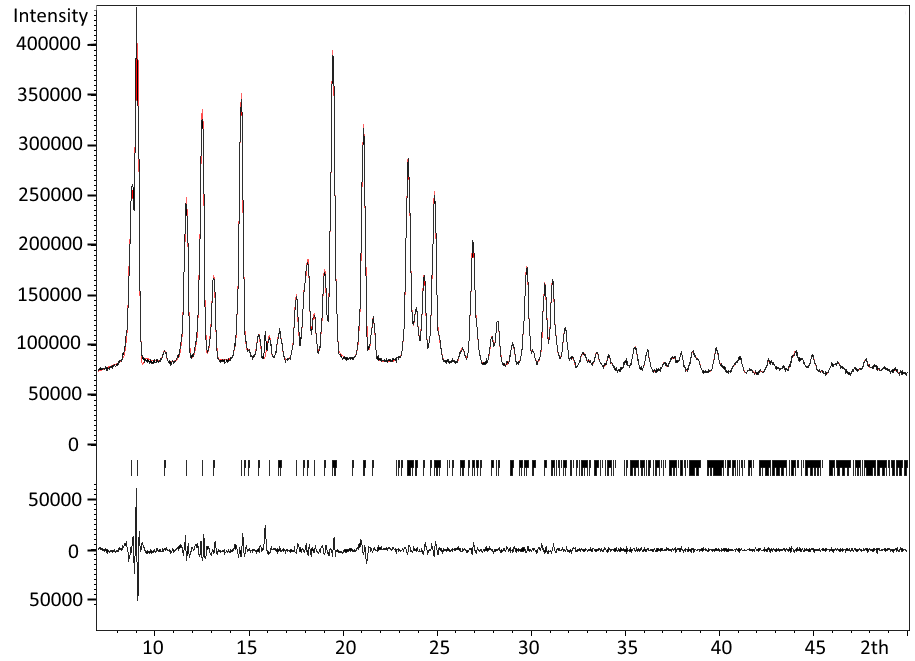


a)

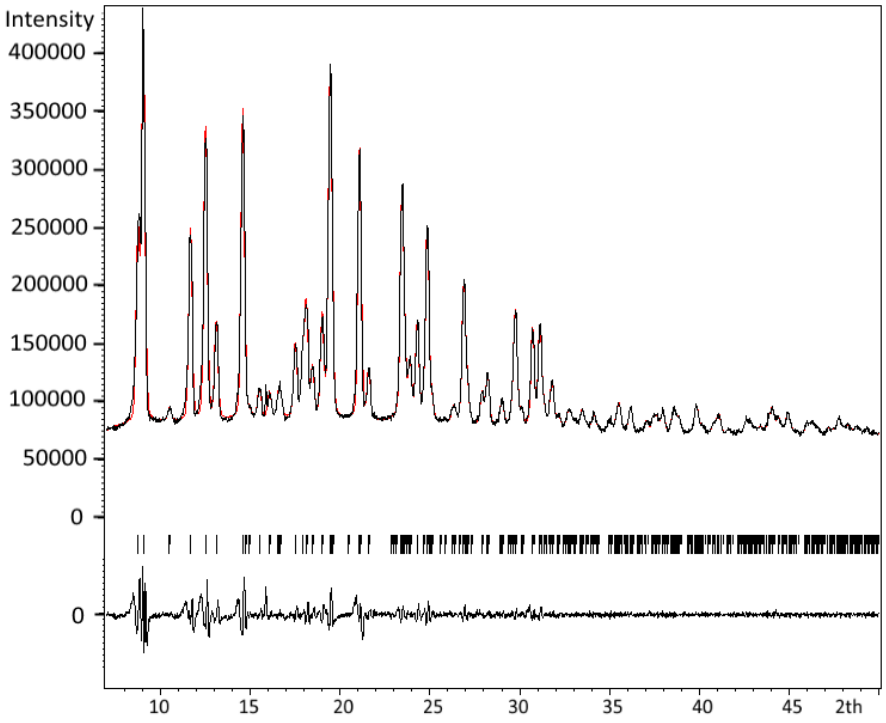


b)

Figure 5.2.1.5 Results of Le Bail refinement of the powder diffraction pattern of **4**, with the starting unit-cell parameters taken from the a) room-temperature, b) low-temperature data set. Observed data are black, calculated data are drawn as red.

[Ni(*o-van-en*)]·$H_2O$·EtOH (**5**)

The molecular structure of **5** contains the same complex molecule [Ni(*o-van-en*)] like the previous compound. The nickel(II) central atom lies in the square planar inner coordination site of the Schiff base ligand $(o\text{-}van\text{-}en)^{2-}$ with the $\{O_2N_2\}$ donor set. The Ni–O and Ni–N bond distances are in line with those of the previously commented crystal structures (Tab. 5.2.1.1). The outer cavity of the ligand is occupied by a relatively strongly anchored water solvate molecule. The water molecule is bonded by two bifurcated-donor hydrogen bonds of the O–H···O type to all four oxygen atoms of the Schiff base ligand. In addition, the asymmetric unit of **5** contains an ethanol solvate molecule, hydrogen bonded to the water solvate mentioned above (Fig. 5.2.1.6a). The O6 oxygen atom of the ethanol solvate forms two hydrogen bonds in two different directions, which is probably the cause of its positional disorder represented by O6A and O6B atomic sites.

Additionally to the above mentioned hydrogen bonds, the crystal structure of **5** consists of rich system of weaker intermolecular forces. However, ethanol solvate molecules are located in certain channels along the *a* axis and bonded weakly enough to move across the crystal structure. This is the probable cause of the low stability of crystals of **5** at room temperature out of its mother liquor. Hydrogen bonds of the water solvate molecule mentioned above together with the weaker C8–H8···O5$^{i}$ (i = – *x*, 1 – *y*, 1 – *z*) hydrogen bond and potential Cg1···Ni1$^{iii}$ (iii = 1 – *x*, 1 – *y*, 1 – *z*) ring-metal interaction form supramolecular dimeric units of $\{[Ni(o\text{-}van\text{-}en)]\cdot H_2O\}_2$. Ring···metal distance in the ring-metal interaction mentioned above is 3.545 Å, the perpendicular distance is 3.333 Å and the β angle equals 19.92°. Dimeric units are then connected by hydrogen bonding system with ethanol solvate molecules in the *b* direction and Ni1···Ni1$^{iii}$ interactions (metal-metal distance is 3.3379 (3) Å) in the *a* direction forming supramolecular layers parallel to the *ab* plane (Fig. 5.2.1.6b); Tab. 5.2.1.4). The observed short Ni···Ni distances may correspond to metal-metal interactions [Thomas & Underhill, 1972; Siegler & Lutz, 2009].

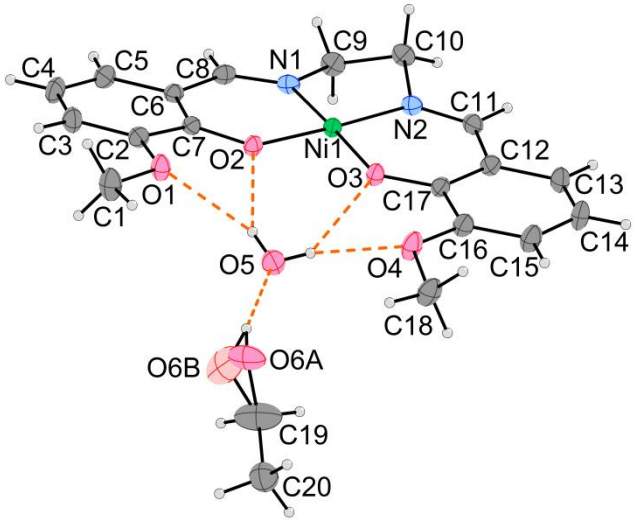


a)

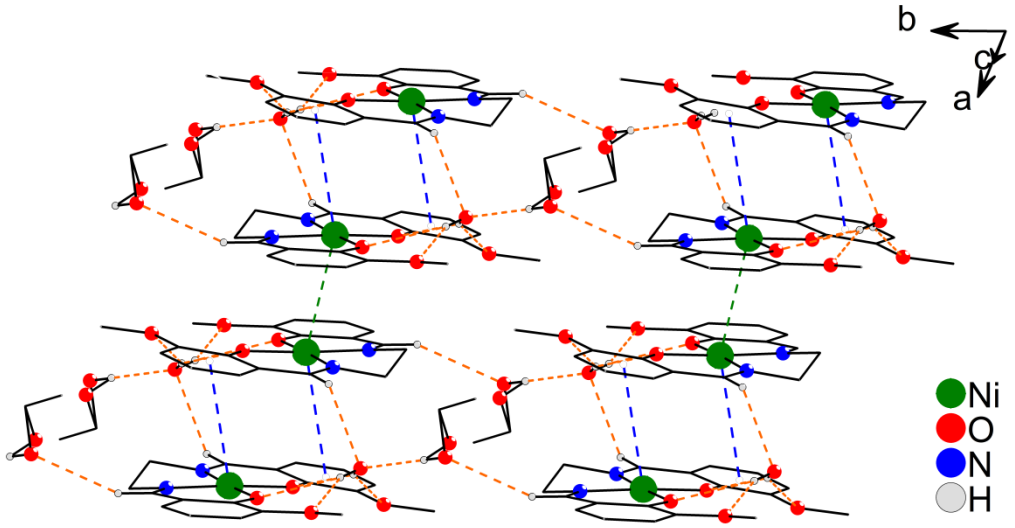


b)

Figure 5.2.1.6 a) The asymmetric unit of **5** along with the atom numbering scheme. The thermal ellipsoids are drawn at the 50 % probability level. The second disordered position of O6 (O6B) is depicted in a light colour for clarity.

b) The packing diagram of **5**. Potential hydrogen bonds, ring-metal and metal-metal interactions are denoted as orange, blue and green dashed lines, respectively. For clarity, hydrogen atoms not involved in hydrogen bonds are omitted and carbon atoms are drawn in „sticks“ model.

Table 5.2.1.4 Potential hydrogen bonds in **5**.

| **D–H···A** | **D–H [Å]** | **H···A [Å]** | **D···A [Å]** | **D–H···A [°]** |
|---|---|---|---|---|
| O5–H5A···O1 | 0.79 (3) | 2.23 (3) | 2.9021 (18) | 143 (2) |
| O5–H5A···O2 | 0.79 (3) | 2.23 (3) | 2.9247 (16) | 146 (2) |
| O5–H5B···O3 | 0.76 (3) | 2.40 (2) | 2.9726 (16) | 134 (2) |
| O5–H5B···O4 | 0.76 (3) | 2.14 (3) | 2.8483 (18) | 155 (2) |
| O6A–H6···O5 | 0.79 (3) | 1.94 (3) | 2.699 (6) | 163 (3) |
| O6B–H6···O5 | 0.87 (4) | 1.94 (3) | 2.724 (13) | 151 (4) |
| C8–H8···O5$^{i}$ | 0.952 (19) | 2.549 (18) | 3.226 (2) | 128.2 (14) |
| C11–H11···O6A$^{ii}$ | 0.938 (18) | 2.63 (2) | 3.496 (8) | 153.8 (14) |

Symmetry codes: i: $-x$, $1-y$, $1-z$; ii: $x$, $1+y$, $z$.

[Ni(*o-van-en*)]·$H_2O$·iPrOH (**6**)

The third compound of the Ni-(*o-van-en*) series, compound **6** has a similar molecular structure to the two previous compounds **4** and **5**. Its asymmetric unit consists of the same [Ni(*o-van-en*)] complex molecule and water solvate molecule located in the outer coordination site of the Schiff base ligand $(o\text{-}van\text{-}en)^{2-}$ as donor in two bifurcated hydrogen bonds. Additionally, it possesses one isopropanol solvate molecule which is hydrogen-bonded to the above mentioned water solvate (Fig. 5.2.1.7a).

Similarly to **5**, the crystal structure of **6** contains dimeric units of complex molecules $[Ni(o\text{-}van\text{-}en)]_2$ which are held by metal-metal interaction between Ni(II) central atoms. The metal-metal distance within the supramolecular dimer is 3.3714 (6) Å. A view of the dimer from above shows that the $\pi$ systems of the aromatic rings do not overlap (Fig. 5.2.1.7b). Additionally, the supramolecular dimers are connected by weak intermolecular forces between aromatic rings formed by C2 – C7 atoms and Ni(II) central atoms of the neighbouring complex molecules, forming supramolecular chains along the *b* axis (Fig. 5.2.1.7c), d). The 3D crystal packing is supported only by weak intermolecular forces.

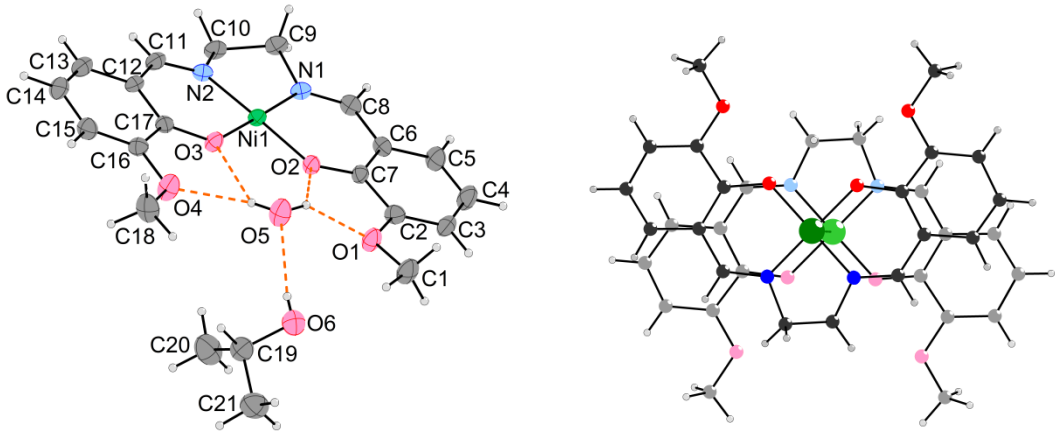


a) b)

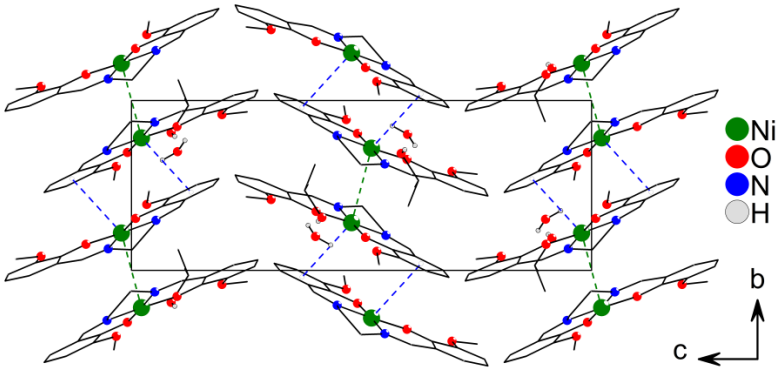


c)

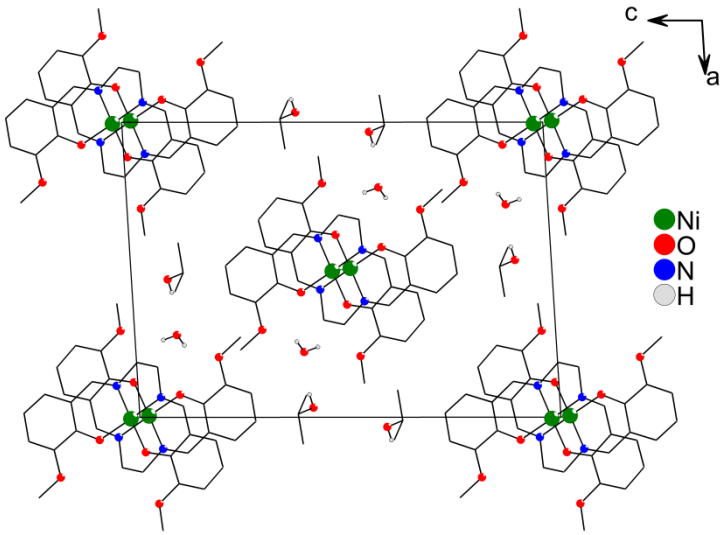


d)

Figure 5.2.1.7 a) Molecular structure of **6** along with the atom numbering scheme. Hydrogen bonds are depicted as orange dashed lines.

b) View from above a supramolecular dimer formed by metal-metal interaction. The lower molecule is depicted in light colours for clarity.

c), d) The packing diagrams of **6** – the *bc* and *ac* plane view, respectively.

Table 5.2.1.5 Potential hydrogen bonds in **6**.

| **D–H···A** | **D–H [Å]** | **H···A [Å]** | **D···A [Å]** | **D–H···A [°]** |
|---|---|---|---|---|
| O5–H5A···O1 | 0.78 (6) | 2.11 (6) | 2.778 (4) | 144 (6) |
| O5–H5A···O2 | 0.78 (6) | 2.49 (6) | 3.057 (3) | 131 (5) |
| O5–H5B···O3 | 0.77 (4) | 2.45 (4) | 3.060 (4) | 138 (4) |
| O5–H5B···O4 | 0.77 (4) | 2.09 (5) | 2.784 (4) | 150 (4) |
| O6–H6···O5 | 0.67 (4) | 2.16 (4) | 2.819 (4) | 169 (5) |

### 5.2.2 {Co(II)/Co(III) – (*o-van-en*)} complexes

In an attempt to prepare the Co(II)-Ln dinuclear complexes, we tried several synthetic routes leading to isolation of precursors containing the [$Co^{II}$(*o-van-en*)] unit. We note that the literature reports the [$Co^{II}$(*o-van-en*)($H_2O$)] complex which was prepared by *in situ* solvothermal synthesis starting from 2-hydroxy-3-methoxy-benzaldehyde, ethane-1,2-diamine and cobalt(II) nitrate [Jiang *et al*., 2007]. Varying the synthetic conditions we have isolated 3 different products, including the above mentioned one.

The previously reported complex [$Co^{II}$(*o-van-en*)($H_2O$)] (**7**) was isolated in microcrystalline form by the direct reaction of cobalt(II) hydroxide with the Schiff base $H_2$(*o-van-en*) using mild conditions under an inert argon atmosphere. The orange microcrystalline sample, isolated from the mother liquor is stable in air, resistant to a contingent oxidation. An attempt to recrystallize the microcrystalline product **7** from acetonitrile at room temperature in the presence of air led to oxidation of Co(II) to Co(III) and formation of the monoclinic form of [$Co^{III}_2$(*o-van-en*)$_3$]·4$CH_3CN$ (**8**). Direct reaction of the Schiff base with $Co(OH)_2$ in the presence of air led to a black microcrystalline crude product; the colour change clearly indicated oxidation of Co(II) to Co(III). When the resulting crude product was recrystallized from hot acetonitrile, crystals of the triclinic form of [$Co^{III}_2$(*o-van-en*)$_3$]·4$CH_3CN$ (**9**) were separated. We note that both forms of the newly prepared complex [$Co^{III}_2$(*o-van-en*)$_3$]·4$CH_3CN$ (**8**, **9**) are unstable outside of the mother liquor.

Following our strategy of the stepwise reaction, the complex [$Co^{II}$(*o-van-en*)($H_2O$)] (**7**) proved to be the best candidate for a [Tr(*o-van-en*)] precursor for the last step. Using the gadolinium chloride as an initial source of the lanthanide, we carried out the syntheses under mild conditions in ethanol and acetonitrile, respectively. In both cases, the lanthanide atom did not enter the coordination site of the Schiff base ligand. In addition, we isolated and identified the oxidised products of the reactions. Complexes [$Co^{III}$(*o-van-en*)($H_2O$)Cl] (**10**) and [$Co^{III}$(*o-van-en*)($H_2O$)Cl]·2$CH_3CN$ (**11**) were isolated in crystalline form, available for X-ray diffraction analysis.

[$Co^{II}$(*o-van-en*)($H_2O$)] (**7**)

The identity of the product **7** prepared by us and that reported by Jiang *et al*. was corroborated by comparison of the measured powder diffraction pattern with the pattern

calculated using the structural data reported by Jiang *et al*. [2007]. For a detailed comparison, the Le Bail refinement was applied using the program Jana2006 (Fig. 5.2.2.1) [Le Bail *et al.*, 1988; Le Bail, 2005; Petříček *et al.*, 2014]. In this case, the best appropriate least-squares-fitted peak profile option was the Pseudo-Voigt function, convoluting the Gaussian and Lorentzian functions. Gaussian parameters were not used except the *W* parameter (influence of monochromator). Particle and strain broadening was fitted by using both, *X* and *Y* parameters of the Lorentzian part of the fitting peak-shape function. The peak asymmetry due to axial divergence was corrected by Jana2006, too. The refined cell parameters for orthorhombic space group *Pnma* are (the values reported by Jiang *et al.*, 2007 are given in brackets) $a$ = 8.9941(18) [8.9827 (6)] Å, $b$ = 24.970(4) [24.8632 (16)] Å, $c$ = 7.7011(9) [7.5784 (5)] Å. The obtained R-values are $R(p)$ = 0.0541, $R(wp)$ = 0.0754 and goodness of fit = 1.91.

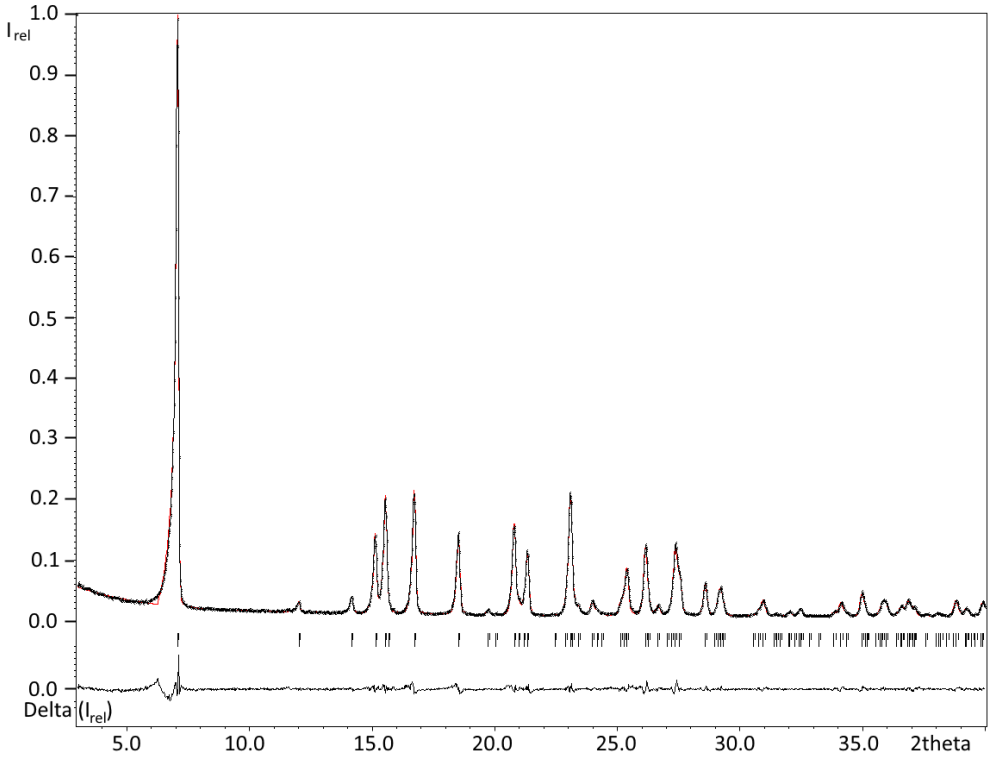


Figure 5.2.2.1 Results of Le Bail refinement of the powder diffraction pattern of **7**, with the starting unit-cell parameters taken from the known crystal structure of [Co(*o-van-en*)($H_2O$)] [Jiang *et al.*, 2007]. Observed data are black, calculated data are drawn as red.

The molecular structure of **7** is built up of complex [$Co^{II}$(*o-van-en*)($H_2O$)] molecules. The central Co(II) atom is pentacoordinated, with the $N_2O_2$ donor atoms from the Schiff base ligand occupying the basal plane of the square pyramid while the apical position is occupied by the aqua ligand (Fig. 5.2.2.2a). We note that the observed

positional disorder of the carbon atoms from the ethylenediamine part of the Schiff base ligand is imposed by the presence of a mirror plane (space group is P*nma*) cutting the complex in two symmetric halves. The supramolecular structure is formed by zig-zag hydrogen bonded (O–H···O type) chains (Fig. 5.2.2.2b). Propagation of the crystal structure in all three dimensions is realized by weak C–H···C close contacts and π-π stacking interactions.

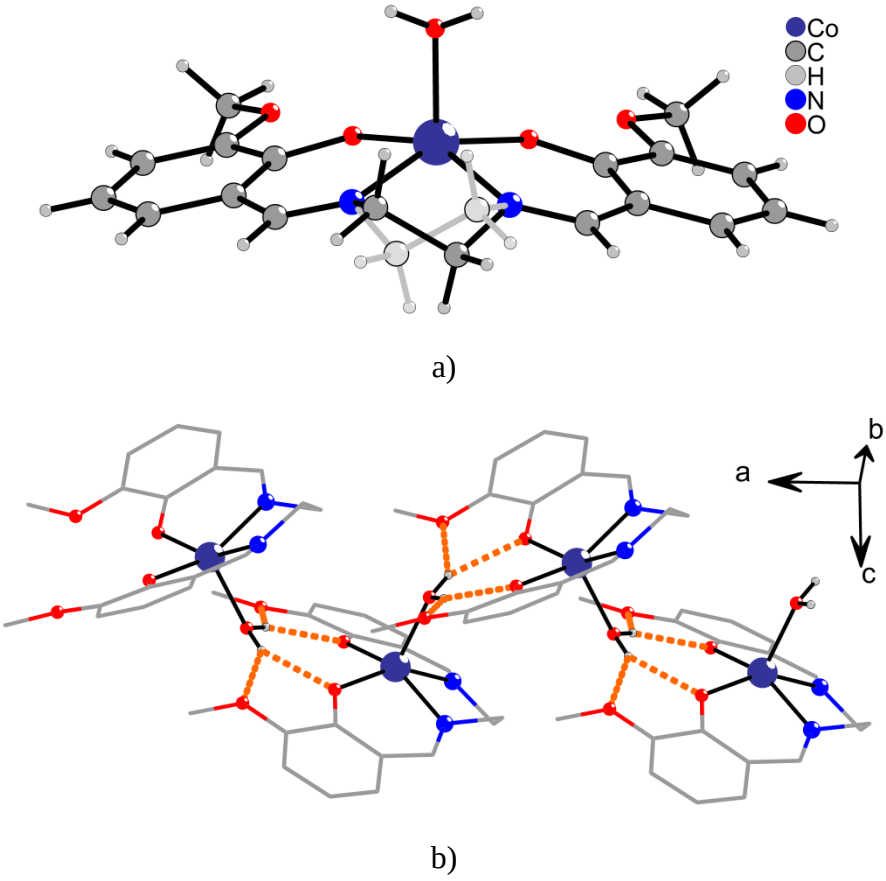


Figure 5.2.2.2 a) The molecular stucture of the complex [$Co^{II}$ (*o-van-en*)($H_2O$)] (**7**) published by Jiang *et al*. The second position of the positional disorder is drawn in light colour; b) the zig-zag supramolecular chains in the crystal structure of **7**. Hydrogen bonds are denoted as orange dashed lines. For clarity, hydrogen atoms not involved in hydrogen bonds are omitted and carbon atoms are drawn in „sticks“ model [Jiang *et al.*, 2007].

$[Co^{III}_2(o\text{-}van\text{-}en)_3]\cdot 4CH_3CN$ (form I = **8**, form II = **9**)

Both forms of $[Co^{III}_2(o\text{-}van\text{-}en)_3]\cdot 4CH_3CN$ (form I = **8**, form II = **9**), isolated under aerobic conditions were crystallographically studied as polymorphs. Along with the detailed characterization of their crystal and molecular structures, the two

polymorphic forms were also compared and analiezed by Hirshfeld surface analysis and FIM method with the aim of elucidating the factors responsible for the polymorphism of this system [Spackman & Jayatilaka, 2009; Wood *et al.*, 2013]. The results of our comprehensive study are discussed below.

Form I of $[Co^{III}_2(o\text{-}van\text{-}en)_3]\cdot 4CH_3CN$ (compound **8**) crystallizes in the monoclinic space group $P2_1/c$ while Form II of the polymorph (compound **9**) crystallizes in triclinic space group P-1. The crystal structures of both **8** and **9** are built up of centrosymmetric dinuclear complex molecules $[Co^{III}_2(o\text{-}van\text{-}en)_3]$ and, in addition, the asymmetric units of both polymorphs contain two $CH_3CN$ solvate molecules (Fig. 5.2.2.3). In both forms, Co(III) atoms are coordinated by one chelate bonded tetradentate $(o\text{-}van\text{-}en)^{2-}$ ligand in an uncommon bent fashion and the pseudooctahedral coordination of the Co(III) atoms is completed by one {ON} donor set originating from the same arm of the bridging $(o\text{-}van\text{-}en)^{2-}$ ligand. Similar coordination modes were reported for $[Fe_2(o\text{-}van\text{-}en)_3]\cdot CH_2Cl_2\cdot 0.5H_2O$ [Costes *et al.*, 2010]. We note that there is already reported $[Co^{III}_2(o\text{-}van\text{-}en)_3]\cdot 2Me_2SO\cdot 2H_2O$ complex (REF Code: COMSAL) which contains the same complex molecule. However, the absence of the atomic coordinates for COMSAL obviates its closer comparison with our two polymorphs [Calligaris *et al*., 1970]. In form I, the methyl group at C1 is disordered and split into two parts, C1A and C1B, both with half occupancies. Disorder is present also in form II; the solvate MeCN molecule is split into two parts with occupancies constrained to sum to unity and with C–C and C–N bonds restrained to be the same lengths in both congeners (see atoms C30-C31A-N5A and C30-C31B-N5B, resp. in the Fig. 5.2.2.3b). The superposition of the two dinuclear complex molecules depicted in Fig. 5.2.2.3d) clearly shows small but significant differences with respect to their geometrical parameters such as deviations of the aromatic rings and torsion angles involving the methoxy groups on the tail end of the Schiff base ligand.

The observed Co-O and Co-N bond distances in **8** and **9** (see Tab. 5.2.2.1), are in good agreement with the corresponding values found for similar Co(III) complexes, *e.g.* in $[Co^{III}(salen)(acac)]\cdot 1.5H_2O$ [Bailey *et al.*, 1972] and $[Co^{III}(salen)(acac)]\cdot 0.7H_2O$ [Calligaris *et al.*, 1972]. As expected for the smaller ionic radius of the Co(III) atom, these bond distances are shorter than those reported for the Co(II) complex **7** [Shannon, 1976].

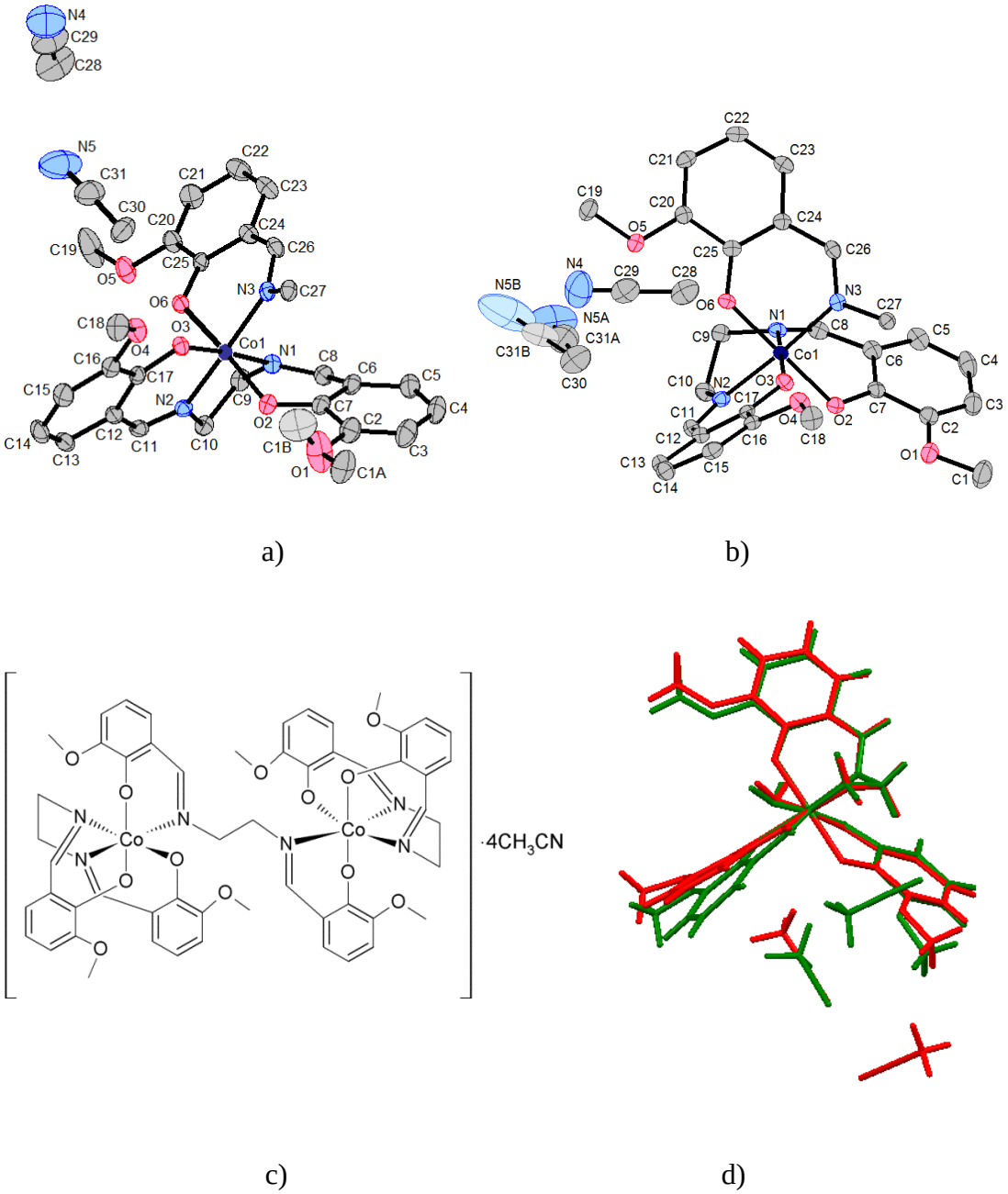


a) b)

c) d)

Figure 5.2.2.3 The asymmetric units of **8** (a) and **9** (b) with the atom numbering scheme. The thermal ellipsoids are drawn at the 50 % probability level. Half of the dinuclear molecule without hydrogen atoms is depicted for the sake of clarity. The second positions of positionally disordered molecules are drawn in light colours. c) Chemical diagram of $[Co_2(o\text{-}van\text{-}en)_3]\cdot 4CH_3CN$. d) "Capped sticks" models of the molecular structures for compounds **8** (red) and **9** (green). The structures are superimposed in such a way that the positions of the Co central atoms as well as the donor atoms are overlapped as nearly as possible. Only the asymmetric part of the dinuclear complex molecule is shown for clarity.

Table 5.2.2.1 Selected bond lengths [Å] for **8** and **9**, compared with [$Co^{III}$(*salen*)(*acac*)]·1.5$H_2O$ (*a*) [Bailey *et al.*, 1972], [$Co^{III}$(*salen*)(*acac*)]·0.7$H_2O$ (*b*) [Calligaris *et al.*, 1972] and [$Co^{II}$(*o-van-en*)($H_2O$)] (*c*) [Jiang *et al.*, 2007].

| | **8** | **9** | ***a*** | ***b*** | ***c*** |
|---|---|---|---|---|---|
| Co1–O3 | 1.8915 (16) | 1.8966 (13) | 1.887 (4) | 1.88 (1) | 1.979 (2) |
| Co1–O2 | 1.9073 (17) | 1.9002 (13) | 1.888 (4) | 1.92 (1) | 1.979 (2) |
| Co1–O6 | 1.9093 (16) | 1.9118 (13) | – | – | – |
| Co1–N1 | 1.8894 (19) | 1.8993 (16) | 1.898 (5) | 1.89 (1) | 2.036 (3) |
| Co1–N2 | 1.9041 (19) | 1.9133 (16) | 1.881 (5) | 1.90 (2) | 2.036 (3) |
| Co1–N3 | 1.9445 (19) | 1.9271 (16) | – | – | – |

The outer shell of the complex molecules of both polymorphs has a deficiency of suitable donors of classical hydrogen bonds and among the weak hydrogen bonding interactions of the =C–H···A or $C_{ar}$–H···A types (A = O or N), there is only one such hydrogen bond in each of the polymorphs, in both cases intermolecular.

In polymorph **8**, there are no classical intramolecular hydrogen bonds, unless one may consider that close contacts of the C–H···O type with hydrogen atoms from a methoxy group (disordered C1 atom in position B) or methylene groups (C9 and C27) may help to stabilize the conformation of the complex molecule (Tab. 5.2.2.2). Among the intermolecular forces, the only weak hydrogen bonding interaction is C8–H8···$O5^{iii}$ with participation of the imine hydrogen atom (Table 5.2.2.2). This interaction links the complex molecules into supramolecular layers in the *bc* plane (Fig. 5.3.2.4a). This supramolecular layer is supported by weak C–H···π interaction of the C11-H11 bond of the other imine group directed toward the π-system of the aromatic ring $C2^{iii}$ – $C7^{iii}$; this interaction has an H···Cg distance of 2.91 (3) Å and a γ angle between the Cg–H vector and ring normal of 12.41°. We note that additional intermolecular contacts of the C–H···X (X = N, O) type with hydrogen atoms from the methyl groups and close contacts of the C–H···π type with participation of methylene and methyl hydrogen atoms can also be considered to contribute to the intermolecular cohesion (see Tab. 5.2.2.2).

Similarly in polymorph **9**, the only intramolecular interaction is contact of the C–H···O type with hydrogen atoms from methylene groups of the ligand (Tab. 5.2.2.3). Among the intermolecular forces, only one non-classical hydrogen bond of the $C_{ar}$–H···N type, namely C5–H5···$N5B^{iv}$ is present (Tab. 5.2.2.3, Fig. 5.2.2.4b) and this

links the complex molecules with the disordered $CH_3CN$ molecule in the more populated position (N5B). The packing of the crystal structure is additionally supported by a weak C–H···π interaction in which H21 from the aromatic ring as donor and the π-system of the aromatic ring C12$^{v}$ – C17$^{v}$ are involved; the H···Cg distance is 2.64 Å and the γ angle between the Cg–H vector and the ring normal is 8.82°. These interactions link the complex molecules into supramolecular chains running along the *a* axis (Fig. 5.2.2.4b). The crystal packing is also stabilized by additional contacts of the C–H···X (X = O, N) and C–H···π types coming from both $CH_3CN$ solvate molecules and the methylene group of the Schiff base ligand (Tab. 5.2.2.3).

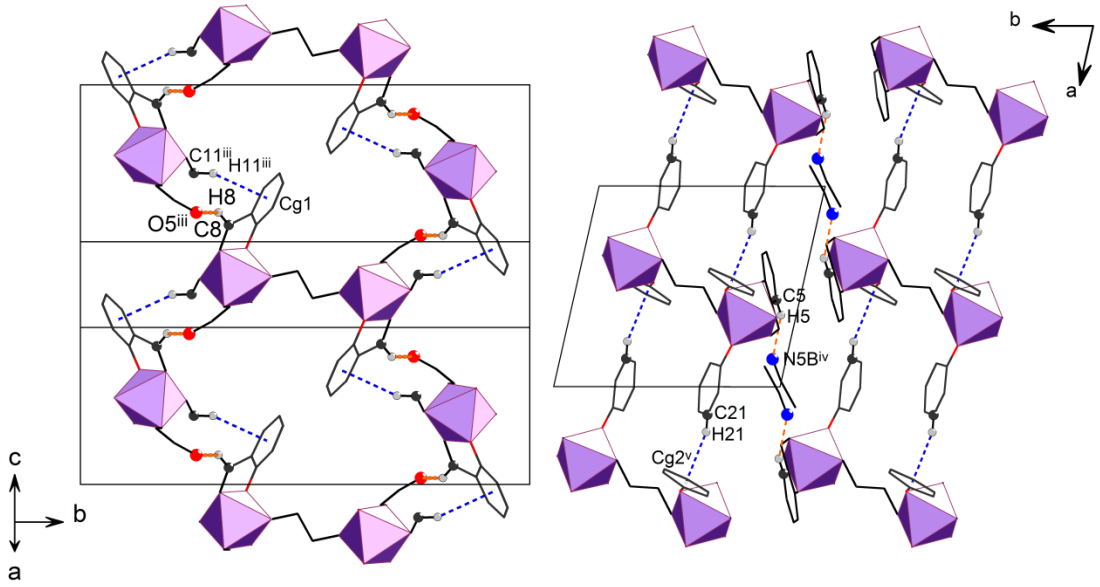


a) b)

Figure 5.2.2.4 a) Supramolecular layer formed by weak intermolecular hydrogen bond C8–H8···O5 (orange dashed line) and C–H···π interaction C11–H11···Cg1 (blue dashed line) in **8**; view projected on the *bc* plane. Cg1 represents the centre of gravity of the C2 – C7 aromatic ring.

b) Packing mediated by the hydrogen bond C5–H5···N5B (orange dashed line) and the $C21_{ar}$–H21···Cg2 interaction (blue dashed line) in **9**. Cg2 represents the centre of gravity of the C12 – C17 aromatic ring.

Symmetry codes: iii: *x*, 1/2 – *y*, 1/2 + *z*; iv: 2 – *x*, – *y*, 1 – *z*;
v: 1 + *x*, *y*, *z*.

Table 5.2.2.2 Hydrogen bonds, C–H···π interactions and close contacts in **8**.

| **D–H···A** | **D–H [Å]** | **H···A [Å]** | **D···A [Å]** | **D–H···A [°]** |
|---|---|---|---|---|
| C1B–H1BA···N4$^{ii}$ | 0.98 | 2.59 | 3.333(10) | 133 |
| C1B–H1BB···O2 | 0.98 | 2.44 | 2.985(9) | 115 |
| C8–H8···O5$^{iii}$ | 0.96(3) | 2.34(3) | 3.119(3) | 138(2) |
| C9–H9B···O6 | 1.00(3) | 2.51(2) | 2.924(3) | 104.6(17) |
| C27–H27A···O2 | 0.94(3) | 2.45(2) | 3.042(3) | 121.1(18) |
| C27–H27B···O3$^{i}$ | 0.93(2) | 2.53(2) | 3.180(3) | 127.5(18) |
| C28$^{ii}$–H28C$^{ii}$···O1 | 0.98 | 2.52 | 3.266(5) | 133 |
| C30–H30C···O3 | 0.98 | 2.52 | 3.188(4) | 126 |
| C30–H30C···O6 | 0.98 | 2.34 | 3.245(4) | 153 |
| **C–H···π** | **C–H [Å]** | **H··· Cg [Å]** | **γ [°]** | **C–H··· Cg [°]** |
| C21$^{iii}$-H21$^{iii}$···Cg1 | 0.96(2) | 2.91(3) | 12.41 | 148(2) |

Symmetry codes: i: 1 – *x*, 1 – *y*, 1 – *z*; ii: –1 + *x*, *y*, *z*; iii: *x*, 1/2 – *y*, 1/2 + *z*. Cg1 is the centre of gravity of the aromatic ring formed by C2 – C7 atoms.

Table 5.2.2.3 Hydrogen bonds, C–H···π interactions and close contacts in **9**.

| **D–H···A** | **D–H [Å]** | **H···A [Å]** | **D···A [Å]** | **D–H···A [°]** |
|---|---|---|---|---|
| C5–H5···N5B$^{iv}$ | 0.95 | 2.57 | 3.454(19) | 156 |
| C9–H9B···O6 | 0.99 | 2.50 | 2.955(2) | 107 |
| C27–H27A···O3$^{i}$ | 0.99 | 2.50 | 3.148(2) | 123 |
| C27–H27A···O4$^{i}$ | 0.99 | 2.56 | 3.463(2) | 151 |
| C27–H27B···O2 | 0.99 | 2.40 | 2.980(2) | 117 |
| C28–H28A···O6 | 0.98 | 2.29 | 3.256(3) | 169 |
| C30–H30D···N4 | 0.98 | 2.56 | 3.451(5) | 151 |
| **C–H···π** | **C–H [Å]** | **H··· Cg [Å]** | **γ [°]** | **C–H··· Cg [°]** |
| C21–H21···Cg2$^{v}$ | 0.95 | 2.63 | 8.86 | 151 |

Symmetry codes: i: 1 - *x*, 1 - *y*, 1- *z*; iv: 2 - *x*, - *y*, 1 - *z*; v: 1 + *x*, *y*, *z*. Cg2 = centre of gravity of the aromatic ring: C12-C13-C14-C15-C16-C17.

The Full Interaction Map is a knowledge-based tool introduced by the Cambridge Crystallographic Data Centre. The application provides a visual 3D map of interaction preferences for a given molecule. The map is calculated considering every chemical fragment or functional group in a given structure, searching how often they have been observed to interact with different types of neighbours – for example with H-bond donors or acceptors and taking into account the environmental effects of combinative factors and steric exclusion to create a full 3D picture of molecular interaction preferences. [Macrae *et al.*, 2008; Wood *et al.*, 2013]. The map is assembled using the crystal-structure information held in the Cambridge Structural Database, which as of this writing is exceeding one million structures. We constructed the FIMs for structures **8** and **9** (forms I and II, respectively) to see if indeed more than one possible favourable donor-acceptor set could be identified. This would indicate that more than one arrangement of molecules in a crystal would produce stabilizing interactions or in other words, if it is possible to produce another polymorphic form of the same chemical entity.

The deprotonated $H_2$(*o-van-en*) molecule contains two potential donor sites at imine carbon atoms (Fig. 5.2.2.5, red arrows) and six acceptor sites (blue arrows in Fig. 5.2.2.5). Only two of the acceptor sites, namely the methoxy oxygen atoms, are good candidates for intermolecular interactions, since the nitrogen atoms of the imine groups and the oxygen atoms of the deprotonated hydroxy groups are used in formation of coordination bonds to the Co(III) central atom.

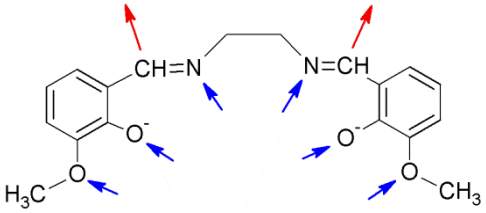


Figure 5.2.2.5 Donor (red arrows) and acceptor (blue arrows) sites of the deprotonated ligand.

In order to generate the Full Interaction Map of compound **8**, we used the complex molecule with only one disordered position of the methoxy group (atoms C1B, H1BA, H1BB and H1BC with s.o.f.s of 50 %). The FIM displays four strong red (H-bond acceptor) regions, two of them symmetry-independent (Fig. 5.2.2.6a). They represent H-bond acceptors in the vicinity of the imine C-H group of the distal ligand. Furthermore, we observe a weak blue region near the potential acceptor site at methoxy

oxygen atom O1 (circled in Fig. 5.2.2.6a). The oxygen atom of this orientation of the methoxy group is more exposed on the surface of the complex molecule which is also reflected on the corresponding FIM.

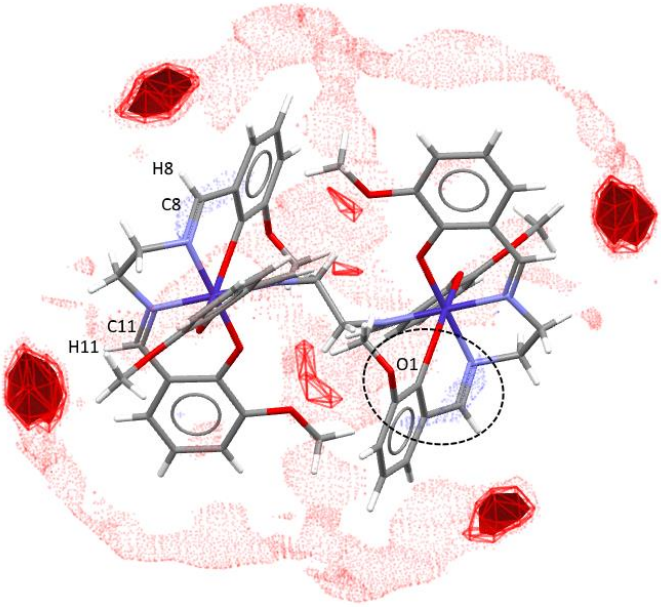


a)

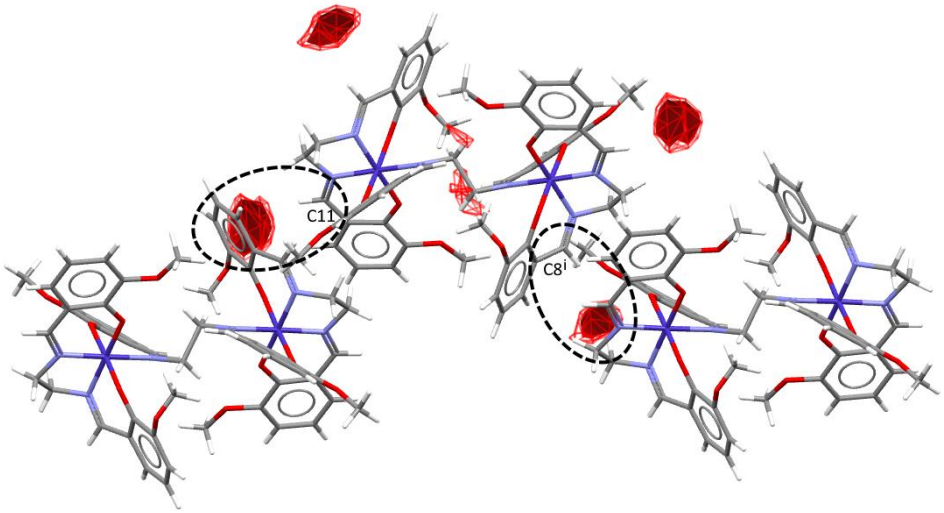


b)

Figure 5.2.2.6 a) FIM for complex molecules of **8**. H-bond donor regions are represented in blue; acceptor regions are red. Dots, wireframe and solid regions represent frequencies of 2, 4 and 6 times those expected for a random distribution of contacts.
b) Environments of two symmetrically independent donor regions in the FIM of compound **8**. Only the 4- and 6-times levels are shown.

In compound **8**, the acceptor region near the donor C11-H11 imine group, pictured in the FIM as a red region, is not fully occupied, unless the nearby electron density of the π-system of the aromatic ring $C2^{iii}$ - $C7^{iii}$ can be considered as a potential H-acceptor (left circle in Fig. 5.2.2.6b). However, this aromatic ring is involved in a weak C-H···π interaction with $C_{ar}$21-H21 of the adjacent bridging ligand (Tab. 5.2.2.2). The acceptor region for the C8-H8 imine group is not occupied by any acceptor group (right circle in Fig. 5.2.2.6b).

Just like for compound **8** (Form I), the FIM of the complex molecule in **9** (Form II) shows four regions with a strong presence of H-bond acceptors in known structures (red regions in Fig. 5.2.2.7a), two per asymmetric unit), reflecting the donor capabilities of the CH imine groups C8-H8 and C11-H11 and their symmetry relatives. The only possible acceptor sites (methoxy and oxy groups) are oriented toward the interior of the complex molecule, mostly forming intramolecular interactions, so the FIM does not show any potential donor region.

In compound **9**, the donor C8-H8 imine group is involved in a rather weak intermolecular close contact C8-H8···$O5^{iv}$ (left circled interaction in Fig. 5.2.2.7b), beyond the default limits of PLATON, and similarly, the donor site at the C11-H11 imine group is involved in a weak C-H···π interaction (right circled interaction in Fig. 5.2.2.7b), also beyond the PLATON conventional limits. It is suggested that these interactions, weak though they be, act as directors for the packing of complex molecules in the structure of **9**.

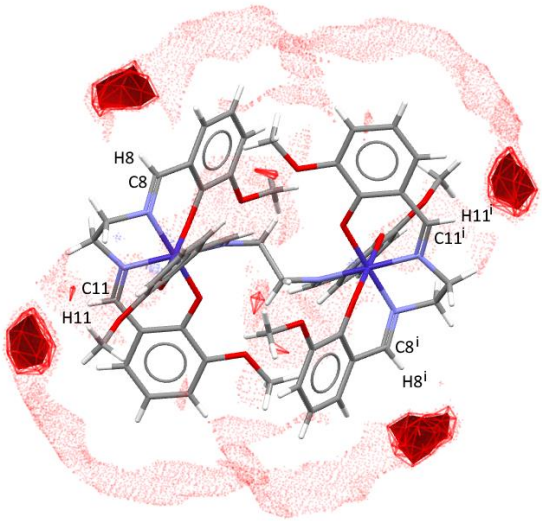


a)

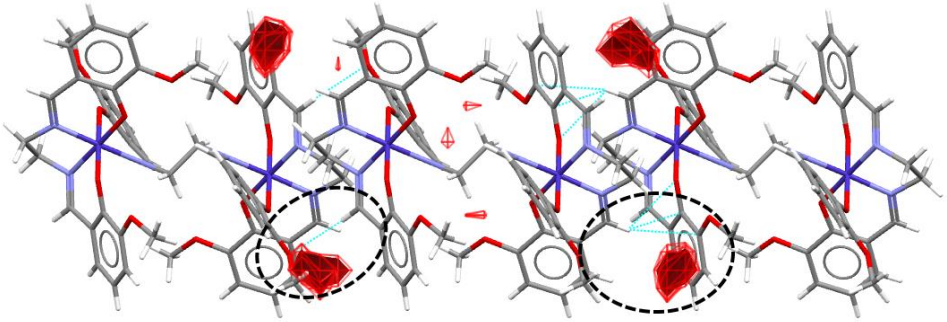

b)

Figure 5.2.2.7 a) FIM for complex molecules of **9**. H-bond donor regions are represented in blue; acceptor regions are red. Dots, wireframe and solid regions represent frequencies of 2, 4 and 6 times those expected for a random distribution of contacts.
b) Environments of two symmetrically independent donor regions in the FIM of compound **9**. Only the 4- and 6-times levels are shown.

In general, in **8** and **9**, the strongest regions of intermolecular interactions in the FIMs are occupied by symmetry related molecules mediated by weak C-H···O type hydrogen bonds and C-H···π interactions or not occupied at all. None of the interactions mentioned above lies exactly in the interaction region (the acceptor is too far away). MeCN molecules do not enter the donor or acceptor regions of the complex molecules in either of these two polymorphs.

From the FIM analysis we can conclude that the complex molecule $[Co^{III}_2(o\text{-}van\text{-}en)_3]$ (for both forms, I and II) does not possess a strong capacity for self-recognition with significant interactions. Even though the molecules record four regions

with significant capacity for H-bond donation they are not matched by any segments with the corresponding capacity to accept hydrogen bonds. Intermolecular interactions in **8** and **9** are rather energetically poor and therefore, the polymorphism of $[Co^{III}_2(o\text{-}van\text{-}en)_3]\cdot 4MeCN$ is not a result of a surfeit of molecular arrangements leading to highly stabilizing interactions. According to the above mentioned considerations and their low stability outside of their mother liquor at the temperature at which they are formed, it is not surprising that there would be more than one way to achieve a lesser level of stability.

The Hirshfeld surface analysis and fingerprint plots of the two polymorphs were done in an attempt to have a detailed graphical view of the two polymorphic forms. Unlike the FIM analysis, the Hirshfeld surface shows only the actual intermolecular interactions of the $[Co^{III}_2(o\text{-}van\text{-}en)_3]$ complex molecule. The Hirshfeld surfaces for both, **8** and **9** are visualized in Fig.5.2.2.8a)-d). In both cases the structures suffer minor disorder. Because the simultaneous presence of two disordered groups of the same disorder assembly will generate the appearance of artificial and impossibly short contacts in the Hirshfeld surfaces and fingerprint plots we will provide the analysis for each disordered part separately. The distributions of intermolecular intersections of Van der Waals´s surfaces (red areas) in the two sets of plots give a clear qualitative indication that the intermolecular spaces in the two structures are organized in different fashions.

We note that in **8**, the C1 methoxy group is positionally disordered over two positions with half occupancies. The reason for this disorder is obvious from Fig. 5.2.2.8a) displaying the Hirshfeld surface; the C1 methyl group in position A (atom C1A) forms a close contact to its symmetry (-1) generated congener ($C1A\cdots C1A^{v}$ is 2.364(11) Å, v is $-x$, 1 - $y$, 1 - $z$) which manifests itself as a strong red spot. The situation for the second disordered position, labelled B is shown on the Fig. 5.2.2.8b); the above mentioned red spot is missing; on the other hand, the second disordered position of this methoxy group (O1-C1B) is close to an MeCN solvate molecule which manifests itself by a weak hydrogen bonding interaction of the C-H···N type with N4 of the MeCN molecule (Tab. 5.2.2.2). We note that in this disordered position B an additional intramolecular hydrogen bonding interaction of the C-H···O type (C1B-H1BB···O2) is formed, too. The above mentioned close contacts can be interpreted also by Fingerprint plots [Spackman & McKinnon, 2002] generated by Hirshfeld surface of

dinuclear complex molecule of **7** (disorder A and B) (Fig. 5.2.2.9). The closest contact observed in disorder A associated with C1A methoxy group corresponds to short H···H, C···C and C···H contacts with short $d_i+d_e$ sums up to 2.4 Å, displaying as two lobes at the lower left part of the diagram. This feature is naturally missing in the Fingerprint plot for disordered position B. On the other hand, in the case of the second disordered methyl position of **7** labelled B the two above-mentioned weak hydrogen bonds of C-H···N and C-H···O types formed which leads to a certain increase of the O···H/H···O and N···H/N···H type close contacts displayed on corresponding Fingerprint plots (11.5 vs. 12.6 % and 9.3 vs. 9.5 %, respectively). In addition, Fig. 5.2.2.8a),b) shows that the MeCN solvate molecules are located in the hollows on the surface of the complex molecules and thus contribute to better filling of the intermolecular space (packing) in the unit cell which in turn according to Kitaigorodskii contributes to the stabilization of the structure [Kitaigorodskii, 1965]. We note that calculations using PLATON indicated a lack of any accessible voids in the crystal structure of **8**.

The calculated Hirshfeld surface for the dinuclear complex molecule of **9** is shown in Fig. 5.2.2.8c) and d). In **9** the MeCN molecule involving N5 (as well as C31) is positionally disordered with site occupation factors close to half (0.43 and 0.57 for N5A and N5B atoms, respectively); the left figure shows the situation with the MeCN molecule in A position (atoms N5A and C31A) and the right figure displays the same MeCN molecule in disordered positions B (atoms N5B and C31B). As the disorder pertains only to the solvate molecule and, in addition, the two disordered positions are close to each other (N5A···N5B distance is 1.29 (3) Å), the Hirshfeld surfaces of the complex molecules for both situations are not affected. The only difference is that in the disordered position N5A a weak hydrogen bonding interaction C18-H18A···N5A is formed while a slightly stronger interaction C5-H5···N5B is formed in disordered position N5B (see red dashed lines on Fig. 5.2.2.8c),d). We note that the second interaction (N5B) is involved in the Tab. 5.2.2.3 while the first one involving N5A is not as the H18A···N5A contact (2.66 Å) is beyond PLATON´s limit for hydrogen bonding interaction. In line with this observation the position N5B is slightly more populated than the first one with N5A. The calculated fingerprint plots for **9** (Fig. 5.2.2.9) also reflect the differences for the two disordered positions of the MeCN molecules, i.e. concern mainly the N···H contacts as these are affected by the present

disorder in the structure. These contacts are shorter in the fingerprint plots for N5B with respect to N5A.

Even though the Hirshfeld surface analysis graphically interprets the differences between the conformations and different intermolecular contacts this does not give us a clear indication of the origins of the polymorphism. To explore that question, the Full Interaction Maps analysis comes out as a better method.

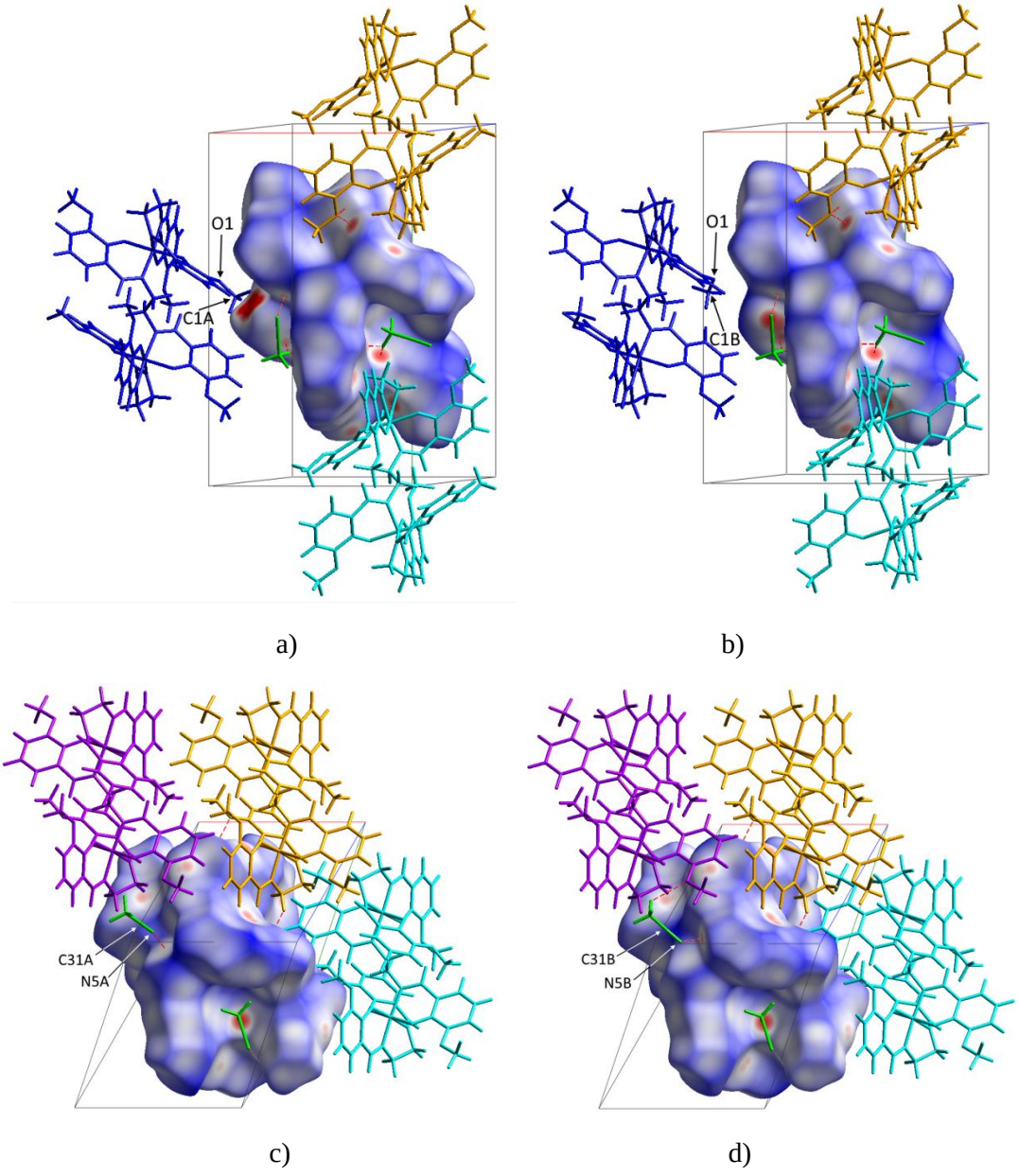


Figure 5.2.2.8 Hirshfeld surfaces of the dinuclear complex molecules of **8** (a,b) and **9** (c,d) plotted over $d_{norm}$ (normalised contact distance) from -0.4000 to 1.5000 a.u. MeCN solvate molecules are displayed in green. Close contacts (O···H ≤ 2.60 Å, N···H ≤ 2.63 Å) are shown as red dashed lines. The neighbouring molecules are drawn using wire models in different colours in order to have a better view of the contacts.

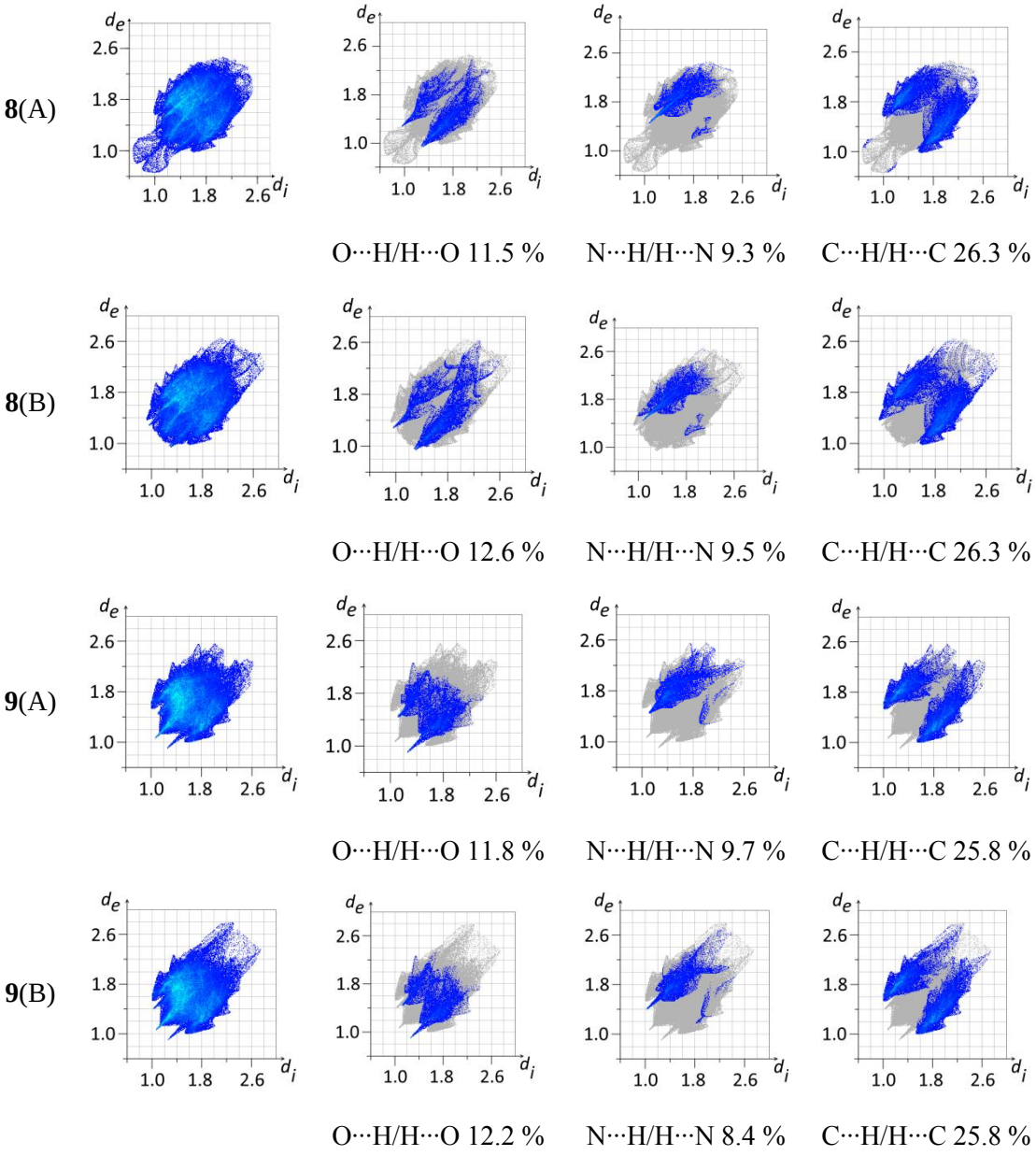


Figure 5.2.2.9 Fingerprint plots of dinuclear complex molecules of **8** and **9**, two different disorders for both structures.

[$Co^{III}$(*o-van-en*)($H_2O$)Cl] (**10**) and [$Co^{III}$(*o-van-en*)($H_2O$)Cl]·2MeCN (**11**)

The molecular structures of both, [$Co^{III}$(*o-van-en*)($H_2O$)Cl] (**10**) and [$Co^{III}$(*o-van-en*)($H_2O$)Cl]·2MeCN (**11**) contain of the [$Co^{III}$(*o-van-en*)($H_2O$)Cl] complex molecules. Compound **11** additionally contains two crystallographically independent MeCN solvate molecules. The Co(III) central atom in the complex molecule is coordinated by the chelating Schiff base ligand $(o\text{-}van\text{-}en)^{2-}$ with the $\{N_2O_2\}$ donor set in the equatorial plane and the hexacoordination of the central atom is completed by aqua and chlorido ligands in axial positions (Figs. 5.2.2.10a) and 5.2.2.11a). The Co-O, Co-N and Co-Cl bond distances found in both **10** and **11** are in the range of the corresponding values found in [$Co^{III}$(*o-van-en*)($H_2O$)Cl]·DMF [Wei *et al.*, 2012] (Tab. 5.2.2.4). We note that the values found in the reported crystal structure of [$Co^{III}$(*o-van-en*)($H_2O$)Cl]·$H_2O$ [Xing, 2009] deviate from expected bond lengths for a Co(III) atom in the corresponding coordination.

Table 5.2.2.4 Selected bond lengths [Å] for **10** and **11** compared with corresponding values found in [$Co^{III}$(*o-van-en*)($H_2O$)Cl]·DMF (***a***) [Wei *et al.*, 2012] and [$Co^{III}$(*o-van-en*)($H_2O$)Cl]·$H_2O$ (***b***) [Xing, 2009].

| | **10** | **11** | ***a*** | ***b*** |
|---|---|---|---|---|
| Co1-O2 | 1.900 (2) | 1.898 (3) | 1.885 (2) | 1.863 (3) |
| Co1-O3 | 1.907 (2) | 1.901 (2) | 1.887 (3) | 1.868 (3) |
| Co1-N1 | 1.885 (3) | 1.894 (3) | 1.884 (3) | 1.957 (4) |
| Co1-N2 | 1.878 (3) | 1.887 (3) | 1.883 (3) | 1.932 (4) |
| Co1-O5 | 1.967 (2) | 1.962 (3) | 1.982 (2) | 2.324 (3) |
| Co1-Cl1 | 2.2197 (10) | 2.2279 (11) | 2.2193 (11) | 2.5513 (17) |

The [$Co^{III}$(*o-van-en*)($H_2O$)Cl] (**10**) complex crystallizes in the orthorhombic space group P*bca*. Its crystal structure is formed by supramolecular [$Co^{III}$(*o-van-en*)($H_2O$)Cl]$_2$ dimeric units held by four hydrogen bonds of the O-H···O type between the aqua ligand of the one complex molecule (*x*, *y*, *z*) and the oxygen atoms of the $(o\text{-}van\text{-}en)^{2-}$ ligand of a second congener (1 – *x*, 1 – *y*, 1 – *z*) generated through the centre of symmetry located in the middle (Fig. 5.2.2.10b). Due to these hydrogen bonds, the aqua ligand occupies the outer coordination site of the Schiff base ligand. The intermolecular interactions in the dimer mentioned above are supported by the π···π stacking interactions between the aromatic rings of the Schiff base ligand. The

corresponding hydrogen bonds and π-π stacking interactions present in the dimer are listed in Tab. 5.2.2.5. An additional C11-H11···Cl1$^{ii}$ weak hydrogen bond links the dimers into supramolecular layers in the *ac* plane in the crystal structure of **10** (Fig. 5.2.2.10c).

The [Co$^{III}$(*o*-*van*-*en*)($H_2O$)Cl]·2MeCN (**11**) complex crystallizes in the monoclinic space group $P2_1/n$. Its crystal structure contains the same type of supramolecular dimeric units as those in the structure of **10** (Fig. 5.2.2.11b). The corresponding hydrogen bonds present in the dimer are listed in Tab. 5.2.2.6. In addition, both C8-H8 and C11-H11 imine groups of the Schiff base ligand are involved in hydrogen bonding interactions of the C-H···N type with the two N3 and N4 atoms of MeCN solvate molecules, respectively (Tab. 5.2.2.6). The 3D supramolecular structure is held only by weak intermolecular close contacts of the C-H···X type where X = O, N or Cl.

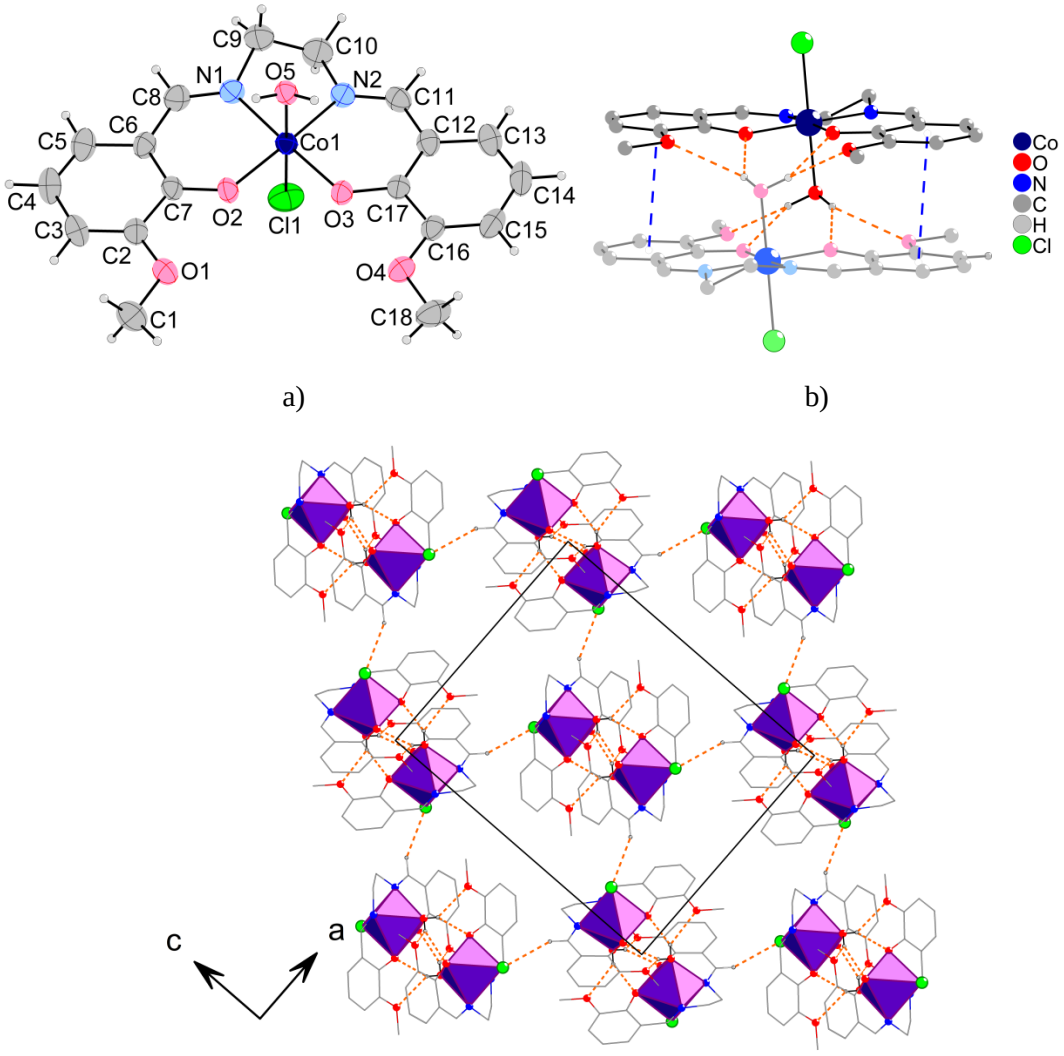


Figure 5.2.2.10

a) The asymmetric unit of [$Co^{III}$(*o-van-en*)($H_2O$)Cl] (**10**) with the atom numbering scheme. The thermal ellipsoids of non-hydrogen atoms are drawn at the 50 % probability level.

b) The supramolecular dimer in **10**. The second congener of the dimer is drawn in light colours and H-atoms not involved in hydrogen bonds are not shown for clarity. Hydrogen bonds and $\pi\cdots\pi$ stacking interactions are drawn as orange and blue dashed lines, respectively.

c) Packing diagram of **10**. The *ac* plane is shown. Carbon atoms are drawn in stick model and H-atoms not involved in hydrogen bonding (orange dashed lines) are not shown for clarity.

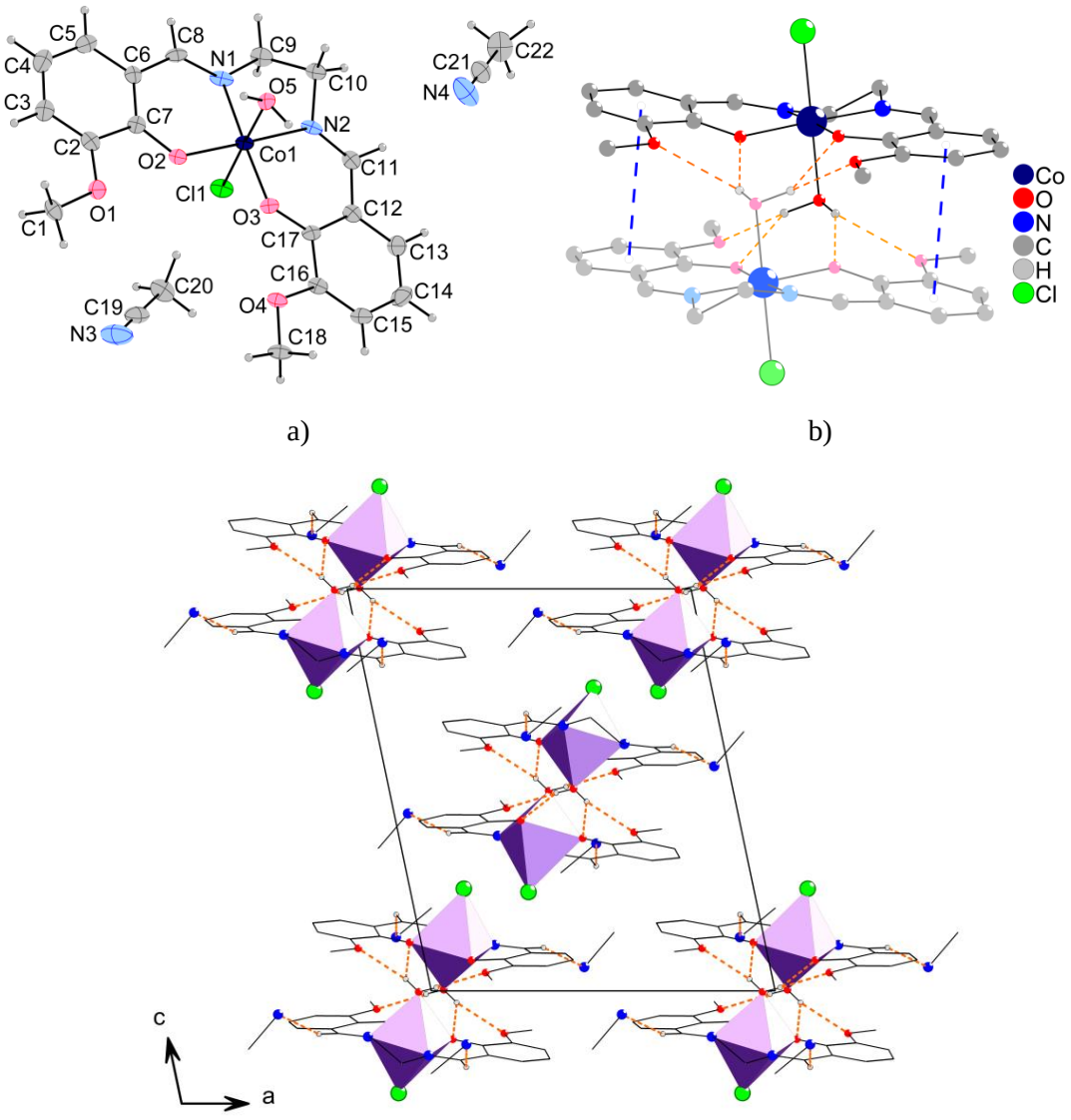


Figure 5.2.2.11

a) The asymmetric unit of [Co$^{III}$(*o-van-en*)($H_2O$)Cl]·2MeCN (**11**) with the atom numbering scheme. The thermal ellipsoids of non-hydrogen atoms are drawn at the 50 % probability level. b) The supramolecular dimer in **11**. The second congener of the dimer is drawn in light colours and H-atoms not involved in hydrogen bonding are not shown for clarity. Hydrogen bonds and $\pi\cdots\pi$ stacking interactions are drawn as orange and blue dashed lines, respectively. c) Packing diagram of **11**. The *ac* plane is shown. Carbon atoms are drawn in stick model and H-atoms not involved in hydrogen bonding (orange dashed lines) are not shown for clarity.

Table 5.2.2.5 Hydrogen bonds and $\pi$-$\pi$ stacking interactions in **10**.

| **D-H···A** | **D-H [Å]** | **H···A [Å]** | **D···A [Å]** | **D-H···A [°]** |
|---|---|---|---|---|
| O5-H1W···O3$^{i}$ | 0.836 (10) | 2.06 (2) | 2.776 (3) | 144 (3) |
| O5-H1W···O4$^{i}$ | 0.836 (10) | 2.32 (2) | 3.015 (4) | 142 (3) |
| O5-H2W···O1$^{i}$ | 0.837 (10) | 2.32 (2) | 2.994 (3) | 138 (3) |
| O5-H2W···O2$^{i}$ | 0.837 (10) | 1.997 (19) | 2.726 (3) | 145 (3) |
| C11-H11···Cl1$^{ii}$ | 0.93 | 2.82 | 3.679 (4) | 153.6 |

| **π···π** | **Cg···Cg [Å]** | **α [°]** | **β [°]** | **γ [°]** | **Slippage [Å]** |
|---|---|---|---|---|---|
| Cg1···Cg2$^{i}$ | 3.571 (2) | 2.36 (18) | 18.6 | 20.0 | 1.141 |

Symmetry codes: i: 1 – *x*, 1 – *y*, 1 – *z*; ii: 1/2 + *x*, *y*, 3/2 – *z*. Cg1 is the centre of gravity of the aromatic ring formed by C2 – C7 atoms; Cg2 is the centre of gravity of the aromatic ring formed by C12 – C17 atoms.

Table 5.2.2.6 Hydrogen bonds and $\pi$-$\pi$ stacking interactions in **11**.

| **D-H···A** | **D-H [Å]** | **H···A [Å]** | **D···A [Å]** | **D-H···A [°]** |
|---|---|---|---|---|
| O5-H1W···O1$^{i}$ | 0.842 (10) | 2.27 (3) | 2.942 (4) | 137 (3) |
| O5-H1W···O2$^{i}$ | 0.842 (10) | 2.10 (2) | 2.821 (4) | 143 (3) |
| O5-H2W···O3$^{i}$ | 0.837 (10) | 2.00 (2) | 2.740 (4) | 146 (3) |
| O5-H2W···O4$^{i}$ | 0.837 (10) | 2.28 (3) | 2.934 (4) | 135 (3) |
| C8-H8···N3$^{ii}$ | 0.95 | 2.65 | 3.443 (6) | 141.1 |
| C11-H11···N4 | 0.95 | 2.55 | 3.449 (6) | 158.2 |

| **π···π** | **Cg···Cg [Å]** | **α [°]** | **β [°]** | **γ [°]** | **Slippage [Å]** |
|---|---|---|---|---|---|
| Cg1···Cg2$^{i}$ | 3.720 (2) | 9.2 (2) | 18.0 | 21.3 | 1.152 |

Symmetry codes: i: 1 – *x*, 1 – *y*, 1 – *z*; ii: *x*, *y* – 1, *z*. Cg1 is the centre of gravity of the aromatic ring formed by C2 – C7 atoms; Cg2 is the centre of gravity of the aromatic ring formed by C12 – C17 atoms.

## 5.3 {Ni – (*o-van-en*) – Ln} complexes

After successful isolation and characterization of the [Ni(*o-van-en*)]·$n$H$_2$O (**4**) precursor, we followed the stepwise reaction method designed in Chapter 5.2. Among our first experiments in this method, we started with gadolinium(III) nitrate as the lanthanide salt. The synthesis was carried out in ethanol using reflux conditions. The microcrystalline product which was isolated by filtration straight after the reaction was recrystallized from several solvents or from mixtures of solvents (liquid-to-liquid diffusion techniques) with the aim of obtaining crystals. Single crystals were obtained only by recrystallization from acetonitrile yielding the complex [Ni(*o-van-en*)Gd(NO$_3$)$_3$]·2CH$_3$CN (**12**) where the solvent acts as the solvate in the crystal structure. We note that the crystals obtained, when removedfrom their mother liquor at the room temperature, were unstable due to loss of CH$_3$CN.

In subsequent experiments, the same self-assembly method using [Ni(*o-van-en*)]·nH$_2$O (**4**) as the Tr precursor was adopted while lanthanide(III) chlorides were used as the lanthanide source. The syntheses were carried out using reflux conditions yielding orange microcrystalline powder products of general composition [Ni(*o-van-en*)LnCl$_3$(H$_2$O)] for Ln being cerium(III) (**13**), gadolinium(III) (**14**) and dysprosium(III) (**15**). The identity and the purity of the powder samples were confirmed using IR spectroscopy, elemental analysis and X-ray powder diffraction analysis. After attempts using several different recrystallization techniques, single crystals of all three resulting compounds were isolated and crystallographically studied using single-crystal X-ray diffraction analysis.

However, recrystallization procedures yielded further compounds which will be commented below in this work as well. To sum up, five different processes were used starting from the dinuclear complex [Ni(*o-van-en*)LnCl$_3$(H$_2$O)] (Ln = Ce, Dy; see Scheme 5.3.1). Despite the fact that they were isolated fortuitously, we do not consider them as side products and approach them with full analysis.

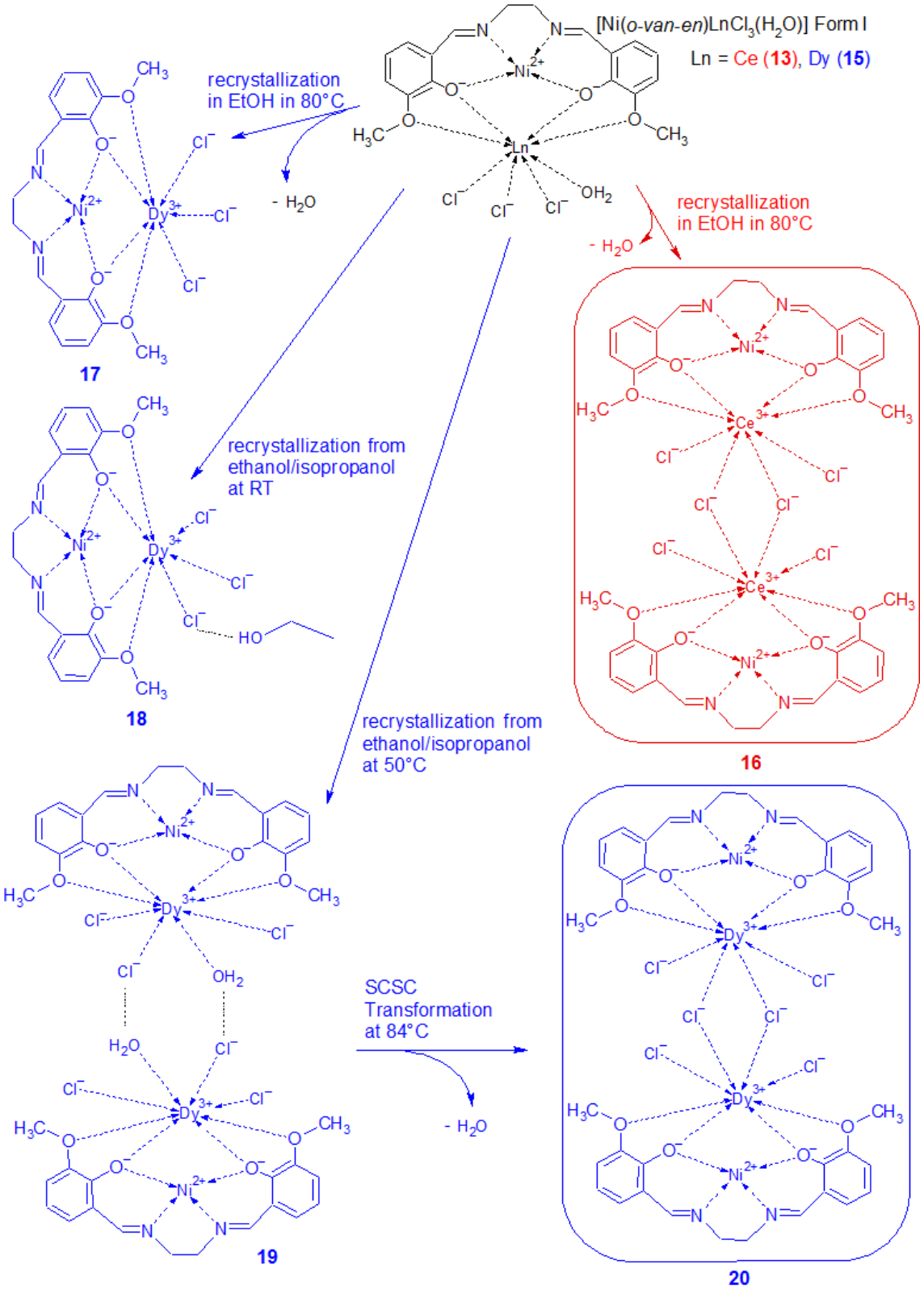


Scheme 5.3.1 The reaction processes of [Ni(*o-van-en*)$LnCl_3(H_2O)$] (Ln = Ce (**13**), Dy (**15**)) yielding five different products **16**, **17**, **18**, **19** and **20**, including one intermediate (**19**).

In the course of our experiments on recrystallization of the powder sample of [Ni(*o*-*van*-*en*)$CeCl_3(H_2O)$] (**13**), we conducted the recrystallization from ethanol in a closed flask placed in the oven at 80°C. After several hours of heating, red-orange rhombic crystals appeared at the bottom of the flask. We removed the flask from the oven and the crystals were separated by filtration while the solution was still hot. Single-crystal X-ray diffraction analysis demonstrated that the new tetranuclear complex [$Ni_2Ce_2$(*o*-*van*-*en*)$_2Cl_6$] (**16**) had been formed. Its formation can be explained by the loss of the aqua ligand from [Ni(*o*-*van*-*en*)$CeCl_3(H_2O)$], presumably by heating, followed by dimerization of the intermediate dehydrated complex.

The same recrystallization procedure was also employed using the dysprosium powder sample of [Ni(*o*-*van*-*en*)$DyCl_3(H_2O)$] (**15**). Despite an assumed analogy between cerium and dysprosium atoms, in this case no dimerization was observed and rather the crystalline dehydrated dinuclear complex [Ni(*o*-*van*-*en*)$DyCl_3$] (**17**) formed. Our conjecture is that dysprosium(III) with a smaller ionic radius than cerium(III) [Shannon, 1976] displays higher stability of its coordination sphere with lower coordination number 7 and therefore, the dehydrated complex **17** does not dimerize. We assume that the observed dimerization in the cerium(III) compound is a consequence of the tendency of the larger cerium(III) atom to fill its coordination sphere as much as possible, hence, after the loss of the aqua ligand from the coordination sphere upon heating, the Ce(III) prefers to coordinate chloride ligand as a bridge. Such behaviour depending on the ionic radii has been reported previously [Kano *et al.*, 2003; Baisch *et al.*, 2004; Deacon *et al.*, 2002; Wong *et al.*, 2006; Chen *et al.*, 2011].

Subsequently, we carried out several recrystallizations using diffusion techniques. The diffusion of an ethanol solution of [Ni(*o*-*van*-*en*)$DyCl_3(H_2O)$] (**15**) into isopropanol at room temperature yielded crystals of [Ni(*o*-*van*-*en*)$DyCl_3$]·EtOH (**18**). This result supports our previous presumption about the stability of the dysprosium(III) central atom with coordination number 7.

Changing the recrystallization technique, the dysprosium(III) sample was subjected to crystallization at increased temperature in an open system. We proceeded the diffusion experiment from an ethanol solution of [Ni(*o*-*van*-*en*)$DyCl_3(H_2O)$] (**15**) into isopropanol at room temperature and subsequently, after diffusion was completed, the open tube was placed on a 50°C hot plate. As a result of this experiment we obtained red-orange prismatic crystals of the stereoisomer of the initial complex,

namely Form II of [Ni(*o*-*van*-*en*)$DyCl_3(H_2O)$] (**19**) suitable for single-crystal X-ray analysis. The main difference in molecular structures between the two forms (Form I as **15** and Form II as **19**) of [Ni(*o*-*van*-*en*)$DyCl_3(H_2O)$] complex concerns the arrangement of the chlorido and aqua ligands in the coordination sphere of the dysprosium(III) central atom.

Besides the recrystallization experiments, we probed a different means of provoking a reaction. Upon detailed examination of the supramolecular dimeric structure of **19**, we predicted the possibility of forcing the dysprosium(III) complex to dimerize to a tetranuclear one. The supramolecular dimer of **19** appears to be correctly diposed to permit a topotactic reaction after dehydration. That assumption was proved correct by a series of experiments on the single-crystal X-ray diffractometer that produced the new complex $[Ni_2Dy_2$(*o*-*van*-*en*)$_2Cl_6]$ (**20**) as the result of the topotactic reaction. The details of the process are discussed in the following Section 5.3.1.

[Ni(*o*-*van*-*en*)$Gd(NO_3)_3]\cdot 2CH_3CN$ (**12**)

The molecular structure of **12** consists of the [Ni(*o*-*van*-*en*)$Gd(NO_3)_3$] complex molecules in which the square-coordinated Ni(II) atom lies in the inner coordination site of the Schiff base ligand $(o\text{-}van\text{-}en)^{2-}$ with the $\{O_2N_2\}$ donor set and the Gd(III) central atom occupies the outer coordination site of the ligand. The coordination sphere of the large lanthanide atom is completed by three chelate bonded nitrato ligands. Additionally, the asymmetric unit of **12** possesses two acetonitrile solvate molecules (Fig. 5.3.1a). The Ni–O, Ni–N and Gd–O bond distances were compared with those found in similar complexes [Ni*L*$Gd(NO_3)_3$] ($H_2L$ = *N*,*N*′-bis(3-methoxysalicylidene)cyclohexane-1,2-diamine) and [Ni$(MeOH)_2$*L*$Gd(NO_3)_3]\cdot 2MeOH$ ($H_2L$ = *N*,*N*′-bis(2-hydroxy-3-methoxybenzylidene)-1,3-diaminopropane) [Wen *et al.*, 2015; Jana *et al.*, 2010] (Tab. 5.3.1). The selected bond length values are in line with expectations.

The compound [Ni(*o*-*van*-*en*)$Gd(NO_3)_3]\cdot 2CH_3CN$ (**12**) crystallizes in the orthorhombic space group P*na*$2_1$. The crystal structure is mediated by weak hydrogen bonding interactions of the $C_{ar}$–H···O and $C_{imine}$–H···N types and $\pi\cdots\pi$ stacking interactions between aromatic rings of neighbouring molecules, forming a supramolecular layer in the *bc* plane (Fig. 5.3.1b). The 3D packing is then supported by weaker intermolecular interactions and close contacts.

Table 5.3.1 Selected bond lengths in Ni-Gd bimetallic complexes **12**, [Ni*L*Gd$(NO_3)_3$] (***a***) [Wen *et al.*, 2015] and [Ni$(MeOH)_2$*L*Gd$(NO_3)_3$]·2MeOH (***b***) [Jana *et al.*, 2010].

| | **12** | ***a*** | ***b*** |
|---|---|---|---|
| Ni1–O2 | 1.851 (9) | 1.851 (9) | 2.027 (2) |
| Ni1–O3 | 1.865 (8) | 1.856 (9) | 2.037 (2) |
| Ni1–N1 | 1.870 (10) | 1.840 (12) | 2.034 (2) |
| Ni1–N2 | 1.826 (11) | 1.852 (10) | 2.018 (3) |
| Gd1–O1 | 2.528 (8) | 2.525 (8) | 2.540 (2) |
| Gd1–O2 | 2.368 (8) | 2.365 (9) | 2.323 (2) |
| Gd1–O3 | 2.442 (8) | 2.398 (9) | 2.319 (2) |
| Gd1–O4 | 2.546 (9) | 2.530 (8) | 2.552 (2) |
| Gd1–O5 | 2.497 (8) | 2.477 (11) | 2.638 (4) |
| Gd1–O6 | 2.448 (9) | 2.483 (9) | 2.506 (3) |
| Gd1–O8 | 2.559 (9) | 2.500 (10) | 2.582 (3) |
| Gd1–O9 | 2.477 (8) | 2.509 (10) | 2.482 (3) |
| Gd1–O11 | 2.464 (10) | 2.509 (9) | 2.488 (3) |
| Gd1–O12 | 2.476 (7) | 2.520 (9) | 2.589 (3) |

Table 5.3.2 Potential hydrogen bonds and $\pi$-$\pi$ stacking interactions in **12**.

| **D–H···A** | **D–H [Å]** | **H···A [Å]** | **D···A [Å]** | **D–H···A [°]** |
|---|---|---|---|---|
| C4–H4···O5$^{i}$ | 0.95 | 2.43 | 3.277 (15) | 148 |
| C11–H11···N6$^{ii}$ | 0.82 (14) | 2.60 (14) | 3.37 (2) | 158 (13) |
| C13–H13···O5$^{ii}$ | 0.95 | 2.58 | 3.433 (16) | 150 |
| C15–H15···O11$^{iii}$ | 0.95 | 2.56 | 3.372 (17) | 143 |

| ***π*···*π*** | **Cg···Cg [Å]** | **α [°]** | **β [°]** | **γ [°]** | **Slippage [Å]** |
|---|---|---|---|---|---|
| Cg1···Cg2$^{i}$ | 3.720 (2) | 9.2 (2) | 18.0 | 21.3 | 1.152 |

Symmetry codes: i: *x*, *y*, 1 + *z*; ii: 3/2 – *x*, –1/2 + *y*, –1/2 + *z*; iii: *x*, *y*, –1 + *z*. Cg1 is the centre of gravity of the aromatic ring formed by C2 – C7 atoms; Cg2 is the centre of gravity of the aromatic ring formed by C12 – C17 atoms.

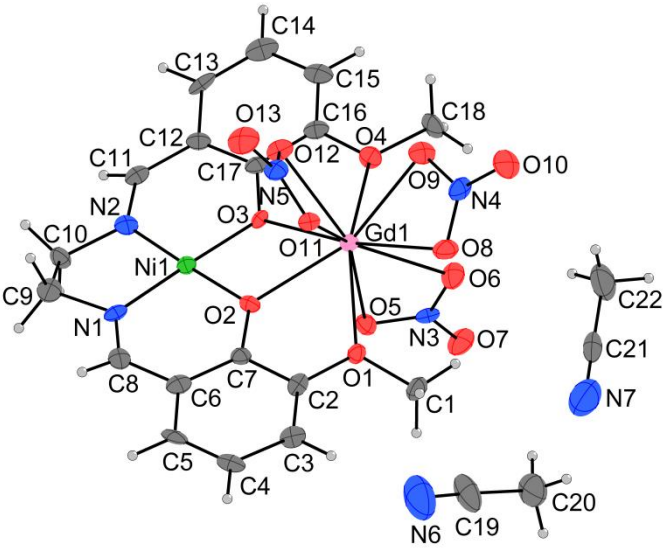


a)

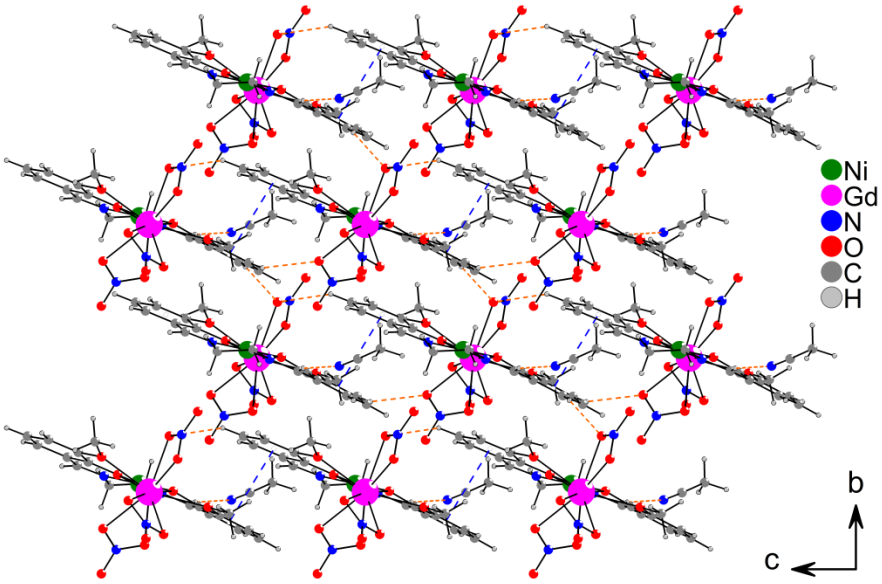


b)

Figure 5.3.1 a) The molecular structure of **12** along with its atom numbering scheme. The thermal ellipsoids of non-hydrogen atoms are drawn at the 50 % probability level. b) Crystal structure of **12**. The *bc* plane is pictured. Hydrogen bonds and $\pi\cdots\pi$ stacking interactions are drawn as orange and blue dashed lines, respectively.

[Ni(*o-van-en*)$LnCl_3(H_2O)$] (Ln = Ce in **13**, Gd in **14**, Dy in **15**)

Compounds **13** – **15** are isomorphous, so we will limit our description and discussion to complex **13** with the corresponding geometric parameters of **14** and **15** given in parentheses. The molecular structure of **13** consists of neutral heterodinuclear complex molecules of [Ni(*o-van-en*)$Ce(H_2O)Cl_3$] (Fig. 5.3.2a). The Ni(II) atom is coordinated in square-planar form by the $\{N_2O_2\}$ donor set of the potentially ditopic ligand $(o\text{-}van\text{-}en)^{2-}$. The Ce(III) central atom is octacoordinated by four oxygen atoms from the $(o\text{-}van\text{-}en)^{2-}$ ligand, one aqua and three chlorido ligands, yielding an $\{LnCl_3O_5\}$ chromophore. The observed Ni–N and Ni–O as well as the Ce–O bond distances are similar to those reported in the analogous complexes [$Ni_2$(*o-van-en*)$_2Ce(NO_3)_2$]($NO_3$) [Güngör & Kose, 2017], ([Ni*L*Gd$(NO_3)_3$] and [Ni*L*Dy$(NO_3)_3$] ($H_2L$ = *N*,*N*′-bis(3-methoxysalicylidene) cyclohexane-1,2-diamine), [Wen *et al.*, 2015]) (Tab. 5.3.3). The Ln–Cl bond distances in **13** are from the range of 2.717(2) – 2.802(2) Å [2.630(3) – 2.714(3) Å for **14** and 2.6005(10) – 2.6955(9) Å for **15**], which can be compared to the average Ce–Cl distance of 2.7467 Å (2.6829 Å for Gd–Cl and 2.6357 Å for Dy–Cl) found in the CSD [Allen *et al.*, 1994].

Table 5.3.3 Selected bond lengths in Ni-Ln complexes **13**, **14**, **15**, [$Ni_2$(*o-van-en*)$_2Ce(NO_3)_2$]($NO_3$) (***a***) [Güngör & Kose, 2017], [Ni*L*Gd$(NO_3)_3$] (***b***) and [Ni*L*Dy$(NO_3)_3$] (***c***) [Wen *et al.*, 2015].

| | **13** | **14** | **15** | ***a*** | ***b*** | ***c*** |
|---|---|---|---|---|---|---|
| Ni1–O2 | 1.843 (5) | 1.842 (7) | 1.843 (2) | 1.876 (15) | 1.851 (9) | 1.807 (19) |
| Ni1–O3 | 1.843 (5) | 1.833 (7) | 1.842 (2) | 1.843 (16) | 1.856 (9) | 1.842 (18) |
| Ni1–N1 | 1.827 (6) | 1.816 (9) | 1.834 (3) | 1.82 (2) | 1.840 (12) | 1.89 (2) |
| Ni1–N2 | 1.829 (7) | 1.825 (9) | 1.836 (3) | 1.84 (2) | 1.852 (10) | 1.91 (2) |
| Ln1–O1 | 2.710 (5) | 2.658 (7) | 2.654 (2) | 2.835 (17) | 2.525 (8) | 2.47 (2) |
| Ln1–O2 | 2.485 (5) | 2.396 (7) | 2.364 (3) | 2.539 (13) | 2.365 (9) | 2.309 (16) |
| Ln1–O3 | 2.469 (5) | 2.385 (7) | 2.343 (2) | 2.544 (15) | 2.398 (9) | 2.361 (19) |
| Ln1–O4 | 2.697 (5) | 2.650 (7) | 2.648 (2) | 2.96 (2) | 2.530 (8) | 2.441 (16) |

There are four dinuclear molecules per unit cell of **13** (and likewise for **14** and **15**). The packing of the complex molecules is governed by medium-strength hydrogen bonds of the O-H···Cl type yielding a chain-like supramolecular structure running along the *a* axis with additional, weaker $C_{ar}$–H···Cl, $C_{imine}$–H···Cl type hydrogen bonds and weak π-π stacking interactions of the aromatic rings of the neighbouring chains forming supramolecular layers in the *ab* plane (Fig. 5.3.2b), Tab. 5.3.4). There are only close contacts of the C-H···Cl type between planes, involving methyl and methylene groups of the ligand.

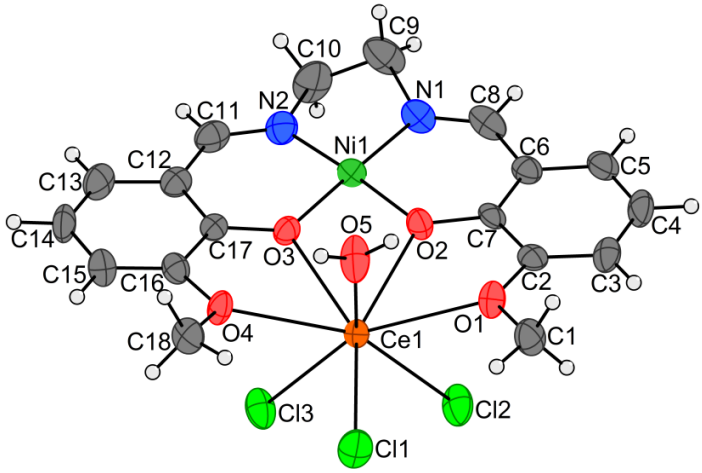


a)

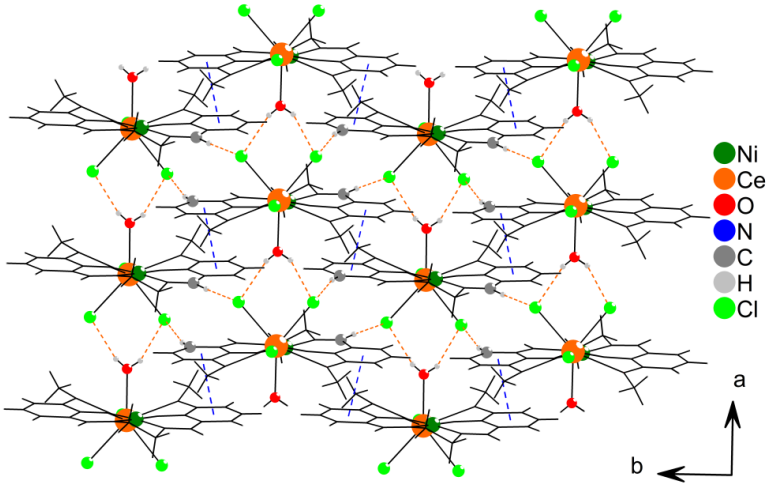


b)

Figure 5.3.2 a) Molecular structure of **13** along with its atom numbering scheme. The thermal ellipsoids of non-hydrogen atoms are drawn at the 50 % probability level.

b) Crystal structure of **13**. The *ab* plane is shown. Hydrogen bonds and *π-π* stacking interactions are drawn as orange and blue dashed lines, respectively. Carbon atoms are drawn in stick model and H-atoms not involved in hydrogen bonding are not shown for clarity.

Table 5.3.4 Potential hydrogen bonds in **13** – **15**.

| **D–H···A** | **D–H [Å]** | **H···A [Å]** | **D···A [Å]** | **D–H···A [°]** |
|---|---|---|---|---|
| Complex **13** | | | | |
| O5-H1W···Cl3$^{i}$ | 0.845 (11) | 2.32 (3) | 3.122 (5) | 157 (7) |
| O5-H2W···Cl2$^{i}$ | 0.842 (11) | 2.35 (3) | 3.125 (5) | 154 (6) |
| C11-H11···Cl2$^{ii}$ | 0.93 | 2.65 | 3.577(8) | 178.9 |
| Complex **14** | | | | |
| O5-H1W···Cl3$^{i}$ | 0.85 | 2.36 | 3.146 (7) | 155.0 |
| O5-H2W···Cl2$^{i}$ | 0.88 | 2.34 | 3.147 (8) | 152.8 |
| C11-H11···Cl2$^{ii}$ | 0.95 (10) | 2.63 (10) | 3.572 (13) | 173 (9) |
| Complex **15** | | | | |
| O5-H1W···Cl3$^{i}$ | 0.836 (10) | 2.363 (18) | 3.149 (3) | 157 (3) |
| O5-H2W···Cl2$^{i}$ | 0.836 (10) | 2.39 (2) | 3.148 (3) | 151 (3) |
| C11-H11···Cl2$^{ii}$ | 0.93 | 2.63 | 3.562 (4) | 176.9 |

| ***π*···*π*** | **Cg···Cg [Å]** | **α [°]** | **β [°]** | **γ [°]** | **Slippage [Å]** |
|---|---|---|---|---|---|
| Complex **13** | | | | | |
| Cg1···Cg2$^{iii}$ | 3.619 (5) | 2.5 (4) | 19.6 | 19.9 | 1.211 |
| Complex **14** | | | | | |
| Cg1···Cg2$^{iii}$ | 3.630 (7) | 3.5 (5) | 21.6 | 22.5 | 1.336 |
| Complex **15** | | | | | |
| Cg1···Cg2$^{iii}$ | 3.665 (2) | 3.50 (17) | 22.4 | 23.5 | 1.398 |

Symmetry codes: i: 1 + *x*, *y*, *z*; ii: –1/2 – *x*, 1/2 + *y*, 1/2 – *z*; iii: 3/2 – *x*, –1/2 + *y*, 3/2 – *z*. Cg1 is the centre of gravity of the aromatic ring formed by C2 – C7 atoms; Cg2 is the centre of gravity of the aromatic ring formed by C12 – C17 atoms.

$[Ni_2(o\text{-}van\text{-}en)_2Ce_2Cl_6]$ (**16**)

The molecular structure of **16** is formed by the neutral dimeric complex molecule $[Ni_2(o\text{-}van\text{-}en)_2Ce_2Cl_6]$ (Fig. 5.3.3a). In the monomeric unit, the Schiff base ligand $(o\text{-}van\text{-}en)^{2-}$ provides two coordination sites – the inner, smaller cavity is occupied by nickel(II) with square-planar coordination forming an $\{NiN_2O_2\}$ chromophore; and the outer, larger coordination site accommodates the cerium(III) central atom surrounded by four oxygen atoms of the ligand and three chlorido ligands. The second monomeric unit is related by the centre of symmetry [i: 1 – *x*, 1 – *y*, 1 - *z*].

Monomeric units are linked by two $\mu$-chlorido ligands (Cl3 and Cl3$^{i}$) whith a Ce···Ce distance in the dimer of 4.5232 (3) Å. The Ni–O, Ni–N, Ce–O and Ce–Cl bond distances were compared with those found in **20**, $[Ni_2(o\text{-}van\text{-}en)_2Ce(NO_3)_2](NO_3)$ and $[NiLDy(NO_3)_3]$ ($H_2L$ = *N*,*N*′-bis(3-methoxysalicylidene)cyclohexane-1,2-diamine), [Güngör & Kose, 2017; Wen *et al.*, 2015] (Tab. 5.3.5).

Table 5.3.5 Selected bond lengths in **16**, **20**, $[Ni_2(o\text{-}van\text{-}en)_2Ce(NO_3)_2](NO_3)$ (*a*) [Güngör & Kose, 2017] and $[NiLDy(NO_3)_3]$ (*b*) [Wen *et al.*, 2015].

| | **16** | **20** | ***a*** | ***b*** |
|---|---|---|---|---|
| Ni1–O2 | 1.857 (2) | 1.838 (9) | 1.876 (15) | 1.807 (19) |
| Ni1–O3 | 1.849 (2) | 1.841 (10) | 1.843 (16) | 1.842 (18) |
| Ni1–N1 | 1.841 (3) | 1.830 (12) | 1.82 (2) | 1.89 (2) |
| Ni1–N2 | 1.839 (3) | 1.830 (12) | 1.84 (2) | 1.91 (2) |
| Ln1–O1 | 2.687 (2) | 2.592 (9) | 2.835 (17) | 2.47 (2) |
| Ln1–O2 | 2.499 (2) | 2.332 (10) | 2.539 (13) | 2.309 (16) |
| Ln1–O3 | 2.455 (2) | 2.349 (10) | 2.544 (15) | 2.361 (19) |
| Ln1–O4 | 2.676 (2) | 2.572 (9) | 2.96 (2) | 2.441 (16) |
| Ln1–Cl1 | 2.7586 (9) | 2.730 (4) | – | – |
| Ln1–Cl2 | 2.7334 (10) | 2.605 (5) | – | – |
| Ln1–Cl3 | 2.8534 (9) | 2.636 (4) | – | – |

Hydrogen bonding interactions play an important role in crystal packing in **16**. The propagation of the hydrogen bonding interaction of the imine group C8–H8 and the Cl1$^{ii}$ chlorine atom forms a supramolecular chain along the *c* axis (Fig. 5.3.3b), Tab. 5.3.6). The distance between Ce(III) atoms in neighbouring dimers is 8.9361 (2) Å. There are no classical $\pi$-$\pi$ stacking interactions with Cg···Cg distance smaller than 5 Å and neither do any classical C–H···$\pi$ interactions contribute to the crystal packing. On the other hand, the distance of 3.501 Å between the central Ni1 atom and the centre of gravity of the aromatic ring formed by carbon atoms from C2$^{ii}$ to C7$^{ii}$ is rather short and can be considered as ring-metal interaction (symmetry code: ii: 1 – *x*, 1 – *y*, – *z*). The line through Ni1 and the Cg$^{ii}$ centre of gravity deviates only 7.65° from the normal to the equatorial plane of Ni1 composed of O3, O2, N1 and N2. This intermolecular interaction links dimeric molecules into the supramolecular chain along the *c* axis (Fig.

5.3.3b) which is supported only by the hydrogen bonding interaction mentioned before. Supramolecular 3D structure is then formed by other close contacts of the C–H···Cl type.

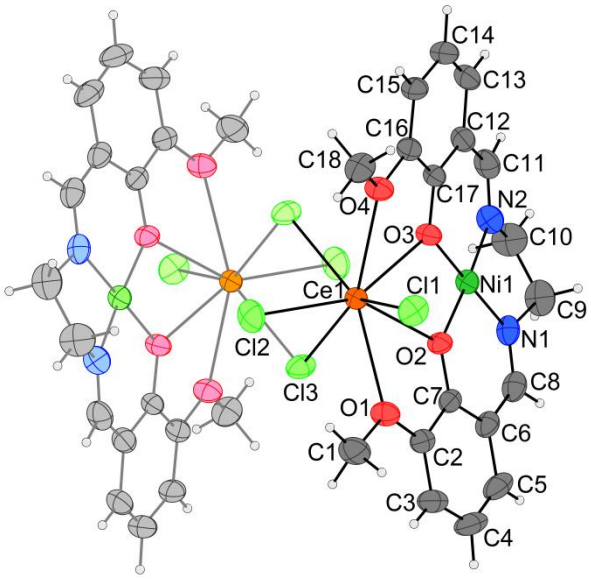


a)

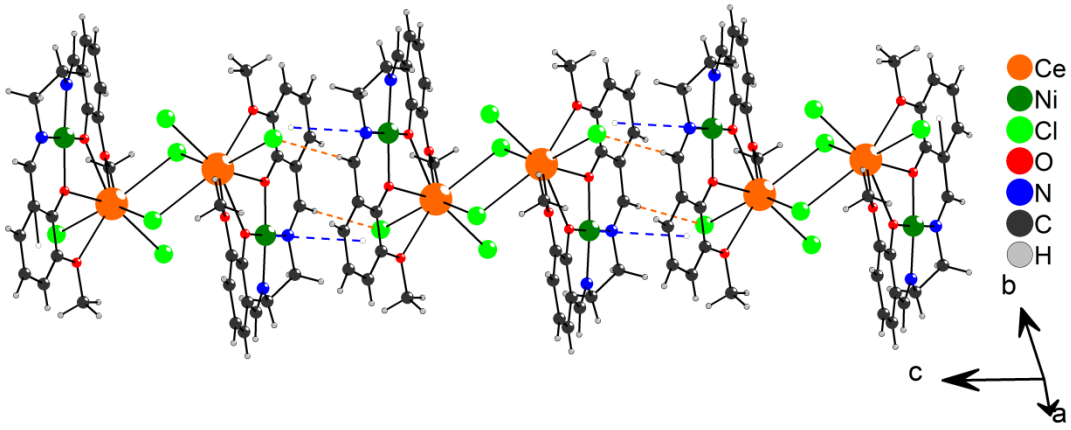


b)

Figure 5.3.3

a) The molecular structure of **16** along with its atom numbering scheme. The second part of the dimer generated by the centre of symmetry is drawn with light colours for clarity. The thermal ellipsoids of non-hydrogen atoms are drawn at the 50 % probability level.

b) Crystal structure of **16**. The *bc* plane is drawn. Hydrogen bonds and $\pi$-$\pi$ stacking interactions are drawn as orange and blue dashed lines, respectively.

Table 5.3.6 Potential hydrogen bonds and ring-metal interaction in **16**.

| **D–H···A** | **D–H [Å]** | **H···A [Å]** | **D···A [Å]** | **D–H···A [°]** |
|---|---|---|---|---|
| C8–H8···Cl1$^{ii}$ | 0.97 (4) | 2.67 (4) | 3.546 (4) | 150 (3) |
| ***π*···M** | **Cg···M [Å]** | **M–Perp [°]** | ***β* [°]** | |
| Cg1···Ni1$^{ii}$ | 3.501 | -3.408 | 13.20 | |

Symmetry code: ii: 1 – *x*, 1 – *y*, – *z*. Cg1 is the centre of gravity of the aromatic ring formed by C2 – C7 atoms.

[Ni(*o-van-en*)$DyCl_3$] (**17**) and [Ni(*o-van-en*)$DyCl_3$]·EtOH (**18**)

The molecular structure of both complexes **17** and **18** consists of bimetallic complex molecules [Ni(*o-van-en*)$DyCl_3$] with the nickel(II) central atom in square planar coordination by the Schiff base ligand (*o-van-en*)$^{2-}$ and the dysprosium(III) central atom located in the outer coordination site of the ligand. The coordination sphere of Dy(III) is then completed by three chlorido ligands (Figs. 5.3.4a) and 5.3.5a). Additionally, the asymmetric unit of **18** possesses an ethanol solvate molecule attached to the complex by a hydrogen bonding interaction of the O–H···Cl type. The Ni–O, Ni–N and Dy–O distances are listed in Table 5.3.7, compared with those found in [Ni*L*Dy$(NO_3)_3$] ($H_2L$ = *N*,*N*′-bis(3-methoxysalicylidene)cyclohexane-1,2-diamine), [Wen *et al.*, 2015]. The Dy–Cl bond distances are in line with the average value of 2.6357 Å for Dy–Cl bond lengths found in the CSD [Allen *et al.*, 1994].

The complex [Ni(*o-van-en*)$DyCl_3$] (**17**) crystallizes in triclinic space group P-1. Its crystal structure is held by weaker hydrogen bonds of the C–H···Cl type forming supramolecular chains along the *a* axis. The hydrogen bonding system is supported by *π*-*π* stacking interactions between the neighbouring aromatic rings formed by C12 – C17, also along the *a* axis (Fig. 5.3.4b). The 3D packing is then held by weaker intermolecular interactions and close contacts.

Complex **18** crystallizes in monoclinic space group $P2_1/c$. Its crystal structure is built up of complex [Ni(*o-van-en*)$DyCl_3$] units and EtOH solvate molecules which are linked together by hydrogen bonding interactions of the O–H···Cl, C–H···O and C–H···Cl types (Tab. 5.3.9). The crystal packing is then supported by intermolecular interactions of the aromatic rings between each other and interaction of the *π* system of the aromatic ring formed by C12 – C17 and the Ni1 central atom (Tab. 5.3.9, Fig. 5.3.5b).

Table 5.3.7 Selected bond distances in **17**, **18** and [Ni*L*Dy($NO_3$)$_3$] (***a***) [Wen *et al.*, 2015].

| | **17** | **18** | ***a*** |
|---|---|---|---|
| Ni1–O2 | 1.832 (5) | 1.8536 (17) | 1.807 (19) |
| Ni1–O3 | 1.858 (5) | 1.8466 (16) | 1.842 (18) |
| Ni1–N1 | 1.822 (7) | 1.838 (2) | 1.89 (2) |
| Ni1–N2 | 1.835 (7) | 1.837 (2) | 1.91 (2) |
| Dy1–O1 | 2.481 (5) | 2.5136 (7) | 2.47 (2) |
| Dy1–O2 | 2.305 (5) | 2.3165 (17) | 2.309 (16) |
| Dy1–O3 | 2.320 (5) | 2.3163 (16) | 2.361 (19) |
| Dy1–O4 | 2.528 (5) | 2.4987 (17) | 2.441 (16) |
| Dy1–Cl1 | 2.566 (2) | 2.5986 (7) | – |
| Dy1–Cl2 | 2.6015 (19) | 2.6222 (6) | – |
| Dy1–Cl3 | 2.625 (2) | 2.6071 (7) | – |

Table 5.3.8 Potential hydrogen bonding and *π*-*π* stacking interactions in **17**.

| **D–H···A** | **D–H [Å]** | **H···A [Å]** | **D···A [Å]** | **D–H···A [°]** |
|---|---|---|---|---|
| C11–H11···Cl3$^{i}$ | 0.95 | 2.75 | 3.654 (8) | 158 |
| C13–H13···Cl1$^{ii}$ | 0.95 | 2.80 | 3.571 (8) | 139 |

| ***π*···*π*** | **Cg···Cg [Å]** | **α [°]** | **β [°]** | **γ [°]** | **Slippage [Å]** |
|---|---|---|---|---|---|
| Cg1···Cg1$^{ii}$ | 3.535 (4) | 0.0 (4) | 15.8 | 15.8 | 0.965 |

Symmetry codes: i: 1 – *x*, 1 – *y*, 1 – *z*; ii: 2 – *x*, 1 – *y*, 1 – *z*. Cg1 is the centre of gravity of the aromatic ring formed by C12 – C17.

Table 5.3.9 Potential hydrogen bonding, *π*-*π* stacking and ring-metal interactions in **18**.

| **D–H···A** | **D–H [Å]** | **H···A [Å]** | **D···A [Å]** | **D–H···A [°]** |
|---|---|---|---|---|
| O5–H5W···Cl2 | 1.09 (7) | 2.31 (7) | 3.293 (3) | 150 (5) |
| C8–H8···O5$^{i}$ | 0.95 | 2.57 | 3.458 (4) | 155 |
| C11–H11···Cl1$^{ii}$ | 0.95 | 2.75 | 3.643 (3) | 157 |

| ***π*···*π*** | **Cg···Cg [Å]** | **α [°]** | **β [°]** | **γ [°]** | **Slippage [Å]** |
|---|---|---|---|---|---|
| Cg1···Cg1$^{iii}$ | 3.8727 (15) | 0.0 (12) | 27.5 | 27.5 | 1.788 |
| Cg1···Cg2$^{iv}$ | 3.8021 (16) | 8.65 (13) | 22.7 | 16.9 | 1.466 |

Table 5.3.9 Continued.

| $\pi\cdots$M | Cg$\cdots$M [Å] | M–Perp [°] | $\beta$ [°] |
|---|---|---|---|
| Cg2$\cdots$Ni1$^{ii}$ | 3.875 | -3.360 | 29.88 |

Symmetry codes: i: $x$, 1/2 – $y$, 1/2 + $z$; ii: 1 – $x$, 1 – $y$, 1 – $z$; iii: 2 – $x$, – $y$, 1 – $z$; iv: $x$, – 1 + $y$, $z$. Cg1 is the centre of gravity of the aromatic ring formed by C2 – C7; Cg2 is the centre of gravity of the aromatic ring formed by C12 – C17. Parameters $\alpha$, $\beta$ and $\gamma$ are defined as in Platon.

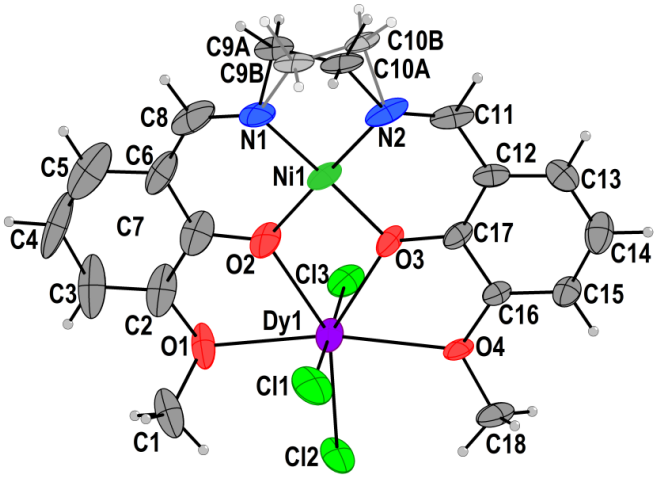


a)

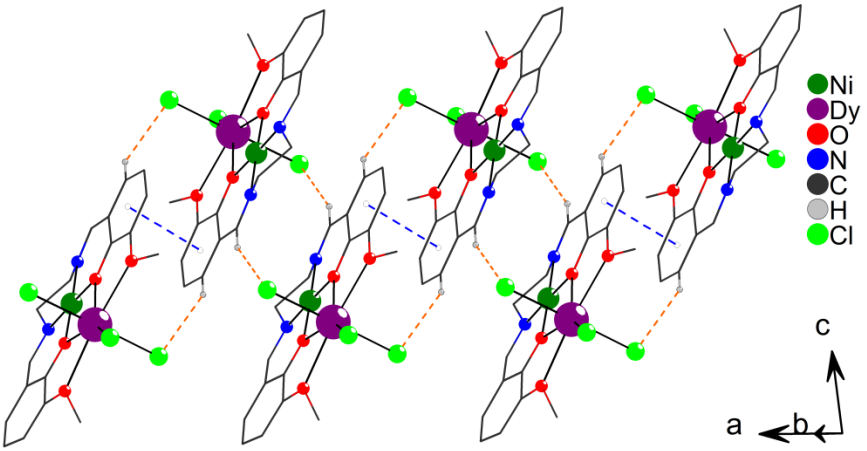


b)

Figure 5.3.4 a) The molecular structure of **17** along with its atom numbering scheme. The second part of the disordered group is drawn with light colours for clarity. The thermal ellipsoids of non-hydrogen atoms are drawn at the 50 % probability level.

b) Crystal structure of **17**. The supramolecular chain along the a axis is drawn. Hydrogen bonds and $\pi$-$\pi$ stacking interactions are drawn as orange and blue dashed lines, respectively. Carbon atoms are drawn in stick model and H-atoms not involved in hydrogen bonding are not shown for clarity.

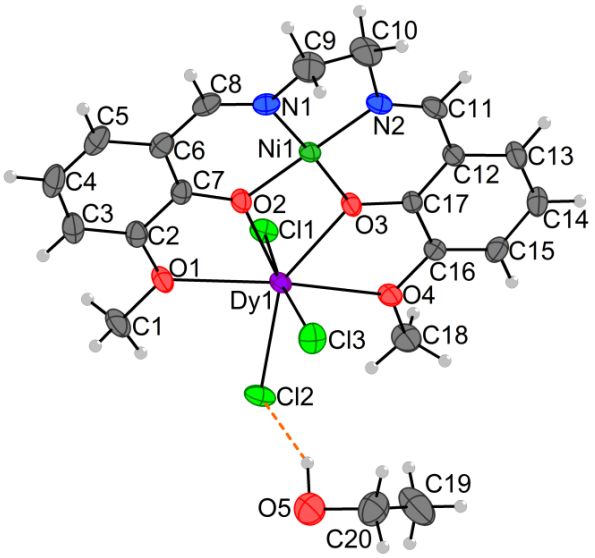


a)

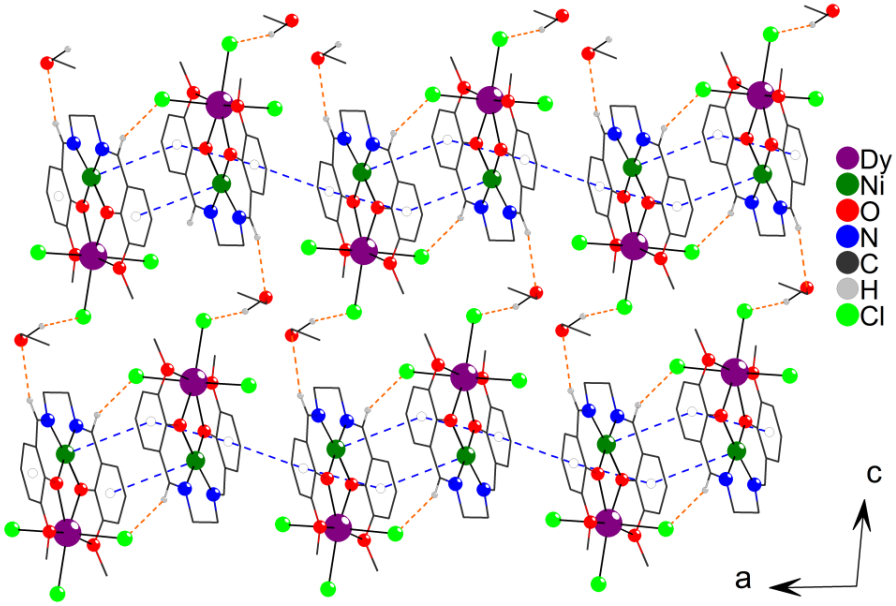


b)

Figure 5.3.5

a) The molecular structure of **18** along with its atom numbering scheme. The thermal ellipsoids of non-hydrogen atoms are drawn at the 50 % probability level.

b) The crystal structure of **18**, the *ac* plane is drawn. Hydrogen bonds and $\pi$-$\pi$ stacking / ring metal interactions are drawn as orange and blue dashed lines, respectively. Carbon atoms are drawn in stick model and H-atoms not involved in hydrogen bonding are not shown for clarity.

[Ni(*o-van-en*)$DyCl_3(H_2O)$] Form II (**19**)

The molecular structure of **19** consists of the same complex unit [Ni(*o-van-en*)$DyCl_3(H_2O)$] found in **15**. The Ni(II) central atom lies in the square planar coordination site of the Schiff base ligand $(o\text{-}van\text{-}en)^{2-}$. The ditopic ligand then binds the Dy(III) central atom in its outer coordination site. The coordination sphere of the lanthanide is then completed by three chlorido ligands and one aqua ligand (Fig. 5.3.6a). The difference between the molecular structures of **15** and **19** lies in the different relative position of the aqua and chlorido ligands. Looking parallel to the Schiff base ligand plane, two chlorido ligands and one aqua ligand are disposed above and below the plane. While the aqua ligand in **15** is located on the opposite side from the two chlorido ligands, the aqua ligand in **19** is on the same side as one chlorido ligand while the second chlorido ligand lies alone on the opposite side (Fig. 5.3.6b). The different layout of the ligands in **15** and **19** defines them as isomorphs. The Ni–O, Ni–N, Dy–O and Dy–Cl bond lengths in **19** were compared with those found in **15** and in [Ni*L*Dy$(NO_3)_3$] ($H_2L$ = *N*,*N*′-bis(3-methoxysalicylidene)cyclohexane-1,2-diamine), [Wen *et al.*, 2015] (Tab. 5.3.10). The Dy–Cl bond distances are in line with the average value of 2.6357 Å for Dy–Cl bond lengths found in the CSD [Allen *et al.*, 1994].

Table 5.3.10 Selected bond lengths in **15**, **19** and [Ni*L*Dy$(NO_3)_3$] (***a***) [Wen *et al.*, 2015].

| | **15** | **19** | ***a*** |
|---|---|---|---|
| Ni1–O2 | 1.843 (2) | 1.8420 (19) | 1.807 (19) |
| Ni1–O3 | 1.842 (2) | 1.846 (2) | 1.842 (18) |
| Ni1–N1 | 1.834 (3) | 1.835 (3) | 1.89 (2) |
| Ni1–N2 | 1.836 (3) | 1.824 (3) | 1.91 (2) |
| Dy1–O1 | 2.654 (2) | 2.619 (2) | 2.47 (2) |
| Dy1–O2 | 2.364 (3) | 2.352 (2) | 2.309 (16) |
| Dy1–O3 | 2.343 (2) | 2.3168 (19) | 2.361 (19) |
| Dy1–O4 | 2.648 (2) | 2.570 (2) | 2.441 (16) |
| Dy1–O5 | 2.375 (3) | 2.399 (3) | – |
| Dy1–Cl1 | 2.6005 (10) | 2.6273 (8) | – |
| Dy1–Cl2 | 2.6940 (9) | 2.6357 (8) | – |
| Dy1–Cl3 | 2.6955 (9) | 2.7432 (9) | – |

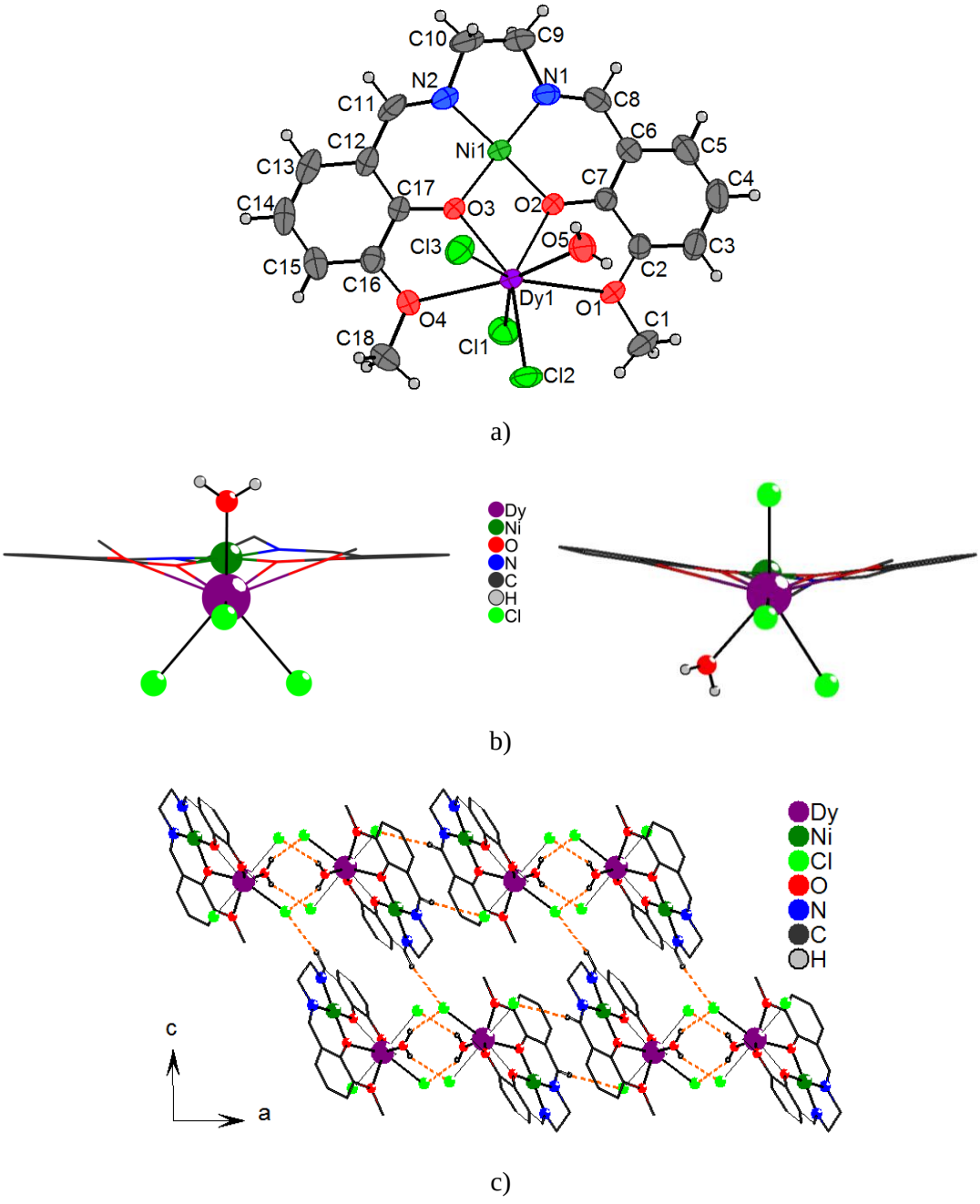


Figure 5.3.6

a) The molecular structure of **19** along with its atom numbering scheme. The thermal ellipsoids of non-hydrogen atoms are drawn at the 50 % probability level.

b) Comparison of the isomers **15** (left) and **19** (right).

c) The crystal structure of **19**, the *ac* plane is drawn. Hydrogen bonds are drawn as orange dashed lines. Carbon atoms are drawn in stick model and H-atoms not involved in hydrogen bonding are not shown for clarity.

The compound **19** crystallizes in monoclinic space group $P2_1/n$. Its crystal packing is supported by relatively strong hydrogen bonding interactions of the

O–H···Cl type forming a supramolecular dimeric crystal structure. The 3D crystal packing is then held by weaker interactions of the C–H···Cl type (Tab. 5.3.11, Fig. 5.3.6c).

Table 5.3.11 Potential hydrogen bonding interactions in **19**.

| **D–H···A** | **D–H [Å]** | **H···A [Å]** | **D···A [Å]** | **D–H···A [°]** |
|---|---|---|---|---|
| O5–H5W1···Cl2$^{i}$ | 0.79 (5) | 2.45 (5) | 3.138 (3) | 147 (4) |
| O5–H5W2···Cl3$^{i}$ | 0.72 (4) | 2.52 (4) | 3.194 (3) | 155 (4) |
| C8–H8···Cl1$^{ii}$ | 0.93 | 2.76 | 3.523 (4) | 140 |
| C11–H11···Cl2$^{iii}$ | 0.93 | 2.58 | 3.484 (4) | 164 |

Symmetry codes: i: $-x$, $1-y$, $1-z$; ii: $1-x$, $1-y$, $1-z$; iii: $1/2+x$, $1/2-y$, $-1/2+z$.

$[Ni_2(o\text{-}van\text{-}en)_2Dy_2Cl_6]$ (**20**)

The molecular structure of **20** resembles that of compound **16** with the difference in the lanthanide atom (Dy instead of Ce). Its molecular structure consists of the two monomeric $[Ni(o\text{-}van\text{-}en)DyCl_3]$ units linked by two $\mu$-chlorido bridges. The symmetry-related monomer is generated through a centre of symmetry lying in the centre of the dimer (Fig. 5.3.7a). The Ni–O, Ni–N and Dy–O bond distances were compared with those found in $[NiLDy(NO_3)_3]$ ($H_2L$ = *N*,*N*′-bis(3-methoxysalicylidene)cyclohexane-1,2-diamine), [Wen *et al.*, 2015] (Tab. 5.3.5). The Dy–Cl bond distances are in line with the average value of 2.6357 Å for Dy–Cl bond lengths found in the CSD [Allen *et al.*, 1994].

Even though compounds **16** and **20** contain the analogous chemical entities $[Ni_2Ln_2(o\text{-}van\text{-}en)_2Cl_6]$ (Ln = Ce and Dy, respectively), their crystal structures differ significantly. The complex **20** crystallizes in monoclinic space group $P2_1/n$ unlike the triclinic P-1 space group of **16**. From the intermolecular interactions in **20**, the C8–H8···Cl2$^{ii}$ weak hydrogen bond can be considered, forming supramolecular layers parallel to the *bc* plane (Fig. 5.3.7b). Beyond that, the extended structure is mediated only by weak intermolecular contacts, which results in the structure being unstable.

Table 5.3.12 Potential hydrogen bonding interactions in **20**.

| **D–H···A** | **D–H [Å]** | **H···A [Å]** | **D···A [Å]** | **D–H···A [°]** |
|---|---|---|---|---|
| C8–H8···Cl2$^{ii}$ | 0.95 | 2.60 | 3.545 (17) | 171 |

Symmetry code: ii: $1/2+x$, $-1/2-y$, $-1/2+z$.

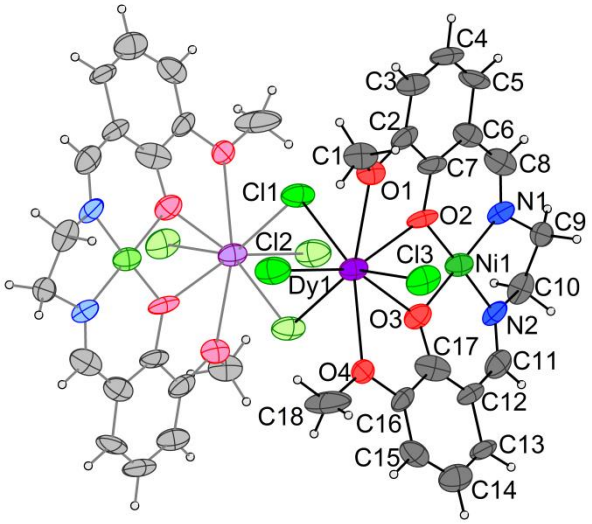


a)

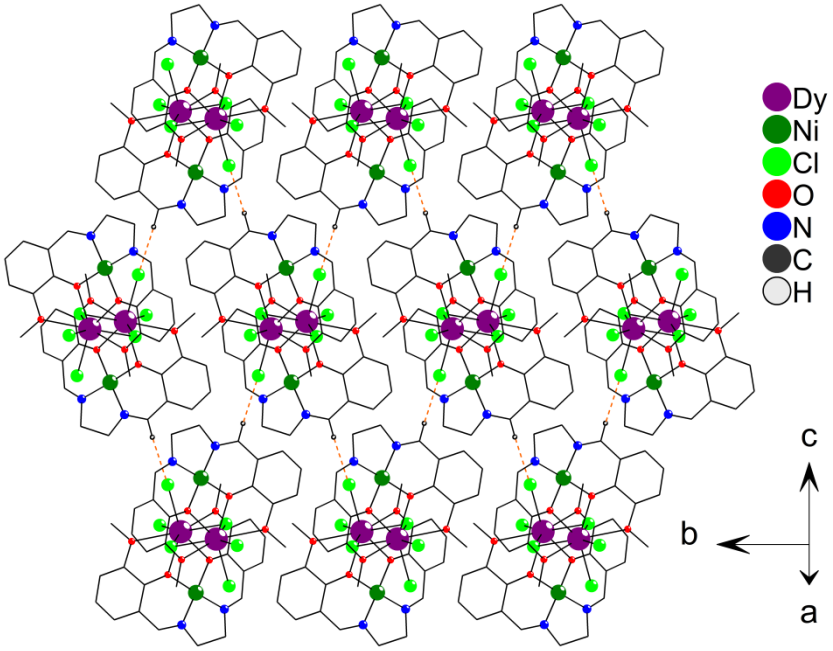


b)

Figure 5.3.7

a) The molecular structure of **20** along with its atom numbering scheme. The second part of the dimer generated by centre of symmetry is drawn with light colours for clarity. The thermal ellipsoids of non-hydrogen atoms are drawn at the 50 % probability level.

b) Crystal structure of **20**. The *bc* plane is drawn. Hydrogen bonds are drawn as orange dashed lines. Carbon atoms are drawn in stick model and H-atoms not involved in hydrogen bonding are not shown for clarity.

### 5.3.1 Crystalline Transformations

The chemical and magnetic properties of the newly prepared {Ni-Ln} complexes were studied. Before the report of magnetic properties of our final products, I would like to present the further crystallographic study of their chemical nature. During our effort to prepare single crystals of newly synthesized compounds, we observed several crystalline transformations yielding new crystal structures. Before their description, a brief review of the terminology and theory of such phenomena is needed. To simplify the interpretation of the issues mentioned later on, firstly, we can limit our use of the terms transformation/transition to the solid state and classify phase transitions from the structural or rather crystallographic perspective.

In general, a first-order phase transition is *an event which entails a discontinuous (sudden) change of at least one property of the material* [Müller, 2013]. This conversion always involves a structural change as the response to a certain stimulus such as a change of temperature, pressure, electric field, magnetic field, or mechanical forces. The structural change is understood to be a change in the space group, lattice parameters, occupied positions or/and atomic coordinates.

Through the years many attempts to classify phase transitions have been made. Ehrenfest´s classification of first- and second-order phase transition is based on purely thermodynamic arguments and macroscopic measured variables [Ehrenfest, 1933]. Even though it does not take into account the interatomic interactions and structure of substances, this theory is still used today. Later on, this classification was replaced by terms of discontinuous and continuous phase transition. Nevertheless, both classifications are used simultaneously as synonyms to each other.

According to Buerger´s structural classification of phase transitions, we can distinguish three basic types, namely reconstructive phase transitions, displacive phase transitions and order-disorder transitions [Buerger, 1951]. The first of these involves breakage and/or formation of covalent or non-covalent bonds, accompanied by structural rearrangement in the crystalline phase. Such a conversion is also classified as a first order transition.

Another well adopted terminology and the best one for our purposes was established by Hertel in [1931] and later by Lotgering in [1959] who proposed a term "topotactical (or topotaxial)" reaction or "topotaxy" as *the solid state reaction that leads to a material with crystal orientations which are correlated with crystal orientations in*

*the initial product* [Hertel, 1931; Lotgering, 1959]. The explanation of the symmetry relation between initial and final product lies in the process of nucleation which is the controlling factor of topotactic reactions. Nuclei (of the changed crystal) are formed in the matrix of the original crystal. Generally, nuclei that have the appropriate orientation have a higher probability of being formed and to continue to grow. As a result, the orientation of topotactic texture arises from the orientation of nuclei of crystallization which is determined by the matrix of the initial crystal. However, it is important to note that both crystal structures are directionally related but there is no need for a crystallographic group-subgroup relationship between the initial and final product. However, there are also such related systems and also, there are cases when the original space group is retained.

#### 5.3.1.1 Crystalline transformation I: topotactic reaction

Now, let's see the first crystalline transformation in this work – the topotactic reaction of [Ni(*o-van-en*)$DyCl_3(H_2O)$] Form II (**19**) yielding the complex [$Ni_2Dy_2$(*o-van-en*)$_2Cl_6$] (**20**). With the detailed look on the supramolecular dimeric structure of **19**, we predicted the possibility of forcing the dysprosium(III) complex to became a dimeric tetranuclear one. The supramolecular dimer of **19** seems to be correctly disposed to enable the formation of the dimer after dehydration. The prediction was confirmed by a series of experiments on the single-crystal X-ray diffractometer.

Diffraction data were measured using one single-crystal sample at several temperatures, with the temperature being raised in steps (Tab. 5.3.1.1.1). We started with pre-experiment **I** at a temperature of 277 K, recorded the unit cell parameters and then began to raise the temperature slowly in several steps. We observed the volume of the unit cell increasing with rising temperature; see pre-experiments **I** – **IV** in the table. We stopped rasing the temperature when the unit-cell volume stopped increasing (pre-experiment **V**) and left the crystal at that temperature, T = 357 K (on its Mitegen mount, on the diffractometer, in the nitrogen current) while we monitored the unit cell changes (pre-experiments **VI** – **VIII**). At that point we collected a full set of diffraction data. We observed a slight decrease in the unit-cell volume; see the full data collection **IX**. The analysis of the crystal structure of **IX** confirmed our previous conjecture and revealed the new crystal structure. Chemically, the complex [Ni(*o-van-en*)$DyCl_3(H_2O)$] (Form II,

**19**) had been dehydrated and had dimerized to form $[Ni_2(o\text{-}van\text{-}en)_2Dy_2Cl_6]$ (**20**) while retaining its single crystal character (Fig. 5.3.1.1.1).

Table 5.3.1.1.1 Evolution of the unit cell parameters of the sample **19** while varying the temperature.

| **Exp. No.** | **I** (pre) | **II** (pre) | **III** (pre) | **IV** (pre) |
|---|---|---|---|---|
| T [K] | 277 | 307 | 332 | 347 |
| *a* [Å] | 13.494 (6) | 13.514 (6) | 13.534 (7) | 13.548 (7) |
| *b* [Å] | 9.379 (4) | 9.412 (4) | 9.422 (4) | 9.425 (5) |
| *c* [Å] | 17.213 (9) | 17.199 (11) | 17.193 (12) | 17.205 (12) |
| *β* [°] | 91.19 (4) | 91.25 (5) | 91.25 (5) | 91.16 (5) |
| V [Å$^3$] | 2178 (2) | 2187 (2) | 2192 (2) | 2197 (2) |
| **Exp. No.** | **V** (pre) | **VI** (pre) | **VII** (pre) | **VIII** (pre) |
| T [K] | 357 | 357 | 357 | 357 |
| *a* [Å] | 13.555 (8) | 13.538 (8) | 13.555 (16) | 13.529 (18) |
| *b* [Å] | 9.430 (5) | 9.444 (5) | 9.422 (8) | 9.437 (8) |
| *c* [Å] | 17.191 (12) | 17.198 (12) | 17.206 (12) | 17.21 (2) |
| *β* [°] | 91.12 (6) | 91.19 (7) | 90.81 (11) | 90.72 (11) |
| V [Å$^3$] | 2197 (2) | 2198 (2) | 2197 (3) | 2197 (5) |
| **Exp. No.** | **IX** (FD) | **X** (pre) | **XI** (FD) | |
| T [K] | 357 | 223 | 223 | |
| *a* [Å] | 12.095 (2) | 12.078(8) | 12.0999(11) | |
| *b* [Å] | 9.4280 (11) | 9.409(6) | 9.4050 (4) | |
| *c* [Å] | 18.642 (3) | 18.53(2) | 18.5619(14) | |
| *β* [°] | 92.561 (13) | 91.60(9) | 91.754 (7) | |
| V [Å$^3$] | 2123.7 (6) | 2105(3) | 2111.3 (3) | |

pre = pre-experiment, FD = full data

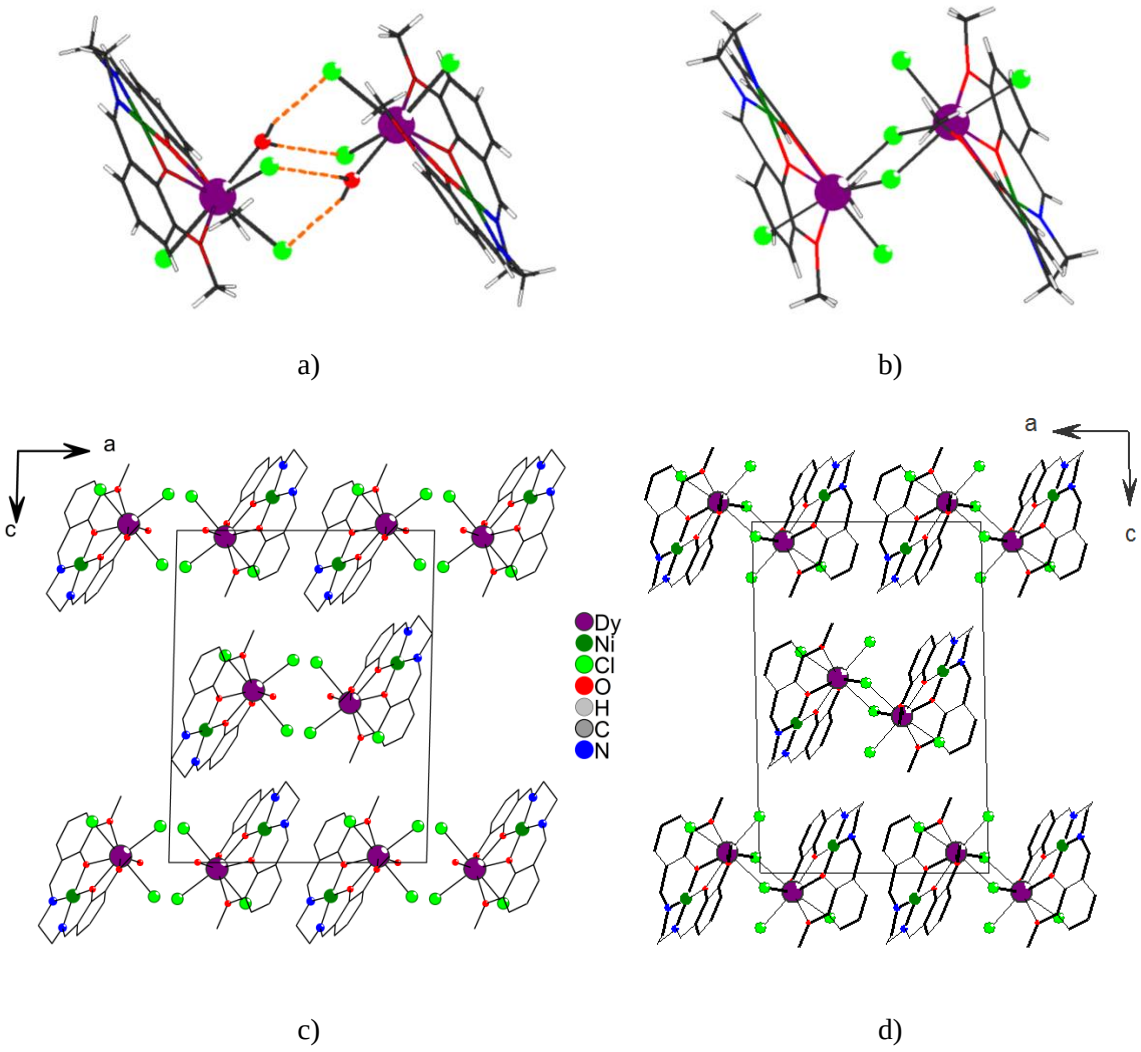


Figure 5.3.1.1.1 a) The supramolecular dimer in [Ni(*o-van-en*)$DyCl_3(H_2O)$] (Form II, **19**).
b) The molecular structure of [$Ni_2$(*o-van-en*)$_2Dy_2Cl_6$] (**20**).
The comparison of the crystal structures of **19** (a) and **20** (b).

In order to see if the "changed" crystal structure was stable, we lowered the temperature to 223 K and collected data again (see pre-experiment **X** and data collection **XI** in Tab. 5.3.1.1.1). The new crystal structure was retained and the crystal did not collapse after the heating, reaction and cooling down processes.

To sum up, we conducted three such experiments with three different single crystals of **19** and we observed the same behaviour. That proves that this reaction is not intermittent or fortuitous but rather is an intrinsic property of the compound in the crystalline state. We note that after our last experiment, the "changed" crystal was removed from the nitrogen current and exposed to the ambient conditions of the laboratory at room temperature for about 6 hours. After that time, the same crystal was

again put into the nitrogen current at 173 K and fixed to the diffractometer. The resulting full structure analysis revealed the backward change from the tetranuclear structure of [$Ni_2$(*o-van-en*)$_2Dy_2Cl_6$] (**20**) to the dinuclear structure of [Ni(*o-van-en*)$DyCl_3(H_2O)$] Form II (**19**).

A detailed look at the orientation of the molecules of the final product reveals the relation between the initial and final crystal structures (Fig. 5.3.1.1.1c),d). The release of water molecules gave rise to the motion of the supramolecular dimers closer to each other and the formation of the two chloride bridges. This process can be classified as a topotactic reaction. On the other hand, the orientation of the two unit cells is not in a line. Following the specific rules of topotaxy, it is important to use a cell setting for the final product that is related to that of the precursor. In the present case, that imperative obviates the use of what would otherwise be the conventional cell. Specifically the precursor-related cell setting for the final product is monoclinic with beta < 90º. The transformation from the diffractometer-selected "standard cell" to the topotactic product cell is as follows:

$$\begin{pmatrix} a' \\ b' \\ c' \end{pmatrix} \cdot \begin{pmatrix} -1 & 0 & 0 \\ 0 & -1 & 0 \\ 0 & 0 & 1 \end{pmatrix} = \begin{pmatrix} a \\ b \\ c \end{pmatrix}$$

where *a´*, *b´*, *c´* are the unit cell parameters given by the data collection program and *a*, *b*, *c* are the corrected unit cell parameters. The final unit cell parameters are collected up in Tab. 5.3.1.1.2.

Table 5.3.1.1.2. The initial and final unit cell parameters of the topotactic change.

| | **[Ni(*o-van-en*)$DyCl_3(H_2O)$] (19)** | **[$Ni_2$(*o-van-en*)$_2Dy_2Cl_6$] (20)** |
|---|---|---|
| ***T* [K]** | 173 | 173 |
| ***a* [Å]** | 13.4168 (3) | 12.118 (3) |
| ***b* [Å]** | 9.3666 (2) | 9.3732 (9) |
| ***c* [Å]** | 17.2733 (4) | 18.545 (3) |
| ***β* [°]** | 91.377 (2) | 88.535 (16) |
| ***V* [Å$^3$]** | 2170.11 (9) | 2105.7 (6) |

Now, we can see that the topotactic reaction resulted in the reduction of the unit cell size and the monoclinic angle *β* decreased to a value smaller than 90° (Tab. 5.3.1.1.2).

It is instructive to look at the X-ray diffraction patterns taken during the process of topotaxy. The topotactic reaction happens throughout the whole volume of the crystal only rarely and often we can see both phases, initial and product structures in the diffraction pattern at the same time. At first glance, this can be observed in reciprocal-lattice reconstructions ("precession photos" in popular terminology) of the "changed" structure of **20** and the restored structure of **19** after one full cycle of the topotactic reaction (Fig. 5.3.1.1.2). Nevertheless, we have not found the presence of both structures in crystal space.

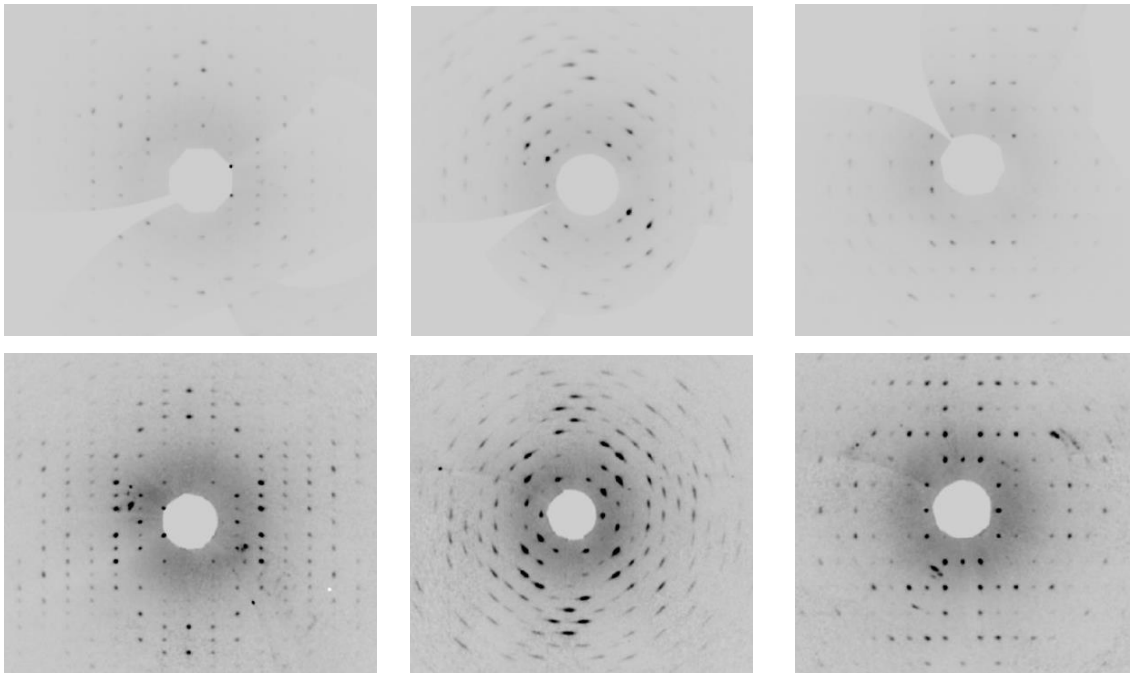

Figure 5.3.1.1.2. Precession photogaphs of the 0*kl*, *h*0*l* and *hk*0 layers (left to right) from the data of $[Ni_2(o\text{-}van\text{-}en)_2Dy_2Cl_6]$ (**20**) (top) and restored $[Ni(o\text{-}van\text{-}en)DyCl_3(H_2O)]$ (**19**) (bottom) measured at 173 K.

What we see in *h*0*l* can be explained in terms of the large mosaic that is generated as a result of strain throughout the crystal caused by the change in the unit cell. The precession photographs of the 0*kl* and *hk*0 layers look clean with the diffraction spots well shaped. On the other hand, the *h*0*l* layer shows mosaic diffraction spots. Disparity of directions indicates its origin in symmetry. The mosaic is not that well visible on the 0*kl* and *hk*0 layers, as the biggest difference in unit cell parameters is in the values of *a*, *c* and *β* and they are all included in the precession photograph of the *h*0*l* layer.

The fact that the crystal structures of the two tetranuclear complexes $[Ni_2Ln_2(o\text{-}van\text{-}en)_2Cl_6]$ (Ln = Ce in **16** and Dy in **20**) are not isostructural is a

consequence of their having been prepared by two different synthetic pathways (Scheme 5.3.1). While the cerium(III) complex **16** formed the crystal structure with the lowest energy following a reaction with **13** in ethanol as a starting point, the dysprosium(III) sample needed the transformation through the intermediate structure 1**9** followed by topotactic reaction forced by heating the sample. It is important to consider the mechanism of topotactic change in the crystal structure with a detailed look at the topochemical postulate that *reaction in the solid state occurs with a minimum of atomic or molecular movement* [Cohen & Schmidt, 1964]. The postulate says very clearly that solid-state reactions are controlled by the restricted distances and therefore, the crystal packing cannot be further stabilized after dimerization.

#### 5.3.1.2 Crystalline transformation II: Observed in powder diffraction pattern

The study of crystalline transformation of the series of [Ni(*o-van-en*)$LnCl_3(H_2O)$] (Ln = Ce, Gd and Dy) can be very rich as there are several different effects of dehydration in the solid state or in the dissolved form. The last variant we studied was the dehydration of [Ni(*o-van-en*)$DyCl_3(H_2O)$] (Form I, **15**) in the solid state. We observed the topotactic transformation of the complex by heating the powder sample and collecting the powder diffraction data at several temperature steps: RT, 80°C, 100°C, 120°C, 140°C, 160°C, RT. The sample remained 30 mins at each step up to 160°C. The whole process of crystalline changes, as observed through the powder diffraction patterns, is pictured below.

With reference to the powder patterns starting from RT and reaching 120°C, the crystalline phase of the sample is stable. The first change comes at 140°C where we can see the previous phase present along with the additional peaks of the new phase. The pattern clears up at 160°C where we no longer see the initial phase but only the "changed" phase is observed. This phase is clearly present also after cooling the sample down. The reverse process was observed upon keeping the sample at ambient conditions for a longer time. After keeping the sample at RT over the several days (weekend), we collected the powder diffraction data again which showed that the crystal structure had changed back to the initial complex [Ni(*o-van-en*)$DyCl_3(H_2O)$] (Form I) and the sample was still crystalline. After this recovery, the same sample was kept in a humid atmosphere and after several more days, the powder diffraction data collection showed the third phase.

We plan to conduct a single-crystal X-ray diffraction study of these phase changes.

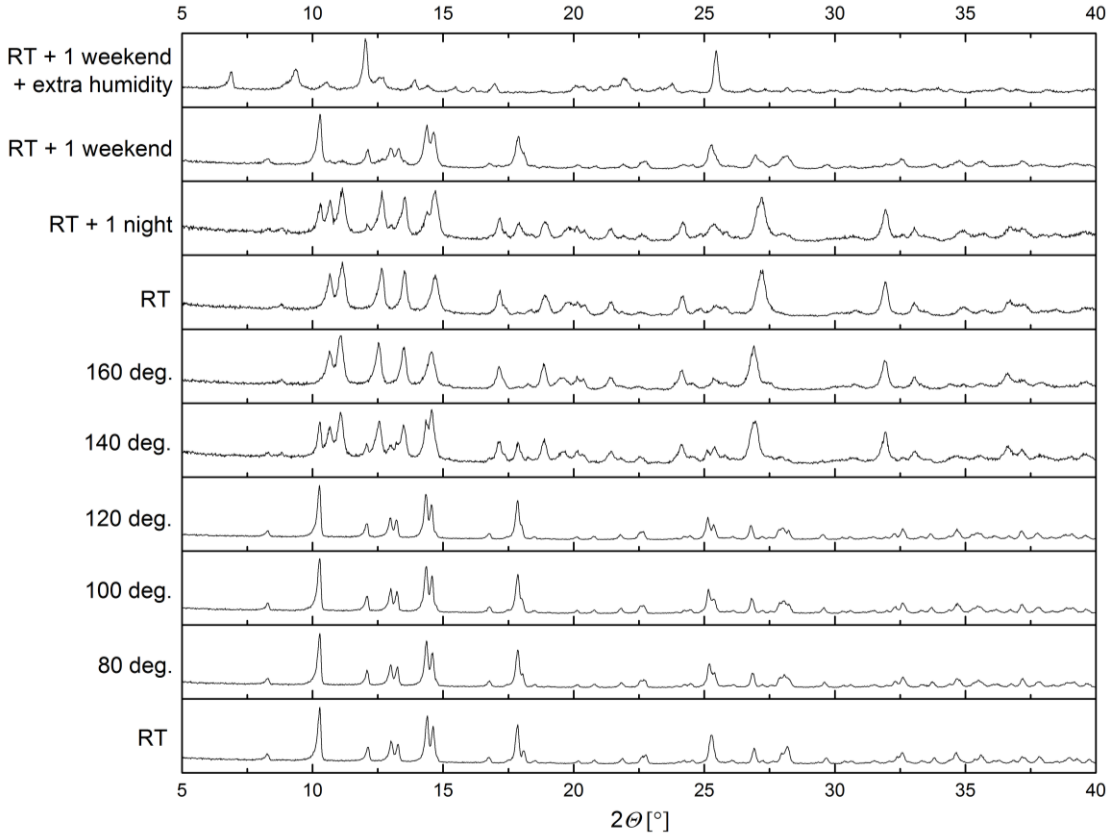


Figure 5.3.1.2.1. The powder diffraction patterns of [Ni(*o*-*van*-*en*)$DyCl_3(H_2O)$] (Form I, **15**) changing at various temperatures and time.

### 5.3.2 Magnetic properties of the [Ni(*o-van-en*)$LnCl_3(H_2O)$] isostructural family

Returning to compounds **13-15**, the powder samples were examined for their magnetic properties. Before the measurements, the samples were strictly purified and their purity was checked by X-ray powder diffraction analysis. The results of the powder diffraction data were compared with the data obtained from single-crystal X-ray diffraction analysis of **13-15** provided at room temperature applying LeBail refinement and using the program Jana2006 [Le Bail *et al.*, 1988; Le Bail, 2005; Petříček *et al.*, 2014].

For the refinement, the Pseudo-Voigt method was used. The Gaussian parameters of basic broadening by slits (U), wave length dispersion (V) and influence of monochromator (W) were freely refined while the parameter of Scherrer coefficient for Gaussian broadening (P) was not refined in the calculations. From the Lorentzian part of the refinement, the particle broadening was refined. The asymmetry of peaks was refined using the Bérar-Baldinozzi correction method with 4 terms, all of them freely refined. Background was corrected using Legendre polynomials (10 – 18 terms) and slightly shifted (shift parameter refined). The refinements are shown in Fig. 5.3.2.1 and the input and refined unit cell parameters and values of *R(p)*, *R(wp)* and GooF for the refinement of all three samples are listed in Tab. 5.3.2.1.

Table 5.3.2.1 The input and refined unit cell parameters and values of *R(p)*, *R(wp)* and *GooF* for samples **13**, **14** and **15**, respectively.

| | | **13** | **14** | **15** |
|---|---|---|---|---|
| ***Input data:*** | ***a* [Å]** | 7.1269 (3) | 7.0236 (3) | 7.00940 (10) |
| | ***b* [Å]** | 14.4698 (6) | 14.3753 (9) | 14.3916 (3) |
| | ***c* [Å]** | 21.0732 (12) | 20.9662 (13) | 20.9556 (5) |
| | ***β* [°]** | 91.377 (2) | 92.216 (9) | 91.833 (2) |
| ***Refined data:*** | ***a* [Å]** | 7.119 (13) | 7.023 (3) | 7.0128 (9) |
| | ***b* [Å]** | 14.46 (3) | 14.381 (6) | 14.4023 (19) |
| | ***c* [Å]** | 21.02 (4) | 20.901 (9) | 20.985 (3) |
| | ***β* [°]** | 92.741 (6) | 92.173 (6) | 91.803 (4) |
| | ***R(p)*** | 0.0396 | 0.0490 | 0.0457 |
| | ***R(wp)*** | 0.0544 | 0.0690 | 0.0616 |
| | ***GooF*** | 1.52 | 1.65 | 1.69 |

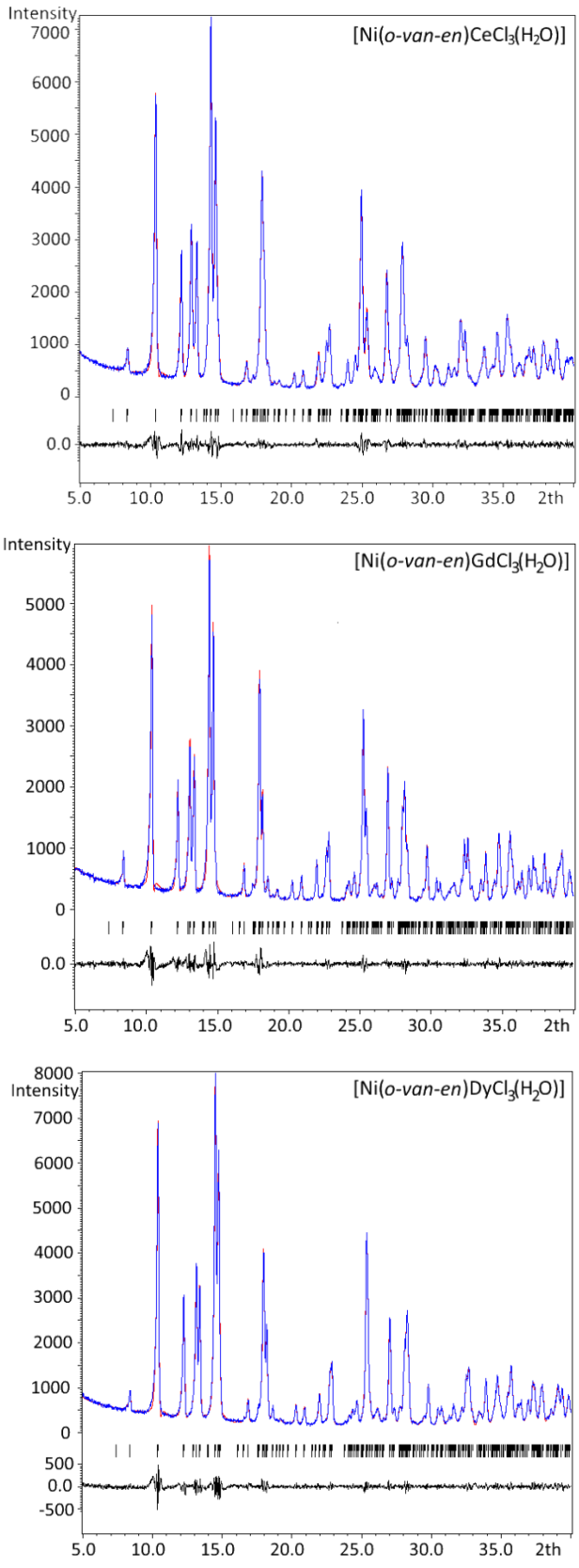


Figure 5.3.2.1 LeBail refinement of the measured powder diffraction patterns of complexes **13**, **14** and **15**, respectively. Red line represents the refined pattern; blue line represents measured data; black line represents the difference.

After the thorough purification and verification of the purity of all three samples, the DC and AC magnetic data were collected in order to study their magnetic properties. Firstly, the DC data will be commented here in this work. We would like to note that all the magnetic data collection and evaluation was done by the group of prof. Boča from the University of Ss. Cyril and Methodius in Trnava.

The crystal structures of **13**, **14** and **15** show the Ni(II) central atom to be in a square planar environment formed by four oxygen donor atoms. Thus, it is magnetically silent, except for some temperature-independent magnetism arising from the presence of low-lying excited states. On the other side, the lanthanide Ln(III) centres possess orbital and spin angular momentum and the ground multiplet is $^2F_{5/2}$ for Ce(III), $^8S_{7/2}$ for Gd(III) and $^6H_{15/2}$ for Dy(III), with the magnetogyric ratios $g_J$ = 6/7, 2 and 4/3, respectively. Thus, the magnetization per formula unit should saturate to $M_1 = M_{mol}/(N_A\mu_B) = g_J \cdot J$ = 6/7 × 5/2 = 15/7, 2 × 7/2 = 7, and 4/3 × 15/2 = 10. The high temperature limit of the effective magnetic moment, based upon the magnetic susceptibility, is $\mu_{eff}/\mu_B = g_J[J(J + 1)]1/2$ = (6/7)(5/2 × 7/2)1/2 = 2.54, 2 × (7/2 × 9/2)1/2 = 7.94, and (4/3) (15/2 × 17/2)1/2 = 10.6, respectively.

The DC magnetic data for **13** are shown in Fig. 5.3.2.2a). Clearly visible linear dependence of the effective magnetic moment between T = 9–300 K indicates some temperature-independent paramagnetism as expected for the Ni(II) centre in a square planar environment: $\chi_{TIP} = 6 \times 10^{-9}$ m$^3$ mol$^{-1}$. The room-temperature effective magnetic moment (the high-temperature limit) adopts a value of $\mu_{eff} = 2.36\mu_B$, that is not far from the single ion value (2.54). The magnetization data at $T$ = 2.0 and $B$ = 7 T, $M_1$ = 1.0, is much lower relative to isolated multiplet $^2F_{5/2}$ for Ce(III) (2.1). Owing to the effect of the crystal field, the six-fold degenerate ground atomic multiplet $^2F_{5/2}$ is split into three crystal-field multiplets (Kramers doublets). The magnetic data was fitted assuming that only the lowest Kramers doublet is thermally populated.

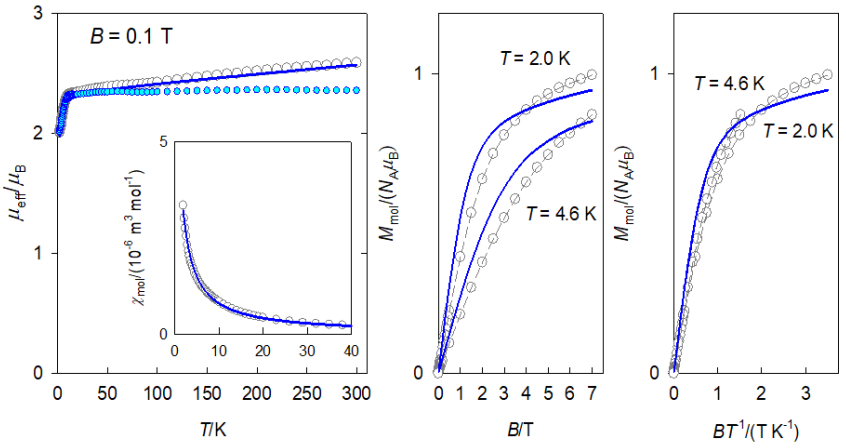


a)

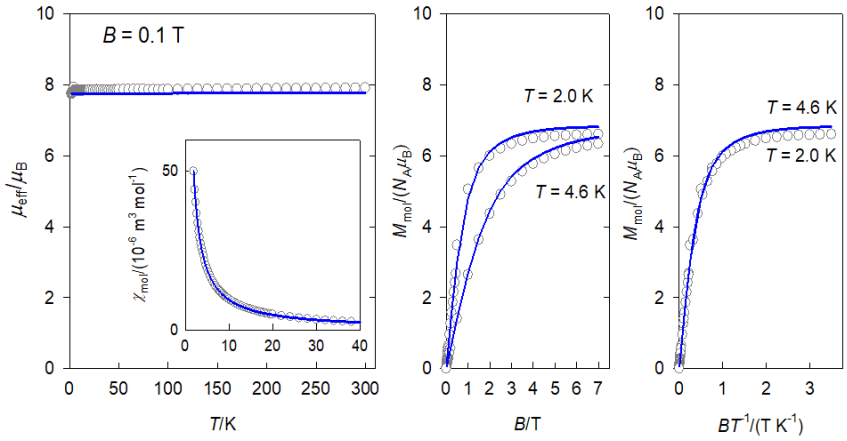


b)

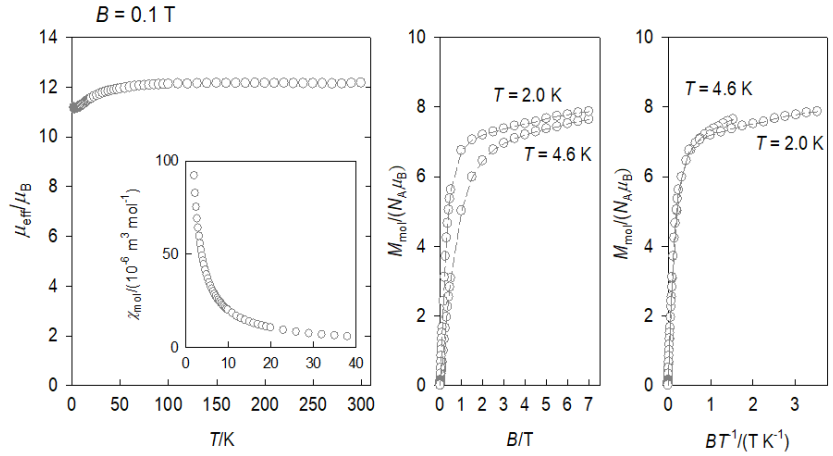


c)

Figure 5.3.2.2 DC magnetic data for **13** (a), **14** (b) and **15** (c). Solid lines represent fitted data, dashed lines are visual guides and coloured circles in a) are TIP corrected data.

The AC susceptibility data were obtained at the field amplitude of $B_{AC}$ = 0.38 mT and depending upon the external magnetic field $B_{DC}$, temperature $T$, and the frequency $f$ of the oscillating field. Within this work, only the frequency dependence of the AC susceptibility will be analysed. For this purpose, the same data sets have been rearranged for all three samples.

Frequency dependence of the in-phase and out-of-phase components of AC susceptibility measured on sample **15** is depicted in Fig. 5.3.2.3. The curve clearly shows the three contributions to the out-of-phase component: low-frequency (LF), intermediate-frequency (IF), and high-frequency (HF). Both, in-phase and out-of-phase susceptibilities were fitted simultaneously by employing the three-set Debye model. At the lowest temperature $T$ = 1.9 K, the LF component dominates while the HF component recovers only a tail. However, the LF component decays progressively with increasing temperature in favor of the HF one and the IF component balances in-between. At temperature $T$ > 5 K, the IF component cannot be fitted satisfactorily and then only a two-set Debye model is applicable. At the lowest measurement temperature, $T$ = 1.9 K, the three relaxation times are $\tau$(LF) = 1.29 s, $\tau$(IF) = 74 ms, and $\tau$(HF) = 964 μs. In contrast, at T = 6.3 K, $\tau$(LF) = 0.064 s and $\tau$(HF) = 5.8 μs.

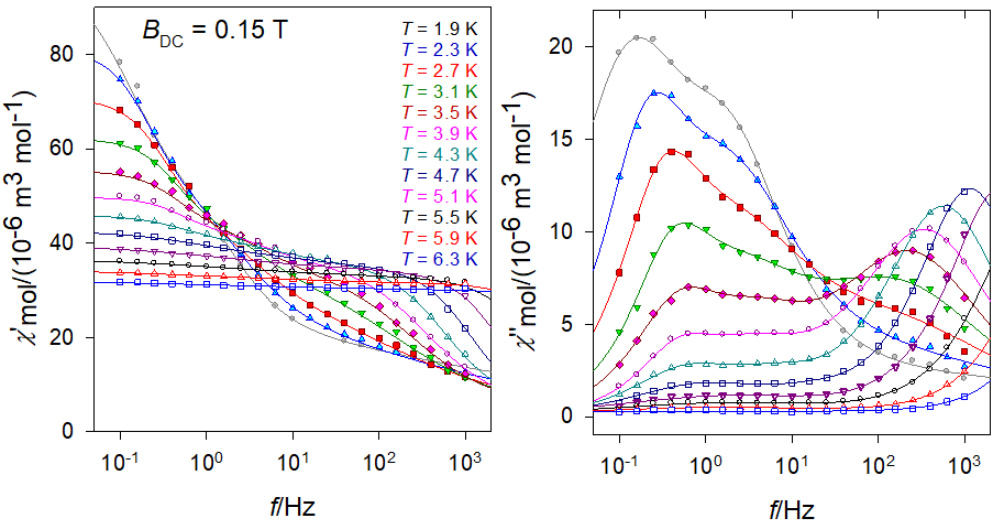


Figure 5.3.2.3 AC magnetic data for **15**. Solid lines – fitted by the extended three-set Debye model.

The presence of the three components can also be substantiated using the Argand diagram showing three distorted semicircles (arcs) of different height, position and width, see Fig. 5.3.2.4. The temperature evolution of the HF relaxation time can be

represented by various graphs. Arrhenius-like plot ln $\tau$ vs. $T^{-1}$ is depicted on the right for the individual relaxation processes, where the HF relaxation process was fitted using Raman and quantum tunneling processes.

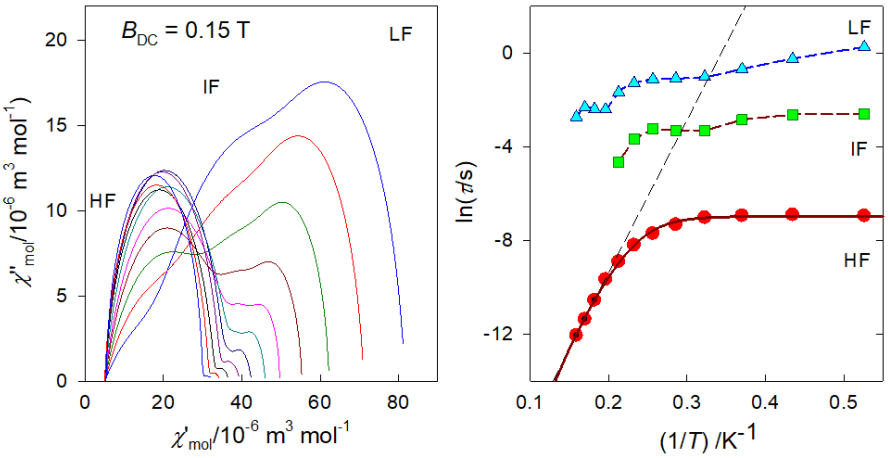


Figure 5.3.2.4 Argand diagram (left) and the Arrhenius-like plot (right) for **15**. Straight line – high-temperature limit of the Arrhenius equation referring to the Orbach process. Solid curve – fitted using Raman and quantum tunneling processes.

The frequency dependence of the AC susceptibility components for **13** (cerium(III) sample) is shown in Fig. 5.3.2.5. For $T$ = 1.9 K the well-developed peak of $\chi''$ at f ~ 10 Hz implies the relaxation time $\tau$(LF) ~ 16 ms. This is much shorter as compared to that of the dysprosium(III) sample. However, the peak is slightly asymmetric with an arm, and its reliable fit requires a two-set Debye model where the HF component is also considered. On heating the peak is shifted to higher frequencies but for $T$ > 4 K the two-set model becomes unstable; thus the single-set model has been applied for higher temperatures. We observed also a visible effect of the external magnetic field on the relaxation behaviour of **13**. The relaxation time at $T$ = 1.9 K and $B_{DC}$ = 0.5 T becomes $\tau$(LF) = 60.3(5) ms as compared to 18.7(11) ms at $B_{DC}$ = 0.1 T. The Argand diagram and Arrhenius-like plot for **13** are displayed in Fig. 5.3.2.6.

The SIM behaviour of the Ce(III) ions has been reviewed recently [Pointillart *et al.*, 2017; Hino *et al.*, 2013; Hino *et al.*, 2013; Le Roy *et al.*, 2014; Khélifa *et al.*, 2015; Singh *et al.*, 2015]. For instance, AC susceptibility studies of single-molecule magnet behaviour in polynuclear assembly of Ce(III) with polymolybdates reveal a two-channel slow relaxation with the relaxation times $\tau$ = 6009 and 217 μs at $T$ = 1.9 K and $B_{DC}$ = 0.02 T [Khélifa *et al.*, 2015]. There is a sizable field influence since at $B_{DC}$ = 0.14 T the relaxation times merge to $\tau$ = 605 μs.

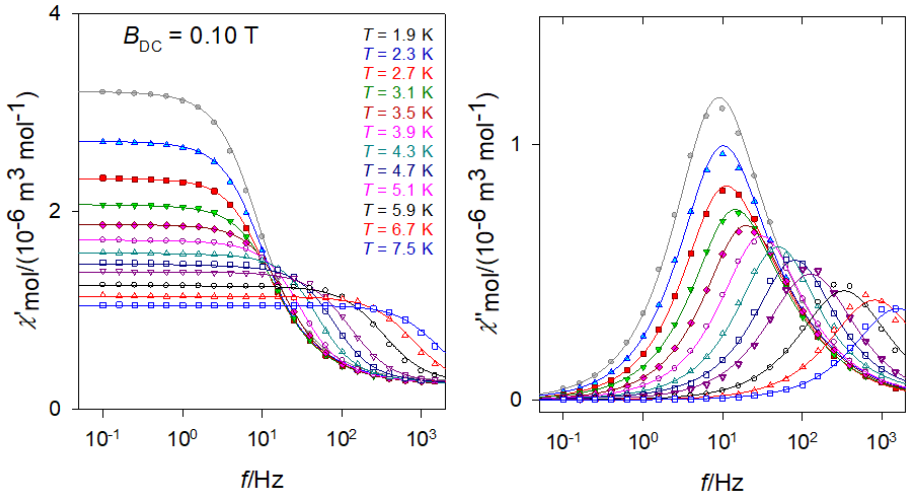


Figure 5.3.2.5 AC magnetic data for **13**. Solid lines – fitted by the extended twoset Debye model.

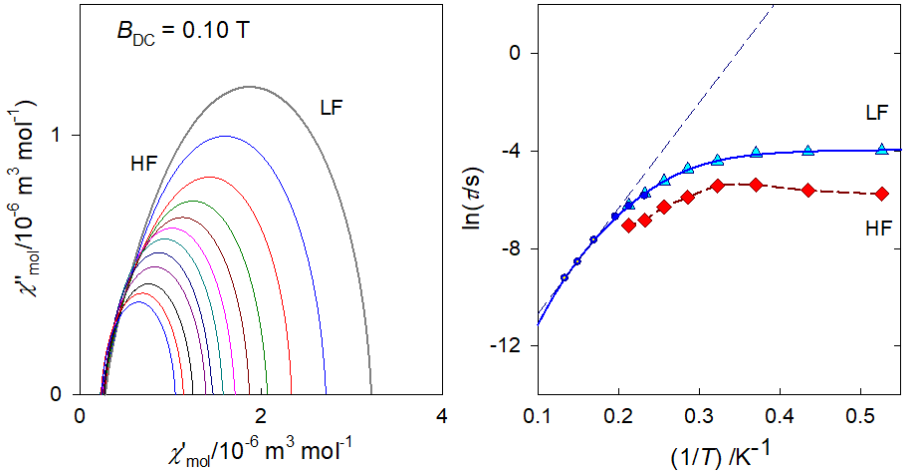


Figure 5.3.2.6 Argand diagram (left) and the Arrhenius-like plot (right) for **13**. Full circles – single-set Debye model; solid curve – fitted with Raman and tunneling process; dashed – three-point linear extrapolation for the Orbach process.

The last analysis we have done on the Ni-Ln family was the magnetic study of the gadolinium(III) sample. The existence of slow magnetic relaxation in the case of the isotropic gadolinium(III) centre was unexpected. Therefore, our findings required increased attention in evaluating, interpreting data and literature research.

The frequency dependence of the AC susceptibility components for the Gd(III) compound **14** is shown in Fig. 5.3.2.7. In this case the two-set Debye model reproduces the experimental data with well separated branches. Two individual relaxation processes are also well recognized on the Argand diagram with two well defined semicircles (arcs) (Fig. 5.3.2.8 left). Even more surprising is the Arrhenius-like plot drawn in Fig.

5.3.2.8 (right) where the HF relaxation time is only slightly temperature dependent between 1.9 and 6.5 K. Moreover, the HF branch shows a "strange" behaviour: on cooling the relaxation time passes through a maximum and then it is shortened: $\tau$(HF) = 223 μs at $T$ = 3.9 K as compared to $\tau$(HF) = 120 μs at $T$ = 1.9 K. The fitting procedure of this "strange" behaviour was developed by the group of prof. Boča by addition of the "strange" parameter $E_\tau$ representing another critical influence of the relaxation process. This method was recently applied to Cu(II), Ni(II), Co(II), and Mn(II) complexes showing distorted octahedral geometry [Boča *et al.*, 2017; Titiš *et al.*, 2018; Boča *et al.*, 2018; Rajnák *et al.*, 2019].

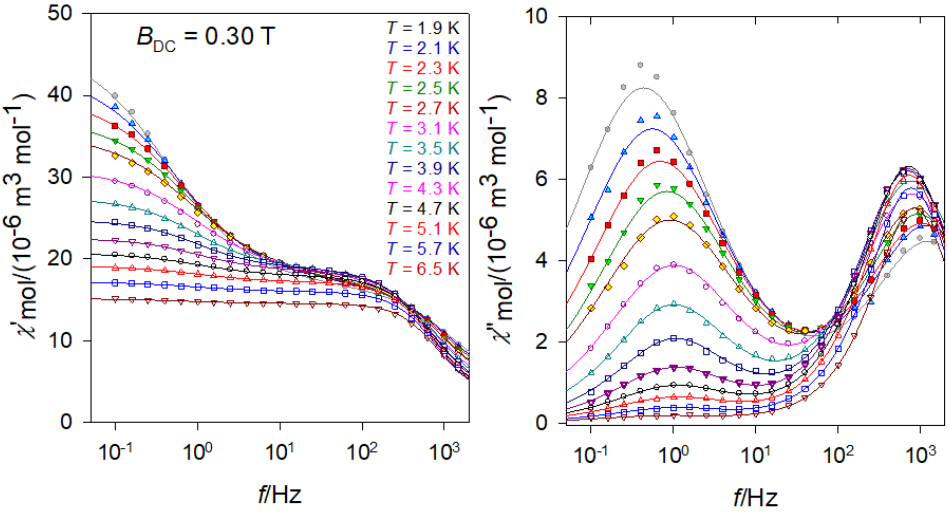


Figure 5.3.2.7 AC magnetic data for **14**. Solid lines – fitted by the extended two-set Debye model.

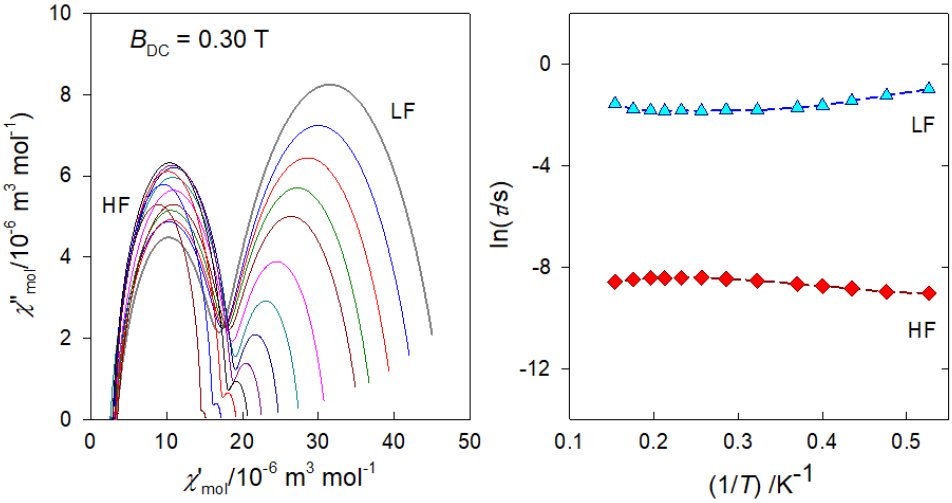


Figure 5.3.2.8 Argand diagram (left) and the Arrhenius-like plot (right) for **14**.

The geometry and the electron density of the coordination sites has been proved to exert a very important influence on the SMM behaviour of lanthanide ions. There are few studies of the influence of ions and since the number of chlorido derivatives is smaller than for instance, nitrato, the studies reported about the influence of the chlorido ligands in the SMM behaviour are very rare and it may require more research.

All three of our compounds, including the Gd(III) one, with three $Cl^-$ ligands and under applied external field, show slow relaxation. From Fig. 5.3.2.9, it can be seen that the three coordinated chlorido atoms in our compounds **13**–**15** are in what can be called a *fac*-configuration – that is, located at the vertices of one triangular face of the coordination polyhedron, while the previously mentioned chloride compounds present a more symmetrical distribution. We may propose that this configuration has to affect the electron distribution in the coordination sphere and support the SMM behaviour, even rare for Gd(III) complexes.

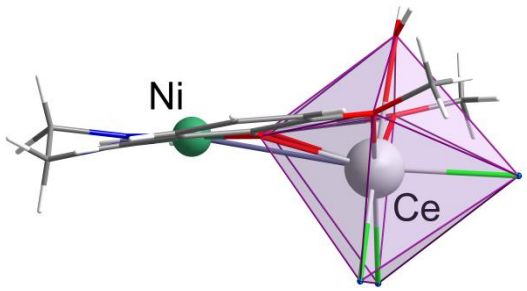


Figure 5.3.2.9 Molecular drawing of **13** showing the "*fac*" disposition of the three chlorido ligands.

## 5.4 Benzoic acid as O-donor ligand – conserving the oxidation state of Co(II)

Research into the magnetism of Co(II) complexes has yielded a number of unexpected results in recent times. Generally speaking, these systems possess a very high magnetic anisotropy that grows in the series of tetra-, penta- and hexacoordinate complexes [Craig & Murrie, 2015; Gómez-Coca *et al.*, 2015; Frost *et al*., 2016]. Due to the fact that we were not able to conserve the oxidation state +II of cobalt complexes using our selected Schiff base ligand we tried a different approach, namely using a ligand which is strictly an O-donor – benzoic acid. The trihydrate of cobalt(II) benzoate (**21**) in single crystal form was prepared by the direct reaction of cobalt(II) carbonate with benzoic acid in boiling water followed by crystallization. We note that several alternatives of cobalt(II) benzoate were prepared using different synthetic and crystallization conditions, namely two different polymorphs of anhydrous form [Sisqueira *et al.*, 2007; Spohn & Strähle, 1988; Gavrilenko *et al.*, 2005], dihydrate [Ephraim & Pfister, 1925] and tetrahydrate form [Ephraim & Pfister, 1925; Balarew *et al.*, 1985].

The resulting single crystals of **21** were characterized chemically and spectroscopically. The crystal structure of **21** is ionic, composed of positively charged $[Co(Bz)(H_2O)_2]_n^{n+}$ chains, benzoate anions and stoichiometrically one solvate water molecule (Fig. 5.4.1). The same type of crystal structure was reported for the isostructural Ni(II) analogue [Vráblová *et al.*, 2016] and for the similar Cu(II) complex which, however, crystallizes in a different space group [Koizumi *et al.*, 1963]. The chains in **21** are formed by Co(II) atoms triply bridged by two $\mu_2$-aqua ligands and one *syn–syn* benzoato bridge. Due to the triple bridging, neighbouring Co(II) atoms are relatively close to each other, with a Co···Co distance of 3.1159(2) Å; this value is longer than the corresponding Ni···Ni separation of 3.0671(1) Å in the isostructural nickel complex [Vráblová *et al.*, 2016]. Somewhat longer Co···Co distances were found in the monoclinic (3.145(1) Å) and orthorhombic (3.1657(4) and 3.1957(4) Å) forms of anhydrous cobalt(II) benzoate [Spohn & Strähle, 1988; Gavrilenko *et al.*, 2005].

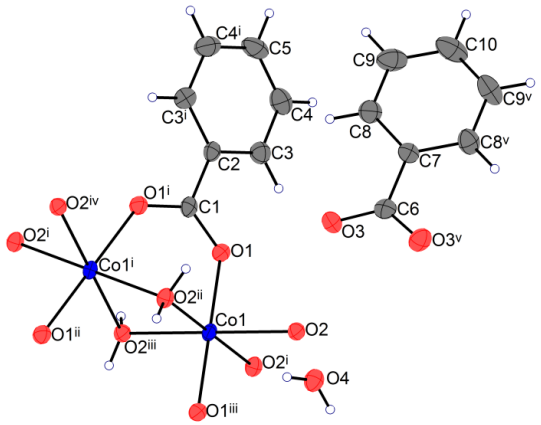


Figure 5.4.1 One segment of the structure of **21** displaying the coordination mode of two triply bridged Co(II) atoms and benzoate anions along with the atom numbering scheme. Displacement ellipsoids are drawn at the 50% probability level. Symmetry codes: i: 0.5 − *x*, *y*, − *z*; ii: 0.5 + *x*, 1 − *y*, *z*; iii: 1 − *x*, 1 − *y*, − *z*; iv: 1.5 − *x*, *y*, − *z*; v: 1 + *x*, *y*, *z*; vi: 0.5 − *x*, *y*, 1 − *z*.

Alternatively, the chains in **21** can be viewed as formed of {$CoO_6$} octahedra with common edges; neighbouring octahedra are canted (Fig. 5.4.2) with an angle of 26.27° between the $O_{ax}$–Co–$O_{ax}$ vectors in the adjacent octahedra. In the hydrate complex **21** the central Co(II) atom occupies a special position (centre of inversion) and is hexacoordinated [$O_2$(benzoate)$O_4$(aqua) donor set]. Comparison of the axial Co–O bond of 1.9775(16) Å (twice) with the mean equatorial Co–O bond of 2.158(19) Å (Tab. 5.4.1) shows that the coordination polyhedron can be viewed as a tetragonally compressed octahedron, with the observed compression of the octahedron expressed by the ratio $\kappa = (Co–O)_{ax}/(Co–O)_{eq} = 0.92$. The neighbouring chains in **21** are interconnected, with the participation of solvate water molecules (O4 atoms) and benzoate anions, by rather strong hydrogen bonds of the O–H···O type with a mean O···O distance of 2.66(3) Å (Fig. 5.4.3, Tab. 5.4.2), forming supramolecular layers.

Table 5.4.1 Selected geometric parameters [Å, °] for **21**.

| | | | |
|---|---|---|---|
| Co1–O1 | 1.9775 (16) | O2–Co1–$O2^{i}$ | 83.83 (7) |
| Co1–O2 | 2.1418 (18) | $O2^{i}$–Co1–$O2^{iii}$ | 96.17 (7) |
| Co1–$O2^{i}$ | 2.1745 (18) | O1–Co1–$O1^{iii}$ | 180 |
| Co1–$Co1^{iv}$ | 3.1159 (2) | Co1–$O2^{ii}$–$Co1^{iv}$ | 92.42 (7) |
| C1–O1 | 1.271 (2) | O1–C1–$O1^{i}$ | 124.5 (3) |
| C6–O3 | 1.265 (2) | O3–C6–$O3^{vi}$ | 124.2 (3) |

Symmetry codes: i: 0.5 − *x*, *y*, − *z*; ii: 0.5 + *x*, 1 − *y*, *z*; iii: 1 − *x*, 1 − *y*, − *z*; iv: 1.5 − *x*, *y*, − *z*; v: 1 + *x*, *y*, *z*; vi: 0.5 − *x*, *y*, 1 − *z*.

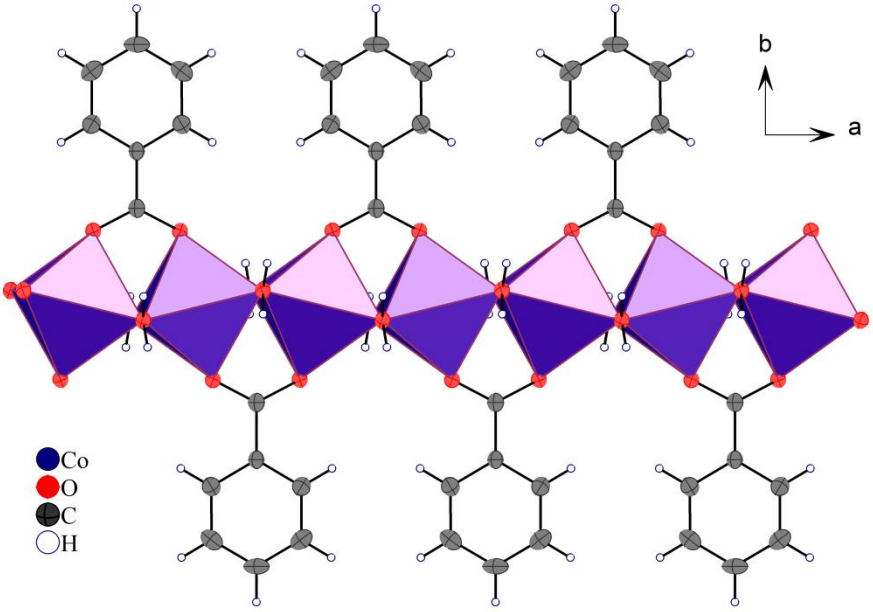


Figure 5.4.2 View of the positively charged $[CoBz(H_2O)_2]_n^{n+}$ chain running along the *a* axis with delineated polyhedra $\{CoO_6\}$.

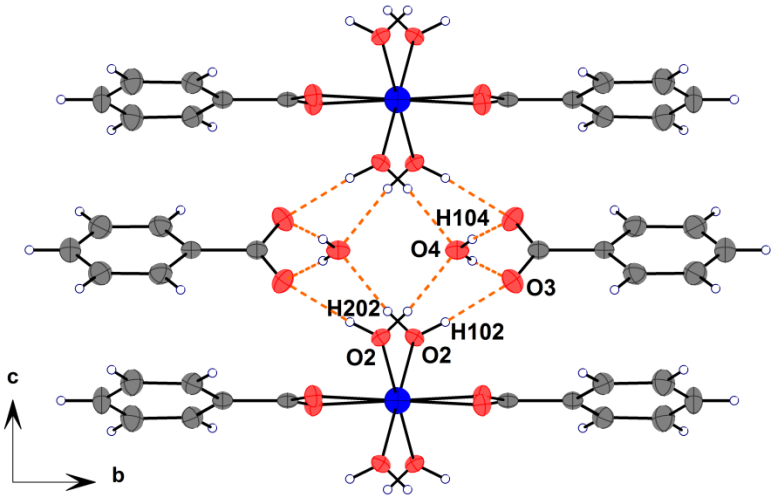


Figure 5.4.3 Hydrogen bonding system in **21**. Hydrogen bonds are drawn as orange dashed lines. The *bc* plane is pictured.

Table 5.4.2 Possible hydrogen bonds [Å, °] for **21**.

| **D–H···A** | **D–H [Å]** | **H···A [Å]** | **D···A [Å]** | **D–H···A [°]** |
|---|---|---|---|---|
| O2–H2A···O3 | 0.85 (3) | 1.79 (3) | 2.630 (2) | 170 (3) |
| O2–H2B···O4 | 0.77 (3) | 1.93 (3) | 2.679 (2) | 163 (3) |
| O4–H4A···O3$^{vii}$ | 0.85 (3) | 1.84 (3) | 2.681 (2) | 175 (3) |

Symmetry code: vii: *x* – 0.5, -*y* + 1, *z*.

The identity and phase purity of the bulk sample was checked by powder X-ray diffraction. The results of powder diffraction data were compared with the data obtained from single-crystal X-ray diffraction analysis applying LeBail refinement and using the program Jana2006 [Le Bail *et al.*, 1988; Le Bail, 2005; Petříček *et al.*, 2014].

For the refinement, the Pseudo-Voigt peak-shape model was used. The Gaussian parameters U, V and P were freely refined while the influence of the monochromator (W) was not refined in the calculations. Particle and strain broadening was fitted by using both, *X* and *Y* parameters of the Lorentzian part of the fitting peak-shape function. The asymmetry of peaks was refined using the Bérar-Baldinozzi correction method with 4 terms, only the first of them freely refined. Background was corrected using Legendre polynomials (11 terms). The refinement is shown in Fig. 5.4.4 and the input and refined unit cell parameters and values of *R(p)*, *R(wp)* and GooF for the refinement of all three samples are listed in the Tab. 5.4.3.

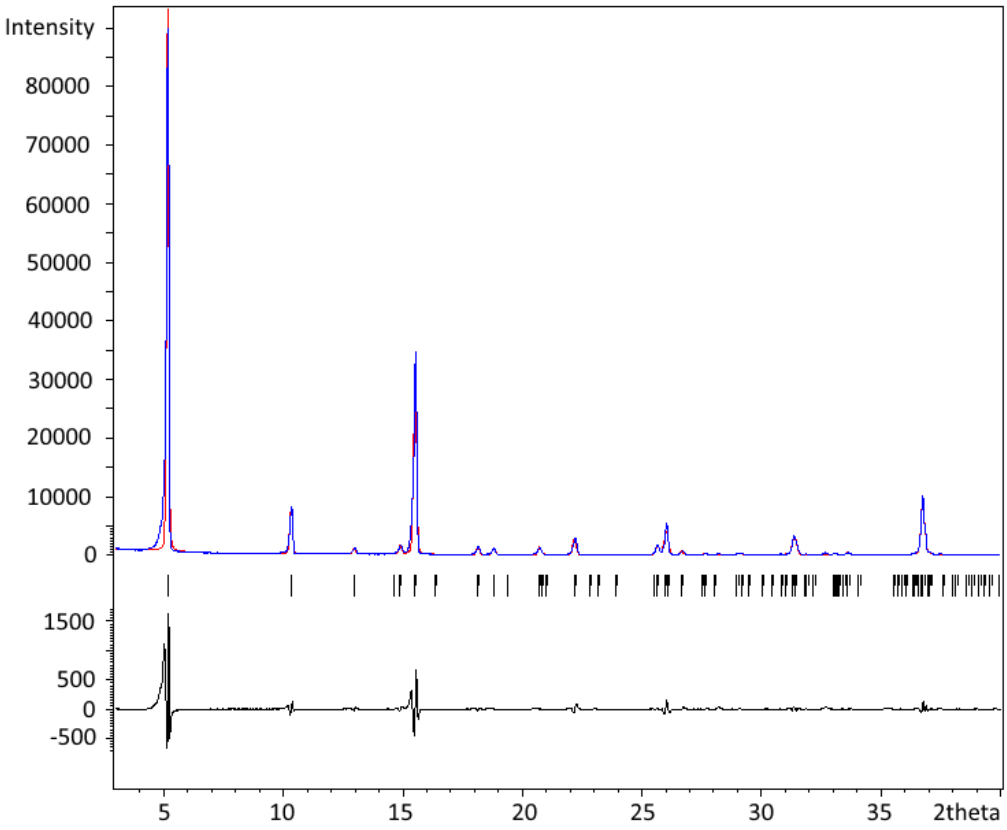


Figure 5.4.4 Results of Le Bail refinement of the powder diffraction pattern of **21**. Red line represents the refined pattern; blue line represents measured data; black line represents the difference.

Table 5.4.3 The input and refined unit cell parameters and values of *R(p), R(wp)* and *GooF* from the LeBail analysis for **21**.

| | **Input Data** | **Refined Data** |
|---|---|---|
| ***a* [Å]** | 6.2299 (4) | 6.202 (2) |
| ***b* [Å]** | 34.115 (3) | 34.287 (3) |
| ***c* [Å]** | 6.9101 (4) | 7.0189 (10) |
| ***β* [°]** | 95.689 (7) | 96.71 (3) |
| ***R(p)*** | | 0.1929 |
| ***R(wp)*** | | 0.2821 |
| ***Goof*** | | 8.74 |

### 5.4.1 Magnetic properties of 21

Based on the DC measurements, the effective magnetic moment increases from its room-temperature value of $\mu_{eff}$ = 5.6$\mu_B$ to its maximum $\mu_{eff}$ = 15.9$\mu_B$ at $T$ = 6.5 K; then it drops rapidly to a value of $\mu_{eff}$ = 8.0$\mu_B$ at $T$ = 1.9 K (Fig. 5.4.1.1). The molar magnetic susceptibility reaches a maximum on cooling and below 3.4 K it stays constant. These data indicate a transition of the paramagnetic phase with exchange interactions of a ferromagnetic nature to the antiferromagnetic phase at the Néel temperature $T_N$ = 5.5 K. The position of this critical temperature slightly depends on the applied DC magnetic field ($B_{DC}$ = 0.01 or 0.1 T). The higher temperature tail above the Néel temperature is unaffected by the magnetic field (Fig. 5.4.1.1b) and c).

The frequency dependence of the AC susceptibility components is presented in Fig. 5.4.1.2. The data show two maxima in the $\chi''$ vs. $f$ curve, indicating two relaxation channels. The onset of the low-frequency (LF) mode is well visible in the range $T$ = 1.9 – 3.3 K. Above 3.9 K the out-of-phase susceptibility is suppressed and then the sample becomes a paramagnet. The high-frequency (HF) branch possesses its maximum between 1 and 1000 Hz and it continues above 1500 Hz. Both components of the AC susceptibility have been fitted simultaneously and a two-set Debye model was applied in reconstructing the AC susceptibility data. The LF branch at $\chi''$ starts growing below 1 Hz and its maximum lies outside the limits of the measurements −0.1 Hz. Therefore the relaxation time is $\tau$(LF) > 1.6 s for a set of low temperatures irrespective of the data fitting (this indicates that $\tau_{LF}$(2.1 K) = 14 s). The out-of-phase susceptibility component

for $B_{DC}$ = 0.1 T rises to its maximum at $T$ = 4.1 K and then it attenuates rapidly on further heating. At $T_N$ > 4.7 K it is almost zero because of the paramagnetic phase.

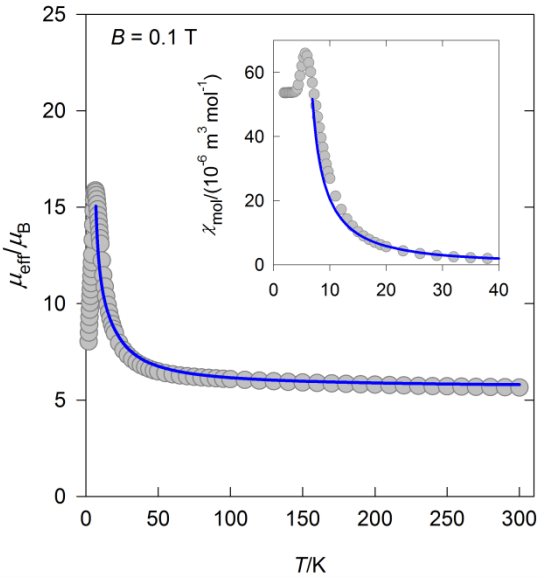


a)

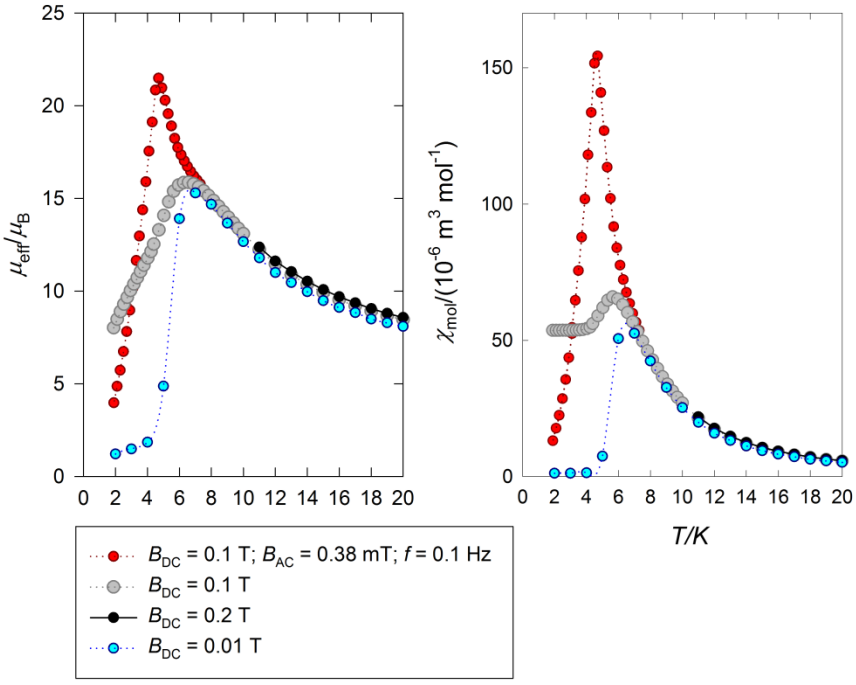


b) c)

Figure 5.4.1.1 DC magnetic data of **21**. a) Effective magnetic moment (inset: low temperature susceptibility data); b, c) effective magnetic moment and susceptibility data taken at different fields.

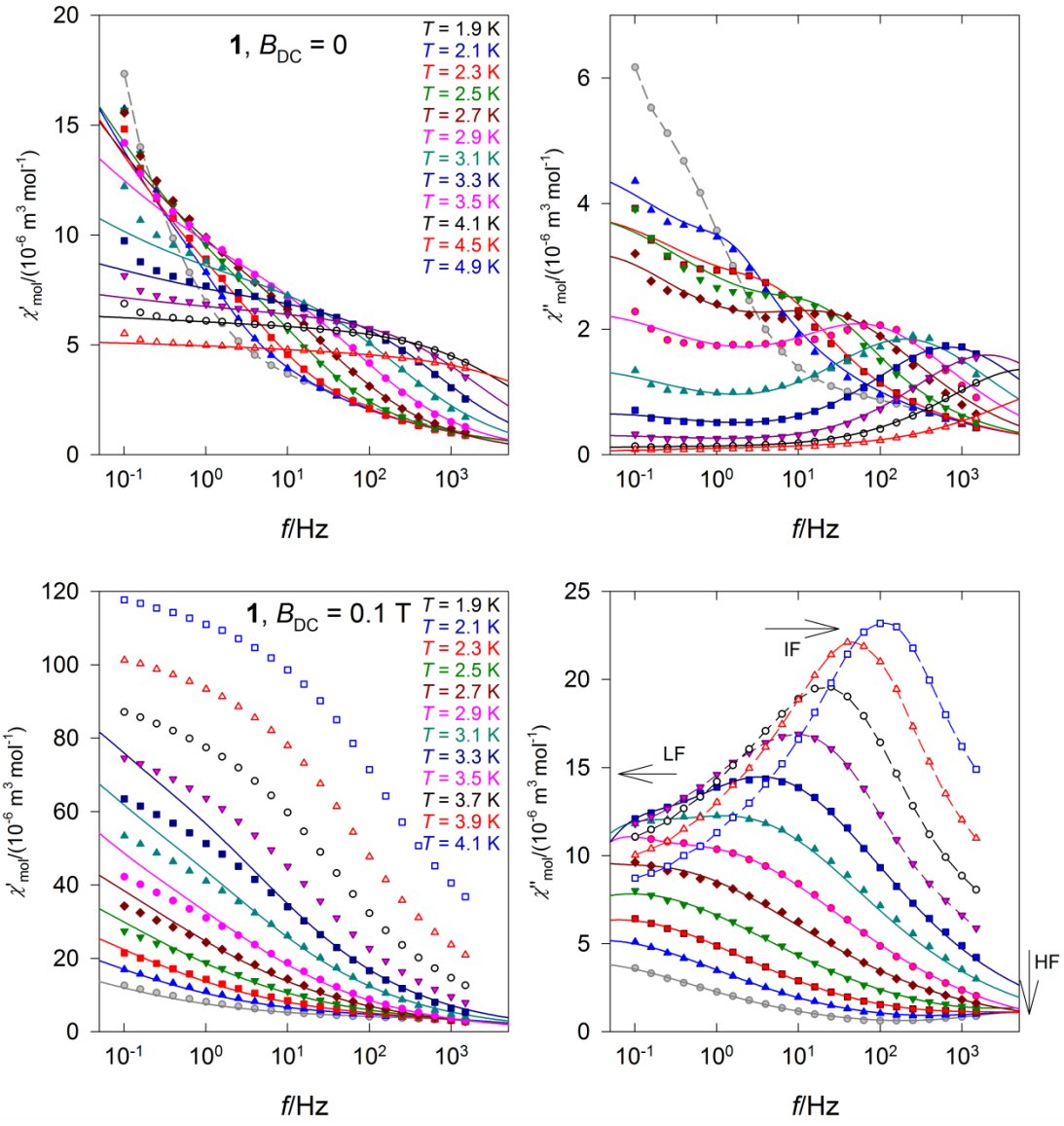


Figure 5.4.1.2 Frequency dependence of the AC susceptibility components for **21**. Full lines – calculated interpolation/extrapolation and dashed – visual guide.

A plot of the out-of-phase versus the in-phase component of the AC susceptibility (Fig. 5.4.1.3, left) is depicted on an Argand diagram consisting of two overlapping arcs. The relaxation times derived from the data fitting are used for constructing the Arrhenius-like plot (Fig. 5.4.1.3, right). As far as the HF branch is concerned, two relaxation regimes operate. The high-temperature one was analysed in terms of the Arrhenius equation $\tau = \tau_0 \exp(U/k_BT)$ where the barrier to spin reversal $U$ and the extrapolated relaxation time $\tau_0$ appear. The linear fit using three higher-temperature points gave $U/k_B$ = 81.3 K and $\tau_0 = 6.6 \times 10^{-15}$ s. The low-temperature regime is dominated by the Raman process for which the relaxation time follows a power-law equation $\tau^{-1} = CT^n$ or $\ln \tau = -\ln C - n \ln T$. The linear regression gave $C$ =

$1.5 \times 10^{-3}$ $s^{-1}$ $K^{-n}$ and $n$ = 12.1. The full data set was fitted with a joint relaxation equation $\tau^{-1} = \tau_0 - 1 \exp(-U/k_BT) + CT^n$ which gave $U/k_B$ = 88.7 K, $\tau_0 = 1.2 \times 10^{-15}$ s, and $C = 1.4 \times 10^{-3}$ $s^{-1}$ $K^{-12}$ for $n$ = 12. These data were used for reconstructing the interpolation and extrapolation line in the curved Arrhenius-like plot.

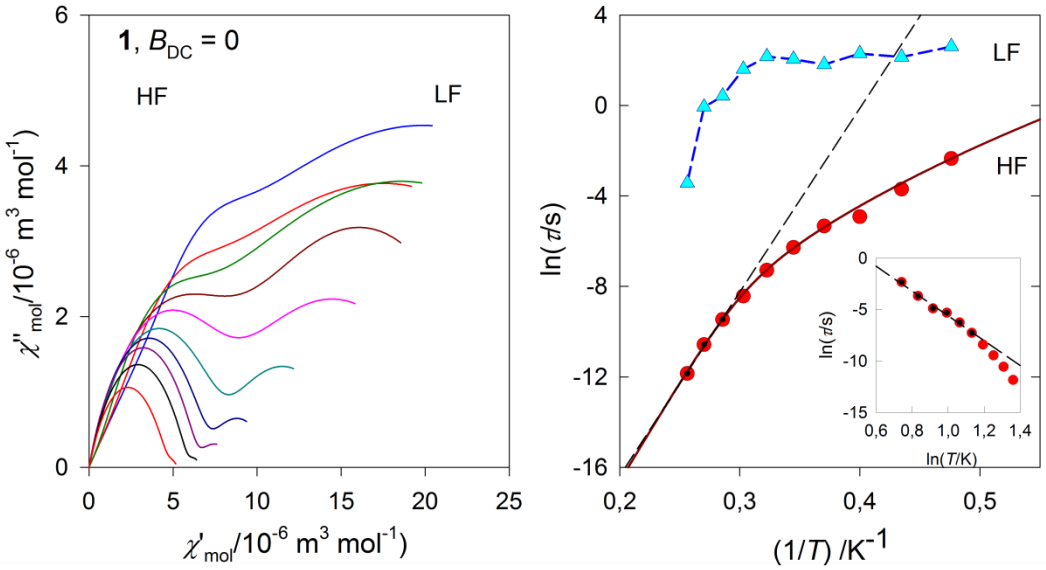


Figure 5.4.1.3 Argand diagram – left, and the Arrhenius-like plot – right for **21** at $B_{DC}$ = 0. Dashed straight lines – fit for a limited data set. Non-linear curve – a fit to the full data set.

# 6 Conclusions

In conclusion, a series of novel Ni(II) and Co(II) compounds as well as bimetallic 3*d*-4*f* complexes using selected N,O- and O-donor ligands were prepared and chemically, spectroscopically and crystallographically studied. In the final phase, a magnetic study of selected complexes was carried out.

Considering the aims and all the achieved results of the present thesis, it can be concluded:

1. Theoretical aspects of single-molecule magnetism were described with respect to transition metals and lanthanides. Special emphasis was placed on Ni(II) and Co(II)/Co(III) as 3*d* transition metals and Ce(III), Gd(III) and Dy(III) among the lanthanides. The coordination chemistry of selected transition metals and lanthanides was introduced, too. The last part of the theoretical part of the thesis is dedicated to the characterization of the selected ligands and description of the results of a literature survey of known complexes based on the selected ligands.
2. Effort in the laboratory with full attention to details along with literature searches led to the design of optimal synthetic strategies for the preparation of the series of Tr(II)-Ln(III) heterodinuclear complexes. A self-assembly step-wise approach yielded several precursors and final products, which were isolated in crystalline form, purified and characterized. There were 21 compounds prepared, 18 of them are metal complexes, 17 of them are newly prepared. Among them, 9 were heteronuclear.
3. X-ray single-crystal structure analysis was used for the crystallographic study of 3 organic coumpounds and 18 complexes (3 based on Ni(II), 2 based on Co(II), 4 based on Co(III) and 9 Ni-Ln complexes). The results of structure analysis have shown that 8 complexes exhibit molecular mononuclear structures, 9 molecular heterobimetallic and 1 1D ionic structure. Using structure analysis, the phenomena of solvatomorphism, polymorphism, isomorphism and isostructurality were identified. In addition, in the case of two solids peculiar temperature dependent structural changes were identified and analysed in detail. These processes in the solid state made it possible to elucidate the crystal structures of complexes not accessible by solution methods. This allowed us to

determine the crystal structure of compound/s which were not easily preparable by solution methods.

4. 4 metal complexes were chosen for magnetic studies, three Ni-Ln bimetallic compounds and one of cobalt(II) benzoate trihydrate. All four complexes displayed field induced slow magnetic relaxation. Outstanding findings came with cerium(III) and gadolinium(III) samples as these two metal ions are not considered as "typical" SMM ions as is dysprosium(III). Especially, a Ni-Gd complex with a diamagnetic Ni(II) ion and the usually magnetically isotropic Gd(III) ion brought new insight into the theory of single molecule magnetism.
5. The experimental results obtained were published in international scientific journals and presented at several scientific conferences as lectures and posters.

# 7 Resumé v slovenskom jazyku

## 7.1 Úvod

V posledných troch desaťročiach výskum v oblasti anorganickej chémie venoval významnú pozornosť prechodným kovom prvého prechodového radu, ako napríklad Mn(III), Fe(III), Fe(II), Co(II) a Ni(II), z hľadiska molekulového magnetizmu. Najintenzívnejšia pozornosť sa bezpochyby venuje tzv. jednomolekulovým magnetom (SMM). Základnou vlastnosťou SMM je to, že pri ich magnetizácii vonkajším magnetickým poľom sú, po vypnutí tohto poľa, schopné túto magnetizáciu zachovať určitý čas (pri určitej teplote). Táto magnetická hysterézia sa nazýva pomalá magnetická relaxácia. Pretože táto relaxácia má čisto molekulový pôvod, pozorovaný jav sa nazýva jednomolekulový magnetizmus. Takéto materiály môžu perspektívne nájsť uplatnenie v spinových elektronických zariadeniach na uchovávanie informácií s vysokou hustotou.

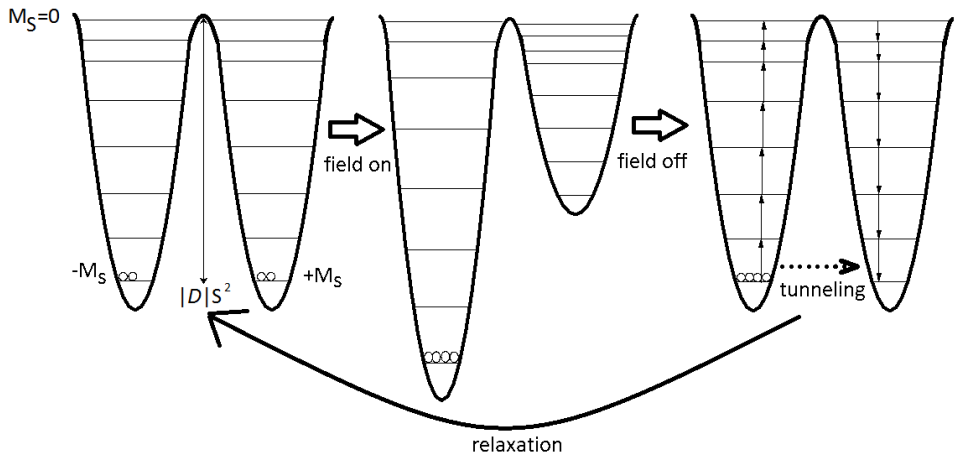


Schéma 7.1.1 Dvojhladinový diagram znázorňujúci proces magnetizácie a relaxácie v SMM.

Pomalú magnetickú relaxáciu možno opísať pomocou jednoduchého diagramu (schéma 7.1.1). Všetky energetické hladiny $M_S$ sú lokalizované v dvoch rovnakých základných stavoch, $-M_S$ vľavo, $+M_S$ vpravo na diagrame. Ak nie je aplikované žiadne vonkajšie pole, všetky energetické úrovne $\pm M_S$ sú degenerované páry (s výnimkou $M_S$ = 0) a oba základné stavy sú rovnako obsadené. Vo vonkajšom magnetickom poli rovnobežnom so smerom magnetizácie sa hladiny $-M_S$ stabilizujú na úkor hladín $+M_S$ (poznámka: aplikované pole je rovnobežné s osou z, hladiny $+M_S$ zodpovedajú projekcii magnetizácie antiparalelne s poľom a hladiny $-M_S$ zodpovedajú magnetizácii

rovnobežnej s aplikovaným vonkajším poľom). Po odstránení vonkajšieho poľa sa systém vráti do rovnovážneho stavu.

Veľkosť efektívnej energetickej bariéry ($U_{eff}$) medzi oboma stavmi je ovplyvnená dvoma parametrami, a to celkovým spinom základného stavu ($S$) a parametrom magnetickej anizotropie ($D$). Jednoducho povedané, čím väčšia je energetická bariéra $U_{eff}$ medzi hladinami základných stavov s opačnými spinmi, tým dlhší relaxačný čas bude pozorovaný. Vo všeobecnosti je pre SMMs vyžadovaná vysoká hodnota celkového spinu v kombinácii so silnou magnetickou anizotropiou [Neese & Pantazis, 2011]. Pre SMMs na báze prechodných kovov sú tieto dva parametre navzájom nepriamo úmerné, čo bráni významnému zlepšeniu vlastností SMM [Ahmed a kol., 2014]. Vzhľadom na to sa, s cieľom zvýšiť hodnotu magnetickej anizotropie, použila kombinácia lantanoidov a iónov prechodného kovu.

Nedávna štúdia komplexov 3*d*-4*f* s diamagnetickými 3*d* kovovými iónmi, ako sú zinok(II) alebo kobalt(III), poukázala na zvýšenie bariéry $U_{eff}$ v porovnaní s ich mononukleárnymi analógmi iba na báze lantanoidov [Fondo a kol., 2017]. Predpokladá sa, že prítomnosť diamagnetického 3*d* katiónu v blízkosti centrálneho atómu lantanoidu, pričom obidva centrálne atómy zdieľajú spoločný mostíkový atóm kyslíka, indukuje veľkú polarizáciu náboja na premosťujúcom atóme kyslíka, čo následne vedie k zvýšeniu energetickej bariéry $U_{eff}$. Toto pozorovanie viedlo k novej stratégii prípravy 3*d*-4*f* komplexov s diamagnetickým 3*d* iónom [Langley a kol., 2012; Langley a kol., 2013; Upadhyay a kol., 2014; Sun a kol., 2016; Upadhyay a kol., 2017].

Rastúci záujem o heterometalické komplexy v rôznych oblastiach viedol k príprave nových ligandov komorového typu schopných koordinovať požadovaný počet a druh centrálnych atómov. „Self-assembly“ syntézy, pri ktorých sa pracuje s prekurzormi ako stavebnými blokmi, sú užitočným nástrojom na získanie požadovaných produktov, najmä ak chceme dosiahnuť komplex so špeciálnymi fyzikálnymi alebo chemickými vlastnosťami. Kontrola náboja, nuklearity alebo rozmernosti konečných produktov môže byť kľúčovým faktorom úspechu cielenej syntézy.

Schiffove bázy sa často používajú ako ligandy na koordináciu prechodných kovov a lantanoidov kvôli ich multidonorovým vlastnostiam a následnej univerzálnosti [Andruh, 2015]. Pripravujú sa organickou kondenzačnou reakciou aldehydu a amínu. Konkrétne Schiffove bázy salenového typu, pripravené zo salicylaldehydu a

akéhokoľvek diamínu v molárnom pomere 2 : 1, sa často používajú ako ligandy ponúkajúce dutinu $\{N_2O_2\}$ ideálnej geometrie na chelatáciu 3*d* iónov [Khandar a kol., 2006]. Modifikácia týchto ligandov pridaním metoxy (alebo etoxy) substituenta na salicylaldehyd do *orto* polohy rozširuje ich chelatačnú kapacitu o ďalšiu susednú dutinu s donorovým setom $\{O_4\}$. Vnútorná $\{N_2O_2\}$ dutina je schopná koordinácie 3*d* iónu, zatiaľ čo vonkajšie a väčšie koordinačné miesto $\{O_4\}$ môže viazať 4*f* ión [Andruh a kol., 2009] (schéma 7.1.2.). Okrem toho, špecifická chemická povaha iónov 3*d* a 4*f* iónov uľahčuje selektivitu koordinačných miest ligandu [Liu a kol., 2015]. Podľa teórie tvrdých a mäkkých kyselín a zásad (HSAB) [Pearson, 1963] majú ióny 3*d* a 4*f* kovov prioritu koordinácie ligandov s rôznymi donorovými atómami, ako sú dusík a kyslík.

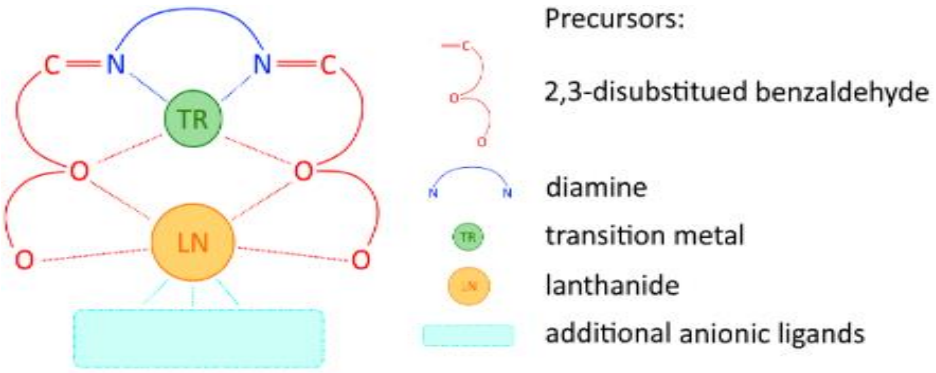


Schéma 7.1.2 „Self-assembly" koncept využitia prekurzorov ako stavebných blokov na vytvorenie všeobecného heterodinukleárneho 3*d*-4*f* komplexu s ligandom Schiffovej bázy salenového typu.

## 7.2 Ciele dizertačnej práce

Hlavným cieľom tejto dizertačnej práce je pripraviť a následne študovať rad nových zlúčenín Ni(II), Co(II) a lantanoidov, ako aj ich 3*d*-4*f* bimetalických komplexov pomocou vhodných N, O- a / alebo O-donorových ligandov. Medzi ciele patrí aj návrh a následné zlepšovanie syntetických postupov vedúcich k príprave požadovaných produktov, ktoré sa budú charakterizovať chemickými, spektroskopickými a kryštalografickými metódami, ako aj realizovať štúdium magnetických vlastností vybraných komplexov. Na dosiahnutie tohto celkového cieľa práce boli stanovené nasledovné čiastkové ciele:

1. Rešerš aktuálneho stavu problematiky sa uskutoční pomocou aktuálnych bibliografických a kryštalografických databáz. Prehľad bude zameraný na

prípravu, kryštálovú štruktúru a vlastnosti známych komplexov 3*d* prvkov Ni(II), Co(II), 4*f* prvkov Gd(III), Ce(III) a Dy(III), ako aj na ich bimetalické kombinácie 3*d*-4*f*. Pozornosť sa sústredí najmä na komplexy obsahujúce ligandy na báze Schiffových zásad a karboxyláto ligandy.

2. Podľa predchádzajúceho teoretického štúdia sa navrhnú a uskutočnia syntetické experimenty vrátane vlastnej prípravy ligandov s cieľom pripraviť a izolovať nové 3*d*, 4*f* a 3*d*-4*f* zlúčeniny na báze horeuvedených centrálnych atómov a ligandov. Pozornosť sa sústredí na variabilitu koordinačnej sféry centrálnych atómov, topológiu a štruktúrnu dimenzionalitu výsledných produktov, ktoré by viedli k rôznorodosti najmä magnetických vlastností výsledných zlúčenín. Preferovaná je príprava produktov v podobe monokryštálov, ktorá umožní ich následnú kompletnú štruktúrnu charakterizáciu.
3. Predpokladá sa príprava a izolácia veľkého počtu nových zlúčenín. Pripravené látky sa budú charakterizovať najmä chemicky (elementárna analýza), spektroskopicky (IČ, UV-VIS) a ich kryštálové a molekulové štruktúry sa určia pomocou monokryštálovej röntgenovej štruktúrnej analýzy. V prípade potreby sa na charakterizáciu použijú aj ďalšie metódy ako napr. rtg. prášková difraktometria alebo termická analýza, prípadne ďalšie metódy.
4. V prípade vybraných zlúčenín sa budú študovať ich magnetické vlastnosti. Pozorované magnetické vlastnosti budú korelované so známymi kryštálovými štruktúrami študovaných komplexov.
5. Získané experimentálne výsledky sa budú prezentovať na vedeckých podujatiach formou posterov alebo prednášok a publikovať v medzinárodných vedeckých časopisoch.

## 7.3 Výsledky a diskusia

### 7.3.1 Návrh syntetických postupov

„Self-assembly“ metóda prípravy cieľových bimetalických komplexov typu 3*d*-4*f* bola navrhnutá s ohľadom na všeobecné reakčné schémy opísané Costesom a kol. [Costes a kol., 1997]; pričom tieto reakčné schémy boli modifikované aj poznatkami uvedenými v práci Ghoseho [Ghose, 1984]. Prvým krokom cielenej syntézy je príprava a izolácia Schiffovej bázy ako ligandu ($H_2L$). Druhým krokom je príprava prekurzora – komplexu 3*d* kovu so Schiffovou bázou $L^{2-}$ zloženia {Tr-*L*}. Izolácia tohto prekurzora

môže zabrániť tvorbe nežiaducich vedľajších produktov, ktoré vznikajú pri rozklade ligandu v kyslom prostredí. Syntéza samotného dvojjadrového komplexu {Tr-Ln-*L*} je tretím a posledným krokom syntetického postupu.

Ligand $H_2$(*o-van-en*) typu Schiffovej zásady (**1**) sa pripravil v etanole za podmienok refluxu reakciou etyléndiamínu a *o*-vanilínu v molárnom pomere 1: 2. Produkt **1** sa pripravil v mikrokryštalickej forme a jeho identifikácia a čistota bola potvrdená rôznymi technikami, vrátane $^1$H-NMR, $^{13}$C-NMR, IČ, UV-Vis spektroskopie a elementárnej analýzy. Ihlicovité žlté monokryštály **1** sa získali pomalým odparovaním matečného lúhu po niekoľkých hodinách a boli charakterizované röntgenovou štruktúrnou analýzou. Podotýkame, že kryštálové štruktúry $H_2$(*o-van-en*) boli publikované Cunninghamom a kol. [2004] (*cis* izomér) a Correiom a kol. [2005] (*trans* izomér); nami pripravený produkt bol *cis* izomér.

### 7.3.2 Príprava a charakterizácia prekurzorov heteronukleárnych komplexov

Pri príprave prekurzora [Ni(*o-van-en*)] sa vychádzalo z uhličitanu nikelnatého. Jeho výber bol motivovaný tým, že počas reakcie sa uhličitanový anión rozloží na oxid uhličitý, ktorý sa varom z vody odstráni a tým sa zabráni vzniku kyslého prostredia, ktoré môže rozkladať ligand $H_2$(*o-van-en*). Takýmto postupom sa pripravil prekurzor v podobe mikrokryštalického produktu. S cieľom pripraviť [Ni(*o-van-en*)] v monokryštálovej podobe na štúdium jeho kryštálovej štruktúry sa mikrokryštalická vzorka rekryštalizovala z rôznych rozpúšťadiel. Z acetónu, etanolu a izopropanolu sa izolovali tri rôzne produkty vhodné na monokryštálovú rtg. analýzu, a to [Ni(*o-van-en*)]·*n*$H_2O$ (**4**), [Ni(*o-van-en*)]·$H_2O$·EtOH (**5**) a [Ni(*o-van-en*)]·$H_2O$·*i*PrOH (**6**). Výsledky ich štruktúrnej analýzy ukázali, že všetky tri látky obsahujú rovnakú neutrálnu komplexnú jednotku [Ni(*o-van-en*)], kde centrálny atóm Ni(II) sa nachádza v štvorcovo-planárnej koordinácii ligandu $(o\text{-}van\text{-}en)^{2-}$, konkrétne v menšej koordinačnej dutine {$N_2O_2$}. Druhú, väčšiu dutinu obsadzuje molekula vody, ktorá je v dutine viazaná systémom relatívne silných vodíkových väzieb typu O–H···O.

V snahe pripraviť dinukleárne $Co^{II}$-Ln komplexy sa vyskúšalo niekoľko syntetických ciest vedúcich k izolácii prekurzora [$Co^{II}$(*o-van-en*)]. Je vhodné uviesť, že komplex [$Co^{II}$(*o-van-en*)($H_2O$)], pripravený *in situ* solvotermálnou syntézou za použitia z 2-hydroxy-3-metoxybenzaldehydu, etán-1,2-diamínu a dusičnanu kobaltnatého, už bol popísaný [Jiang a kol., 2007]. Variáciou experimentálnych podmienok syntézy sme izolovali 3 rôzne produkty vrátane vyššie uvedeného jednojadrového komplexu [$Co^{II}$(*o-*

*van-en*)($H_2O$)] (**7**); v našom prípade sa tento komplex **7** izoloval v mikrokryštalickej forme priamou reakciou hydroxidu kobaltnatého so Schiffovou bázou $H_2$(*o-van-en*) za miernych podmienok v inertnej argónovej atmosfére. Suchá mikrokryštalická vzorka izolovaná z matečného lúhu je už na vzduchu stabilná a odolná voči prípadnej oxidácii; jeho identita a čistota boli potvrdené práškovou difraktometriou. Pokus o rekryštalizáciu mikrokryštalického produktu **7** z acetonitrilu pri laboratórnej teplote v prítomnosti vzduchu viedol k oxidácii Co(II) na Co(III) a tvorbe monoklinickej formy dvojjadrového komplexu [$Co^{III}_2$(*o-van-en*)$_3$]·4$CH_3CN$ (**8**). Priama reakcia Schiffovej bázy s $Co(OH)_2$ v prítomnosti vzduchu viedla k čiernemu mikrokryštalickému surovému produktu; zmena farby jasne indikovala oxidáciu Co(II) na Co(III). Keď sa výsledný surový produkt rekryštalizoval z horúceho acetonitrilu, vylúčili sa kryštály triklinickej formy dvojjadrového komplexu [$Co^{III}_2$(*o-van-en*)$_3$]·4$CH_3CN$ (**9**). V oboch polymorfných modifikáciách **8** a **9** sú oba atómy Co(III) hexakoordinované, pričom jeden (*o-van-en*)$^{2-}$ ligand vystupuje ako mostíkový ligand spájajúci dva atómy Co(III). Následne sa obe polymorfné modifikácie študovali z hľadiska medzimolekulových interakcií pomocou metódy FIM a analýzy Hirshfeldových povrchov. Analýza FIM poukázala na 4 miesta s vysokým donorovým potenciálom pre vodíkové väzby, avšak ani jedno z nich nie je obsadené vhodným akceptorom. Analýza Hirshfeldových povrchov nám graficky potvrdila, že v štruktúre oboch polymorfov sa nachádzajú iba slabé medzimolekulové interakcie medzi dvojjadrovými komplexami, resp. medzi komplexami a solvatujúcou molekulou ACN. Poznamenávame, že obidve formy pripraveného komplexu [$Co^{III}_2$(*o-van-en*)$_3$]·4$CH_3CN$ (**8**, **9**) sú mimo matečného lúhu nestabilné v dôsledku ich desolvatácie. Podľa vyššie uvedených skutočností nie je prekvapujúce, že existuje viac ako jeden spôsob usporiadania kryštálovej štruktúry tejto látky.

Podľa našej stratégie krokovej reakcie sa komplex [$Co^{II}$(*o-van-en*)($H_2O$)] (**7**) javí ako najlepší kandidát na prekurzor typu [Tr(*o-van-en*)] v poslednom kroku syntézy. V tomto poslednom kroku syntézy sa použil chlorid gadolinitý. Vykonali sa viaceré experimenty za miernych podmienok, ale ani v jednom prípade sa atóm lantanoidu nekoordinoval; počas týchto experimentov sme však izolovali a identifikovali oxidované produkty – komplexy [$Co^{III}$(*o-van-en*)($H_2O$)Cl] (**10**) a [$Co^{III}$(*o-van-en*)($H_2O$)Cl]·2$CH_3CN$ (**11**). Ich kryštálové štruktúry sú tvorené jednojadrovými komplexami; v oboch je centrálny atóm Co(III) hexakoordinovaný, pričom v axiálnych polohách sú umiestnené chlorido a akva ligandy.

### 7.3.3 Príprava a charakterizácia heteronukleárnych zlúčenín

Po úspešnej izolácii a charakterizácii prekurzora [Ni(*o*-*van*-*en*)]·$n$$H_2O$ (**4**) sa postupovalo podľa už uvedenej stratégie. Najprv sa vykonali experimenty s dusičnanom gadolinitým ako lantanoidovou soľou. Syntéza sa uskutočňovala v etanole pri podmienkach refluxu. Mikrokryštalický produkt, ktorý sa izoloval filtráciou bezprostredne po reakcii, sa rekryštalizoval z niekoľkých rozpúšťadiel alebo z ich zmesi (difúzne techniky kvapalina-kvapalina) s cieľom získať monokryštály. Monokryštály sa získali iba rekryštalizáciou z acetonitrilu, čím sa získal požadovaný 3*d*-4*f* bimetalický komplex [Ni(*o*-*van*-*en*)Gd$(NO_3)_3$]·2$CH_3CN$ (**12**), v ktorom atómy Ni(II) a Gd(III) sú premostené dvoma O-monoatómovými mostíkmi a atóm Gd(III) si dopĺňa koordinačnú sféru (k.č. = 10) tromi chelátovými nitráto ligandmi. Kryštály **12** po izolácii z matečného lúhu sú nestabilné v dôsledku desolvatácie.

V ďalších experimentoch pomocou už uvedenej „self-assembly“ metódy sa v kombinácii s prekurzorom [Ni(*o*-*van*-*en*)]·$n$$H_2O$ (**4**) použili miesto dusičnanov chloridy lantanoidov. Syntézy sa uskutočňovali pri podmienkach refluxu, pričom sa izolovali oranžové mikrokryštalické práškové produkty všeobecného zloženia [Ni(*o*-*van*-*en*)$LnCl_3(H_2O)$], pričom Ln predstavuje Ce (**13**), Gd (**14**) a Dy (**15**). Identita a čistota mikrokryštalických vzoriek bola potvrdená pomocou IČ spektroskopie, elementárnej analýzy a práškovej rtg. difrakčnej analýzy. Využitím rôznych rekryštalizačných techník boli zlúčeniny **13**, **14** a **15** pripravené aj v podobe monokryštálov. Výsledky štruktúrnej analýzy ukázali, že všetky tri komplexy sú navzájom izomorfné; kryštalizujú v monoklinickej grupe $P2_1/n$. Ich molekulová štruktúra pozostáva z neutrálnej bimetalickej dvojjadrovej komplexnej molekuly [Ni(*o*-*van*-*en*)$LnCl_3(H_2O)$], v ktorej centrálny atóm Ni(II) je štvorcovo-planárne koordinovaný donorovým setom {$N_2O_2$} pochádzajúcim z ligandu Schiffovej bázy (*o*-*van*-*en*)$^{2-}$ (Obr. 7.3.1). Koordináciu centrálneho atómu lantanoidu tvoria 4 atómy kyslíka z ligandu (*o*-*van*-*en*)$^{2-}$, jeden atóm kyslíka akva ligandu a tri chlorido ligandy. Kryštálová štruktúra zlúčenín **13**, **14** a **15** je podporená stredne silnými vodíkovými väzbami typu O-H···Cl, čím sa vytvára supramolekulová reťazová štruktúra pozdĺž osi *a*. Ďalšie slabšie vodíkové väzby typu $C_{ar}$–H···Cl a $C_{imine}$–H···Cl a π-π interakcie medzi aromatickými jadrami susedných retiazok vytvárajú supramolekulové vrstvy v *ab* rovine. Medzi supramolekulovými rovinami sa našli len slabšie medzimolekulové

kontakty typu C-H···Cl pochádzajúce z metylových a metylénových skupín ligandu (*o-van-en*)$^{2-}$.

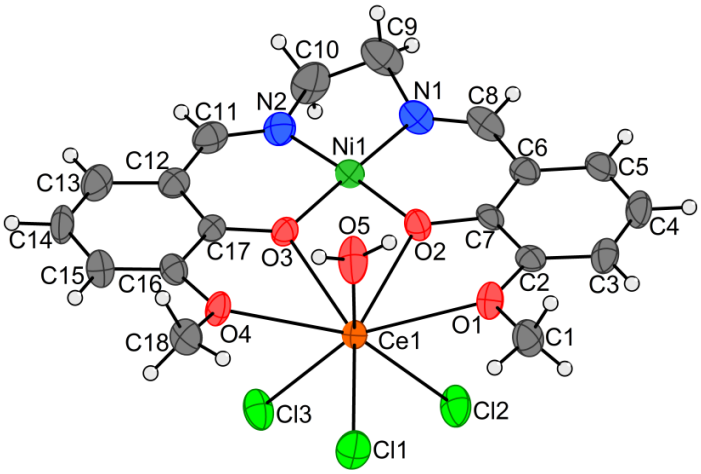


Obrázok 7.3.1 Molekulová štruktúra komplexu **13**. Teplotné elipsoidy (okrem atómov vodíka) sú vyobrazené s 50 % úrovňou pravdepodobnosti.

Rekryštalizáciou dvojjadrových komplexov [Ni(*o-van-en*)LnCl$_3$(H$_2$O)] (Ln = Ce, Dy) sa reprodukovateľne izolovali ďalšie komplexy: [Ni$_2$Ce$_2$(*o-van-en*)$_2$Cl$_6$] (**16**), [Ni(*o-van-en*)DyCl$_3$] (**17**) a [Ni(*o-van-en*)DyCl$_3$]·EtOH (**18**). Tieto boli charaketrizované obvyklými metódami a ich kryštálové štruktúry (viď nižšie) boli stanovené metódou štruktúrnej analýzy.

V rámci našich experimentov s rekryštalizáciou práškovej vzorky [Ni(*o-van-en*)CeCl$_3$(H$_2$O)] (**13**) sme uskutočnili rekryštalizáciu z etanolu v uzavretej nádobe umiestnenej v peci nastavenej na 80 °C. Monokryštálová štruktúrna analýza vytvorených červenooranžových kryštálov ukázala, že ide o nový štvorjadrový komplex [Ni$_2$Ce$_2$(*o-van-en*)$_2$Cl$_6$] (**16**). Jeho vznik sa dá vysvetliť dimerizáciou dvoch štruktúrnych jednotiek [Ni(*o-van-en*)CeCl$_3$(H$_2$O)] v dôsledku uvoľnenia akva ligandov a následným vytvorením dvoch chlorido mostíkov medzi atómami Ce(III) vzniklo jadro {CeCl$_2$Ce}), čím sa koordinačné číslo 8 atómu Ce(III) zachováva.

Rovnaký rekryštalizačný postup sa aplikoval aj na práškovej vzorke komplexu [Ni(*o-van-en*)DyCl$_3$(H$_2$O)] (**15**). Napriek predpokladanej analógii medzi atómami céru a dysprózia sa v tomto prípade dimerizácia nepozorovala, ale po dehydratácii sa vytvoril dvojjadrový dehydratovaný komplex [Ni(*o-van-en*)DyCl$_3$] (**17**). Predpokladáme, že Dy(III) s menšími iónovým polomerom ako Ce(III) [Shannon, 1976] vykazuje vyššiu stabilitu svojej koordinačnej sféry aj s nižším koordinačným číslom 7, a preto komplex **17** nemá tendenciu dimerizovať. Pozorovaná dimerizácia v zlúčenine Ce(III) môže byť

teda dôsledkom snahy väčšieho atómu Ce(III) zachovať si koordinačné číslo 8 koordináciou mostíkových chlorido ligandov. Takéto správanie v závislosti od iónových polomerov už bolo v minulosti pozorované [Kano a kol., 2003; Baisch a kol., 2004; Deacon a kol., 2002; Wong a kol., 2006; Chen a kol., 2011].

Následne sme uskutočnili experimenty rekryštalizácií pomocou difúznych techník. Difúzia etanolového roztoku [Ni(*o*-*van*-*en*)$DyCl_3(H_2O)$] (**15**) do izopropanolu pri laboratórnej teplote poskytla kryštály [Ni(*o*-*van*-*en*)$DyCl_3$]·EtOH (**18**). Molekulová štruktúra komplexu **18** obsahuje neutrálnu bimetalickú komplexnú jednotku [Ni(*o*-*van*-*en*)$DyCl_3$], v ktorej centrálny atóm Ni(II) leží vo vnútornej dutine ligandu Schiffovej bázy s donorovým setom $\{N_2O_2\}$ a centrálny atóm Dy(III) obsadzuje vonkajšiu dutinu $\{O_4\}$. Jeho koordinačný polyéder je doplnený tromi chlorido ligandami. Tento výsledok podporuje náš predchádzajúci predpoklad o stabilite centrálneho atómu Dy(III) s koordinačným číslom 7.

Pri zmene podmienok rekryštalizácie bola látka [Ni(*o*-*van*-*en*)$DyCl_3(H_2O)$] (**15**) rozpustená v zmesi etanol/izopropanol. Kryštalizáciou z tohto roztoku pri zvýšenej teplote (50 °C) sme získali červenooranžové prizmatické kryštály stereoizoméru pôvodného komplexu, konkrétne formu II komplexu [Ni(*o*-*van*-*en*)$DyCl_3(H_2O)$] (**19**). Štúdium jeho kryštálovej štruktúry ukázalo, že v komplexe **19** (forma II) oproti komplexu **15** (forma I) sú chlorido ligandy umiestnené v koordinačnom polyédri Dy(III) odlišným spôsobom; kým v **15** sú tri chlorido ligandy umiestnené na jednej ploche polyédra, v **19** sú tri chlorido ligandy umiestnené v jednej rovine rezu polyédra (Obr. 7.3.2a). Dôsledkom je, že v **19** vznikajú pomocu vodíkových väzieb typu O-H···Cl supramolekulové diméry.

Dimerizáciu [Ni(*o*-*van*-*en*)$DyCl_3(H_2O)$] (**19**) za vzniku štvorjadrového komplexu [$Ni_2Dy_2$(*o*-*van*-*en*)$_2Cl_6$] (**20**) sa podarilo dosiahnuť reakciou dehydratácie v tuhej fáze. Priebeh dehydratácie sa študoval na monokryštále **19**. Po jeho ohreve na teplotu asi 84 °C prebehla dehydratácia a kedže sa pri tom zachoval monokryštálový charakter vzorky, bolo možné stanoviť kryštálovú štruktúru **20**. Táto je tvorená dvoma štruktúrnymi jednotkami [NiDy(*o*-*van*-*en*)$Cl_3$] prepojenými dvoma mostíkovými chlorido ligandmi (Obr. 7.3.2b). Uvedený proces dehydratácie predstavuje topotaktickú reakciu typu SC-SC (Single Crystal-to-Single Crystal).

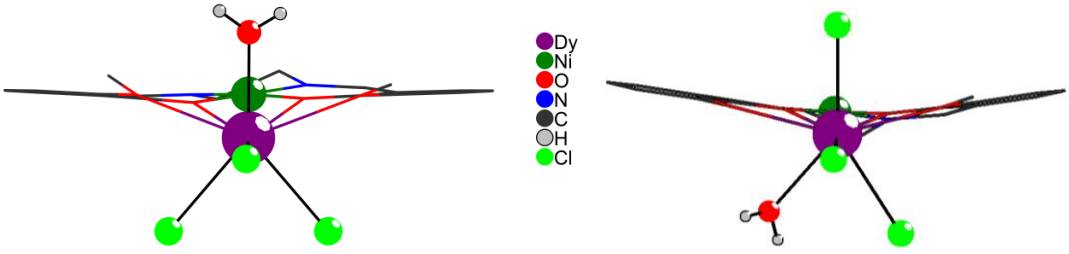


a)

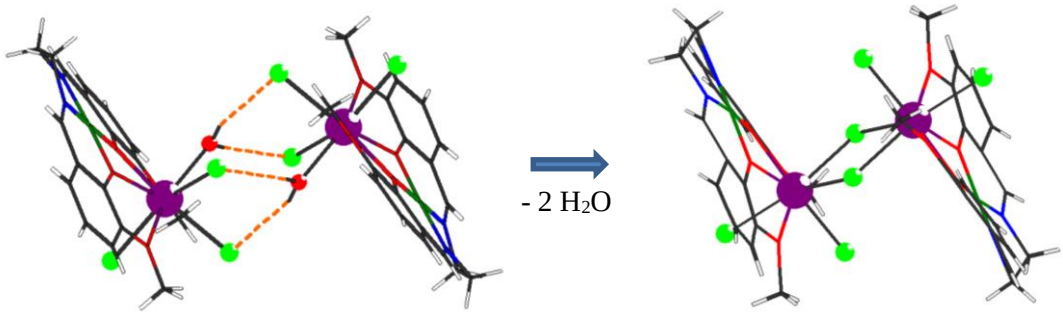


b)

Obrázok 7.3.2 a) Porovnanie izomérov **15** (vľavo) a **19** (vpravo).
b) Zmena molekulovej štruktúry počas topotaktickej dehydratácie: 2 **19** → **20** + 2 $H_2O$.

### 7.3.4 Magnetické vlastnosti série heteronuklárnych komplexov [Ni(*o-van-en*)LnCl$_3$(H$_2$O)] [Ln = Ce (13), Gd (14), Dy (15)]

Na štúdium magnetických vlastností boli vybrané dvojjadrové Ni-Ln bimetalické zlúčeniny **13**, **14**, **15** a zlúčenina Co(II) **21**. Fázová čistota študovaných vzoriek bola potvrdená röntgenovou práškovou difrakčnou analýzou. Výsledky práškových difrakčných meraní boli porovnané s difrakčnými údajmi vypočítanými z výsledkov monokryštálovej štruktúrnej analýzy **13-15** vykonanej pri izbovej teplote, pričom sa použila LeBailova metóda v programe Jana2006 [Le Bail a kol., 1988; Le Bail, 2005; Petříček a kol., 2014].

Magnetické merania sa vykonali okrem DC režimu aj v AC režime s cieľom overiť prípadné SMM chovanie študovaných látok. Samotné experimenty a vyhodnotenie boli realizované pracovnou skupinou prof. Boču z Univerzity sv. Cyrila a Metoda v Trnave.

Z výsledkov štruktúrnej analýzy Ni-Ln dvojjadrových komplexov **13**, **14** a **15** (viď vyššie) vyplýva, že atóm Ni(II) v týchto komplexoch je koordinovaný štvorcovo, teda je diamagnetický. Dôsledkom uvedeného je, že magnetické vlastnosti komplexov **13**, **14** a **15** sú určené prítomnými atómami Ln, ktoré vykazujú orbitálový aj spinový moment hybnosti. Ich základné stavy sú multiplety $^2F_{5/2}$ pre Ce(III), $^8S_{7/2}$ pre

Gd(III) a $^6H_{15/2}$ v prípade Dy(III), a ich príslušné hodnoty $g_J$ sú 6/7, 2 a 4/3. Magnetizácie v prepočte na vzorcovú jednotku sa majú saturovať pri hodnotách $M_1 = M_{mol}/(N_A\mu_B) = g_J \cdot J = 6/7 \times 5/2 = 15/7$, $2 \times 7/2 = 7$ a $4/3 \times 15/2 = 10$ pre Ce(III), Gd(III) a Dy(III). Efektívny magnetický moment, $\mu_{eff}/\mu_B = g_J[J(J + 1)]1/2$, pre jednotlivé komplexy dosahuje limitné hodnoty 2,54 $\mu_B$, 7,94 $\mu_B$, a 10,6 $\mu_B$.

Experimentálne zistené efektívne magnetické momenty jednotlivých komplexov **13, 14** a **15** pri laboratórnej teplote vykazujú hodnoty $\mu_{eff}$ = 2,36 $\mu_B$ (Ce), 7,9 $\mu_B$ (Gd) a 12,15 $\mu_B$ (Dy), pričom očakávané hodnoty sú 2,54 (Ce), 7,94 (Gd) a 10,6 $\mu_B$ (Dy). Vyššiu pozorovanú hodnotu pre **15** (Dy) je možné vysvetliť prítomnosťou nízko ležiacich excitovaných stavov susedného atómu Ni(II). Existenciu príspevku teplotne nezávislého paramagnetizmu (TIP) v dôsledku prítomného atómu Ni(II) potvrdzuje aj mierne lineárna teplotná závislosť $\mu_{eff}$ v prípade komplexu **13**.

Experimentálne hodnoty saturácie magnetizácie pri $T$ = 2,0 K a $B$ = 7 T pre jednotlivé komplexy sú $M_1$ = 1,0 (Ce), 6,6 (Gd) a 7,9 (Dy), pričom vypočítané hodnoty pre izolované ióny sú 2,1 (Ce), 7,0 (Gd) a 10,0 (Dy). Nižšia pozorovaná hodnota v prípade komplexu Ce(III) naznačuje, že v dôsledku pôsobenia kryštálového poľa je obsadený iba najnižší z troch Kramerových dubletov. Na druhej strane, výrazne nižšia pozorovaná hodnota magnetizácie v prípade komplexu Dy(III) naznačuje zníženie orbitálového príspevku buď v dôsledku asymetrie koordinačnej sféry atómu Dy(III) a / alebo vplyvu štiepenia základného multipletu kryštálového poľa v nulovom poli.

Údaje o AC susceptibilite sa získali pri amplitúde poľa $B_{AC}$ = 0,38 mT a merali sa v závislosti od vonkajšieho magnetického poľa $B_{DC}$, teploty $T$ a frekvencie $f$ oscilujúceho poľa. AC magnetické merania všetkých troch komplexov vrátane nominálne izotropného systému na báze Gd(III) (**14**) ukázali, že všetky tri komplexy **13**, **14** a **15** vykazujú poľom indukovanú pomalú magnetickú relaxáciu s dvoma alebo tromi relaxačnými kanálmi.

V prípade komplexu **13** (Ce) frekvenčná závislosť mimofázovej zložky susceptibility $\chi''$ poukazuje pri teplotách pod 4 K na existenciu dvoch relaxačných kanálov s dominantným príspevkom nízkofrekvenčnej zložky, pričom nad touto teplotou príspevok HF zložky vymizne. Relaxačný čas pri $T$ = 1,9 K a $B_{DC}$ = 0,5 T má hodnotu $\tau$(LF) = 60,3 ms, ktorý je dlhší v porovnaní s hodnotou $\tau$(LF) = 18,7 ms pri $B_{DC}$ = 0,1 T.

Existencia pomalej magnetickej relaxácie v prípade izotropného atómu Gd(III) bola prekvapujúca. Frekvenčná závislosť oboch zložiek AC susceptibility pre zlúčeninu **14** odhalila existenciu dvoch relaxačných kanálov, pričom sa zistilo, že v teplotnom intervale 1,9 až 6,5 K je relaxačný čas HF kanála teplotne iba mierne závislý. Okrem toho vysokofrekvenčný kanál HF vykazuje „zvláštne" správanie: pri ochladení relaxačný čas prechádza maximom a následne sa skracuje: $\tau$(HF) = 223 μs pri $T$ = 3,9 K v porovnaní s $\tau$(HF) = 120 μs pri $T$ = 1,9 K. Relaxačný čas pre LF proces pri $B_{DC}$ = 0.3 T a T = 1,9 K je $\tau$(LF) = 0,37 s.

Analýzou frekvenčnej závislosti fázovej a mimofázovej časti AC susceptibility vzorky **15** (Dy) sa zistila existencia troch relaxačných kanálov: nízkofrekvenčného (LF), stredofrekvenčného (IF) a vysokofrekvenčného (HF). Kým pri najnižšej meranej teplote $T$ = 1,9 K dominuje nízkofrekvenčná zložka, jej príspevok s rastúcou teplotou klesá v prospech vysokofrekvenčnej zložky. Pri najnižšej meracej teplote, $T$ = 1,9 K a pri $B_{DC}$ = 0.15 T sa identifikovali tri relaxačné časy $\tau$(LF) = 1,29 s, $\tau$(IF) = 74 ms a $\tau$(HF) = 964 μs.

Z horeuvedeného vyplýva, že všetky tri študované zlúčeniny, vrátane Gd(III) (**14**), vykazujú pomalú magnetickú relaxáciu. Vo všetkých troch zlúčeninách sú všetky tri chlorido ligandy umiestnené na jednej ploche koordinačného polyédra. Tento spôsob umiestnenia pripomína *fac*-konfiguráciu a znamená, že sú koncentrované v tej istej časti koordinačnej sféry, zatiaľ čo iné študované analogické komplexy vykazujú symetrickejšiu distribúciu chlorido ligandov. Usudzujeme, že táto konfigurácia ovplyvňuje distribúciu elektrónov na centrálnom atóme (vnáša anizotropiu do distribúcie) a podporuje SMM správanie týchto komplexov, a to zriedkavo aj pre komplex Gd(III). Ukázalo sa, že geometria a hustota elektrónov koordinačných miest majú veľmi dôležitý vplyv na SMM správanie lantanoidových iónov.

Výskum magnetizmu komplexov Co(II) v posledných časoch ukázal, že tieto systémy majú veľmi vysokú magnetickú anizotropiu, ktorá rastie v poradí tetra-, penta- a hexakoordinácie komplexov [Craig & Murrie, 2015; Gomez-Coca a kol., 2015; Frost a kol., 2016]. Z uvedeného dôvodu sa na štúdium magnetických vlastností vybral aj komplex **21** obsahujúci centrálny atóm Co(II), pričom atómy Co(II) sú navyše usporiadané do reťazca.

Merania v DC poli ukázali, že efektívny magnetický moment $\mu_{eff}$ látky **21** sa pri poklese teploty zvyšuje z hodnoty $\mu_{eff}$ = 5,6 $\mu_B$ na maximum $\mu_{eff}$ = 15,9 $\mu_B$ pri T = 6,5

K a následne potom rýchlo klesne na hodnotu $\mu_{eff}$ = 8,0 $\mu_B$ pri $T$ = 1,9 K. Tieto údaje naznačujú prechod paramagnetickej fázy s výmennými interakciami feromagnetickej povahy na antiferomagnetickú fázu pri teplote $T_N$ = 5,5 K.

Frekvenčná závislosť oboch zložiek susceptibility v AC poli poukázala na existenciu dvoch maxím v krivke $\chi''$ oproti $f$, ktorá naznačuje prítomnosť dvoch relaxačných kanálov. Nástup nízkofrekvenčného (LF) módu je dobre viditeľný v rozsahu $T$ = 1,9 - 3,3 K. Nad 3,9 K je mimofázová susceptibilita potlačená a potom sa vzorka stáva paramagnetom. LF pás začína rásť pod 1 Hz a jeho maximum leží mimo limít merania – 0,1 Hz. Relaxačný čas tak dosahuje hodnotu $\tau$(LF) > 1,6 s pri nízkych teplotách bez ohľadu na spôsob fitovania (to znamená, že $\tau_{LF}$ (2,1 K) = 14 s). Mimofázová zložka susceptibility pre $B_{DC}$ = 0,1 T stúpa na maximum pri $T$ = 4,1 K a potom sa pri ďalšom zahrievaní rýchlo zoslabuje. Pri $T_N$ > 4,7 K je takmer nulová kvôli paramagnetickej fáze.

## 7.4 Záver

Výsledky predkladanej dizertačnej práce s ohľadom na jej stanovené ciele je možné zhrnúť v nasledovaných bodoch:

1. Bola opísaná teória jednomolekulového magnetizmu s ohľadom na prechodné kovy a lantanoidy. Osobitný dôraz sa kládol na magnetické vlastnosti vybraných 3*d* prvkov Ni(II) a Co(II) / Co(III) a vybraných 4*f* prvkov Ce(III), Gd(III) a Dy(III). Na základe poznatkov získaných vlastnou rešeršou v pôvodnej literatúre a databázach bola diskutovaná aj koordinačná chémia uvedených vybraných 3*d* a 4*f* centrálnych atómov, ako aj použitých typov ligandov.
2. Na základe údajov literárnej rešerše a experimentálnych skúseností sa vypracoval návrh stratégie syntéz heterodinukleárnych komplexov Tr(II)-Ln(III). Tento tzv. „self-assembly“ syntetický postup je trojkrokový a jeho použitie viedlo k izolácií viacerých zlúčenín, ktoré boli izolované, v prípade potreby prečistené rekryštalizáciou a následne charakterizované chemickými, spektroskopickými a ďalšími metódami. Bolo pripravených 21 zlúčenín, z ktorých 18 sú komplexné zlúčeniny (17 nových) a 3 organické látky. Spomedzi 18 komplexných zlúčenín bolo 9 3*d*-4*f* heteronukleárnych. Osobitný dôraz sa kládol na prípravu monokryštálov, preto na ich prípravu sa použili rôzne difúzne techniky.

3. Pomocou metódy štruktúrnej analýzy sa študovala kryštálová štruktúra 3 organických zlúčenín, 3 zlúčenín Ni(II), 2 zlúčenín Co(II), 4 Co(III), ako aj 9 Ni-Ln komplexov. Výsledky štruktúrnej analýzy ukázali, že 8 komplexov malo molekulovú jednojadrovú štruktúru, 9 molekulovú heterobimetalickú a jedna zlúčenina vykazovala iónovú 1D štruktúru. Pomocou výsledkov tejto metódy sa identifikovali dvojice, resp. trojice komplexov, ktoré vykazovali solvatomorfizmus a polymorfiu, resp. boli izoštruktúrne. V prípade dvoch {Ni-Ln} dvojjadrových komplexov sa pozorovali a podrobne analyzovali teplotne závislé štruktúrne zmeny, pri ktorých sa zachovával monokryštálový charakter vzorky; to umožnilo stanovenie kryštálovej štruktúry látky, ktorú nebolo možné pripraviť roztokovými metódami.
4. Študovali sa magnetické vlastnosti štyroch vybraných komplexov, trihydrátu benzoanu kobaltnatého s 1D štruktúrou a troch Ni-Ln dvojjadrových molekulových komplexov. Všetky študované látky vykazovali pomalú magnetickú relaxáciu a teda patria do kategórie SMM. Ako najvýznamnejší výsledok v tejto oblasti je možné považovať SMM charakter Ni-Gd komplexu obsahujúceho nominálne izotropný ión Gd(III) v prítomnosti diamagnetického atómu Ni(II).
5. Získané experimentálne výsledky boli publikované vo vedeckých časopisoch a prezentované na rôznych vedeckých podujatiach formov posterov a prednášok.

# 8 Resumen en español

## 8.1 Introducción

En las últimas tres décadas, se han estudiado metales de transición de primera fila como Mn(III), Fe(III), Fe(II), Co(II) y Ni(II) desde el punto de vista del magnetismo molecular. Sin lugar a dudas, la atención más intensa se presta a los llamados "single-molecule magnets" (SMMs) que son especies moleculares que muestran varias propiedades magnéticas características, como la tunelización de la magnetización y la relajación lenta de la magnetización.

El aspecto fundamental de los SMMs es que pueden magnetizarse mediante un campo magnético externo y, una vez que se elimina el campo, pueden preservar esta magnetización durante un tiempo determinado (a una temperatura determinada). Esta histéresis magnética se llama relajación lenta de la magnetización. Como esta relajación tiene un origen puramente molecular, el material se llama "single-molecule magnet". Estos materiales se pueden utilizar en dispositivos electrónicos de almacenamiento de información de alta densidad basados en espines.

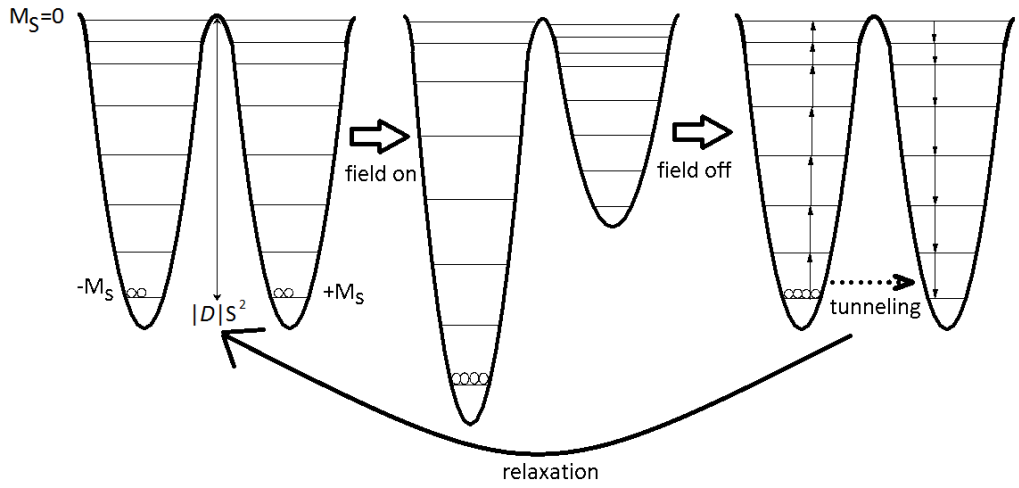


Esquema 8.1.1 Diagrama de "doble pozo" que muestra el proceso de magnetización y relajación en SMM.

La relajación lenta de la magnetización se puede describir mediante el simple diagrama de "doble pozo" (Esquema 8.1.1.). Todos los niveles de energía $M_S$ están localizados en dos pozos iguales, $–M_S$ en la izquierda, + $M_S$ en la derecha. Cuando no se aplica un campo externo, todos los niveles de energía de ± $M_S$ son pares degenerados (excepto $M_S$ = 0) y los pozos están igualmente poblados. En el campo magnético

externo paralelo al eje de magnetización, los niveles de $-M_S$ se estabilizan en perjuicio de los de + $M_S$ (nota: el campo aplicado es paralelo al eje z, los niveles de + $M_S$ corresponden a una proyección de la magnetización antiparalela al campo y – $M_S$ niveles corresponden a la magnetización paralela al campo externo aplicado). Cuando se elimina un campo externo, el sistema vuelve al equilibrio térmico.

El tamaño de la barrera de energía efectiva ($U_{eff}$) se ve afectado por dos parámetros, a saber, el estado de espín básico ($S$) y el parámetro de anisotropía magnética ($D$). Por el enfoque simple, cuanto mayor sea la barrera de energía $U_{eff}$ entre los niveles de espín inversos, mayor será el tiempo de relajación observado. En general, un estado fundamental de alto espín combinado con una fuerte anisotropía magnética es la característica requerida para los SMMs [Neese & Pantazis, 2011]. Esos dos parámetros que afectan el tamaño de la barrera de energía efectiva ($U_{eff}$) para los SMM basados en metales de transición, son inversamente proporcionales entre sí, lo que evita un mejora significativa en las propiedades SMM [Ahmed *et al*., 2014]. Con respecto a eso, se ha usado una combinación de lantánidos e iones de metales de transición en un esfuerzo por aumentar la anisotropía magnética máxima.

Un estudio reciente sobre los complejos 3*d*-4*f* con iones metálicos 3*d* diamagnéticos como el zinc(II) o el cobalto(III) mostró la mejora de la barrera $U_{eff}$ en comparación con sus análogos de lantánidos mononucleares [Fondo *et al*., 2017]; se sugirió que la presencia de un catión 3*d* diamagnético cerca del átomo central de lantánido, ambos compartiendo un átomo de puente de oxígeno, induce una gran polarización de carga en el átomo de oxígeno de puente que favorece un aumento en la barrera $U_{eff}$. Esta observación invoca una nueva estrategia en el diseño de los complejos 3*d*-4*f* con iones diamagnéticos 3*d* [Langley *et al*., 2012; Langley *et al*., 2013; Upadhyay *et al*., 2014; Sun *et al*., 2016; Upadhyay *et al*., 2017].

El creciente interés en los complejos heterometálicos en varios campos ha inspirado el diseño de ligandos capaces de coordinar un número solicitado y un tipo de centro de metal. El autoensamblaje sintetiza el manejo de precursores, ya que los bloques de construcción son una instalación útil para obtener productos deseables, especialmente cuando queremos lograr un complejo con propiedades físicas o químicas especiales. El control sobre la carga, la nuclearidad o la dimensionalidad de los productos finales puede ser el factor crítico en el éxito de una síntesis dirigida.

Las bases de Schiff se usan a menudo como ligandos para la coordinación de metales de transición y lantánidos debido a sus propiedades multidonores y la consiguiente versatilidad [Andruh, 2015]. Se pueden sintetizar fácilmente mediante la reacción orgánica de base de Schiff de un aldehído y una amina. Más específicamente, las bases *salen* de Schiff, preparadas a partir de salicilaldehído y cualquier diamina en la relación molar 2 : 1, se usan ampliamente como ligandos que ofrecen una cavidad $\{N_2O_2\}$ de una geometría ideal para quelar un ion 3*d* [Khandar *et al.*, 2006]. Una extensión de estos ligandos hecha mediante la adición de un sustituyente metoxi (o etoxi) en la posición orto del salicilaldehído los transforma en ligandos compartimentales con dos cavidades diferentes. Una cavidad interna $\{N_2O_2\}$ es capaz de coordinar un ion 3*d* mientras que el sitio de coordinación externo y más grande $\{O_4\}$ puede unir un ion 4*f* [Andruh *et al.*, 2009] (Esquema 9.1.2). Además, la naturaleza química específica de los iones 3*d* y 4*f* facilita la selectividad de los sitios de coordinación del ligando [Liu *et al.*, 2015]. De acuerdo con el concepto de ácidos y bases duros y blandos (HSAB) [Pearson, 1963], los iones metálicos 3*d* y 4*f* tienen prioridad para coordinarse con diferentes átomos donantes como el nitrógeno y el oxígeno, respectivamente.

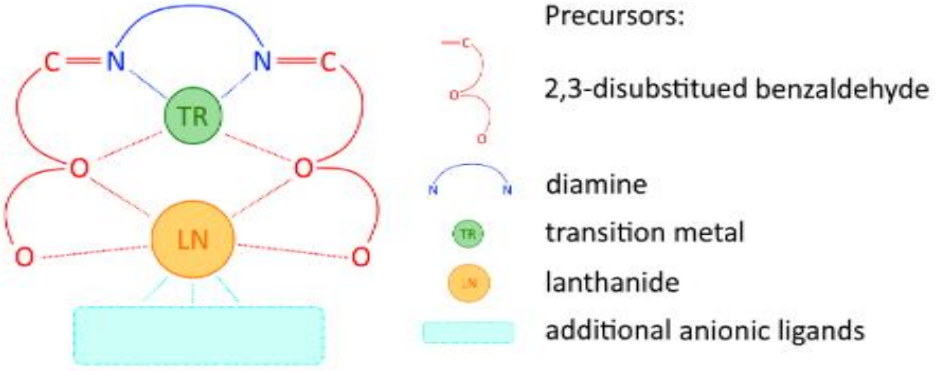


Esquema 9.1.2 Concepto de autoensamblaje del uso de precursores como bloques de construcción para crear un complejo 3*d*-4*f* heterodinuclear general con ligando de base de Schiff de tipo saleno.

## 8.2 Objetivos de la tesis

El objetivo de la disertación resultante es preparar y estudiar una serie de nuevos compuestos de Ni(II), Co(II) y lantánidos, así como complejos bimetálicos 3*d*-4*f* que usan ligandos de donantes N, O y / u O. El objetivo es diseñar y, posteriormente, mejorar los procedimientos sintéticos que conducen a la preparación de productos deseables que se estudiarán química, espectroscópica y cristalográficamente. El estudio magnético de los complejos seleccionados se llevará a cabo en la fase final. Para lograr este propósito, se establecieron los siguientes objetivos parciales:

1. La revisión reciente de los antecedentes teóricos y la literatura se llevará a cabo utilizando modernas bases de datos cristalográficas y bibliográficas. La revisión se centrará en la preparación, la estructura cristalina y las propiedades de los complejos conocidos de Ni(II), Co(II), Gd(III), Ce(III) y Dy(III), así como sus combinaciones bimetálicas 3*d*-4*f*. Se hará especial hincapié en la selección de ligandos, principalmente la base de Schiff y los ligandos de carboxilato.
2. De acuerdo con investigaciones teóricas previas, se diseñarán y llevarán a cabo los procedimientos sintéticos adecuados en un esfuerzo por preparar y aislar nuevos compuestos 3*d*, 4*f* y 3*d*-4*f*. El objetivo es preparar una rica variedad de geometrías de especies moleculares que conducen a diferentes propiedades, especialmente magnéticas, de los compuestos resultantes. La preparación de monocristales es altamente preferida. El ligando base de Schiff conveniente se sintetizará, aislará y usará como material de partida para la síntesis con iones metálicos.
3. Se supone la preparación y el aislamiento de una gran cantidad de nuevos compuestos. Los productos finales, así como los secundarios, se caracterizarán químicamente (análisis elemental) y espectroscópicamente (IR, UV-Vis) y sus estructuras cristalinas y moleculares se determinarán mediante análisis de estructura de rayos X. La combinación de todas las técnicas disponibles se utilizará para determinar la geometría exacta de las especies moleculares y determinar la pureza de las muestras finales.
4. En el caso de compuestos seleccionados, se estudiarán sus propiedades magnéticas. Las propiedades magnéticas observadas se correlacionarán con las estructuras cristalinas conocidas de los complejos estudiados.

5. Los resultados experimentales obtenidos se publicarán en revistas científicas, carteles o conferencias en eventos científicos como conferencias, reuniones, etc.

## 8.3 Resultados y discusión

### 8.3.1 Diseño de procedimientos sintéticos

El método de preparación del autoensamblaje se diseñó considerando las vías de reacción generales resumidas en [Costes *et al*., 1997]; las condiciones de reacción de Schiff descritas en [Ghose, 1984] se tuvieron en cuenta y también se modificaron. El primer paso en la síntesis dirigida es la preparación y el aislamiento de la base de Schiff como ligando ($H_2L$). El segundo paso es la preparación del complejo intermedio {Tr-*L*} como precursor. El aislamiento de este precursor puede evitar la formación de productos secundarios no deseados que surgen de la descomposición del ligando en medio ácido. La síntesis del complejo dinuclear {Tr-Ln-*L*} es el tercer y último paso en el procedimiento sintético.

El ligando de base de Schiff $H_2$(*o-van-en*) se preparó en etanol a reflujo haciendo reaccionar etilendiamina y *o*-vanilina en una relación molar de 1 : 2. El producto (**1**) se preparó en forma microcristalina y su identificación y pureza se confirmaron mediante diversas técnicas, incluyendo $^{1}$H-NMR, $^{13}$C-NMR, IR, espectroscopía UV-Vis y análisis elemental. Los monocristales amarillos en forma de aguja se obtuvieron por evaporación lenta de las aguas madres después de varias horas y se caracterizaron por análisis estructural de rayos X. Tenga en cuenta que las estructura cristalina de $H_2$(*o-van-en*) fueron publicadas por Cunningham *et al.* [2004] (isómero *cis*) y Correio *et al*. [2005] (isómero *trans*); el producto que preparamos fue el isómero *cis*.

### 8.3.2 Preparación y caracterización de precursores de complejos heteronucleares

El precursor [Ni(*o-van-en*)] se preparó a partir de carbonato de níquel. Su elección fue motivada por el hecho de que durante la reacción el anión carbonato se descompone en dióxido de carbono, que se elimina de la ebullición por agua hirviendo y, por lo tanto, evita la formación de un ambiente ácido que puede descomponer el ligando $H_2$(*o-van-en*). De esta manera, se preparó un precursor en forma de un producto microcristalino. Para preparar [Ni(*o-van-en*)] en forma de monocristal para estudiar su estructura cristalina, se recristalizó una muestra microcristalina a partir de diversos disolventes. Se aislaron tres productos diferentes adecuados para análisis de rayos X de

monocristal a partir de acetona, etanol e isopropanol, concretamente [Ni(*o-van-en*)]·$n$H$_2$O (**4**), [Ni(*o-van-en*)]·H$_2$O·EtOH (**5**) y [Ni(*o-van-en*)]·H$_2$O·iPrOH (**6**). Los resultados de su análisis estructural mostraron que las tres sustancias contienen la misma unidad compleja neutra [Ni(*o-van-en*)], donde el átomo central de Ni(II) se encuentra en la coordinación plana cuadrada del ligando (*o-van-en*)$^{2-}$, específicamente en la cavidad de coordinación más pequeña {N$_2$O$_2$}. La segunda cavidad más grande está ocupada por una molécula de agua, que está unida en la cavidad por un sistema de enlaces de hidrógeno relativamente fuertes del tipo O–H···O.

En un intento de preparar complejos dinucleares de Co$^{II}$-Ln, se han probado varias rutas sintéticas que conducen al aislamiento del precursor [Co$^{II}$(*o-van-en*)]. Cabe señalar que el complejo [Co$^{II}$(*o-van-en*)(H$_2$O)], preparado por síntesis solvotermal *in situ* utilizando 2-hidroxi-3-metoxibenzaldehído, etano-1,2-diamina y nitrato de cobalto, ya se ha descrito [Jiang *et al*., 2007]. Al variar las condiciones experimentales de la síntesis, aislamos 3 productos diferentes, incluido el complejo mononuclear mencionado anteriormente [Co$^{II}$(*o-van-en*)(H$_2$O)] (**7**). En nuestro caso, este complejo **7** se aisló en forma microcristalina por reacción directa de hidróxido de cobalto con base de Schiff H$_2$(*o-van-en*) en condiciones suaves en una atmósfera de argón inerte. La muestra microcristalina seca aislada de las aguas madres ya es estable en el aire y resistente a la oxidación posible; su identidad y pureza fueron confirmadas por difractometría de polvo. Un intento de recristalizar el producto microcristalino **7** del acetonitrilo a temperatura ambiente en presencia de aire condujo a la oxidación de Co(II) a Co(III) y a la formación de una forma monoclínica del complejo dinuclear [Co$^{III}_2$(*o-van-en*)$_3$]·4CH$_3$CN (**8**). La reacción directa de la base de Schiff con Co(OH)$_2$ en presencia de aire dio como resultado un producto crudo microcristalino negro; el cambio de color indicaba claramente la oxidación de Co(II) a Co(III). Cuando el producto bruto resultante se recristalizó en acetonitrilo caliente, precipitaron cristales de la forma triclínica del complejo dinuclear [Co$^{III}_2$(*o-van-en*)$_3$]·4CH$_3$CN (**9**). En ambas modificaciones polimórficas **8** y **9**, ambos átomos de Co(III) están hexacoordinados, con un ligando (*o-van-en*)$^{2-}$ que actúa como un ligando puente que conecta los dos átomos de Co(III). Posteriormente, ambas modificaciones polimórficas se estudiaron para las interacciones intermoleculares utilizando el método FIM y el análisis de superficie de Hirshfeld. El análisis FIM indicó 4 sitios con alto potencial de donantes para enlaces de hidrógeno, pero ninguno de ellos está ocupado por un aceptor adecuado. El análisis de las superficies de Hirshfeld nos confirmó gráficamente que en la

estructura de ambos polimorfos solo hay interacciones intermoleculares débiles entre complejos dinucleares, resp. entre los complejos y la molécula solvatadora de ACN. Notamos que ambas formas del complejo preparado $[Co^{III}_2(o\text{-}van\text{-}en)_3]\cdot 4CH_3CN$ (**8**, **9**) son inestables fuera de las aguas madres debido a su desolvatación. En vista de lo anterior, no es sorprendente que haya más de una forma de organizar la estructura cristalina de esta sustancia.

De acuerdo con nuestra estrategia de reacción escalonada, el complejo $[Co^{II}(o\text{-}van\text{-}en)(H_2O)]$ (**7**) parece ser el mejor candidato para un precursor [Tr(*o*-*van*-*en*)] en el último paso de la síntesis. Se usó cloruro de gadolinio en este último paso de la síntesis. Se realizaron varios experimentos en condiciones moderadas, pero en ninguno de los casos se coordinó el átomo de lantánido; sin embargo, durante estos experimentos aislamos e identificamos productos oxidados: complejos $[Co^{III}(o\text{-}van\text{-}en)(H_2O)Cl]$ (**10**) y $[Co^{III}(o\text{-}van\text{-}en)(H_2O)Cl]\cdot 2CH_3CN$ (**11**). Sus estructuras cristalinas están formadas por complejos mononucleares; en ambos, el átomo central de Co(III) está hexacoordinado, con ligandos cloruro y aqua ubicados en las posiciones axiales.

### 8.3.3 Preparación y caracterización de complejos heteronucleares

Después de aislar y caracterizar con éxito el precursor $[Ni(o\text{-}van\text{-}en)]\cdot nH_2O$ (**4**), se siguió la estrategia ya mencionada. Primero, se realizaron experimentos con nitrato de gadolinio como la sal de lantánido. La síntesis se realizó en etanol bajo condiciones de reflujo. El producto microcristalino, que se aisló por filtración inmediatamente después de la reacción, se recristalizó en varios disolventes o una mezcla de los disolventes (técnicas de difusión líquido-líquido) para obtener monocristales. Los monocristales se obtuvieron solo por recristalización en acetonitrilo para dar el complejo bimetálico 3*d*-4*f* deseado $[Ni(o\text{-}van\text{-}en)Gd(NO_3)_3]\cdot 2CH_3CN$ (**12**), en el que los átomos de Ni(II) y Gd(III) están unidos por dos puentes O-monoatómicos y el átomo de Gd(III) complementa la esfera de coordinación (el número de coordinación = 10) con tres ligandos de nitrato de quelato. Los cristales de **12** después del aislamiento de las aguas madres son inestables debido a la desolvatación.

En otros experimentos, se usaron cloruros de lantánidos en lugar de nitratos en combinación con el precursor $[Ni(o\text{-}van\text{-}en)]\cdot nH_2O$ (**4**) usando el método de autoensamblaje mencionado anteriormente. Las síntesis se realizaron bajo condiciones de reflujo, aislando productos en polvo microcristalino naranja de composición general

[Ni(*o-van-en*)LnCl$_3$(H$_2$O)], en donde Ln representa Ce (**13**), Gd (**14**) y Dy (**15**). La identidad y pureza de las muestras microcristalinas se confirmó mediante espectroscopía IR, análisis elemental y análisis de difracción de rayos X de polvo. Usando diversas técnicas de recristalización, los compuestos **13**, **14** y **15** también se prepararon como monocristales. Los resultados del análisis estructural mostraron que los tres complejos son isomórficos entre sí; cristalizar en el grupo monoclínico $P2_1/n$. Su estructura molecular consiste en una unidad de complejo dinuclear bimetálico neutro [Ni(*o-van-en*)LnCl$_3$(H$_2$O)], en la que el átomo central de Ni(II) está coordinado de forma cuadrada por un conjunto de donantes {N$_2$O$_2$} derivado de un ligando de base de Schiff (*o-van-en*)$^{2-}$ (Fig. 8.3.1). La coordinación del átomo central de lantánido consta de 4 átomos de oxígeno del ligando (*o-van-en*)$^{2-}$, un átomo de oxígeno del ligando aqua y tres ligandos de cloruro. La estructura cristalina de los compuestos **13**, **14** y **15** está soportada por enlaces de hidrógeno de fuerza media del tipo O–H···Cl, formando así una estructura de cadena supramolecular a lo largo del eje *a*. Otros enlaces de hidrógeno más débiles del tipo C$_{ar}$–H···Cl y C$_{imine}$–H···Cl y las interacciones π-π entre los núcleos aromáticos de las cadenas adyacentes forman capas supramoleculares en el plano *ab*. Solo se encontraron contactos intermoleculares de tipo C–H···Cl más débiles derivados de los grupos metilo y metileno del ligando (*o-van-en*)$^{2-}$ entre los planos supramoleculares.

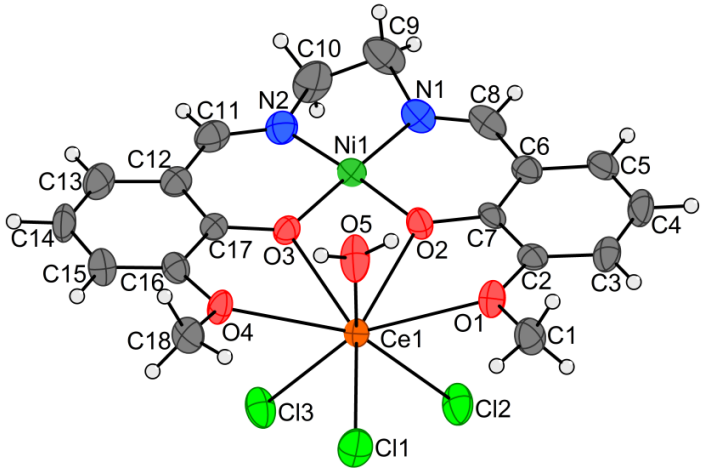


Figura 8.3.1 Estructura molecular de **13** junto con su esquema de numeración atómica. Los elipsoides térmicos de los átomos que no son de hidrógeno se dibujan con un nivel de probabilidad del 50%.

Sin embargo, los procedimientos de recristalización a partir de complejos dinucleares [Ni(*o-van-en*)LnCl$_3$(H$_2$O)] (Ln = Ce, Dy) también condujeron a un aislamiento reproducible de otros complejos: [Ni$_2$Ce$_2$(*o-van-en*)$_2$Cl$_6$] (**16**) , [Ni(*o-van-*

*en)*$DyCl_3$] (**17**) y [Ni(*o-van-en*)$DyCl_3$] · EtOH (**18**). Estos se caracterizaron por métodos convencionales y los resultados de su análisis estructural, resumidos a continuación, confirmaron la formación de nuevas sustancias después de la disolución en el disolvente apropiado.

En nuestros experimentos con recristalización de la muestra de polvo de [Ni(*o-van-en*)$CeCl_3(H_2O)$] (**13**) se recristalizó en etanol en un recipiente cerrado colocado en un horno a 80 ºC. El análisis estructural monocristalino de los cristales rojo-naranja formados mostró que se trataba de un nuevo complejo de cuatro núcleos [$Ni_2Ce_2$(*o-van-en*)$_2Cl_6$] (**16**). Su formación puede explicarse por la dimerización de dos unidades estructurales [Ni(*o-van-en*)$CeCl_3(H_2O)$] debido a la liberación de ligandos aqua y la posterior formación de dos puentes de cloruro entre los átomos de Ce (el núcleo {$CeCl_2Ce$} se formó), coordinando así el número 8 de Ce(III) retiene.

El mismo procedimiento de recristalización se aplicó a la muestra de polvo del complejo [Ni(*o-van-en*)$DyCl_3(H_2O)$] (**15**). A pesar de la presunta analogía entre los átomos de cerio y el disprosio, en este caso no se observó dimerización, pero después de la deshidratación se formó un complejo dinuclear deshidratado [Ni(*o-van-en*)$DyCl_3$] (**17**). Suponemos que Dy(III) con un radio iónico más pequeño que Ce(III) [Shannon, 1976] muestra una mayor estabilidad de su esfera de coordinación incluso con un número de coordinación 7 y, por lo tanto, el complejo **17** no tiende a dimerizarse. Por lo tanto, la dimerización observada en Ce(III) puede deberse al esfuerzo del átomo de Ce(III) más grande para retener el número de la coordinación 8 mediante la coordinación de los ligandos de cloruro puenteados. Tal comportamiento dependiente del radio iónico se ha observado en el pasado [Kano *et al.*, 2003; Baisch *et al*., 2004; Deacon *et al*., 2002; Wong *et al*., 2006; Chen *et al*., 2011].

Posteriormente, realizamos experimentos de recristalización utilizando técnicas de difusión. La difusión de una solución de etanol de [Ni(*o-van-en*)$DyCl_3(H_2O)$] (**15**) en isopropanol a temperatura ambiente dio cristales de [Ni(*o-van-en*)$DyCl_3$]·EtOH (**18**). La estructura molecular del complejo **18** contiene una unidad de complejo bimetálico neutro [Ni(*o-van-en*)$DyCl_3$], donde el átomo central de Ni(II) se encuentra en la cavidad interna del ligando base de Schiff con el conjunto de donantes {$N_2O_2$} y el átomo central de Dy(III) llena el exterior cavidad {$O_4$}. Su coordinación se complementa con tres ligandos de cloruro. Este resultado respalda nuestra suposición anterior sobre la estabilidad del átomo central Dy(III) con el número de coordinación 7.

Cuando se cambiaron las condiciones de recristalización, se disolvió [Ni(*o-van-en*)$DyCl_3(H_2O)$] (**15**) en etanol / isopropanol. La cristalización de esta solución a temperatura elevada (50 °C) proporcionó cristales prismáticos rojo-naranja del estereoisómero del complejo original, a saber, la forma II del complejo [Ni(*o-van-en*)$DyCl_3(H_2O)$] (**19**). Un estudio de su estructura cristalina mostró que en el complejo **19** (forma II) versus el complejo **15** (forma I) los ligandos de cloruro se ubican en el poliedro de coordinación Dy(III) de una manera diferente; mientras que en **15** los tres ligandos de clorido están ubicados en una superficie del poliedro, en **19** los tres ligandos de clorido están ubicados en un plano de la sección de poliedro (Fig. 8.3.2a). Como resultado, los dímeros supramoleculares se forman en **19** por medio de enlaces de hidrógeno del tipo O–H···Cl.

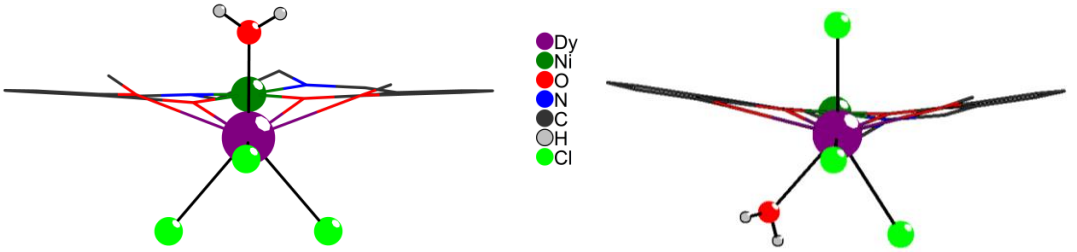


a)

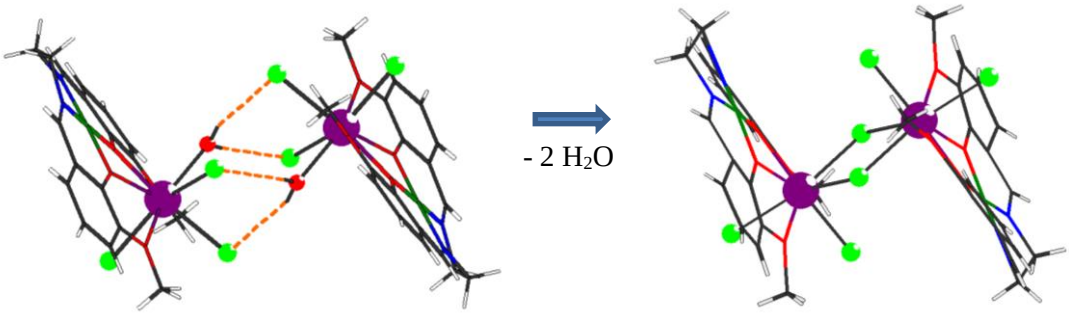


b)

Figura 8.3.2 a) Comparación de los isómeros **15** (izquierda) y **19** (derecha).
b) Cambio en la estructura molecular debido a la reacción topotáctica: 2 **19** → **20** + 2 $H_2O$.

La dimerización de [Ni(*o-van-en*)$DyCl_3(H_2O)$] (**19**) para dar el complejo de cuatro núcleos [$Ni_2Dy_2$(*o-van-en*)$_2Cl_6$] (**20**) se logró mediante una reacción de deshidratación en fase sólida. El curso de la deshidratación se estudió en un monocristal **19**. Al calentar a una temperatura de aproximadamente 84 °C, tuvo lugar la deshidratación, y como se conservó el carácter de un monocristal de la muestra, fue posible determinar la estructura del cristal **20**. Consiste en dos unidades estructurales [NiDy(*o-van-en*)$Cl_3$] unidos por dos ligandos de cloruro puenteados (Fig. 8.3.2b).

Dicho proceso de deshidratación representa una reacción topotáctica del tipo SC-SC (Single Crystal-to-Single Crystal).

### 8.3.4 Propiedades magnéticas de una serie de complejos heteronucleares [Ni(*o-van-en*)LnCl$_3$(H$_2$O)] [Ln = Ce (13), Gd (14), Dy (15)]

Para estudiar las propiedades magnéticas, se seleccionaron los compuestos bimetálicos dinucleares Ni-Ln **13**, **14**, **15** y el compuesto Co(II) **21**. La pureza de fase de las muestras estudiadas se confirmó mediante análisis de difracción de rayos X en polvo. Los resultados de los datos de difracción de polvo se compararon con los datos de difracción calculados a partir de los resultados de un análisis estructural de monocristal de **13**-**15** realizado a temperatura ambiente, utilizando el método LeBail en Jana2006 [Le Bail *et al*., 1988; Le Bail, 2005; Petříček *et al*., 2014].

Se realizaron mediciones magnéticas en modo DC y AC para verificar el posible comportamiento SMM de las sustancias estudiadas. Los experimentos y la evaluación fueron realizados por el grupo de trabajo del prof. Boča de la Universidad de St. Cirilo y Metodio en Trnava (Eslovaqía).

Los resultados del análisis estructural de los complejos dinucleares de Ni-Ln **13**, **14** y **15** (ver arriba) muestran que el átomo de Ni(II) en estos complejos es de coordinación cuadrada, es decir, es diamagnético. La consecuencia de esto es que las propiedades magnéticas de los complejos **13**, **14** y **15** están determinadas por los átomos de Ln presentes, que exhiben tanto el impulso orbital como el spin. Sus estados basales son multipletes $^2F_{5/2}$ para Ce(III), $^8S_{7/2}$ para Gd(III) y $^6H_{15/2}$ para Dy(III), y sus respectivos valores de $g_J$ son 6/7, 2 y 4/3. Las magnetizaciones por unidad deben estar saturadas en $M_1 = M_{mol}/(N_A\mu_B) = g_J \cdot J = 6/7 \times 5/2 = 15/7$, $2 \times 7/2 = 7$ y $4/3 \times 15/2 = 10$ para Ce(III), Gd(III) y Dy(III). El momento magnético efectivo, $\mu_{eff}/\mu_B = g_J[J(J + 1)]1/2$, para complejos individuales alcanza los valores límite de 2.54 $\mu_B$, 7.94 $\mu_B$ y 10.6 $\mu_B$.

Los momentos magnéticos efectivos determinados experimentalmente de los complejos individuales **13**, **14** y **15** a temperatura ambiente muestran valores de $\mu_{eff}$ = 2.36 $\mu_B$ (Ce), 7.9 $\mu_B$ (Gd) y 12.15 $\mu_B$ (Dy), mientras que los valores esperados son 2.54 (Ce), 7.94 (Gd) y 10.6 $\mu_B$ (Dy). El mayor valor observado para **15** (Dy) puede explicarse por la presencia de estados excitados bajos del átomo de Ni (II) adyacente. La existencia de la contribución del paramagnetismo independiente de la temperatura

(TIP) debido a la presencia del átomo de Ni(II) también se confirma por la dependencia de la temperatura ligeramente lineal de $\mu_{eff}$ en el caso del complejo **13**.

Los valores experimentales de la saturación de magnetización en $T$ = 2.0 K y $B$ = 7 T para complejos individuales son $M_1$ = 1.0 (Ce), 6.6 (Gd) y 7.9 (Dy), mientras que los valores calculados para iones aislados son 2.1 (Ce), 7.0 (Gd) y 10.0 (Dy). El valor más bajo observado para el complejo de Ce(III) indica que solo el más bajo de los tres dobletes Kramer está ocupado debido a la acción del campo cristalino. Por otro lado, el valor de magnetización observado significativamente más bajo para el complejo Dy(III) indica una disminución en la contribución orbital debido a la asimetría de la esfera de coordinación del Dy(III) y / o al efecto de escisión del multiplete básico de campo de cristal en el campo cero.

Los datos de susceptibilidad de CA se obtuvieron a una amplitud de campo $B_{AC}$ = 0,38 mT y se midieron en función del campo magnético externo del $B_{DC}$, la temperatura $T$ y la frecuencia $f$ del campo oscilante. Las mediciones magnéticas de AC de los tres complejos, incluido el sistema nominalmente isotrópico basado en Gd(III) (**14**), mostraron que los tres complejos **13**, **14** y **15** muestran relajación magnética lenta inducida por campo con dos o tres canales de relajación.

En el caso del complejo **13** (Ce), la dependencia de la frecuencia del componente de susceptibilidad no fase $\chi''$ indica a temperaturas inferiores a 4 K la existencia de dos canales de relajación con una contribución dominante del componente de baja frecuencia, mientras que por encima de esta temperatura la contribución del componente HF desaparece. El tiempo de relajación en $T$ = 1.9 K y $B_{DC}$ = 0.5 T tiene un valor de $\tau$(LF) = 60.3 ms, que es más largo en comparación con el valor de $\tau$(LF) = 18.7 ms en $B_{DC}$ = 0.1 T.

La existencia de relajación magnética lenta en el caso del átomo isotrópico Gd(III) fue sorprendente. La dependencia de la frecuencia de los dos componentes de la susceptibilidad de AC para el compuesto **14** reveló la existencia de dos canales de relajación, y se encontró que en el rango de temperatura de 1.9 a 6.5 K, el tiempo de relajación del canal de HF depende solo ligeramente de la temperatura. Además, el canal de alta frecuencia muestra un comportamiento "especial": cuando se enfría, el tiempo de relajación pasa a través del máximo y luego se acorta: $\tau$(HF) = 223 μs a $T$ = 3.9 K en comparación con $\tau$(HF) = 120 μs a $T$ = 1.9 K. El tiempo de relajación para el proceso LF a $B_{DC}$ = 0.3 T y $T$ = 1.9 K es $\tau$(LF) = 0.37 s.

El análisis de la dependencia de la frecuencia de las porciones de fase y no fase de la susceptibilidad de AC de la muestra **15** (Dy) reveló la existencia de tres canales de relajación: baja frecuencia (LF), frecuencia media (IF) y alta frecuencia (HF). Mientras que a la temperatura medida más baja $T$ = 1.9 K domina el componente de baja frecuencia, su contribución disminuye con el aumento de la temperatura a favor del componente de alta frecuencia. A la temperatura de medición más baja, $T$ = 1.9 K y a $B_{DC}$ = 0.15 T, se identificaron tres tiempos de relajación $\tau$(LF) = 1.29 s, $\tau$(IF) = 74 ms y $\tau$(HF) = 964 μs.

De lo anterior se deduce que los tres compuestos estudiados, incluido Gd(III) (**14**), muestran una relajación magnética lenta. En los tres compuestos, los tres ligandos de cloruro están ubicados en una superficie del poliedro de coordinación. Este método de colocación se asemeja a una configuración *fac* y significa que se concentran en la misma parte de la esfera de coordinación, mientras que los otros complejos análogos estudiados muestran una distribución más simétrica de los ligandos de clorido. Creemos que esta configuración afecta la distribución de electrones en el átomo central (introduce anisotropía en la distribución) y apoya el comportamiento SMM de estos complejos, rara vez para el complejo Gd(III). Se ha demostrado que la geometría y la densidad electrónica de los sitios de coordinación tienen un efecto muy importante sobre el comportamiento SMM de los iones lantánidos.

La investigación sobre el magnetismo de los complejos de Co(II) ha demostrado recientemente que estos sistemas tienen una anisotropía magnética muy alta, que aumenta en el orden de la coordinación de complejos tetra, penta y hexa [Craig y Murrie, 2015; Gómez-Coca *et al*., 2015; Frost *et al*., 2016]. Por esta razón, el complejo **21** que contiene un átomo central de Co(II), que están dispuestos adicionalmente en una cadena, también fue elegido para estudiar las propiedades magnéticas.

Las mediciones en el campo DC mostraron que el momento magnético efectivo $\mu_{eff}$ de la sustancia **21** aumenta de $\mu_{eff}$ = 5.6 $\mu_B$ a un máximo de $\mu_{eff}$ = 15.9 $\mu_B$ a T = 6.5 K a medida que la temperatura disminuye y luego disminuye rápidamente a $\mu_{eff}$ = 8.0 $\mu_B$ a $T$ = 1.9 K. Estos datos indican la transición de una fase paramagnética con interacciones ferromagnéticas a una fase antiferromagnética a $T_N$ = 5.5 K.

La dependencia de la frecuencia de ambos componentes de susceptibilidad en el campo AC indicó la existencia de dos máximos en la curva $\chi''$ versus $f$, lo que indica la presencia de dos canales de relajación. El inicio del modo de baja frecuencia (LF) es

claramente visible en el rango $T$ = 1.9 - 3.3 K. Por encima de 3.9 K, se suprime la susceptibilidad fuera de fase y luego la muestra se convierte en un imán. La banda LF comienza a crecer por debajo de 1 Hz y su máximo está fuera del límite de medición - 0.1 Hz. El tiempo de relajación alcanza así un valor de $\tau$(LF)> 1.6 s a bajas temperaturas, independientemente del método de ajuste (es decir, $\tau_{LF}$ (2.1 K) = 14 s). El componente de susceptibilidad fuera de fase para $B_{DC}$ = 0.1 T aumenta a un máximo a $T$ = 4.1 K y luego disminuye rápidamente con un mayor calentamiento. En $T_N$ > 4.7 K, es casi cero debido a la fase paramagnética.

## 8.4 Conclusión

Los resultados de la disertación presentada con respecto a sus objetivos establecidos se pueden resumir en los siguientes puntos:

1. Se describió el estudio teórico de los SMMs con respecto a los metales de transición y los lantánidos. Se hizo especial hincapié en Ni(II) y Co(II) / Co(III) como metales de transición y Ce(III), Gd(III) y Dy(III) entre los lantánidos. También se introdujo la química de coordinación de metales de transición y lantánidos seleccionados. La conclusión de la introducción teórica de la tesis está dedicada a la selección de los ligandos y al estudio de complejos previamente preparados que contienen dichos ligandos.
2. El esfuerzo en el laboratorio con atención completa a los detalles junto con la búsqueda de literatura conducen al diseño de la estrategia sintética óptima para la preparación de la serie de complejos heterodinucleares Tr(II)-Ln(III). El enfoque gradual del autoensamblaje produjo varios precursores y productos finales, que se aislaron, purificaron y caracterizaron. Se prepararon hasta 21 compuestos, 18 de ellos son complejos metálicos, 17 de ellos están recién preparados. Entre ellos, 9 eran heteronucleares y 4 complejos metálicos fueron elegidos para estudio magnético.
3. El análisis estructural monocristalino se utilizó para el estudio cristalográfico de 3 complejos orgánicos y 18 complejos (3 basados en Ni(II), 2 basados en Co(II), 4 basados en Co(III) y 9 complejos Ni-Ln). Los resultados del análisis estructural demostraron 8 complejos con estructura molecular mononuclear, 9 heterobimetálica molecular y 1 iónica 1D. Mediante el análisis estructural, se identificaron solvatomorfismo, polimorfismo, isomorfismo y complejos

isoestructurales. Además, se observaron cambios estructurales poco frecuentes con dependencia de la temperatura en las dos muestras sólidas y se analizaron en detalle. Esto nos permitió determinar la estructura cristalina de los compuestos que no eran fácilmente preparables por métodos de solución.

4. Todos los complejos seleccionados para estudios magnéticos mostraron una relajación magnética lenta y contribuyeron a la teoría del fenómeno llamado "single-molecule magnet". Hallazgos sobresalientes llegaron con muestras de cerio(III) y gadolinio(III) ya que estos dos iones metálicos no se alinean con los iones SMM "típicos" como el disprosio(III). Especialmente, el complejo Ni-Gd con iones diamagnéticos de Ni(II) y iones en general magnéticamente isotrópicos de gadolinio(III) trajo una nueva luz a la teoría del magnetismo de "single-molecule magnet".
5. Los resultados experimentales obtenidos fueron publicados en revistas científicas y presentados por PhD. estudiante en varias conferencias científicas como conferencias y carteles.

# 9 References


Ahmed N., Das C., Vaidya S., Langley S. K., Murray K. S. & Shanmugam M.: Nickel(II)–Lanthanide(III) Magnetic Exchange Coupling Influencing Single-Molecule Magnetic Features in $\{Ni_2Ln_2\}$ Complexes. In *Chem. Eur. J.* (**2014**), 20, pp. 14235-14239, DOI: 10.1002/chem.201404393.

Allen F. H., Bellard S., Brice M. D., Cartwright B. A., Doubleday A., Higgs H., Hummelink T., Hummelink-Peters T., Kennard O., Motherwell W. D. S., Rodgers J. R. & Watson D. G.: Cambridge Structural Database System (CSDS). In *Cambridge, U.K.* (**1994**), update from February 2019.

Amirkhanov O. V., Moroz O. V., Znovjyak K. O., Sliva T. Y., Penkova L. V., Yushchenko T., Szyrwiel L., Konovalova I. S., Dyakonenko V. V., Shishkin O. V., Amirkhanov V. M.: Heterobinuclear Zn–Ln and Ni–Ln Complexes with Schiff-Base and Carbacylamidophosphate Ligands: Synthesis, Crystal Structures, and Catalytic Activity. In *Eur. J. Inorg. Chem.* (**2014**), pp. 3720–3730, DOI:10.1002/ejic.201402224.

Andruh M., Costes J.-P., Diaz C. & Gao S.: 3d-4f Combined Chemistry: Synthetic Strategies and Magnetic Properties. In *Inorg. Chem.* (**2009**), 48, pp. 3342-3359, DOI: 10.1021/ic801027q.

Andruh M.: The exceptionally rich coordination chemistry generated by Schiff-base ligands derived from *o*-vanillin. In *Dalton Trans.* (**2015**), 44, pp. 16619-16966, DOI: 10.1039/c5dt02661j.

De Angelis S., Solari E., Gallo E., Floriani C., Chiesi-Villa A. & Rozzoli C.: Formation of Carbon−Carbon-Bonded Dimers in the Reduction of [$Co^{II}$salophen] [salophen = *N,N*‘-*o*-Phenylenebis(salicylideneaminato)]: Their Reactivity with Electrophiles To Form Co−C Bonds. In *Inorg. Chem.* (**1996**), 35, 21, pp. 5995-6003, DOI: 10.1021/ic951661d.

Ashida T. & Hirokawa S.: The Crystal Structure of Ethylenediammonium Chloride. In *Bulletin of the Chemical Society of Japan* (**1963**), 36, pp. 704-707, DOI: 10.1246/bcsj.36.704.

Assey G., Butcher R. J. & Gultneh Y.: Acetato(aqua){6,6'-dimethoxy-2,2'-[ethane-1,2-diylbis(nitrilomethanylylidene)]diphenolato}cobalt(III) methanol disolvate. In *Acta Cryst.* (**2012**), E68, pp. m962-m963, DOI: 10.1107/S1600536812027687.

Atwood D. A.: The rare earth elements: fundamentals and applications. In *Wiley*, Chichester (**2012**), ISBN: 978-1119950974.

Ayikoé K., Butcher R. J. & Gultneh Y.: {6,6'-Dimeth-oxy-2,2'-[ethane-1,2-diylbis(nitrilo-methanylyl-idene)]diphenolato}nickel(II) dimethylformamide monosolvate. In *Acta Cryst.* (**2011**), E67, p. m328, DOI: 10.1107/S1600536811004818.

Le Bail A., Duroy H. & Fourquet J. L.: *Ab-initio* structure determination of $LiSbWO_6$ by X-ray powder diffraction. In *Mater. Res. Bull.* (**1988**) 23, pp. 447–452, DOI: 10.1016/0025-5408(88)90019-0.

Le Bail A.: Whole powder pattern decomposition methods and applications: A retrospection. In *Powder Diffr.* (**2005**), 20, 4, pp. 316-326, DOI: 10.1154/1.2135315.

Bailey N. A., Higson B. M, & McKenzie E. D.: Crystal and Molecular Structure of Benzoylacetonato-[*NN*'-ethylene*bis*-(salicylideneiminato)]cobalt(III)-1·5 Water. In *J. Chem. Soc., Dalton Trans.* (**1972**), pp. 503-508, DOI: 10.1039/DT9720000503.

Baisch U., Belli Dell Amico D., Calderazzo F., Conti R., Labella L., Marchetti F., Quadrelli E. A.: The mononuclear and dinuclear dimethoxyethane adducts of lanthanide trichlorides $[LnCl_3(DME)_2]_n$, $n$ = 1 or 2, fundamental starting materials in lanthanide chemistry: preparation and structures. In *Inorg. Chim. Acta* (**2004**) 357, pp. 1538-1548, DOI: 10.1016/j.ica.2003.11.011.

Balarew C., Stoilova D. & Krasteva R.: Thermogravimetrical Study on Some Crystal Hydrates of Metal(II) Benzoates. In *Thermochim. Acta* (**1985**), 92, pp. 719-721, DOI: 10.1016/0040-6031(85)85978-5.

Bencini A., Benelli C., Caneschi A., Carlin R. L., Dei A. & Gatteschi D.: Crystal and Molecular Structure of and Magnetic Coupling in Two Complexes Containing Gadolinium(III) and Copper(II) Ions. In *J. Am. Chem. Soc.* (**1985**), 107, pp. 8128-8136. DOI: 10.1021/ja00312a054.

Bérar J.-F. & Baldinozzi G.: Modeling of line-shape asymmetry in powder diffraction. In *J. Appl. Cryst.* (**1993**), 26, pp. 128-129, DOI: 10.1107/S0021889892009725.

Bhowmik P., Chatterjee S., Chattopadhyay S.: Heterometallic inorganic–organic frameworks of sodium–nickel(vanen): Cation–π interaction, trigonal dodecahedral $Na^+$ and unprecedented heptadentate coordination mode of $vanen^{2-}$. In *Polyhedron* (**2013**), 63, pp. 214-221, DOI: 10.1016/j.poly.2013.07.023.

Biswas N., Khanra S., Sarkar A., Bhattacharjee S., Mandal D. P., Chaudhuri A., Chakraborty S. & Choudhury C. R.: Cytotoxicity activity, in silico molecular docking, protein- and DNA-binding study of a new Ni(II) Schiff base complex. In *J. Coord. Chem.* (**2018**), 71, pp. 2740-2766, DOI: 10.1080/00958972.2018. 1492118.

Boča R., Rajnák C., Titiš J. & Valigura D.: Field Supported Slow Magnetic Relaxation in a Mononuclear Cu(II) Complex. In *Inorg. Chem.* (**2017**), 56, 3, pp. 1478-1482, DOI: 10.1021/acs.inorgchem.6b02535.

Boča R., Rajnák C., Moncoľ J., Titiš J. & Valigura D.: Breaking the Magic Border of One Second for Slow Magnetic Relaxation of Cobalt-Based Single Ion Magnets. In *Inorg. Chem.* (**2018**), 57, 22, pp. 14314-14321, DOI: 10.1021/acs.inorgchem.8b02287.

Bruno G. & Randaccio L.: A refinement of the benzoic acid structure at room temperature. In *Acta Cryst.* (**1980**), B36, pp. 1711-1712, DOI: 10.1107/S0567740880007030.

Buerger M. J.: A new approach to crystal-structure analysis. In *Acta Cryst.* (**1951**), 4, 6, pp. 531-544, DOI: 10.1107/S0365110X51001756.

Bujak M., Sikorska L. & Zaleski J.: Structure and Phase Transitions in Ethylenediammonium Dichlorideand its Salts with Antimony Trichloride. In *Z. Anorg. Allg. Chem.* (**2000**), 626, pp. 2535-2542, DOI: 10.1002/1521-3749(200012)626:12<2535::AID-ZAAC2535>3.0.CO;2-U.

Calahorro A. J., Oyarzabal I., Fernández B., Seco J. M., Tian T., Fairen-Jimenez D., Colacio E. & Rodriguez-Diéguez A.: Rare earth anthracenedicarboxylate metal – organic frameworks: slow relaxation of magnetization of $Nd^{3+}$, $Gd^{3+}$, $Dy^{3+}$, $Er^{3+}$ and $Yb^{3+}$ based materials. In *Dalton Trans.* (**2016**), 45, pp. 591-598, DOI: 10.1039/c5dt03946k.

Calligaris M., Nardin G. & Randaccio L.: The Crystal and Molecular Structure of a Binuclear Cobalt(III) Complex with Bis-(3-methoxysalicylaldehyde)ethylenediimine. Evidence for the Bridging Ability of Some Quadridentate Schiff Bases. In *J. Chem. Soc.* (**1970**), pp. 1079-1080, DOI: 10.1039/C29700001079.

Calligaris M., Nardin G. & Randaccio L.: The structure of *NN′*-ethylene-*bis*(acetylacetoneiminato)methyl pyridino Cobalt(III). In *Inorg. Nucl. Chem. Letters* (**1972**), 8, 5, pp. 477-480, DOI: 10.1016/0020-1650(72)80257-5.

Chambers C. & Holliday A. K.: Modern inorganic chemistry. In *Butterworths*, Chichester (**1975**), ISBN: 978-0408706636.

Chen C., Liu Y., Li P., Zhou H. & Shen X.: Construction of $Ni^{II}Ln^{III}M^{III}$ (Ln = $Gd^{III}$, $Tb^{III}$; M = $Fe^{III}$, $Cr^{III}$) clusters showing slow magnetic relaxations. In *Dalton Trans.* (**2015**), 44, pp. 20193-20199, DOI: 10.1039/C5DT03620H.

Chen P., Chen H., Yan P., Wang Y. & Li G.: Effect of lanthanide contraction and rigid ligand on the structure of salen-type lanthanide complexes. In *CrystEngComm* (**2011**), 13, pp. 6237-6242, DOI: 10.1039/c1ce05501a.

Cohen M. D. & Schmidt G. M. J.: Topochemistry. Part I. A Survey. In *J. Chem. Soc.* (**1964**), pp. 1996-2000, DOI: 10.1039/JR9640001996.

Cohen C. T., Thomas Ch. M., Peretti K. L., Lobkovsky E. B. & Coates G. W.: Copolymerization of cyclohexene oxide and carbon dioxide using (salen)Co(III) complexes: synthesis and characterization of syndiotactic poly(cyclohexene carbonate). In *Dalton Trans.* (**2006**), 1, pp. 237-249, DOI: 10.1039/B513107C.

Correia I., Costa Pessoa J., Duarte M. T., Minas da Piedade M. F., Jackush T., Kiss T., Castro M. M. C. A., Geraldes C. F. G. C. & Avecilla F.: Vanadium(IV and V) Complexes of Schiff Bases and Reduced Schiff Bases Derived from the Reaction of Aromatic o-Hydroxyaldehydes and Diamines: Synthesis, Characterisation and Solution Studies. In *Eur. J. Inorg. Chem.* (**2005**), pp. 732-744, DOI: 10.1002/ejic.200400481.

Costes J.-P., Dahan F., Dupuis A. & Laurent J.-P.: A General Route to Strictly Dinuclear Cu(II)/Ln(III) Complexes. Structural Determination and Magnetic Behavior of Two Cu(II)/Gd(III) Complexes. In *Inorg. Chem.* (**1997**), 36, pp. 3429-3433, DOI: 10.1021/ic970264v.

Costes J.-P., Dahan F., Dumestre F. & Tuchagues J.-P.: A novel di-iron(III) structure based on an ageless ligand. In *Polyhedron* (**2010**), 29, pp. 787-790, DOI: 10.1016/j.poly.2009.10.030.

Costes J.-P., Dahan F., Duhayon C. & Mota A. J.: Can novel dinuclear Ni–Gd complexes give supplementary information on the Ni–Gd magnetic interaction? In *Polyhedron* (**2015**), 96, pp. 51-56, DOI: 10.1016/j.poly.2015.04.022.

Costes J.-P., Duhayon C., Vendier L. & Mota A. J.: Reactions of a series of ZnL, CuL and NiL Schiff base and non-Schiff base complexes with $MCl_2$ salts (M = Cu, Ni,

Mn): syntheses, structures, magnetic properties and DFT calculations. In *New J. Chem.* (**2018**), 42, pp. 3683-369, DOI: 10.1039/C7NJ04347C.

Cotton F. A., Wilkinson G., Murillo C. A. & Bochmann M.: Advanced Inorganic Chemistry. In *Wiley*, New York (**1999**), ISBN 0-471-19957-5.

Cotton S.: Lanthanide and actinide chemistry. In *Wiley*, Chichester (**2006**), ISBN 978-0-470-01005-1.

Craig G. A. & Murrie M: 3*d* single-ion magnets. In *Chem. Soc. Rev.* (**2015**), 44, pp. 2135-2147, DOI: 10.1039/C4CS00439F.

Cristóvão B., Kłak J., Pełka R., Miroslaw B. & Hnatejko Z.: Heterometallic trinuclear 3d–4f–3d compounds based on a hexadentate Schiff base ligand. In *Polyhedron* (**2014**), 68, pp. 180-190, DOI: 10.1016/j.poly.2013.10.019.

Cucos A., Ursu A., Madalan A. M., Duhayon C., Sutter J.-P. & Andruh M.: Co-crystallization of coordination compounds through second-coordination sphere interactions. In *CrystEngComm* (**2011**), 13, pp. 3756-3766, DOI: 10.1039/c1ce05112a.

Cunningham D., Gallagher J. F., Higgins T., McArdle P., McGinley J. & O'Gara M.: Transition-metal Schiff-base complexes as ligands in tin chemistry. Part 3. An X-ray crystallographic and tin-119 Mössbauer spectroscopic study of adduct formation between tin(IV) Lewis acids and nickel 3-methoxysalicylaldimine complexes. In *Dalton Trans.* (**1993**), pp. 2183-2190, DOI: 10.1039/DT9930002183.

Cunningham D., Gilligan K., Hannon M., Kelly C., McArdle P. & O'Malley A.: Zwitterionic Forms of Salicylaldimine Donor Ligands in Unusual Adduct Formation with Organotin(IV) Lewis Acids. In *Organometallics* (**2004**), 23 (5), pp. 984-994, DOI: 10.1021/om030540f.

Deacon G. B., Evans D. J. & Junk P. C.: New Variations on the $LnCl_3(L)_n$ (L = tetrahydrofuran or 1,2-dimethoxyethane) Structural Theme – $NdCl_3(dme)_2$ and $YbCl_3(thf)_{3.5}$. In *Z. Anorg. Allg. Chem.* (**2002**), 628, pp. 2033-2036, DOI: 10.1002/1521-3749(200209)628:9/10<2033::AID-ZAAC2033>3.0.CO;2-G.

Dickman M. H.: CCDC 650801: Experimental Crystal Structure Determination. In *CSD Communication* (**2007**), DOI: 10.5517/ccpv6l9.

Dinca S., Shova S., Ion A. E., Maxim C., Loret F., Julve M. & Andruh M.: Ascorbic acid decomposition into oxalate ions: a simple synthetic route towards

oxalato-bridged heterometallic 3d–4f clusters. In *Dalton Trans.* (**2015**), 44, pp. 7148-7151, DOI: 10.1039/c5dt00778j.

Dong R., Y. Liu, X. Wu, H. Zhou & X. Shen: Synthesis, structure and magnetic properties of two new 3d-3d′-4f clusters of $Ni^{II}Ho^{III}M^{III}$ (M = Fe, Co). In *Inorg. Chim. Acta* (**2018**), 482, pp. 687-690, DOI: 10.1016/j.ica.2018.07.013.

Ehrenfest P.: Phasenumwandlungen im ueblichen und erweiterten Sinn, classifiziert nach den entsprechenden Singularitaeten des thermodynamischen Potentiales. In *Proc. Royal Acad. Amsterdam* (**1933**), 36, pp. 153–157.

Ephraim F. & Pfister A.: Uber die Salze einiger aromatischer Carbonsawren und deren Losliehkeit. In *Helv. Chim. Acta* (**1925**), 8, pp. 369-383.

Feng X., Zhou W., Li Y., Ke H., Tang J., Clérac R., Wang Y., Su Z. & Wang E.: Polyoxometalate-Supported 3d–4f Heterometallic Single-Molecule Magnets. In *Inorg. Chem.* (**2012**), 51, 5, pp. 2722-2724, DOI: 10.1021/ic202418y.

Finelli A., Hérault N., Crochet A. & Fromm K. M.: Threading Salen-type Cu- and Ni-Complexes into One-Dimensional Coordination Polymers: Solution versus Solid State and the Size Effect of the Alkali Metal Ion. In *Cryst. Growth Des.* (**2018**), 18, 2, pp. 1215-1226, DOI: 10.1021/acs.cgd.7b01769.

Finger L. W., Cox D. E. & Jephcoat A. P.: A Correction for Powder Diffraction Peak Asymmetry due to Axial Divergence. In *J. Appl. Cryst.* (**1994**), 27, pp. 892-900, DOI: 10.1107/S0021889894004218.

Fogeron T., Retailleau P., Gomez-Mingot M., Li Y. & Fontecave M.: Nickel Complexes Based on Molybdopterin-like Dithiolenes: Catalysts for $CO_2$ Electroreduction. In *Organometallics* (**2019**), 38, 6, pp. 1344-1350, DOI: 10.1021/acs.organomet.8b00655.

Fondo M., Corredoira-Vázquez J., Herrera-Lanzós A., García-Deibe A. M., Sanmartín-Matalobos J., Herrera J. M., Colacio E. & Nuñez C.: Improving the SMM and luminescent properties of lanthanide complexes with $LnO_9$ cores in the presence of $Zn^{II}$: an emissive $Zn_2Dy$ single ion magnet. In *Dalton Trans.* (**2017**), 46, pp. 17000-17009, DOI: 10.1039/c7dt03438e.

Frost J. M., Harriman K. L. M. & Murugesu M.: The rise of 3-d single-ion magnets in molecular magnetism: towards materials from molecules? In *Chem. Sci.* (**2016**), 7, pp. 2470-2491, DOI: 10.1039/C5SC03224E.

Gabro M., Lalancette R. A. & Bernal I.: CCDC 738250: Experimental Crystal Structure Determination. In *CSD Communication* (**2009**), DOI: 10.5517/ccss6j8.

Gangu K. K., Maddila S., Mukkamala S. B. & Jonnalagadda S. B.: Catalytic activity of supra molecular self-assembled Nickel(II) coordination complex in synthesis of indeno-pyrimidine derivatives. In *Polyhedron* (**2019**), 158, pp. 464-470, DOI: 10.1016/j.poly.2018.11.041.

Gavrilenko K. S., Punin S. V., Cador O., Golhen S., Ouahab L. & Pavlishchuk V. V.: In Situ Generation of Carboxylate: An Efficient Strategy for a One-Pot Synthesis of Homo- and Heterometallic Polynuclear Complexes. In *J. Am. Chem. Soc.* (**2005**), 127, 35, pp. 12246-12253, DOI: 10.1021/ja050451p.

Gheorghe R., Andruh M., Müller A. & Schmidtmann M.: Heterobinuclear Complexes as Building Blocks in Designing Extended Structures. In *Inorg. Chem.* (**2002**), 54, pp. 5314-5316, DOI: 10.1021/ic020293s.

Gheorghe R., Andruh M., Costes J.-P., Donnadieu B., Schmidtmann M. & Müller A.: Making 3d–4f hexanuclear clusters from heterotrinuclear cationic building blocks. In *Inorg. Chim. Acta* (**2007**), 360, pp. 4044-4050, DOI: 10.1016/j.ica.2007.05.018.

Ghose B. N.: Synthesis of some Schiff bases. In *Rev. Port. Quim.* (**1983**), 25, pp. 147-150.

Ghose B. N.: Synthesis of some Schiff bases. In *J. Chem. Eng. Data* (**1984**), 29 (2), p. 237, DOI: 10.1021/je00036a042.

Gómez-Coca S., Aravena D., Morales R. & Ruiz, E.: Large magnetic anisotropy in mononuclear metal complexes. In *Coord. Chem. Rev.* (**2015**), 289-290, pp. 379–392, DOI:10.1016/j.ccr.2015.01.021.

Greenwood N. N. & Earnshaw A.: Chemistry of the Elements. In *Butterworth Heinemann*, Oxford (**1997**), ISBN: 0-7506-3365-4.

Guo Z., Li L., Xu T., Li J. & Wang D.: Aqua-{6,6'-dimethoxy-2,2'-[ethane-1,2-diylbis(nitrilomethylidyne)]diphenolato}nickel(II). In *Acta Cryst.* (**2009**), E65, pp. m1158-m1159, DOI: 10.1107/S1600536809034278.

Güngör S. A. & Kose M.: Synthesis, crystal structure, photoluminescence and electrochemical properties of a sandwiched $Ni_2Ce$ complex. In *J. Mol. Struct.* (**2017**), 1150, pp. 274-278, DOI: 10.1016/j.molstruc.2017.08.091.

Hazra S., Meyrelles R., Januário Charmier A., Rijo P., Guedes da Silva M. F. C. & Pombeiro A. J. L.: N–H···O and N–H···Cl supported 1D chains of heterobimetallic $Cu^{II}/Ni^{II}$–$Sn^{IV}$ cocrystals. In *Dalton Trans.* (**2016**), 45, pp. 17929-17938, DOI: 10.1039/c6dt03118h.

Hertel-Bonn E.: Umwandlungenim Kristallgitter. In *Ztschr. Elektrochem.* (**1931**), 37, 8/9, pp 536-538.

Hino S., Maeda M., Kataoka Y., Nakano M., Yamamura T. & Kajiwara T.: SMM Behavior Observed in Ce(III)$Zn(II)_2$ Linear Trinuclear Complex. In *Chem. Lett.* (**2013**), 42, pp. 1276-1278, DOI: 10.1246/cl.130602.

Hino S., Maeda M., Yamashita K., Kataoka Y., Nakano M., Yamamura T., Nojiri H., Kofu M., Yamamuro O. & Kajiwara T.: Linear trinuclear Zn(II)–Ce(III)–Zn(II) complex which behaves as a single-molecule magnet. In *Dalton Trans.* (**2013**), 42, pp. 2683-2686, DOI: 10.1039/c2dt32812g.

Hrnčiar P.: Organická chémia. In *SPN Bratislava* (**1982**).

Huang X.-C., Zhou C., Wen H.-Y. & Wang X.-Y.: End-On Azido-Bridged 3d–4f Complexes Showing Single-Molecule-Magnet Property. In *Inorg. Chem.* (**2013**), 52, 13, pp. 7314-7316, DOI: 10.1021/ic400986y.

Im H. J. & Lee S. W.: Compartment compounds as secondary building units for the preparation of 3d–4f coordination polymers: Preparation, structures, and properties of [NiLn(L)$(NO_3)_2$(4-pyp)(EtOH)] (Ln = Nd, Eu; $H_2L$ = 1,3-bis((3-methoxysalicylidene)amino)propane; 4-Hpyp = 4-pyridinepropionic acid). In *Polyhedron* (**2015**), 101, pp. 48-55, DOI: 10.1016/j.poly.2015.07.047.

Ishikawa N., Sugita M., Ishikawa T., Koshihara S. & Kaizu Y.: Lanthanide Double-Decker Complexes Functioning as Magnets at the Single-Molecular Level. In *J. Am. Chem. Soc.* (**2003**), 125, pp. 8694-8695, DOI: 10.1021/ja029629n.

Ivaniková R., Boča R., Dlháň L., Fuess H., Mašlejová A., Mrázová V., Svoboda I. & Titiš J.: Heteroleptic nickel(II) complexes formed from N-donor bases, carboxylic acids and water: Magnetostructural correlations. In *Polyhedron* (**2006**), 25, pp. 3261-3268, DOI: 10.1016/j.poly.2006.05.040.

Izougu D. C., Yoshida T., Zhang H., Cosquer G., Katoh K., Ogata S., Hasegawa M., Nojiri H., Damjanović M., Wernsdorfer W., Uruga T., Ina T., Breedlove B. K. & Zamashita M.: Slow Magnetic Relaxation in a Palladium–Gadolinium Complex

Induced by Electron Density Donation from the Palladium Ion. In *Chem. Eur. J.* (**2018**), 24, pp. 9285-9294, DOI: 10.1002/chem.201800699.

Jana A., Majumder S., Carrella L., Nayak M., Weyhermueller T., Dutta S., Schollmeyer D., Rentschler E., Koner R. & Mohanta S.: *N,N′-bis*(2-hydroxy-3-methoxybenzylidene)-1,3-diaminopropane dimeric 4*f* and 3*d*–4*f* heterodinuclear complexes: Syntheses, crystal structures and magnetic properties. In *Inorg. Chim. Acta* (**2010**), 363 (14), pp 3706-3713, DOI: 10.1016/j.ica.2010.05.030.

Jia H.-P., Li W., Ju Z.-F. & Zhang J.: Synthesis, structure, and magnetic properties of a novel mixed-bridged heterometal tetranuclear complex $[Mn_2Ni_2(MeOSalen)_2(\mu_{1,1}\text{-}N_3)_2(N_3)_2]$. In *Inorg. Chem. Commun.* (**2007**), 10, 4, pp. 397-400, DOI: 10.1016/j.inoche.2006.12.009.

Jiang G.-B., Zhang S.-H. & Zeng M.-H.: Aqua-{6,6′-dimethoxy-2,2′-[ethane-1,2-diylbis(nitrilomethylidyne)]diphenolato-$\kappa^4$*O,N,N′,O′*}cobalt(II). In *Acta Cryst.* (**2007**), E63, p. m2383, DOI: 10.1107/S1600536807039487.

Jiang L., Liu B., Zhao H.-W., Tian J.-L., Liu X. & Yan S.-P.: Compartmental ligand approach for constructing 3d–4f heterometallic $[Cu^{II}_5Ln^{III}_2]$ clusters: synthesis and magnetostructural properties. In *CrystEngComm* (**2017**), 19, pp. 1816-1830, DOI: 10.1039/c6ce02519f.

Jiang S. D. & Qin S. X.: Prediction of the quantized axis of rare-earth ions: the electrostatic model with displaced point charges. In *Inorg. Chem. Front.* (**2015**), 2, pp. 613-619, DOI: 10.1039/c5qi00052a.

Jin W.-J., Ding L.-Q., Chu Z., Chen L.-L., Lü X.-Q., Zheng X.-Y., Song J.-R. & Fan D.-D.: Controllable bulk solvent-free melt ring-opening polymerization (ROP) of L-lactide catalyzed by Ni(II) and Ni(II)–Ln(III) complexes based on the Salen-type Schiff-base ligand. In *Journal of Molecular Catalysis A: Chemical* (**2011**), 337, pp. 25-32, DOI: 10.1016/j.molcata.2011.01.009.

Jin Z., Bai J., Wei T., Li F., Song C., Luo X. & Xu L.: A new series of mononuclear lanthanide single molecule magnets based on sandwich-type germanomolybdates $[Ln(GeMo_{11}O_{39})_2]^{13-}$ (Ln = $Er^{III}$, $Gd^{III}$, $Dy^{III}$ or $Tb^{III}$). In *New J. Chem.* (**2017**), 41, pp. 13490-13494, DOI: 10.1039/c7nj02104f.

Jin Im H. & Lee S. W.: Compartment compounds as secondary building units for the preparation of 3d–4f coordination polymers: Preparation, structures, and

properties of [NiLn(L)(NO3)2(4-pyp)(EtOH)] (Ln = Nd, Eu; H2L = 1,3-bis((3-methoxysalicylidene)amino)propane; 4-Hpyp = 4-pyridinepropionic acid). In *Polyhedron* (**2015**), 101, pp. 48-55, DOI: 10.1016/j.poly.2015.07.047.

Kaltsoyannis N. & Scott P.: The f elements. In *Oxford University Press*, New York (**1999**), ISBN: 9780198504672.

Kanetomo T., Kihara T., Miyake A., Matsuo A., Tokunaga M., Kind K., Nojiri H. & Ishida T.: Giant Exchange Coupling Evidenced with a Magnetization Jump at 52 T for a Gadolinium-Nitroxide Chelate. In *Inorg. Chem.* (**2017**), 56, pp. 3310-3314, DOI: 10.1021/acs.inorgchem.6b02685.

Kano S., Nakano H., Kojima M., Baba N., Nakajima K.: An effect of the ionic radii of lanthanide(III) ions on the structure and catalytic properties of chiral Schiff base-lanthanide(III) complexes. In *Inorg. Chim. Acta* (**2003**), 349, pp. 6-16, DOI: 10.1016/S0020-1693(03)00052-5.

Khandar A. A., Shaabani B., Belaj F. & Bakhtiari A.: Synthesis, characterization and spectroscopic and electrochemical studies of new axially coordinated cobalt(III) salen (salen = N,N′-bis(salicylidene)-1,2-ethylenediamine) complexes. The crystal structure of $[Co^{III}(salen)(aniline)_2]ClO_4$. In *Polyhedron* (**2006**), 25, pp. 1893-1900, DOI: 10.1016/j.poly.2005.12.001.

Khélifa A. B., Belkhiria M. S., Huang G., Freslon S., Guillou O. & Bernot K.: Single-molecule magnet behaviour in polynuclear assembly of trivalent Cerium ions with Polyoxomolybdates. In *Dalton Trans.* (**2015**), 44, pp. 16458-16464, DOI: 10.1039/c5dt02377g.

King A. P., Gellineau H. A., MacMillan S. N. & Wilson J. J.: Physical properties, ligand substitution reactions, and biological activity of Co(III)-Schiff base complexes. In *Dalton Trans.* (**2019**), 48, pp. 5987-6002, DOI: 10.1039/c8dt04606a.

Kitaigorodskii A. I.: The principle of close packing and the condition of thermodynamic stability of organic crystals. In *Acta Cryst.* (**1965**), 18, pp. 585-590, DOI: 10.1107/S0365110X65001391.

Koizumi H., Osaki K. & Watanabe T.: Crystal Structure of Cupric Benzoate Trihydrate $Cu(C_6H_5COO)_2{\cdot}3H_2O$. In *J. Phys. Soc. Jpn.* (**1963**), 18, pp. 117-124, DOI: 10.1143/JPSJ.18.117.

Kooijman H., Godbole M. D., Bouwman E. & Spek A. L.: CCDC 617333: Experimental Crystal Structure Determination. In *CSD Communication* (**2006**), DOI: 10.5517/ccnqczp.

Kostin G. A., Borodin A. O., Kuratieva N. V., Bogomyakov A. S. & Mikhailov A. A.: Tetranuclear $Ru_2Ln_2$ complexes of heavier lanthanides (Gd, Tb, Dy, Ho, Lu) with $[RuNO(NO_2)_4OH]^{2-}$ anion, combining SMM properties and photoswitchable Ru-NO group. In *Inorg. Chim. Acta* (**2018**), 479, pp. 135-140, DOI: 10.1016/j.ica.2018.04.006.

Kubicki M.: CCDC 741414: Experimental Crystal Structure Determination. In *CSD Communication* (**2009**), DOI: 10.5517/ccswhlq.

Langley S. K., Chilton N. F., Ungur L., Moubaraki B., Chibotaru L. F. & Murray K. S.: Heterometallic Tetranuclear $[Ln^{III}_2Co^{III}_2]$ Complexes Including Suppression of Quantum Tunneling of Magnetization in the $[Dy^{III}_2Co^{III}_2]$ Single Molecule Magnet. In *Inorg. Chem.* (**2012**), 51, pp. 11873-11881, DOI: 10.1021/ic301784m.

Langley S. K., Wielechowski D. P., Vieru V., Chilton N. F., Moubaraki B., Abrahams B. F., Chibotaru L. F. & Murray K. S.: A $\{Cr^{III}_2Dy^{III}_2\}$ Single-Molecule Magnet: Enhancing the Blocking Temperature through 3d Magnetic Exchange. In *Angew. Chem.* (**2013**), 125, pp. 12236-12241, DOI: 10.1002/ange.201306329.

Lis T.: Preparation, Structure, and Magnetic Properties of a Dodecanuelear Mixed-Valence Manganese Carboxylate. In *Acta Cryst.* (**1980**), B36, pp. 2042-2046, DOI: 10.1107/S0567740880007893.

Liu D.-X., Li S.-L., Cui X.-G., Li X.-Y. In *Gaodeng Xuexiao Huaxue Xuebao* (**1993**), 14, p. 897.

Liu D.-F., Lü X.-Q. & Lu R.: Homogeneous and heterogeneous styrene epoxidation catalyzed by copper(II) and nickel(II) Schiff base complexes. In *Transition Met Chem* (**2014**), 39, pp. 705-712, DOI: 10.1007/s11243-014-9853-6.

Liu K., Shi W. & Cheng P.: Toward heterometallic single-molecule magnets: Synthetic strategy, structures and properties of 3d-4f discrete complexes. In *Coord. Chem. Rev.* (**2015**), 289-290, pp. 74-122, DOI: 10.1016/j.ccr.2014.10.004.

Liu Y., Cerveri A., De Nisi A., Monari M., Nieto Faza O., Silva Lopez C. & Bandini M.: Nickel catalyzed regio- and stereoselective arylation and methylation of

allenamides *via* coupling reactions. An experimental and computational study. In *Org. Chem. Front.* (**2018**), 5, pp. 3231-3239, DOI: 10.1039/c8qo00729b.

Liu Y.-P., Di Y.-Y., He D.-H., Kong Y.-X., Yang W.-W. & Dan W.-Y.: Lattice potential energy and thermochemical properties of ethylenediaminedihydrochloride ($C_2H_{10}N_2Cl_2$). In *J. Chem. Thermodynamics* (**2010**), 42, pp. 513–517, DOI: 10.1016/j.jct.2009.11.007.

Long J., Chamoreau L.-M. & Marvaud V.: Heterotrimetallic 3d-4d-4f decanuclear metal-capped square showing single-molecule magnet behaviour. In *Dalton Trans.* (**2010**), 39, pp. 2188-2190, DOI: 10.1039/B924644B.

Lotgering F. K.: Topotactical Reactions with Ferrimagnetic Oxides Having Hehagonal Crystal Structures-I. In *J. Inorg. Nucl. Chem.* (**1959**), 9, pp. 113-123.

Macrae C. F., Bruno I. J., Chisholm J. A., Edgington P. R., McCabe P., Pidcock E., Rodriguez-Monge L., Taylor R., van de Streek J. & Wood P. A.: Mercury CSD 2.0 - New Features for the Visualization and Investigation of Crystal Structures. In *J. Appl. Cryst.* (**2008**), 41, pp. 466-470, DOI: 10.1107/S0021889807067908.

Madalan A. M., Avarvari N. & Andruh M.: Metal complexes as second-sphere ligands. In *New J. Chem*. (**2006**), 30, pp. 521-523, DOI: 10.1039/B517989K.

Müller U.: Symmetry Relationships between Crystal Structures. In *Oxford University Press*, Oxford (**2013**), ISBN: 978–0–19–966995–0.

Neese F. & Pantazis D. A.: What is not required to make a single molecule magnet. In *Faraday Discuss.* (**2011**), 148, pp. 229-238, DOI: 10.1039/C005256F.

Nelyubina Y. V., Puntus L. N. & Lyssenko K. A.: The Dark Side of Hydrogen Bonds in the Design of Optical Materials: A Charge-Density Perspective. In *Chem. Eur. J.* (**2014**), 20, pp. 2860-2865, DOI: 10.1002/chem.201300566.

Osa S., Kido T., Matsumoto N., Re N., Pochaba A. & Mrozinski J.: A Tetranuclear 3d-4f Single Molecule Magnet: $[Cu^{II}LTb^{III}(hfac)_2]_2$. In *J. Am. Chem. Soc.* (**2004**), 126, pp. 420-421, DOI: 10.1021/ja037365e.

Pasatoiu T. D., Sutter J.-P., Madalan A. M., Fellah F. Z. C., Duhayon C. & Andruh M.: Preparation, Crystal Structures, and Magnetic Features for a Series of Dinuclear $[Ni^{II}Ln^{III}]$ Schiff-Base Complexes: Evidence for Slow Relaxation of the Magnetization for the $Dy^{III}$ Derivative. In *Inorg. Chem.* (**2011**), 20, pp. 5890-5898, DOI: 10.1021/ic2004276.

Pasatoiu T. D., Tiseanu C., Madalan A. M., Jurca B., Duhayon C., Sutter J.-P. & Andruh M.: Study of the Luminescent and Magnetic Properties of a Series of Heterodinuclear [$Zn^{II}Ln^{III}$] Complexes. In *Inorg. Chem.* (**2011**), 50, pp. 5879-5889, DOI: 10.1021/ic200426w.

Pearson R. G.: Hard and Soft Acids and Bases. In *J. Am. Chem. Soc.* (**1963**), 85(22), pp. 3533-3539, DOI: 10.1021/ja00905a001.

Petrosyants S. P., Ilyukhin A. B., Efimov N. N., Gavrikov A. V. & Novotortsev V. M.: Self-assembly and SMM properties of lanthanide cyanocobaltate chain complexes with terpyridine as blocking ligand. In *Inorg. Chim. Acta* (**2018**), 482, pp. 813-820, DOI: 10.1016/j.ica.2018.07.029.

Petříček V., Dušek M. & Palatinus L.: Crystallographic Computing System JANA2006: General features. In *Z. Kristallogr.* (**2014**), 229(5), pp. 345-352, DOI: 10.1515/zkri-2014-1737.

Pointillart F., Cador O., Le Guennic B. & Ouahab L.: Uncommon lanthanide ions in purely 4*f* Single Molecule Magnets. In *Coord. Chem. Rev.* (**2017**), 346, pp. 150-175, DOI: 10.1016/j.ccr.2016.12.017.

Rajnák C., Titiš J., Moncoľ J, Mičová R. & Boča R.: Field-Induced Slow Magnetic Relaxation in a Mononuclear Manganese(II) Complex. In *Inorg. Chem.* (**2019**), 58, 2, pp. 991-994, DOI: 10.1021/acs.inorgchem.8b02675.

Reath A. H., Ziler J. W., Tsay C., Ryan A. J. & Yang J. Y.: Redox Potential and Electronic Structure Effects of Proximal Nonredox Active Cations in Cobalt Schiff Base Complexes. In *Inorg. Chem.* (**2017**), 56, 6, pp. 3713-3718, DOI: 10.1021/acs.inorgchem.6b03098.

Reuter H. & Kastner G.: Redetermination of the crystal structure of ethylenediammonium chloride, $C_2H_{10}Cl_2N_2$. In *Z. Kristallogr. NCS* (**1997**), 212, p. 188, DOI: 10.1524/ncrs.1997.212.1.188.

Le Roy J. J., Korobkov I., Kim J. E., Schelter E. J. & Murugesu M.: Structural and magnetic conformation of a cerocene $[Ce(COT'')_2]^-$ exhibiting a uniconfigurational $f^1$ ground state and slow-magnetic relaxation. In *Dalton Trans.* (**2014**), 43, pp. 2737-2740, DOI: 10.1039/c3dt53280a.

Schieber C., Howitt J., Putz U., White J. M., Parish C. L., Donnelly P. S. & Tan S.-S.: Cellular Up-regulation of Nedd4 Family Interacting Protein 1 (Ndfip1) using Low

Levels of Bioactive Cobalt Complexes. In *J. Biol. Chem.* (**2011**), 286, pp. 8555-8564, DOI: 10.1074/jbc.M110.203448.

Seidel R. W.: CCDC 694332: Experimental Crystal Structure Determination. In *CSD Communication* (**2009**), DOI: 10.5517/ccr9htb.

Sessoli R., Gatteschi D., Caneschi A. & Novak M. A.: Magnetic bistability in a metal-ion cluster. In *Nature* (**1993**), 365, pp. 141-143, DOI: 10.1038/365141a0.

Shannon R. D.: Revised effective ionic radii and systematic studies of interatomic distances in halides and chalcogenides. In *Acta Cryst.* (**1976**), A32, pp. 751-767, DOI: 10.1107/S0567739476001551.

Shen Y., Gu Y. & Martin R.: $sp^3$ C–H Arylation and Alkylation Enabled by the Synergy of Triplet Excited Ketones and Nickel Catalysts. In *J. Am. Chem. Soc.* (**2018**), 140, 38, pp. 12200-12209, DOI: 10.1021/jacs.8b07405.

Shiga T., Ito N., Hidaka A., Okawa H., Kitagawa S. & Ohba M.: Series of Trinuclear $Ni^{II}Ln^{III}Ni^{II}$ Complexes Derived from 2,6-Di(acetoacetyl)pyridine: Synthesis, Structure, and Magnetism. In *Inorg. Chem.* (**2007**), 46, pp. 3492-3501, DOI: 10.1021/ic0619153.

Siegler M. A. & Lutz M.: Ni(salen): a System That Forms Many Solvates with Interacting Ni Atoms. In *Cryst. Growth Des.* (**2009**), 9, 2, pp. 1194-1200, DOI: 10.1021/cg801109n.

Singh S. K., Gupta T., Ungur L. & Rajaraman G.: Magnetic Relaxation in Single-Electron Single-Ion Cerium(III) Magnets: Insights from Ab Initio Calculations. In *Chem. Eur. J.* (**2015**), 21, pp. 13812-13819, DOI: 10.1002/chem.201501330.

Sisqueira A. B., Ionashiro E. Y., de Carvalho C. T., Bannach G., Rodrigues E. C. & Ionashiro M.: Synthesis, characterization and thermal behaviour of solid-state compounds of benzoates with some bivalent transition metal ions. In *Quim. Nova* (**2007**), 30, 2, pp. 318-322, DOI: 10.1590/S0100-40422007000200015.

Smolko L., Černák J., Dušek M., Miklovič J., Titiš J. & Boča R.: Three tetracoordinate Co(II) complexes $[Co(biq)X_2]$ (X = Cl, Br, I) with easy-plane magnetic anisotropy as field-induced single-molecule magnets. In *Dalton Trans.* (**2015**), 44, pp. 17565-17571, DOI: 10.1039/c5dt02827b.

Smolko L., Černák J., Dušek M., Titiš J. & Boča R.: Tetracoordinate Co(II) complexes containing bathocuproine and single molecule magnetism. In *New J. Chem.* (**2016**), 40, pp. 6593-6598, DOI: 10.1039/c6nj00372a.

Spackman M. A. & Jayatilaka D.: Hirshfeld surface analysis. In *Cryst. Eng. Comm.* (**2009**), 11, pp. 19-32. DOI: 10.1039/b818330a.

Spackmann M. A. & McKinnon J. J.: Fingerprinting intermolecular interactions in molecular crystals. In *CrystEngComm* (**2002**), 4, pp. 378-392, DOI: 10.1039/B203191B.

Spohn M. & Strähle J.: Benzoatokomplexe des Eisens und Cobalts: Synthese und Eigenschaften von $Fe_3(C_6H_5COO)_4(acac)_2$, $Fe(C_6H_5COO)_2$ und $Co(C_6H_5COO)_2$, Kristallstruktur von $Fe_3(C_6H_5COO)_4(acac)_2$ und $Co(C_6H_5COO)_2$. In *Z. Naturforsch., B*: *Chem. Sci*. (**1988**), 43, pp. 540-546, DOI: 10.1515/znb-1988-0509.

Sreekumar S. S., Mohan N. & Prathapachandra Kurup M. R.: Water-Encapsulated Ni(II) Salphen-Type Host Complexes: Experimental and Theoretical Analysis of Potentially Bioactive Quasi-Isostructural Polymorphs. In *ChemistrySelect* (**2017**), 2, pp. 6493-6502, DOI: 10.1002/slct.201701229.

Sun W.-B., Yan P.-F., Jiang S.-D., Wang B.-W., Zhang Y.-Q., Li H.-F., Chen P., Wang Z.-M. & Gao S.: High symmetry or low symmetry, that is the question – high performance Dy(III) single-ion magnets by electrostatic potential design. In *Chem, Sci.* (**2016**), 7, pp. 684-691, DOI: 10.1039/c5sc02986d.

Thomas T. W. & Underhill A. E.: Metal–metal interactions in transition-metal complexes containing infinite chains of metal atoms. In *Chem. Soc. Rev.* (**1972**), 1, pp. 99-120, DOI: 10.1039/CS9720100099.

Thompson P., Cox D. E. & Hastings J. B.: Rietveld refinement of Debye-Scherrer synchrotron X-ray data from $Al_2O_3$. In *J. Appl. Cryst.* (**1987**), 20, pp. 79-83, DOI: 10.1107/S0021889887087090.

Thurston J. H., Tang C. G.-Z., Trahan D. W. & Whitmire K. H.: Toward Rational Control of Metal Stoichiometry in Heterobimetallic Coordination Complexes: Synthesis and Characterization of $Pb(Hsal)_2(Cu(salen^*))_2$, $[Pb(NO_3)(Cu(salen^*))_2](NO_3)$, $Pb(OAc)_2(Cu(salen^*))$, and $[Pb(OAc)(Ni(salen^*))_2](OAc)$. In *Inorg. Chem.* (**2004**), 43, 8, pp.2708-2713, DOI: 10.1021/ic035427w.

Titiš J., Rajnák C., Valigura D. & Boča R.: Field Influence on the Slow Magnetic Relaxation of Nickel-based Single Ion Magnets. In *Dalton Trans*. (**2018**), 47, pp. 7879-7882, DOI: 10.1039/C8DT01445K.

Upadhyay A., Singh S. K., Das C., Mondol R., Langley S. K., Murray K. S., Rajaraman G. & Shanmugam M.: Enhancing the effective energy barrier of a Dy(III) SMM using a bridged diamagnetic Zn(II) ion. In *Chem. Commun.* (**2014**), 50, pp. 8838-8841, DOI: 10.1039/c4cc02094d.

Upadhyay A., Das C., Vaidya S., Singh S. K., Gupta T., Mondol R., Langley S. K., Murray K. S., Rajaraman G. & Shanmugam M.: Role of the Diamagnetic Zinc(II) Ion in Determining the Electronic Structure of Lanthanide Single-Ion Magnets. In *Chem. Eur. J.* (**2017**), 23, pp. 4903-4916, DOI: 10.1002/chem.201700399.

Visinescu D., Madalan A. M., Andruh M., Duhayon C., Sutter J.-P., Ungur L., Van den Heuvel W. & Chibotaru L. F.: First Heterotrimetallic {3d-4d-4f} Single Chain Magnet, Constructed from Anisotropic High-Spin Heterometallic Nodes and Paramagnetic Spacers. In *Chem. Eur. J.* (**2009**), 15, pp. 11808-11814, DOI: 10.1002/chem.200902408.

Visinescu D., Jeon I.-R., Madalan A. M., Alexandru M.-G., Jurca B., Mathonière C., Clérac R. & Andruh M.: Self-assembly of $[Cu^{II}Tb^{III}]^{3+}$ and $[W(CN)_8]^{3-}$ tectons: a case study of a mixture containing two complexes showing slow-relaxation of the magnetization. In *Dalton Trans.* (**2012**), 41, pp. 13578-13581, DOI: 10.1039/c2dt32081a.

Vladimirova A., Patskovsky Y., Fedorov A. A., Bonanno J. B., Fedorov E. V., Toro R., Hillerich B., Seidel R. D., Richards N. G. J, Almo S. C. & Raushel F. M.: Substrate Distortion and the Catalytic Reaction Mechanism of 5‑Carboxyvanillate Decarboxylase. In *J. Am. Chem. Soc.* (**2016**), 138, pp. 826-836, DOI: 10.1021/jacs.5b08251.

Vráblová A., Falvello L. R., Campo J., Miklovič J., Boča R., Černák J. & Tomás M: New preparation, first structure analysis and magnetism of the long-known nickel benzoate trihydrate: A linear Ni···Ni···Ni polymer and its parallels to the active site of urease. In *Eur. J. Inorg. Chem.* (**2016**), pp. 928-934, DOI: 10.1002/ejic.201501255.

Vráblová A., Černák J., Tomás M. & Falvello L. R.: CCDC 1549602: Experimental Crystal Structure Determination. In *CSD Communication* (**2017**), DOI: 10.5517/ccdc.csd.cc1p0h5c.

Wang W. & Shen Y.-M.: Aqua-(dicyanamido){μ-6,6'-dimethoxy-2,2'-[ethane-1,2-diylbis(nitrilomethylidyne)]diphenolato}nickel(II)sodium. In *Acta Cryst.* (**2009**). E65, p. m557, DOI: 10.1107/S160053680901438X.

Wei Y., Pang T., Liu J., Li M. & Liang L.: Aqua-chlorido{6,6'-dimethoxy-2,2'-[ethane-1,2-diylbis(nitrilomethanylylidene)]diphenolato-$\kappa^2O^1$,N,N',$O^{1'}$}cobalt(III) dimethylformamide monosolvate. In *Acta Cryst.* (**2012**), E68, pp. m455-m456, DOI: 10.1107/S1600536812011324.

Wen H.-R., Liu S.-J., Xie X.-R., Bao J., Liu C.-M. & Chen J.-L.: A family of nickel–lanthanide heterometallic dinuclear complexes derived from a chiral Schiff-base ligand exhibiting single-molecule magnet behaviors. In *Inorg. Chim. Acta* (**2015**), 435, pp. 274-282, DOI: 10.1016/j.ica.2015.07.009.

Wong W.-K., Yang X., Jones R. A., Rivers J. H., Lynch V., Lo W.-K., Xiao D., Oye M. M. & Holmes A. L.: Multinuclear Luminescent Schiff-Base Zn-Nd Sandwich Complexes. In *Inorg. Chem.* (**2006**), 45, pp. 4340-4345, DOI: 10.1021/ic051866e.

Wood P. A., Olsson T. S. G., Cole J. C., Cottrell S. J., Feeder N., Galek P. T. A., Groom C. R. & Pidcock E.: Evaluation of molecular crystal structures using Full Interaction Maps. In *CrystEngComm* (**2013**), 15, pp. 65-72, DOI: 10.1039/c2ce25849h.

Xiao H.-Q.: {$\mu$-6,6'-Dimethoxy-2,2'-[ethane-1,2-diylbis(nitrilomethylidyne)] diphenolato-1$\kappa^4O^6$,$O^1$,$O^{1'}$,$O^{6'}$:2$\kappa^4O^1$,N,N',$O^{1'}$}(methanol-1$\kappa$O)(perchlorato-1$\kappa$O)nickel (II)sodium. In *Acta Cryst.* (**2009**), E65, p. m400, DOI: 10.1107/S1600536809007776.

Xing J.: Aqua-chlorido{6,6'-dimeth-oxy-2,2'-[ethane-1,2-diylbis(nitrilo-dimethyl -idyne)]diphenolato-[kappa]2O1,N,N',O1'}cobalt(III) monohydrate. In *Acta Cryst.* (**2009**), E65, p. m468, DOI: 10.1107/S1600536809011167.

Yaday S., Kumar S. & Gupta R.: Cobalt complexes of pyrrolecarboxamide ligands as catalysts in nitro reduction reactions: influence of electronic substituents on catalysis and mechanistic insights. In *Inorg. Chem. Front.* (**2017**), 4, pp. 324-335, DOI: 10.1039/c6qi00389c.

Yao M. X., Lu X. Y., Zhu Z. X., Deng X. W. & Jing S.: Synthesis, structures and magnetism of a series of dinuclear and one-dimensional Ni–Ln complexes: single-

molecule magnetic behavior in one-dimensional nitrate-bridged Dy analogue. In *New J. Chem.* (**2015**), 39, pp. 8356-8363, DOI: 10.1039/c5nj01708d.

Yu Y.-Y.: {6,6'-Dimethoxy-2,2'-[ethane-1,2-diylbis(nitrilomethylidyne)] diphenolato}nickel(II) chloro-form solvate. In *Acta Cryst.* (**2006**), E62, pp. m948-m949, DOI: 10.1107/S160053680601049X.

Zhang D. & Zhao Z.: CCDC 815382: Experimental Crystal Structure Determination. In *CSD Communication* (**2012**), DOI: 10.5517/ccwcgnb.

Zhang Q., Zhang R., Ma Y., Solan G. A., Liang T. & Sun W.-H.: Branched polyethylenes attainable using thermally enhanced bis(imino)acenaphthene-nickel catalysts: Exploring the effects of temperature and pressure. In *Applied Catalysis A, General* (**2019**), 573, pp. 73-86, DOI: 10.1016/j.apcata.2019.01.016.

# 10 Appendix

1. Vráblová A., Falvello L. R., Campo J., Miklovič J., Boča R., Černák J. & Tomás M.: Preparation, First Structure Analysis, and Magnetism of the Long-Known Nickel Benzoate Trihydrate – A Linear Ni···Ni···Ni Polymer and Its Parallels with the Active Site of Urease. In *Eur. J. Inorg. Chem.* (**2016**), pp. 928-934, DOI: 10.1002/ejic.201501255

2. Vráblová A., Černák J., Rajnák C., Dlháň Ľ., Tomás M., Falvello L. R. & Boča R.: Exceptionally slow magnetic relaxation in cobalt(II) benzoate trihydrate. In *Dalton Trans.* (**2018**), 47, pp. 15523-15529, DOI: 10.1039/c8dt03610a

3. Vráblová A., Černák J., Falvello L. R. & Tomás M.: Polymorphism of the dinuclear $Co^{III}$–Schiff base complex $[Co_2(o\text{-van-en})_3]\cdot 4CH_3CN$ (*o*-van-en is a salen-type ligand). In *Acta Cryst.* (**2019**), C75, pp. 433-442, DOI: 10.1107/S2053229619003115

4. Vráblová A., Tomás M., Falvello L. R., Dlháň Ľ., Titiš J., Černák J. & Boča R.: Slow magnetic relaxation in Ni – Ln (Ln = Ce, Gd, Dy) dinuclear complexes. In *Dalton Trans.* (**2019**), 48, pp. 13943-13952, DOI: 10.1039/c9dt02122a

5. Vráblová A., Tomás M., Titiš J., Černák J. & Falvello L. R.: On new solvatomorphs of the metalloligand [Ni(*o-van-en*)]. In *Inorganica Chimica Acta* (**2020**), 512, art. no. 119874, DOI: 10.1016/j.ica.2020.119874